UNIVERSITY OF BIRMINGHAM

COMBINED NUMERICAL AND MORPHOLOGICAL STUDY OF
THE LUMBAR SPINE: PARAMETRIC FINITE ELEMENT
MODEL AND EVALUATION OF DYNAMIC IMPLANTS

By

Carolina Eleonora Lavecchia

A thesis submitted to the
University of Birmingham
for the degree of
DOCTOR OF PHILOSOPHY

School of Engineering
Department of Mechanical Engineering
University of Birmingham
March, 2018

UNIVERSITY OF BIRMINGHAM

University of Birmingham Research Archive

e-theses repository

Abstract

Low back pain is a major cause of disability and requires the development of new devices to treat pathologies and improve prognosis following surgery. The development of new devices requires the evaluation of new design, prototyping and mechanical testing. Finite Element (FE) Methods represent an appealing solution to provide mechanical evaluations of new devices speeding up the design process, as well as evaluating several anatomical scenarios. Particularly, new implants can be developed following subject-specific geometries and/or using material properties optimized for the particular subject. The overall aim of this thesis was to develop an accurate FE of the lumbar spine and the evaluation of the variability introduced by morphological and material parameters and evaluate the mechanics of two devices: the BDyn, a posterior stabilization device developed by $S14\ Implants$ (Pessac, France) and the GsDyn a device for the paediatric scoliosis developed as part of the Spinal Implant Design (SID) project.

Morphological studies were conducted to evaluate the average dimensions of the lumbar spine and correlation analyses available in literature were compared with subject-specific data-sets. A parametric and scalable geometrical model of the lumbar spine has been developed and the dimensions can be scaled according to either correlation studies or subject-specific measurements from data-scan. The generation of the geometrical model were implemented in a toolbox, the LMG (Lumbar Model Generator) developed in Matlab. It allows the automatic preparation of the FE model, performing the mesh generation and evaluation, assigning material properties, boundary conditions and analysing the results. The model generation and pre-processing are performed in less than five minutes, obtaining then a tool with potential clinical and industrial applications. A L1-L5 model has been generated as proof-of-concept and a functional unit (L1-L2) was analysed and the results were in agreement with experimental and computational results available in literature. One of the advantage of the LMG is the generation and pre-processing of population of models, allowing the evaluation of anatomical variations and material properties of the bodies involved. Thus, preliminary sensitivity analyses on the L1-L2 functional unit were performed, varying morphological parameters and material properties, to identify the most influential parameters in the biomechanics of the spine. A non-linear, dynamic FE model of the BDyn was developed and validated with experimental results. The BDyn was modelled in combination with the GsDyn to evaluate the effects of elastomeric components on the device. The results showed a fourfold reduction of the peak stress on the locking system of the GsDyn which could improve the durability of the device.

Acknowledgements

Contents

List of Figures

List of Tables

Acronyms

AF Anulus Fibrosus.

ALL Anterior Longitudinal Ligament.

CAD Computer Aided Design.

CEP Cartilaginous Endplates.

CT Computer-Tomographic.

DMA Dynamic Mechanical Analysis.

EOS Early Onset Scoliosis.

EPD Endplate Depth.

EPW Endplate Width.

FDA Food and Drug Administration.

FE Finite Element.

FEM Finite Element Model.

FJF Facet Joint Forces.

FSU Functional Spinal Unit.

FU Functional Unit.

HGO Holazpfel-Gasser-Odgen.

IDP Intervertebral Disc Pressure.

ISL Inter-Spinous Ligament.

ITL Inter-Transverse Ligament.

IVD Intervertebral disc.

IVDd Intervertebral Disc Depth.

IVDw Intervertebral Disc Width.

LBP Low Back Pain.

LF Ligamentum Flavum.

LMG Lumbar Model Generator.

LVDT Linear Variable Displacement Trasducer.

MDIC Medical Devices Innovation Consortium.

MRI Magnetic Resonance Images.

NP Nucleus Pulposus.

PCU Polycarbonate Polyurethane.

PDH Pedicle Height.

PDIs Pedicle Inclination-sagittal plane.

PDIt Pedicle Inclination-transverse plane.

PDW Pedicle Width.

PLL Posterior Longitudinal Ligament.

PSD Posterior Stabilization Device.

RoM Range of Motion.

RVDT Rotational Variable Displacement Trasducer.

SCD Spinal Canal Depth.

SCW Spinal Canal Width.

SID Spinal Implant Design.

Sil Silicone.

SPL Spinous Process Length.

SSL Super-Spinous Ligament.

TL Transverse Ligament.

TPW Transverse Process Width.

VBHp Vertebral Body Height (posterior).

VHP Visible Human Project.

VP Volumetric Percentage.

Chapter 1

Introduction

Back pain is one of the main musculoskeletal disorders with major disability effects on the population worldwide [1]. In England, Low Back Pain (LBP) is one of the first causes of activity limitation, sick leave, and hospitalisation. The related economic effects burden governments, individuals and the society more widely [2] and in the USA, from 1998 to 2008, the healthcare costs increased from 4.3 to 33.9 billion [3]. In between the pathological diseases causing the LBP, the IVD degeneration causes disc bulging, and herniation with consequent compression on the spinal nerve. At the early stage of the back pain, non-surgical treatments represent a solution for early stage pathological cases. In these cases, it is still possible to reduce the pain and restore a normal quality of life, re-establishing good postural habits and improving the muscular tone through muscle relaxation and anti-inflammatory medications, steroid injections, physical therapy and spinal manipulations [4]. Surgical intervention is the last resort, with the most common intervention being spinal fusion [5]. In the USA, the number of spinal fusion increased from 174,223 to 413,171 between 1998 and 2008 [3]. Spinal fusion is associated with prolonged recuperation time, loss of mobility at the fused level and has been shown to increase stress at the adjacent unfused levels [6, 7] potentially resulting in degeneration and pseudarthrosis [8]. Indeed, the development of alternatives to the fusion system are needed.

The development of new devices requires the evaluation of new design, prototyping and mechanical testing. Mechanical test can be used to evaluate the mechanical behaviour of a device [9, 10], however a limited number of samples and experimental scenarios can be evaluated and it is not easily possible to predict the stress distribution on the biological structures. *In vitro* studies have been conducted with cadaver specimens, but the storage conditions and the missing active soft-tissues (i.e. muscles) affect the results.
Finite Element (FE) Models represent an appealing alternative to experimental test. Particularly, in the development of spinal implants, they could

help in the development of new design, following subject-specific geometries and/or using material properties optimized for the particular subject [11]. The geometry of the spine presents a high level of complexity [12], characterized by different features at each level of the trunk. The reconstruction of accurate geometrical model of the spine is a key factor in the evaluation of accurate FE models [13, 14, 15]. At the same time, in order to obtain results valid for a wide population, a high number of subject-specific models, able to cover the anatomical variability inter- and intra-subjects, have to be analysed. However, reconstructing and pre-processing subject-specific models is a time consuming process, which introduce a massive gap between the idea of analyse multiple models and the aim of evaluate several designs iteratively in a reduced amount of time than the classic design process (i.e.: concept, design, prototyping, testing, which is subjected to several re-iterations to match the design and regulation criteria), and the possible evaluation of these results for clinical cases. The Food and Drug Administration (FDA) and the Medical Device Innovation Consortium (MDIC) recently underlined the necessity of speeding up the regulatory system providing a methodology to follow in the development of new devices through the use of computational models and simulations [16, 17]. In order to take advantage of these methodologies, accurate models have to be developed.

A solution to these limitations has been proposed in this thesis with the development of a parametric and scalable model, where a baseline model is scaled according to geometric correlations with the height and age of a patient with a given ethnic group or subject-specific dimensions obtained from data-scans. Moreover, the entire pre-processing is completely automatised, allowing the evaluation of several models in a reduced amount of time. The power of such a method can be transferred in clinical application, where the subject-specific variability (i.e. geometry, material properties) would be included in the models (importing the subject-specific dimensions). Potentially, in the future this method could lead clinicians to choose the most appropriate treatment according with the FE analyses.

The development of new devices and the improvements of previous devices already on the market was the focus the Spinal Implant Design (SID) group of the University of Birmingham. These studies were possible also to the collaboration with the S14 Implants (Pessac, France). In this scenario, this PhD thesis was conducted with the goal of supporting and improving the design process through the use of FE models.

The aim of this thesis was to develop an accurate FE of the lumbar spine and the evaluation of the variability introduced by morphological and material parameters and evaluate the mechanics of two devices: the BDyn and GsDyn. The BDyn is a posterior stabilization device developed by *S14 Implants* (Pessac, France) and already on the market. The GsDyn is a device developed as part of the Spinal Implant Design (SID) project [18] to

overcome the actual limitations in the treatment of paediatric scoliosis. These objectives were pursued as follows:

- morphometrical studies were evaluated for developing of parametric models and evaluating anatomical variations (chapter 3);

- a parametric and scalable geometrical model of the lumbar spine was developed and embedded in a Matlab toolbox (Lumbar Model Generation (LMG), chapter 4);

- the pre- and post-processing of the lumbar model are automatically performed in the LMG toolbox (chapter 5). The model of the entire lumbar spine was developed and the validation of a FE model of a spinal functional unit (L1-L2) was performed;

- a sensitivity analyses on the morphological parameters and material properties was evaluated to identify the most influential parameters on the biomechanics of the spine (chapter 6);

- a non-linear FE model of the BDyn was developed and validated with experimental Dynamic Mechanical Analyses (DMA). The BDyn was modelled in combination with the GsDyn and the mechanics of the combined device were assessed (chapter 7).

Chapter 2

Background

The necessity of developing new implants, requires more innovative methods to study the design and optimize the structure and material properties. In this chapter, the theoretical background to understand the spine anatomy, its biomechanics and the devices currently on the market is introduced. The Finite Element (FE) Method has been identified as a possible solution to this research request and an overview of the models developed in the last decades is provided, along with a description of the material properties previously used. The validation of the developed FE models is a key point and experimental test have been described in order to compare experimental and computational results.

2.1 The lumbar spine: anatomy

The spine has a primary function to support the human body during its daily activity [19] and it can be seen as an open chain (Figure 2.1) where vertebral bodies alternate with intervertebral discs (IVD), kept together by ligaments, cartilaginous tissues and muscles. These structures are involved in the movements of the spine, while ligaments and muscles are responsible for limiting the movements and avoid damage.

The vertebral column has thirty-three separate vertebrae, which are categorized in five main areas: cervical, thoracic, lumbar, sacrum and coccyx, and in each of them the structural units have peculiar geometrical features (Figure 2.2). Regardless of the geometrical differences at each level, two areas can be identified: the vertebral body and the posterior elements [12]. The vertebral body has a kidney shaped section in the transverse plane. The external layer is composed of cortical bone and the internal core of cancellous bone, a heterogeneous and anisotropic porous structure of interconnected trabeculae [20]. The posterior elements can be described as follows and illustrated in Figure 2.3:

- the pedicles are rod-like structures which connect the transverse pro-
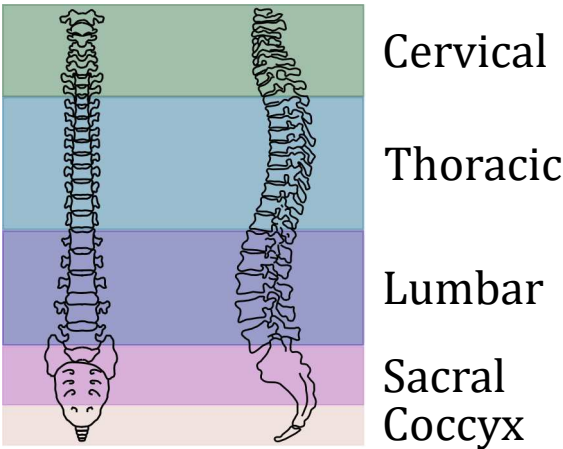
Figure 2.1: Spine anatomy. The main areas (Cervical, Thoracic, Lumbar Sacral and Coccyx) are identified.

cesses and the vertebral body;

- the transverse processes are bony masses extending laterally;

- the lamina which extends from the pedicles posteriorly.

- the inferior and superior articular processes which extend the lamina superiorly and inferiorly. These structures create with the adjacent vertebrae, the zygapophysial joint, a synovial joint which allows the articulation between the vertebrae;

The vertebral foramen is the inner space in between the posterior elements and the vertebral body and the spinal cord pass by inside this space for almost the entire spine length before to split in the cauda equina at the lumbar level.
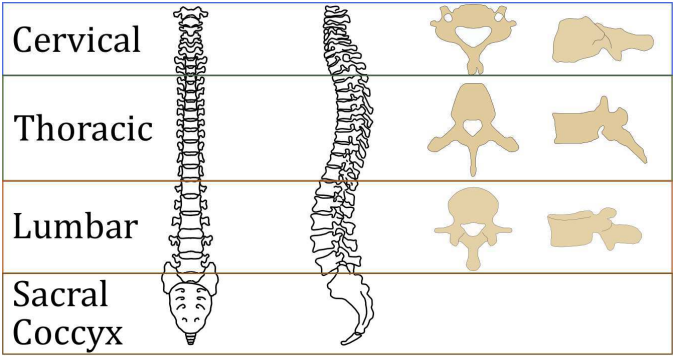
Figure 2.2: Vertebral bodies at each spine level: cervical, thoracic, lumbar, sacral and overview of the vertebrae geometry at each level.
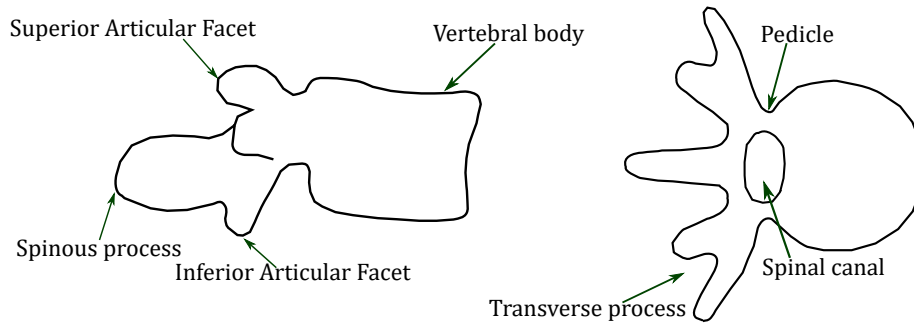
Figure 2.3: Lumbar vertebral body.

2.1.1   Intervertebral Disc

The vertebrae are spaced along the vertebral coloum by intervertebral joints, named Intervertebral Discs (IVD). The body weight, muscle contraction and external loads contribute to load the IVDs [21], which are responsible for the movement between the vertebrae (Figure 2.4). The internal region, the nucleus pulposus (NP), acts like a fluid cushion, which it is confined by the Annulus Fibrosus (AF) and the endplates. The Annulus Fibrosus (AF), has an external structure where layers of collagen fibers, arranged in a criss-crossed pattern, are embedded in a ground substance, a gel-like substance composed by proteoglycans and glycosaminoglycans. The collagen fibers (both type I and type II [12, 22]) are aligned with an angle which varies at each successive layer. Type I, mainly found in tissues which experience more tensile and compressive loading, is more concentrated in the external layer. The collagen content is estimated to be in between 50% to 70% of the dry weight and it varies radially from the outer layer to the inner layer [23, 12, 24, 25].

The internal region of the IVD, the NP, is a gel-like structure composed, in healthy conditions, by 70-90% of water [12], and the dry weight is composed by 30-50% proteoglycans and around 20% of collagen.

  The cartilaginous endplates (CEP) are thin layers of cartilage which connect the superior and inferior surfaces of the IVD to the adjacent vertebrae. They allow the passage of nutrients and fluid from the vertebrae to the IVD.

2.1.2   Ligaments

The ligaments connect the vertebral bones together and support the spinal motion preventing over-flexion and over-extension. The spinal longitudinal ligaments responsible for these functions are illustrated in Figure 2.5 and described as follows:

- the Anterior Longitudinal Ligaments (ALL) and the Posterior Longi-tudinal Ligaments (PLL), which cover the vertebrae and IVDs on the
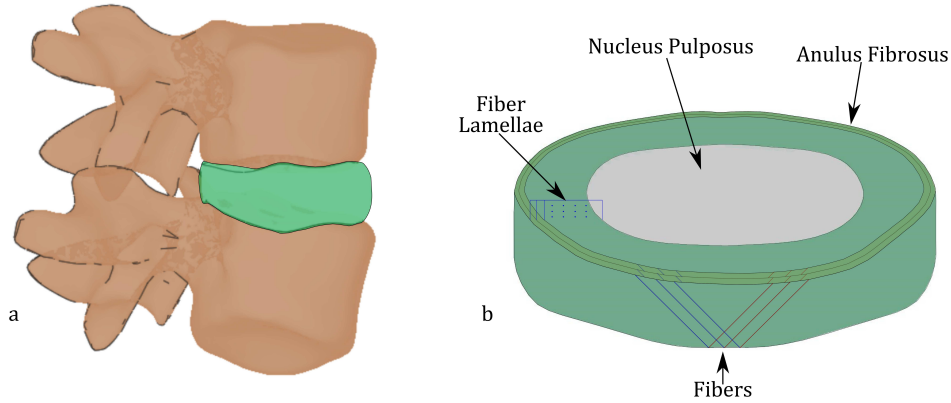
Figure 2.4: Lumbar spine functional unit, composed by two vertebrae and an IVD (a) and the IVD (b) where the AF and NP are shown.

entire length of the spine;

- Inter-transverse Ligaments (ITL) which connect the transverse processes of adjacent vertebrae;

- Inter-Spinous Ligaments (ISL) connecting the spinous processes of the vertebrae;

- Supra-Spinous Ligaments (SSL) which connect the posterior side of the spinous processes.

- Ligamentum Flavum (LF) which connect the vertebrae in the posterior side of the spinal canal.

2.1.3 Average morphometric dimensions

The identification of mean dimensions of the vertebrae structures are necessary to describe the geometry of the spine. Morphological dimensions and their intra- (at different level of the spine) and inter-variability (between subjects) is fundamental in the evaluation of statistical studies for workspace dimensions during surgeries, in the development of new surgery tools and implants [26, 27, 28, 29, 30].
The studies of Panjabi et al. [31, 32, 33, 34] have built the bases for the study of the morphology of the spine and they have been a reference point for research, evaluating the morphometry and its variation [35, 36], as well as the biomechanics of the spine [37, 38]. In particular, the morphometric studies of Panjabi [31] used 12 fresh autopsy, which were prepared and the vertebrae (at all the levels [31, 32, 33]) were separated from all the soft tissues. The anatomical dimensions were measured with a special morphometer, constituted by one linear variable (Linear Variable Displacement
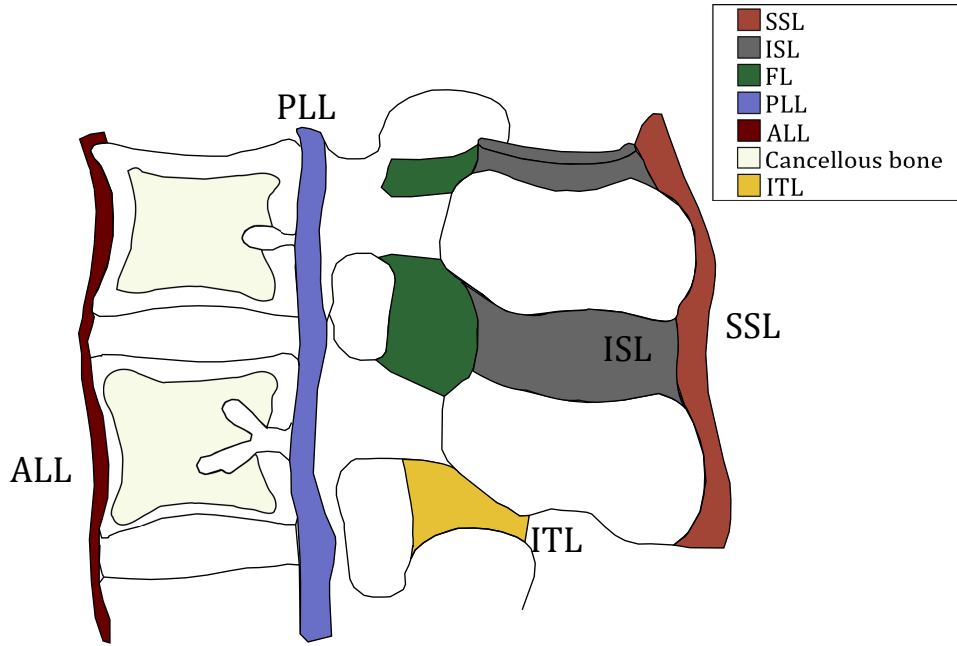
Figure 2.5: Sagittal section of a lumbar spine FU, showing the ligaments acting during the movements.

Trasducer (LVDT)) and two rotational variable (Rotational Variable Displacement Trasducer (RVDT)) displacement transducers which provided a spherical coordinate system to evaluate the dimensions. In these studies, male and female dimensions were collected together, without focusing on the gender differences.

Several studies [39, 40, 41, 42], evaluated the complexity of single anatomical part of the vertebrae, in particular the pedicles, while only a few studies focused on a complete dataset of measurements. Alam et al. [43] and Wolf et al. [26], collected more exhaustive measurements, evaluating a wider group of subjects: respectively 49 Pakistani and 55 Israeli patients and the dimensions were measured from CT scans.

Alam et al. [43] have based their study on CT scans of 49 Pakistani patients, divided in male and female measurements and evaluated the differences with previous studies based on their ethnicity. The measurements are reported in chapter 3, where the two datasets of values, male and female, are listed.

Wolf et al. [26] studied the morphometry of the lumbar spine to evaluate the dimensions interested in the surgical workspace of the lumbar spine, aiming to use statistical analysis on those dimensions for implants design and modelling. The dimensions of 55 CT data scans (25 female and 30 male) have been collected and reported in chapter 3, although not divided by gender.

The methods to collect the dimensions are different, lacking on details

and not exhaustive about all the dimensions characterizing the vertebral
anatomy. For example, Panjabi et al. [31] measured the dimensions on
fresh autopsy, while the other mentioned studies evaluated the dimensions
from data scans. The first method could be affected by measurement errors,
while the precision of the second one relies on the resolution of the scans
acquired. The dimensions taken in consideration are not the same in all the
studies, often lacking in anatomical details and the reference points are not
defined, then not allowing the reproduction of the same measurements. The
dimensions measured in the mentioned studies are shown in Figure 2.6, and
the acronyms explained in Table 3.1. Moreover, as previously introduced,
the measurements are not always divided between male and female subjects
and the ethnicity is not always mentioned.
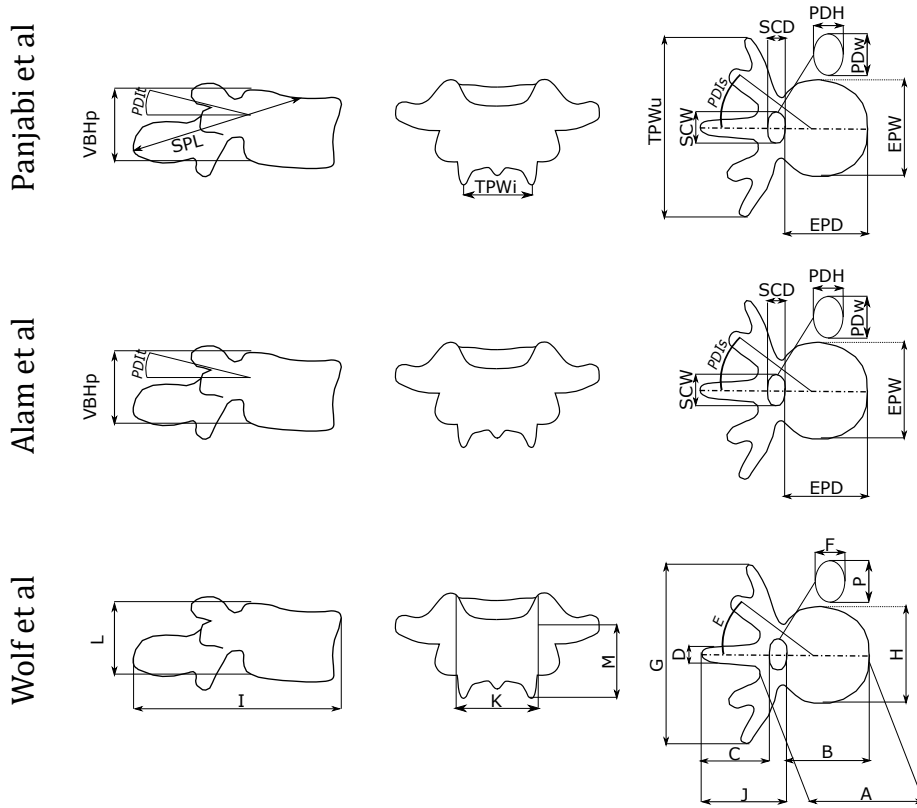
*Figure 2.6: Comparison of all the dimensions evaluated in each study with
the correspondent symbols.   The suffixes s,i,l,r used in the tables of this
chapter refer to superior, inferior, left and right dimensions and are not
shown in this figure.*

Table 2.1: Dimensions identified in the lumbar vertebrae.

Body Structure	Acronym	Description
Vertebral Body	EPW	End Plate Width
	EPD	End Plate Depth
	VBHp	Vertebral Body Height posterior
Spinal Canal	SCW	Spinal Canal Width
	SCD	Spinal Canal Depth
Pedicle	PDH	Pedicle Height
	PDW	Pedicle Width
	PDIt	Pedicle Inclination-transverse plane
	PDIs	Pedicle Inclination-sagittal plane
Spinous process length	SPL	Spinous Process Length
Transverse Process	TPW	Transverse Process Width

2.1.4   Correlation analyses

Correlation analyses of the spine dimensions have been investigated by Kunkel et al. [44] and D.P.Breglia [36]. They independently worked on the development of a parametric model of the spine, based on their correlation studies starting from Panjabi's datasets [31, 32, 33, 34].

The correlation analysis implemented by D.P.Breglia [36], is based on Panjabi's dataset. The dimensions of twelve spines, of representative healthy subjects, were used. In this study, the dimensions of the vertebrae were correlated with the posterior height of the vertebrae, using a linear correlation analysis developed by G.L.Tibbetts [45] and described in chapter 4. The results of this analysis are summarized in chapter 3.

Kunkel et al. [44] based their study on the thoracic and lumbar data obtained from Panjabi [31]. Linear and non-linear regression were evaluated (linear, polynomial, exponential and logarithmic) between the morphological dimensions of the vertebrae against the posterior body height (VBHp). The third-order polynomial function was chosen according to an Anova test for the correlation of one parameter (EPWs) and the coefficients are reported in chapter 3. The correlation analyses are further described in chapter 4. However, 3rd order polynomials are characterised by changes of their curvature, and the validity of the estimations depends on the range of VBHp considered.

2.1.5   Structure of the Intervertebral Disc in degenerated conditions

The degeneration of the IVD is a complex mechanism, which is a result of changes affecting cells, biological structures and mechanical properties of the spinal bodies [46]. The origin of the degeneration, whether it starts from
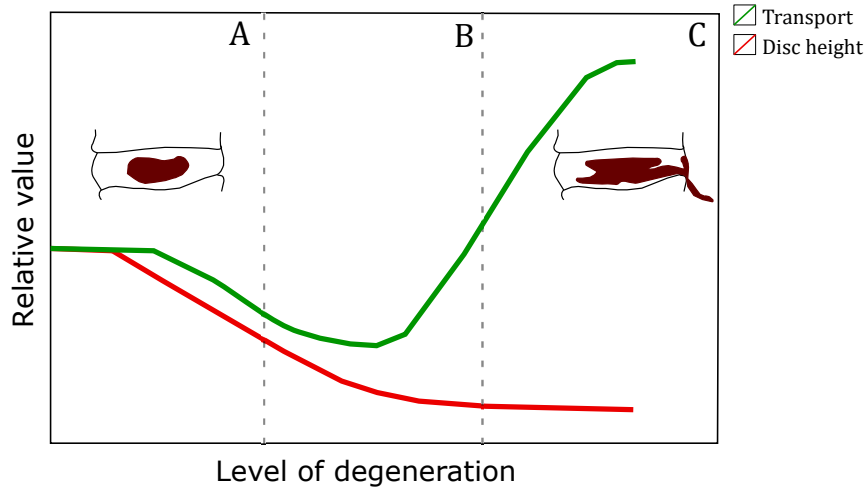
Figure 2.7: The graph describes the changes in transport and disc height. In the non-degenerated condition (A), there is an optimal range of transport; B. The degeneration of the disc, with an increasing amount of long chains molecules in the IVD, affects the transport; C. in advanced degenerated conditions, the disc height is substantially reduced while the transport is enhanced. Graph adapted from DeLucca et al. [49].

ageing processes or degeneration of the biological structures, it is not easy to identify. Degeneration evidences can be found in the lamellae organization, a decrease in disc height, and damages of the NP structure characterized by a decreased water content and more fibrosus structure [47].

The degeneration of the CEP has been correlated with a reduced content of water, proteoglycan and collagen, and calcification [48], which result in a reduced permeability for the nutrients towards the disc [49, 50, 21]. As stated by [49], disc height transport of nutrients and degeneration are correlated (see Figure 2.7) and all these factors affect the spine biomechanics.

A study, conducted by Adams et al. [51], showed the different stages of disc degenerations, which focused on the effects on the AF and NP (Figure 2.8). The discogram technique has been adopted to reveal a radio opaque liquid injected in the NP and how it flows in the disc. Five types of structures of the IVD have been identified and related to different degeneration stages. In the degenerated stages, the radio opaque fluid was found in the AF structure, and in the most degenerated case (corresponding to the NP with herniation), the AF has fissures which allow the fluid to escape from the disc. The NP is more fibrotic, with a reduced content of proteoglycans which are responsible of the osmotic gradient. It results in a decreased water content and collagen fibers trapped inside the NP, which results in a less gel-like structure [52]. The AF is characterised by a change in the structure of the lamellae, which have a less regular structure, with the collagen and elastin fibers
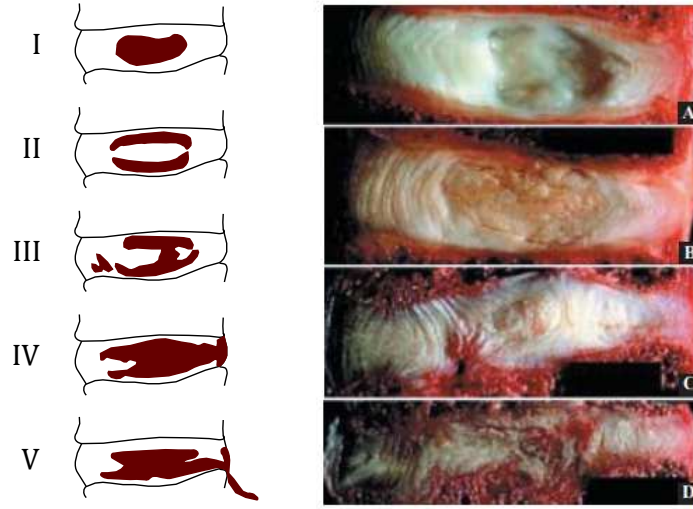
Figure 2.8: Representative illustration of the IVD degeneration stages [51](on the left) and photographs of IVD sections representing real conditions (on the right): (A) Healthy young IVD; (B) disc from a middle-aged adult where structural variations are shown; (C,D) degenerated disc [51]. Pictures adapted from Adams et al. [51] [53]

less organized (as shown in Figure 2.8)[52]. Then, a degenerated disc has a disrupted structure, where lamellae do not have their initial organization and often present defects, the disc height is reduced and the morphometry presents important changes due to radial bulging. These modifications of the structure lead to a reduced length of the spine, more stiff and less mobile [54]. Moreover, the load distribution has a different pattern in degenerated conditions, where the load in the posterior part of the vertebrae and the neural arch increases (around 30%) compared with the healthy condition (around 20%) [55].

2.2 Kinematics of the lumbar spine

The spine supports the human body, provides a safe transport channel for the nervous system, as well as providing flexibility during the physiological movements. During daily activities the spine is subjected by a combination of loads and moments and their magnitude and directions vary in between subjects and are not fully identified [56, 57, 58]. However, the loads and movements applied to the spine can be described as combinations of compression and tension loads and bending and torsional moments Figure 2.9.

In the body, all these loadings are applied simultaneously to the spine and as for all the human system, the structure determines the function:
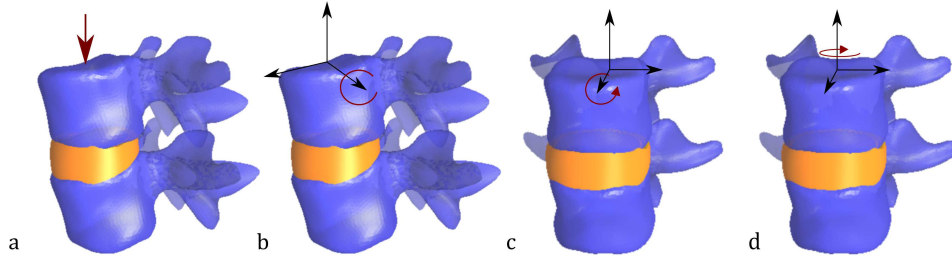
Figure 2.9: Simplified view of the loading cases acting on the spine, represented as example on a lumbar FU: a. compression, b. flexion/extension, c. lateral bending, d. axial rotation.

the inclination of the AF collagen fibers helps in supporting tension loads during bending activities and allowing AF bulging due to an increased NP pressure; longitudinal ligaments, as well supporting only tension loads, allow the spinal mobility yet limiting the range of motion to prevent injuries [59]. Extension and flexion movements cause an increased pressure to the NP and the IVD is subjected, in different regions, to both compression and tension loads. For example, during the flexion of the trunk, the anterior side of the IVD experiences compression load, while the posterior side of the vertebrae and the PLL, ISL, ITL ligaments are in tension [60].

During compression loading, the intradiscal pressure increases in the NP, while the hoop stress is supported by the inner AF layers, where the inclination of the collagen fibers are an answer to the direction of principal strains [25]. Furthermore, the inner and outer layer of the AF bulge outwards [25, 61, 62].

2.3   IVD medical devices

Several solutions are proposed following clinical diagnosis of pathological conditions. LBP at the early-stage is usually treated with conservative treatments. Non-surgical treatments include rest, physiotherapy, activity modification and pharmacological treatments. However, severe cases (10-15% [63]) require surgical interventions, that can affect the bone structure or the IVD. Structural deformity of the vertebral structure, induced by trauma or pathological conditions (e.g.: osteoporosis), can lead to excessive deformations and fractures of the vertebrae [64]. In this case, the treatment usually adopted is the vertebral body replacement.

If pathological conditions, due to IVD degeneration [5], are present fusion system is the actual gold standard treatment [65, 66]. It represents the solution commonly adopted in the past decades, which restore stability at the functional level, fixing two or more vertebrae together. Several studies

evaluated the follow-ups [67, 68] and the clinical data agreed on the issues induced by this type of device: reduced range of motion and degeneration at the adjacent levels [69, 70].

Nucleus pulposus replacement device represented a successful alternative to fusion in early stage degenerated discs [71, 72] where only the inner portion of the IVD is replaced. Intervertebral disc replacement devices interest the whole IVD and they are designed to substitute the degenerated disc and restore the natural biomechanics. The recovery from this surgery is faster than in the case of fusion systems [73, 74]. Nucleus pulposus and intervertebral disc replacement represent a valid alternative to fusion system, however, they require an invasive surgical procedure and an alteration of the natural biomechanics due the interaction between natural tissues and the device.

Dynamic stabilization devices represent an alternative to fusion systems in young patients who are in the early stage of disc degeneration. They can be divided as follows:

- Pedicle screws and artificial ligaments: Dynesys device (Zimmer Biomet, Warsaw, Indiana, United States), and graft ligament;

- Interspinous devices: Wallis system (Zimmer Biomet, Warsaw, Indiana, United States), X Stop (Medtronic, Inc., Minneapolis, Minnesota, United States), indicated in case of spinal stenosis and neurogenic claudication [75], have the function of reducing the hypermobility of pathological spine segment [76];

- Posterior stabilization devices: BDyn (S14 Implants, Pessac, France), Isobar TTL (Scient'x USA, Maitland, Florida, United States).

The aim of these devices is to better distribute and share the load between the posterior structure and the IVD. Moreover, the range of motion is preserved. The surgical procedure can be performed with a minimally invasive surgery, then limiting the damage on adjacent tissues and facilitating the recovery [77].

2.4 Computational modelling

2.4.1 Introduction to the Finite Element Method

The biomechanics of the human body has been the focus of several studies [78, 79, 80, 81, 82], investigating the mechanics of the movements, load and stresses applied and affecting the organs at all the level. The musculo-skeletal apparatus and its functionalities, considering the macro-scale perspective, can be described through a mechanistic approach [83]. The movements and the loads acting to the body, can be described through free body diagrams, however, giving a simplified view of the whole system.

The Finite Element Method, widely used in mechanical and aerospacial applications, offer the advantage to describe the mechanics of a system where an accurate description of the geometry and the material properties is given. The discretization process allows the subdivision of complex systems in a finite number of domains or better defined elements. These elements, are interconnected at vertices, which are the nodes used to define the continuum and the entities used to calculate the unknown variables of the entire system (i.e. nodal displacements). Given the element shown in Figure 2.10, the points n_i are the nodes and the equation:

$$\boldsymbol{KU} = \boldsymbol{F} \tag{2.1}$$

describes the relationship between displacement ($\mathbf{U}$) and the force at the node ($\mathbf{F}$) where $\mathbf{K}$ define the stiffness characteristic of the material. In particular, this equation is valid in case of static equilibrium, while in a more complete form it can be described as

$$\boldsymbol{M\ddot{U}} + \boldsymbol{D\dot{U}} + \boldsymbol{KU} = \boldsymbol{F} \tag{2.2}$$

where where $\mathbf{M}$ is the mass matrix, $\mathbf{D}$ is the damping coefficients matrix and $\dot{\boldsymbol{U}}$ and $\ddot{\boldsymbol{U}}$ the velocity and acceleration respectively. Developing more the static case, when a force is applied to a body, the stress applied on the surfaces of it can be expressed as:

$$\sigma = \lim_{\delta A \to 0} \frac{\delta f_b}{\delta A} \tag{2.3}$$

$$\tau = \lim_{\delta A \to 0} \frac{\delta t}{\delta A} \tag{2.4}$$

where σ and τ are the normal and shear stresses in result of normal (f_b) and tangential forces (t) and A the surface area. Moreover, ϵ is the strain evaluated as the displacement (u) of a node in respect of its initial position (x):

$$\epsilon = \lim_{\delta x \to 0} \frac{\delta u}{\delta x} \tag{2.5}$$

In 3D space (Figure 2.10), stress and strain informations can be summarized in the matricial forms:

$$\sigma = \begin{bmatrix} \sigma_{xx} & \sigma_{xy} & \sigma_{xz} \\ \sigma_{yx} & \sigma_{yy} & \sigma_{yz} \\ \sigma_{zx} & \sigma_{zy} & \sigma_{zz} \end{bmatrix} \tag{2.6}$$

$$\epsilon = \begin{bmatrix} \epsilon_{xx} & \epsilon_{xy} & \epsilon_{xz} \\ \epsilon_{yx} & \epsilon_{yy} & \epsilon_{yz} \\ \epsilon_{zx} & \epsilon_{zy} & \epsilon_{zz} \end{bmatrix} \tag{2.7}$$
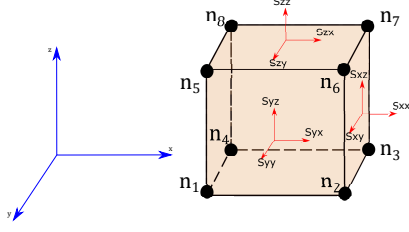
Figure 2.10: The stresses in the Cartesian system, where substiituing 1,2,3 to x,y and z it refers to the matricial formulation above.

and the stress elements are illustrated in Figure 2.10 and the relation between stress and strain is reported in Equation 2.8.

Considering discretized elements in the static equilibrium case, the formulation can be further developed as:

$$\boldsymbol{\sigma} = \boldsymbol{K}\boldsymbol{\epsilon} \tag{2.8}$$

The stiffness matrix is a matrix (Equation 2.10) the elements of which are dependent on the material properties of the structures involved:

$$K = \begin{bmatrix} K_{11} & K_{12} & K_{13} & K_{14} & K_{15} & K_{16} \\ K_{21} & K_{22} & K_{23} & K_{24} & K_{25} & K_{26} \\ K_{31} & K_{32} & K_{33} & K_{34} & K_{35} & K_{36} \\ K_{41} & K_{42} & K_{43} & K_{44} & K_{45} & K_{46} \\ K_{51} & K_{52} & K_{53} & K_{54} & K_{55} & K_{56} \\ K_{61} & K_{62} & K_{63} & K_{64} & K_{65} & K_{66} \end{bmatrix} \tag{2.9}$$

defining symmetry planes the previous matrix can be simplified. For an elastic and isotropic material, the mechanical behaviour is the same in the three directions (x,y,z) and only nine parameters are needed to describe the stress-strain relationship and all of them are function of the Young's modulus (E) and Poisson's ratio (μ):

$$K = \frac{E}{(1+\nu)(1-2\nu)} \begin{bmatrix} (1-\nu) & \nu & \nu & 0 & 0 & 0 \\ \nu & (1-\nu) & \nu & 0 & 0 & 0 \\ \nu & \nu & (1-\nu) & 0 & 0 & 0 \\ 0 & 0 & 0 & \frac{(1-2\nu)}{2} & 0 & 0 \\ 0 & 0 & 0 & 0 & \frac{(1-2\nu)}{2} & 0 \\ 0 & 0 & 0 & 0 & 0 & \frac{(1-2\nu)}{2} \end{bmatrix} \tag{2.10}$$

where the shear modulus of elasticity is defined as:

$$G = \frac{E}{2(1+\nu)} \tag{2.11}$$

Then, the complex system is described through assembling the equations at each node and the condition of equilibrium and displacement continuity

between the nodes have to be satisfied. In particular, the equilibrium condition is based on the virtual work principle [84], where defining σ a stress system, with body forces and surface tractions (f_b and t), and ϵ and u respectively the strains and displacements, it can be defined as:

$$\int_V \delta\epsilon\sigma dV - \int_S \delta utdS - \int_V \delta uf_b dV = 0 \qquad (2.12)$$

This formulation states the equilibrium of the internal and external work, made by the internal and external forces, on each element of the FE model. The solution is obtained iteratively, considering small time increments. Algorithms have been developed for the linearisation and evaluation of the unknown variables (i.e.: Newton's method, quasi-Newton method), and directly implemented in FE software. Extensive description of the FE method and the solution algorithms are reported elsewhere [84].

2.4.2 Finite Element models of the lumbar spine

The Finite Element method has been widely used to describe the mechanical behaviour of the anatomical structure in the past decades. As stated by Maas et al. [85], FE modelling in biomechanics is a widely recognised methodology to either assess and interpret experimental results and as a methodology to adventure in investigation otherwise not possible with the experimental techniques. The first application in the investigation of loads and mechanics of the body has been recorded in Belytschko et al. [86], and since then more studies have been developed and the methodologies have been improved.

The use of Finite Element Models in the study of spinal biomechanics have several advantages. The loading conditions applied to the spinal unit are controlled by the user, defining the type of load and the magnitude applied and no-side effects, related to the loading machine and the setup would affect the results. Also the internal state of stress of the IVD can be accurately evaluated and healthy and degenerated conditions can be simulated, assigning different material properties and/or varying the morphometry of the involved structures. However, several assumptions are applied in the simulations, regarding the loading conditions and the material properties assigned to the bodies. Then, further investigations are required to validate FE models.

Finite Element analyses have been carried out following the setups of experimental studies on single [87, 88, 89] and multilevel FSU [90, 91, 92, 93]. Previous studies analysed the range of motion, Intervertebral Disc Pressure (IDP), Facet Joint Forces (FJF) when compression loads, torque and bending moments were applied singularly or combined [94, 95] to simulate the physiological movements. Healthy and degenerated IVD material properties were evaluated to understand how they affect the biomechanics of

the lumbar spine [96, 97, 98]. In general, the material properties of all the bodies involved in the lumbar spine can widely vary (according to health status, age, gender, and inter-specimen variability) and several combinations of these formulations are possible. Subsequently, probabilistic studies have been carried out, evaluating realistic distribution of the input values and the combination of them has been evaluated through probabilistic methods (i.e. Monte Carlo simulations) [99, 87, 100, 101, 102].

The validity of the FE models presented in the literature is assessed through comparison with the results of experimental tests, providing a proof for the acceptance of this tool. Then, FE models of the spine provide a tool for the evaluation of: (i) biomechanical functionalities; (ii) effects of using implants; (iii) developing new implants; (iv) customize treatments according to the subject-specific geometry [103, 104, 105, 106].

The FE models currently available are subjbect-specific or they represent simplified geometry of the spine, requiring long time to be reconstructed and represent an approximation of the real physiological system. In order to obtain generalized results, parametric and scalable models, which can be quickly reconstructed to represent population of models, are required [17]. In this section, an outline of the fundamental modules to build a FE model is described.

2.4.3 Geometry

Currently, the FE models available are either subject-specific, where the geometry matches a particular specimen, or averaged geometrical models, using approximated anatomy based on average dimensions.

Subject-specific models are reconstructed starting from datascans obained from Computer-Tomographic scans (CT) or Magnetic Resonance Images (MRI), and those are characterized by accurate anatomy, where all the details are well reproduced [107]. However, a level of error in the geometry reconstruction is associated with this method. The quality of the scans depends on the resolution of the instrument used (varying between 0.6 mm to 2.5 mm) and on the segmentation process. The last one is affected by errors due to the operator expertise (RMS errors ranging between 0.39 to 1.22 mm for an expert technician) and/or the technique used (mean RMS errors of around 1 mm) [108, 109].

Generic models of the lumbar spine anatomy, are reconstructed with simple geometrical shapes [15] or developed with a parametrised model [110, 111, 112]. Parametrization functions can be assigned to the geometrical shapes reproduced, so the dimensions of the vertebrae can be changed according to the user needs or the patient dimensions. Morphological studies have been conducted in the past decades, to obtain average dimensions of the vertebrae in the lumbar spine (as described in subsection 2.1.3). The dimensions have been used to investigate the relationships between the dimensions charac-

terizing the vertebral bodies and the IVD.

Models based on medical images precisely represent the subject-specific geometry, however, the process to generate these models is both time consuming and depending on the availability of data-scans. Moreover, to provide wider understanding, beyond a single individual, subject-specific models require a number of models to be solved, for statistical power [113]. However, idealized models based on average dimensions often lack the anatomical detail that is necessary to be of clinical value, with their geometries typically too simplistic. Further, several studies have highlighted the importance of anatomically representative geometry in simulations of the spine [114, 14] due to its effects on the intradiscal pressure, the range of motion and facet joint contact forces.

The ideal scenario for the FE modelling would be the generation of precise anatomical models generated in a reduced amount of time and where the model is not affected by the user-dependent expertise. Semi- and fully-automated procedures to reconstruct FE geometries have been implemented [115, 116, 117, 118], based on statistical shape model and/or landmarks identification, to speed up the segmentation process and generate the lumbar model. These procedures generate accurate geometries, however they require the availability of subject-specific data-scans.

A reference model of the geometry of the human body is the VHP (Visible Human Project), which consists in cryosection photographs of a 38 year old man of height 180.34 cm from a cadaver, where sections were taken at intervals of 1 mm. Considering the acquisition of the VHP model, that is not affected by errors of the acquisition method used, it is considered the gold-standard for human models. The geometry of the lumbar vertebrae and IVDs were segmented from the visible human male dataset into two-dimensional (2D) axial images by professional clinicians [119]. These segmented 2D axial images were then processed in Matlab and were imported into Mimics v. 17.0v. 19.0 (Materialise, Leuven, Belgium) for reconstruction of three-dimensional (3D) geometry of the lumbar vertebrae and IVDs. The lumbar model of the VHP is widely used in this thesis to evaluate the morphological studies (described in the chapter 3) and the parametric model of the lumbar spine (chapter 4).

2.4.4 Material properties

The mechanical behaviour of biological tissues has been extensively studied in the recent decades [120, 121, 122, 123, 124]. Their mechanical properties are of interest to understand the loading effects and also to understand how they influence the physiological and biological functionalities. However, the characterization of biological materials is complicated due to their anisotropic and heterogenous features [125, 126].

Soft-tissue material properties are usually described by non-linear strain energy formulations, where the anisotropic behaviour is defined. Most of the biological tissues have a high fiber content (i.e.: blood vessel, cartilaginous tissues, AF), described by exponential strain density function [127, 128]. Other materials (i.e.: ligaments) are characterized by strain-dependent behaviour, which requires the definition of bilinear or non-linear constitutive laws [129]. In this section the material properties assigned in previous studies have been discussed, while the matematical formulations of the non-linear material properties have been reported in Appendix A.

Vertebra

Studies developed from data-scans adopted the material properties evaluated from the grey-scale level [130]. Several mathematical formulations have been developed, using the Hounsfield values to quantify the CT-scan attenuations, according to the localization and the type of bone [130], where the grey level of each voxel, which is correlated to the density of the material, is used to assign the correspondent material properties.
In other studies [53, 131, 132, 133], the material properties have been assigned following the different bone formation (cortical or cancellous). The external layer of the vertebrae has cortical material properties while the inner core is composed by cancellous material. Different material properties have been assigned to the posterior vertebral structure (lamina, posterior processes and pedicles). In Table 2.2, a range of linear isotropic values assigned in previous studies has been reported.

Table 2.2: Vertebral material properties used in previous studies.

Cancellous bone		Cortical bone		Posterior elements		
E [MPa]	ν	E [MPa]	ν	E [MPa]	ν	Ref
100	0.2	12000	0.3	3500	0.25	[90]
140	0.2	11300	0.2	Rigid	-	[134]
100	0.2	12000	0.3	3500	0.25	[94]

IVD

Following the anatomical description of the IVD, different material properties can be assigned to the AF and NP (Table 2.3). Several material formulations have been evaluated for the AF, considering the anisotropic nature of this material. The ground substance is modelled separately from the fibers which are modelled as separate 1D elements or membrane elements [135, 136], included in a homogenized formulation [137, 138] or included in a continuum approach [139, 127]. A material law formulation, implemented by Holazpfel-Gasser-Odgen [127], initially developed to model blood vessels,

has been widely adopted to describe the AF properties.

In the case of the NP, two different strategies have been used: using solid elements [37, 140], or fluid-like elements[141, 142] Using solid elements the IDP distribution was not constant all over the NP, and the IDP was evaluated in different regions.

Table 2.3: Material properties used in previous studies for the AF and NP

Material formulation	AF ground		AF fibers	NP	ref
	c_1	c_2			
Mooney-Rivlin	0.18	0.045	Non-linear, depending on the layer	Fluid	[90]
Mooney-Rivlin	0.7	0.2	Tension only elements	Fluid	[134]
Mooney-Rivlin	0.3448	0.3	Non-linear depending on the layer	Fluid	[94]
Neo-Hookean	0.3448	0.3	Fibre-reinforced continuum, depending on the layer	Fluid	[143]
Hyperelastic	4.2	0.45	Fibre-reinforced continuum, depending on the layer	Fluid	[131]
Hyperelastic Yeoh	$c_{10} = 0.0146$ $c_{20} = 0.0189$, $c_{30} = 0.041$		Fibre-reinforced continuum, two families of fibers	Linear E=1MPa, $\nu = 0.49$	[131] [11]

Cartilaginous Endplates

Two approaches have been used in the literature to model the CEP: modelling them as separate bodies [98, 144, 145], or including their material formulation with the IVD [49, 146]. The CEP have been modelled following different mathematical formulations: linear isotropic [145, 138, 147, 98, 132, 86], hyperelastic [148], fiber reinforced and biphasic [49]. A summary of the material properties assigned in the mentioned studies is given in Table 2.4.

Ligaments

In the literature, spine ligaments are modelled as tensile only elements, to reproduce their physiological functionalities. The elements usually used were either beam or truss where the cross-section area and the Young's modulus is defined [90, 153, 154], or as spring elements defining the ligament stiffness [155, 96]. The latter solution is used in case of applying non-linear stiffness. The geometrical features assigned to these elements have been evaluated in previous *in vitro* studies. The length and cross-section area of the ligaments were evaluated by Pintar et al. [156] from cadaveric specimens, and the results are reported in Table 2.5. The material properties of the ligaments have typically been evaluated by *in vitro* studies [157, 158, 132, 156, 147] and they are affected by several factors (age, gender, body height, genetics

Table 2.4: *Material properties assigned to the CEP in previous studies. k_0, M and e_0 are the coefficients related to the poroelastic material properties, initial permeability, an empirical coefficient M and the initial value for the tissue deformation, respectively. The strain dependent permeability function is reported in Appendix A [152].*

Material	Material properties					ref
formulation	E	ν	k_0	e_0	M	
	[MPa]		[m^4/Ns]		-	
Linear isotropic	23.8 MPa	0.4	-	-	-	[145]
Linear isotropic	24.0 MPa	0.4	-	-	-	[138, 149]
Linear isotropic	600.0 MPa	0.3	-	-	-	[150]
Linear isotropic	5.0 MPa	0.4	7×10^{-15}	4.0	10.0	[146]
	C_{10}	D_1	k_0	e_0	M	
Hyperelastic, Neo-Hookean	0.3448	0.3	-	-	-	[151]

Table 2.5: *Geometrical features for the lumbar ligaments, evaluated between the T12 and S1 by Pintar et al. [156].*

Ligament	Cross-sectional area [mm^2]		Length [mm]	
	Range	Mean (sd)	Range	Mean (sd)
ALL	10.6-52.5	32.4 (10.9)	30.0-48.5	37.1 (5.0)
PLL	1.6-8.0	5.3 (2.4)	27.8-36.7	33.3 (2.3)
LF	19.0-93.6	43.8 (28.3)	12.8-21.5	16.4 (2.9)
JC	57.2-114.0	84.2 (17.9)	13.0-18.0	15.2 (1.3)
ISL	13.8-60.0	35.1 (15.0)	6.7-20.0	16.0 (3.2)
SSL	6.0-59.8	25.2 (14.0)	17.0-33.5	25.2 (5.6)

and healthy conditions), showing a large variation in between different spec-
imens. The mechanical properties have a non-linear, strain dependent be-
haviour and different mechanical characteristic for each ligament, as shown
in Figure 2.11. Linear, non-linear and piecewise formulation have been used
in previous studies and an overview of the material properties and their ef-
fects is here given.
Momeni Shahraki et al. [89] modelled the ligaments as tension only truss ele-
ments, assigning strain dependent hypoelastic (Appendix A) material prop-
erties (Table 2.6). Their study focused on the evaluation of the IVD material
properties, not investigating the ligaments material formulations, and their
results were in agreement with previous experimental data and FE analyses.
Naserkhaki et al. [159] modelled the ligaments as tensile-only uniaxial spring

*Table 2.6: Hypoelastic material properties assigned by Momeni Shahraki et
al. [89].*

Ligament	Elastic modulus [MPa]	
ALL	7.8 (<12%)	20.0 (>12%)
PLL	10.0 (<11%)	20.0 (>11%)
LF	15.0 (<6.2%)	19.5 (>6.2%)
ITS	10.0 (<18%)	59.7 (>18%)
TL	10.0 (<14%)	11.6 (>14%)
SSL	8.0 (<20%)	15.0 (>20%)
JC	7.5 (<25%)	32.9 (>25%)

elements and linear piecewise material properties were assigned. The ma-
terial properties were evaluated from eight studies, reported in Figure 2.12,
with fixed length and orientation for each ligament and the cross-section
obtained from the reference studies. The effect of the different formulations
were analysed and compared with *in vitro* studies. Naserkhaki et al. [159]
demonstrated the wide variability of the results in terms of range of mo-
tion, IDP, centre of rotation and ligament force/strain, varying the material
properties. Moreover, they hypothesized possible intra-subject variations,
when different length and cross-section area were considered.
 Lan et al. [96] modelled the ligaments with only tension truss elements. The
material properties were implemented through a user-defined subroutine to
simulate either linear and non-linear behaviour of the ligaments, and the
mechanical features are described in Table 2.7. Their results showed that
non-linear constitutive formulations lead the spine to be more flexible then
in the linear case and the activity of each ligament in the different loading
cases were evaluated.
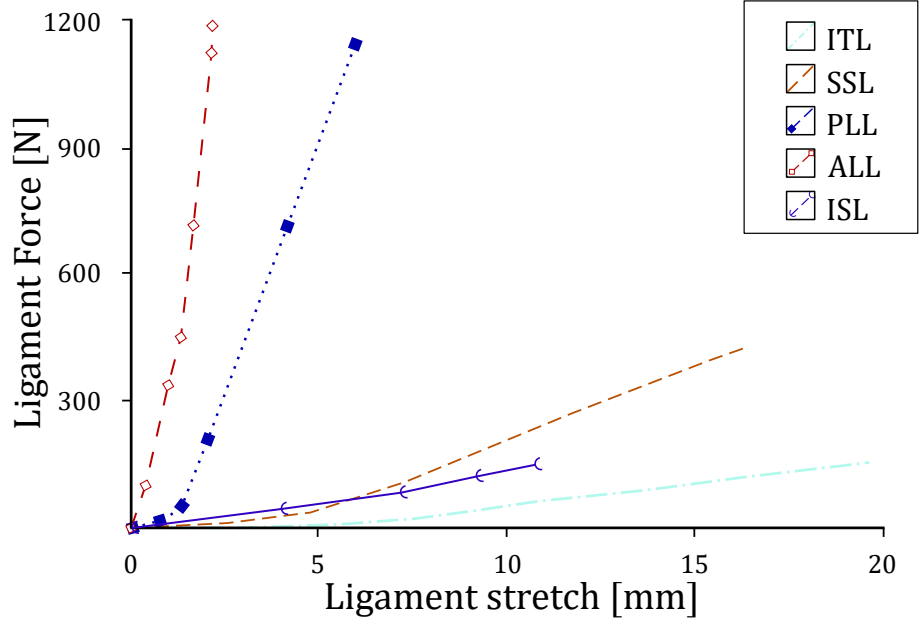
Figure 2.11: *Ligaments mechanical behaviour of the ALL, PLL, ISL, ITL and SSL.*

Table 2.7: *Material properties of the longitudinal ligament used by Lan et al. [96].*

Ligament	ALL	PLL	LF	ISL	SSL	TL
Elastic modulus (small strain) [MPa]	7.8	10	15	10	8	10
Transition strain (%)	12	11	6.2	14	20	18
Elastic modulus (large strain) [MPa]	20	20	19.5	11.6	15	58.7
Cross-sectional area [mm^2]	53	16	67	26	23	1.8
Length [mm]	13	11	19	13	11	22
Max. failure load [N]	510	384	340	130	200	70
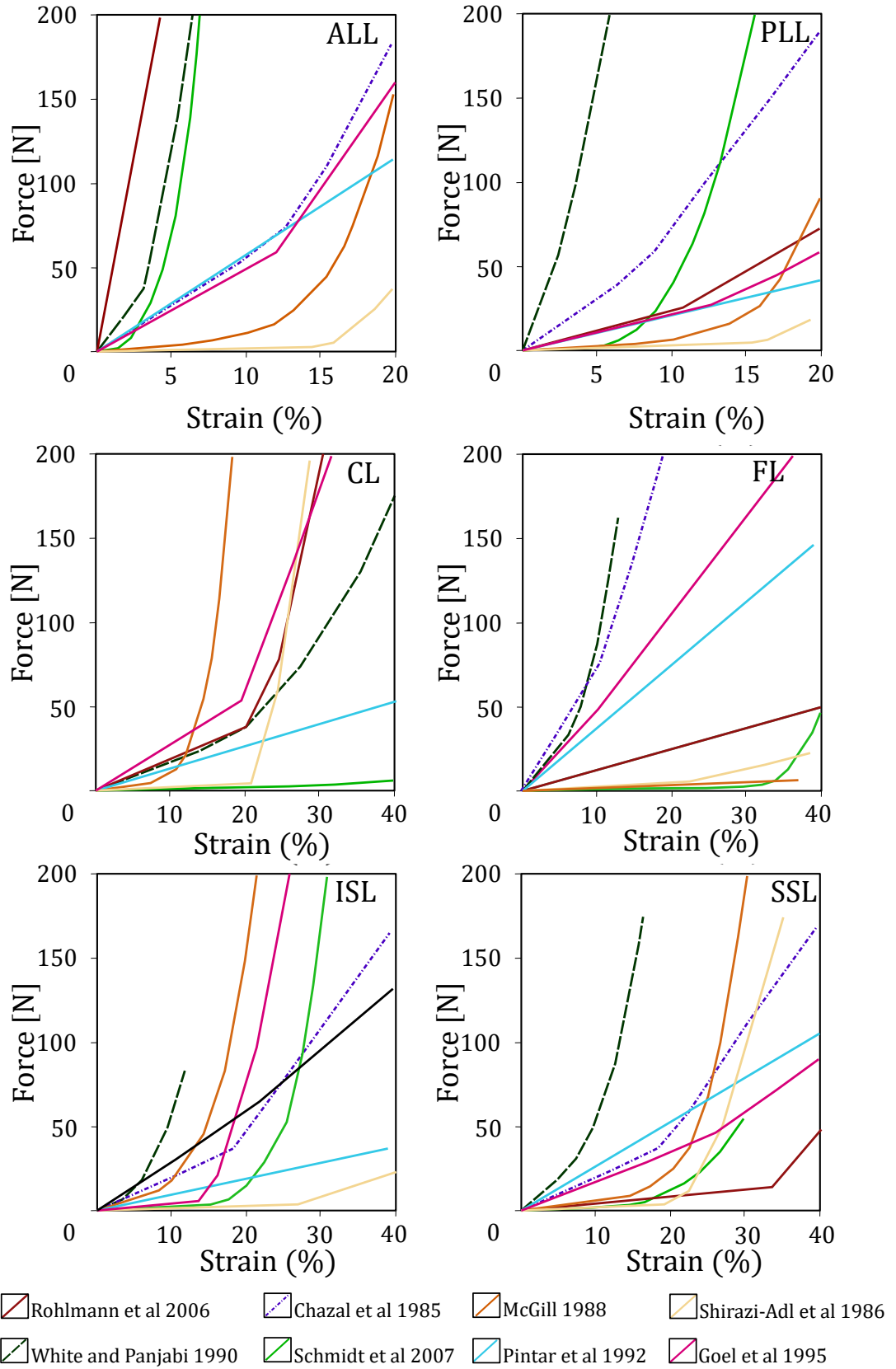
Figure 2.12: Mechanical behaviour for the ALL, PLL, CL, FL, ISL and SSL evaluated by Naserkhaki et al. [159].

2.5   Mesh

Central to FE models is the mesh generation, the process of subdividing the whole volume into a series of smaller volumes, namely mesh elements. Mesh elements can be in 1D, 2D or 3D and the entities where the solutions are calculated are the nodes. In first order elements, the nodes are the vertices of the considered shape, while in superior order elements, the unknown variables are evaluated at different points on the edges of an element. The following geometrical features of these elements are described in Figure 2.13.

- Nodes
- Elements
- Boundary face
- Face
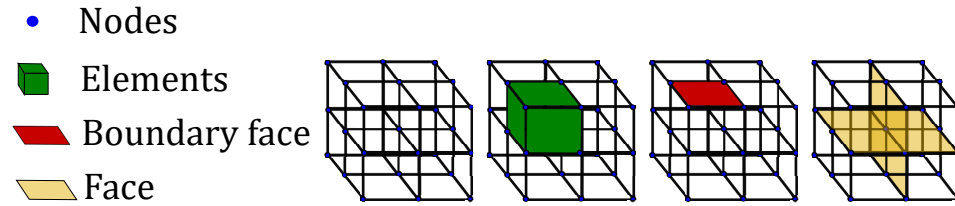
Figure 2.13: Basic features characterizing a FE elements.

The classification of the elements (in 2D and 3D elements) depends on their surface geometry, which can be quadrilateral or triangular (quad- and tri-elements or hexahedral and tetrahedral elements), and an overview of the possible geometries is reported in Figure 2.14.

1D

2D

3D
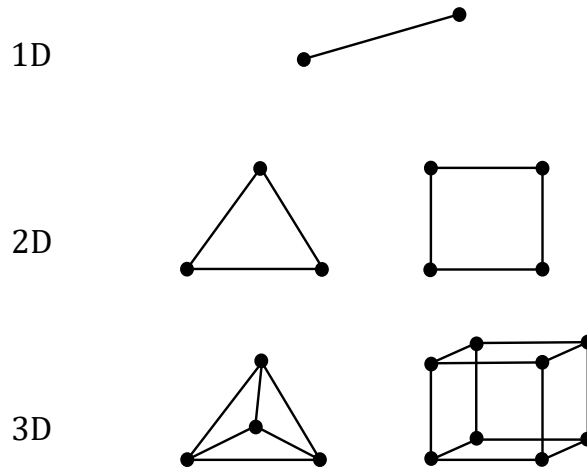
Figure 2.14: 1D, 2D and 3D first order elements.

In FE models reconstructed from subject-specific scans, the mesh generation of the vertebrae is obtained through the generation of voxel volumes based on the grey-scale of the scans and then converted in hexahedral elements [160, 161]. Other studies, dedicated mesh software assigned shell

elements to the outermost layer of the vertebra, to simulate the cortical cortex [162]. A different approach is used for the IVDs, which result opaque in the scans, and the volume between two adjacent vertebrae is recreated by expert users and then meshed [162].

FE models based on averaged dimensions have been developed, these studies typically present semi- and fully-automated procedures for the mesh generation [163, 15, 117]. In between these models, statistical shape models have been generated, in which a morphing procedure is applied to adapt the mesh to new geometries [164]. Other models, presented a mesh developed ad-hoc for those models [14]. These procedures, aim on speeding up the pre-processing of the FE models, by generating hexahedral mesh elements for the IVD and vertebrae. However, as stated in subsection 2.4.3, these models either lack of anatomical accuracy and their generation is based on the availability of data-scans.

2.6 Previous FE Analyses

Finite Element models have the advantages to predict measurements that can not be accurately evaluated *in vivo* studies. The effects of high loads, combined physiological movements, degenerated conditions on the biomechanics have been of interest to several research groups [165, 37, 148, 166, 14, 167, 93, 168, 169, 87]. These models provide reliable results if boundary and loading physiological conditions are applied. However, the physiological loading conditions are still not entirely identified [170].

In literature, either force-control or displacement-control [171, 170] simulations have been developed. In reality, the loading path follows the lumbar arch and it is affected by the action of the muscles. These effects are generally simulated through the implementation of a follower load [170, 172] or in musculoskeletal models the muscles are explicitly included [56, 173, 174, 59]. The follower loads can be simulated through the application of punctual loads at each vertebral level or via a path of unidirectional connector elements. The location of the follower load path has been evaluated in several studies and it is still a point of debate [38, 175]. Thus, another approach has been proposed by Noailly et al. [171], applying pressure load at the surface of each vertebrae.

The loading conditions applied to the FEM of the lumbar spine are pure moments to simulate flexion, extension, lateral bending and axial rotation and combined loadings with compression loads to simulate daily activities. In Table 2.8 and Table 2.9 a brief overview of the loading conditions applied in previous studies is reported. The main outcomes usually evaluated in the FE studies include (i) Range of Motion (RoM), (ii) Intradiscal Pressure IDP and (iii) Facet Joint Forces (FJF). The RoM has been reported as rotational and axial displacements, however, much interest has been shown on

Table 2.8: Loading cases applied on the model when pure moments were singularly applied.

Extension	Flexion	Lateral bending	Axial rotation	ref
[Nm]	[Nm]	[Nm]	[Nm]	
7.5	7.5	7.5	7.5	[176, 11]
10	10	10	10	[87]

Table 2.9: Loading cases applied on the model when combined loads were applied.

Extension		Flexion		Lateral bending		Axial rotation		ref
F [N]	M [Nm]	F [N]	M [Nm]	F [N]	M [Nm]	F [N]	M [Nm]	ref
500	7.5	1175	7.5	700	7.8	720	5.5	[151, 177]

*Table 2.10: Evaluation of the RoM, reported as rotational displacement (Deg), when pure moments were applied. These results were obtained from a comparative study conducted by Dreischarf et al. [165], were the same boundary and loading conditions were applied to eight models [165, 90, 178, 80, 179, 180]. * median values of the FE analyses evaluated.*

-	Extension/Flexion	Lateral bending	Axial rotation
L1-L5	24°-41°	25°-41°	11°-22°
FJF*	32 N/0 N	12 N	87 N

complex movements which involve several spinal structures (extension, flexion, lateral bending and axial rotation) and not many studies reported the results for the simple compression [92]. The RoM and the FJF of the entire lumbar arch, have been estimated in eight models, where similar loading and boundary conditions were applied, and compared by Dreischarf et al. [165], are given in Table 2.10. The IDP at each vertebral level and the RoM are reported in Figure 2.15 and Figure 2.16. These results showed the effects on the biomechanics of the spine of different geometries and material properties.

 Sensitivities analyses, varying material and morphological parameters, have been studied [87, 114, 13, 182]. Coombs et al. [87] performed a probabilistic study on a single FSU, based on the Monte Carlo simulation method, to evaluate the effect of varying the material properties of the soft tissues of the spine. Zander et al. [13] and Niemeyer et al. [114] varied material properties and morphological parameters of a L1-L5 segment and a single FSU respectively and evaluated their impact in the RoM, FJF and IDP. These studies covered a wide variability of material properties, providing data about the effects on the biomechanics. The study of Niemeyer et al. [114] reported the most influential geometrical parameters for the spine biomechanics, however their model is not geometrically accurate, representing an approximate anatomy. In between the morphological variations, the
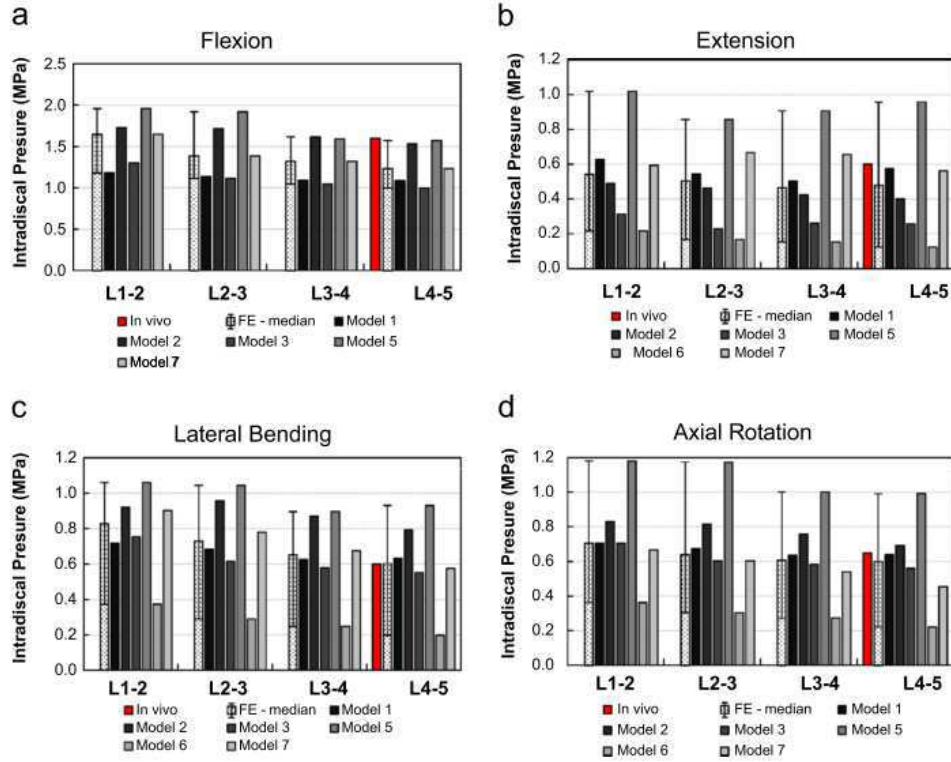
Figure 2.15: IDP compared by Dreischarf et al. [165] from eight FE models [90, 178, 80, 179, 180, 181]. Image from Dreischarf et al. [165].

volumetric ratio of the IVD as well as combined morphological and material properties variations have not been included in these studies. However, to the best knowledge of the author, the models developed in the literature allow the evaluation of material sensitivity analyses [87, 183, 98] or of the geometrical features [14, 182, 114]. Most of these studies required the extensive pre-processing of models while the other based on semi-automated or automated solutions are characterised by a simplified geometry. Understanding the effects on the biomechanics of degenerated conditions, could lead to new treatments and the development of new devices [149], through the design and material optimization.

Healthy and degenerated cases

Degenerated cases have been simulated in FE studies, varying the material properties and the morphologies of the IVD. Different strategies have been followed to simulate the degeneration of the IVD. Kim et al. [184] simulated the degenerated effect removing the hydrostatic behaviour of the NP and increasing the stiffness of the IVD. Kumaresan et al. [150] evaluated
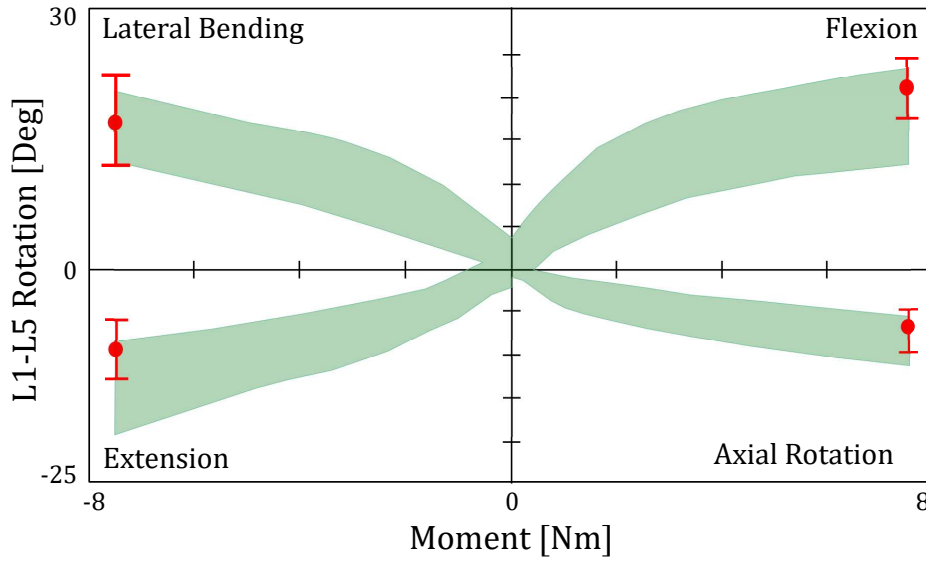
Figure 2.16: RoM between L1-L5 of the lumbar spine. The green area identifies the range of values reported by [165] from eight FE models [90, 178, 80, 179, 180, 181], and the red bad is the in vivo median. Image adapted from Dreischarf et al. [165].

the effects on the biomechanics of the cervical spine, evaluating four grade of degeneration varying with the progression of the degeneration, the disc height, the material properties and the fibers content of the IVD. Rohlmann et al. [142] modelled a single FU evaluating the effects of degenerated IVD conditions, varying the NP compressibility and decreasing the disc height, which resulted in a reduced fiber length. Malandrino et al. [50] evaluated the effects of patient and degeneration specific geometrical and mechanical factors for the IVD. Inoue et al. [185] and Natarajan et al. [186] reported a review of previous studies on the disc degeneration. The first one reported the changes in the viscoelastic properties of the disc of previous studies, while Natarajan et al. [186] reported a review of poroelastic material properties used and the effects under cycling load. In fact, in the degeneration process, the water content reduces and the IVD becomes stiffer, with possible effects on the fluid phase and the supply of nutrients to the inner IVD. They evaluated the effect of cycling loads on healthy and degenerated disc, which resulted in a higher disc loss height at peak load in the healthy disc, demonstrating a larger amount of fluid flow. Cegoñino et al. [187] replicated the experimental test conducted by Iatridis et al. [188] in an FE model. An osmo-hyperelastic constitutive law was assigned to the IVD and the material properties were varied in healthy and degenerated conditions according with Iatridis et al. [188]. Park et al. [90] implemented different stage of IVD degeneration varying the IVD height, the NP compressibility and the mate-

rial properties of the AF fibers and ligaments. These features were assigned in a range of values to evaluate mild, moderate and severe degeneration to compare with a healthy case. The range of motion, IDP and facet forces were analysed when flexion, extension, lateral bending and axial rotation were applied. The inter-segmental rotation and IDP showed a decreasing pattern with the progression of degeneration, while the facet joints force at the degenerated level increased.

2.7 Experimental tests on the lumbar spine

The experimental results are needed to validate FE models [189]. *In vivo* tests have been conducted since the early 1960s [21], but since then have been limited due to the invasiveness of the measurements. The *in vivo* studies were conducted using a discometry system [21] which consisted in a needle transducer inserted in the IVD. The discometry method has been improved in the following studies [190, 191, 192, 193] and the results obtained increased linearly with the compressive load applied (Figure 2.17).

A wide range of IDP has been reported in the literature and the variability
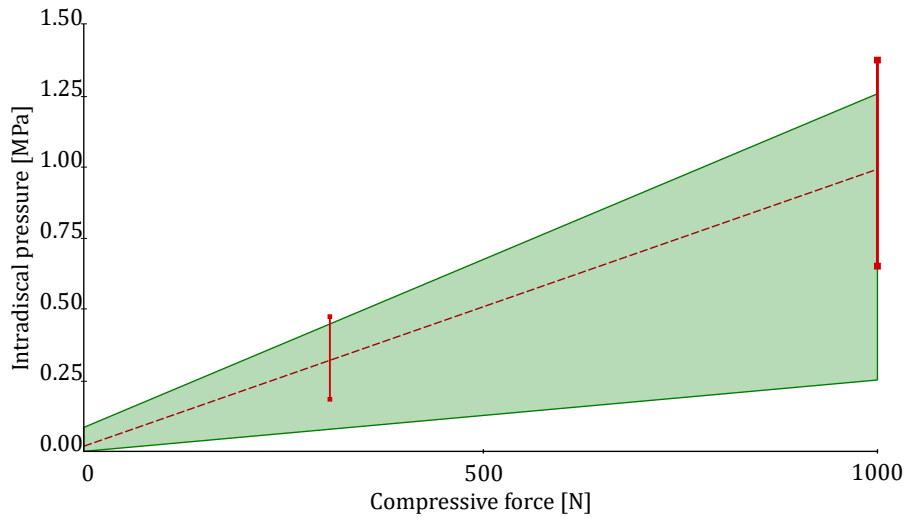
Figure 2.17: IDP compared by Dreischarf et al. [165] from eight FE models [90, 178, 80, 179, 180, 181], where the green area identify the range of variation of the FE results, the red dotted line the experimental results with the bars identifying the standard deviation. Image adapted from Dreischarf et al. [165].

of the results is mainly due to the differences between the subjects, different instrumentations and disc level and subject-specific conditions. Considering the standing position, the IDP values measured *in vivo* have a decreasing trend from the thoracic level ($\sim$ 1 MPa at the T6-T8 levels) to the middle

lumbar level ($\sim$ 0.3 MPa at L3-L4 level) and increasing again at the last functional unit ($\sim$ 0.5 MPa at the L4-L5 level) [190, 191, 194, 195]. Different values have been recorded in sitting and lying positions [193, 196]. *In vitro* experimental test were evaluated either on Functional Unit of the spine (FSU) [197, 198] and on the single components (IVD, specimens extracted from the AF, lamellar structures and ligaments) [199, 200]. Gonzalez-Blohm et al. [198] presented a review of the experimental test evaluated on single [201, 9, 202, 203, 204, 205, 206, 207] or multilevel FSU [208, 209, 210, 211, 212, 213, 214, 215, 216]. Static and dynamic loading conditions were applied, the results usually evaluated included the Range of Motion (RoM), the intradiscal pressure (IDP), the neutral zone and the stiffness of the spinal unit considered.

In vitro studies have been carried out on cadaveric specimens to identify the mechanical behaviour of the individual structure of the IVD. Mechanical tests on volumes extracted from the AF showed that the mechanical behaviour of the AF is region specific and the tensile response differ radially and circumferentially [188, 217, 218, 219, 220].

In order to validate FE models, the setup of the experimental model has to be accurately simulated. The boundary and loading conditions have to be recreated, and the measurement system clearly defined (i.e.: strain gauge positions).

2.8 Summary

In this chapter, the background for the following chapters has been introduced. The topics evaluated can be summarized as follows:

- The anatomy of the spine has been described, focusing on the lumbar segment;

- The morphological studies on the anthropomorphic dimensions have been introduced. Furthermore, the vertebrae dimensions can be correlated with the posterior vertebral height and with the height and age of a person.

- Finite Elements Models can be used to estimate intradiscal pressure (IDP), facet joint forces (FJF) and the range of motion (RoM) of the entire spine or the simple functional unit. This method could lead to the estimation of biomechanics entities that are not measurable through experimental test.

- An overview of previous FE models and the effects of the material properties and morphological features have been discussed.

Chapter 3

Morphometric measurements

3.1 Introduction

The anatomy of the lumbar spine is characterized by a complex geometry which differs with the stature, sex and ethnicity of the subject. Finite Elements (FE) models have been used in the literature to evaluate the load and stress acting on the lumbar spine. These models are mainly subject-specific models which are based on medical images that represent a subject-specific anatomy, whose reconstruction is time consuming and based on the availability of data-scans (chapter 2). However, to obtain a statistical relevance of a clinical study the implementation and solution of several models is required.

Parametric and anatomically accurate models represent an alternative to evaluate the variety of clinical cases, where the anatomical variability between subjects due to different stature, gender and ethnicity can be implemented. A reference geometry can be morphed and scaled accordingly to the dimensions reported from morphological studies and the specific features of the anatomy can be altered according to an anatomical deformity or a degeneration of the bodies involved.

The development of parametric and scalable models rely on anthropomorphic measurements and correlation analyses collected from the literature. The number of datasets evaluated is important, as it allows the inclusion of anatomical variability in the statistical analyses, obtaining correlation functions which reflect the average dimensions. The dimensions should be collected and classified according to the mentioned criteria (ethnicity, gender, etc.). Further, a method to measure the dimensions, defining reference points to collect the dimensions and allowing the reproduction of the same measurements, is required (chapter 2). The dimensions, often reported in the literature, are rarely in agreement with other studies available and the measurements are typically incomplete as regards the description of the full anatomical features. Moreover, the measurements have to be divided accord-

33

ing to gender and ethnicity of the subjects, which would affect correlation studies [43].

Currently, there is no defined method described in the literature to identify the key dimensions of interest of the spine. The dimensions measured in previous studies pursued the aim of each individual study (e.g. to identify the workspace for surgical instruments [26]) but no over-riding rationale for measurements is currently available. For the sake of clarity, a brief recap of the dimensions evaluated in this study is given in Figure 3.3, Figure 3.2 and the acronyms are described in Table 3.1 and described elsewhere (chapter 2, subsection 2.4.3).

Studies by Panjabi and colleagues have provided the basis for the study of the anatomy and biomechanics of the spine [31, 221, 33]. The morphometric study by Panjabi assessed 12 fresh cadaveric spines at autopsy, from which the vertebrae (at all the levels [31, 221, 33]) were separated from the soft tissues. The anatomical dimensions were measured with a morphometer, composed of one linear variable (LVDT) and two rotational variable (RVDT) displacement transducers which provided a spherical coordinate system to evaluate the dimensions. In these studies, dimensions from both male and female cadavers were collected, without distinguishing according to gender.

Correlation studies have been published based in Panjabi's studies [31, 221, 32, 33, 44, 26]. These correlation analyses [44, 36](previously described in chapter 2, subsection 2.1.4), have limited validity due to the low number of specimens, mixed gender and the unknown ethnicity.

Datasets published by Alam et al. [43] and Wolf et al. [26] are based on more numerous datasets (n = 49 and n = 55). These two studies present two ethnic groups and in the case of Alam et al the dimensions have been collected separately for females and male subjects. Therefore, there is the potential to develop more robust, and targeted, correlation studies based on these data-sets which are greater in number than that of Panjabi and colleagues. However, these value of using correlation analyses from morphometric studies is limited if they can not be used to predict anatomy/geometry and dimensions which represent an individual. The accuracy of correlation analyses therefore, require some form of subject-specific validation. This is feasible to do using the dimensions of the Visible Human Project (VHP) dataset, and through comparison to dimensions obtained from the scans of new individuals. The former is of value as it is the most accurate dataset available at present, while the latter enables more cases to be compared.

The aim of this chapter was to evaluate the correlation analyses currently available in the literature, and evaluate new correlations based on datasets present in literature with a wider number of specimens (n = 55 and n = 49). The effect of the number of specimens and gender has been investigated and the validity of the correlation functions has been studied by comparing predictions using correlation analyses, with the VHP data-set and with

subject-specific measurements. Scans of individuals were obtained from Imperial College of London. The workflow of this chapter is represented in Figure 3.1.
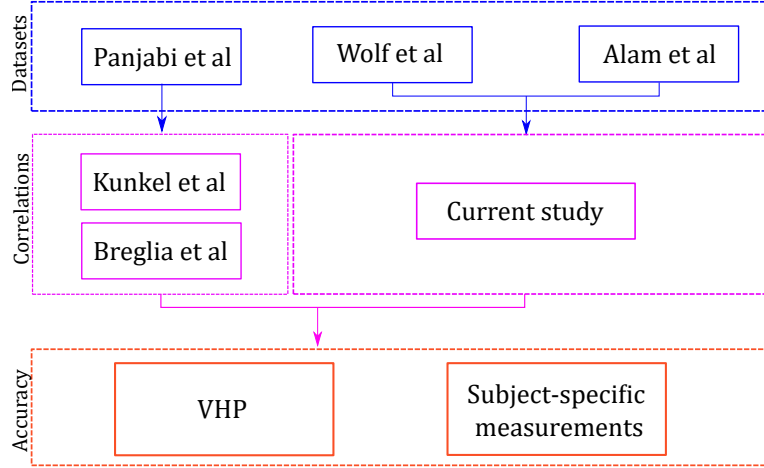
Figure 3.1: Workflow of the chapter.
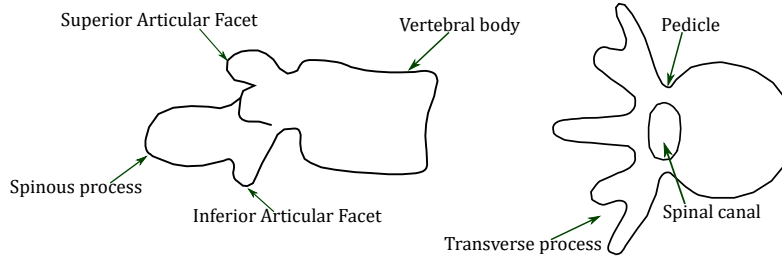
Figure 3.2: Anatomical dimensions to describe the lumbar spine features.
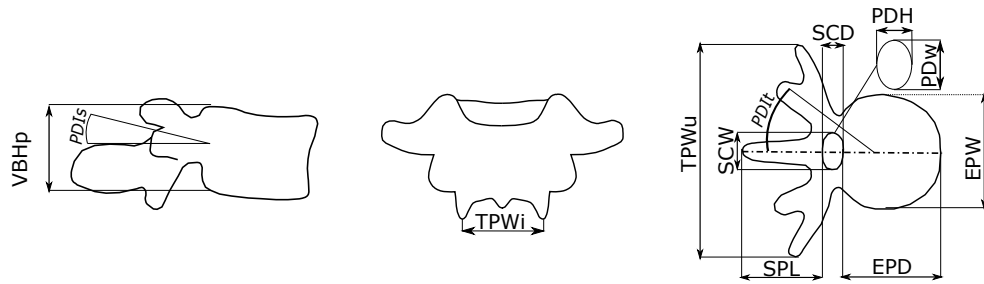
Figure 3.3: Anatomical dimensions to describe the lumbar spine features.

Table 3.1: Dimensions evaluated in previous studies and list of acronyms used in this Chapter. The suffixes, s,i,r,l, usually assigned to some of these dimensions refer to superior, inferior, right and left.

Body Structure	Acronym	Description
Vertebral Body	EPW	End Plate Width
	EPD	End Plate Depth
	VBHp	Vertebral Body Height posterior
Spinal Canal	SCW	Spinal Canal Width
	SCD	Spinal Canal Depth
Pedicle	PDH	Pedicle Height
	PDW	Pedicle Width
	PDIt	Pedicle Inclination-transverse plane
	PDIs	Pedicle Inclination-sagittal plane
Spinous process length	SPL	Spinous Process Lenght
Transverse Process	TPW	Transverse Process Width

3.2 Morphometric data collections

Several studies have focused on the collection of vertebral measurements. Studies have been published on the dimensions of cervical [221] thoracic [222, 223, 34] and lumbar spine [32, 43, 26, 224], as well as on the dimensions of specific areas of the vertebrae: the articular facets [33] and pedicles [41, 42, 39, 225]. However, only Alam et al. [43],Wolf et al. [26] and Panjabi et al. [32] reported the data collected from the measurements identified on the full lumbar spine. In particular, the studies of Panjabi et al. have been extensively used in previous analyses [44, 226, 36] (See section 3.1 and chapter 2).

In this section, the morphometric data, collected by Alam et al. [43] and Wolf et al. [26] have been analysed. Moreover, new measurements have been collected from a new dataset of data-scans supplied by Imperial College London, then used to verify the predictions for subject-specific use. In Figure 3.4, the dimensions evaluated in each study are graphically described.

3.2.1 Datasets from literature: Alam et al. and Wolf et al.

The dataset collected by Alam et al. [43] and Wolf et al. [26], were collected from Israeli [26] and Pakistani [43] subjects, respectively, moreover Alam et al. [43] divided the results between male and female.

Alam et al. [43] have based their study on CT scans of 49 Pakistani patients, divided into male and female measurements and evaluated the differences with previous studies based on other ethnic origins. The results were described in terms of mean values for the two genders for each lumbar vertebrae and here reported in Table 3.2. Wolf et al. [26] studied the mor-
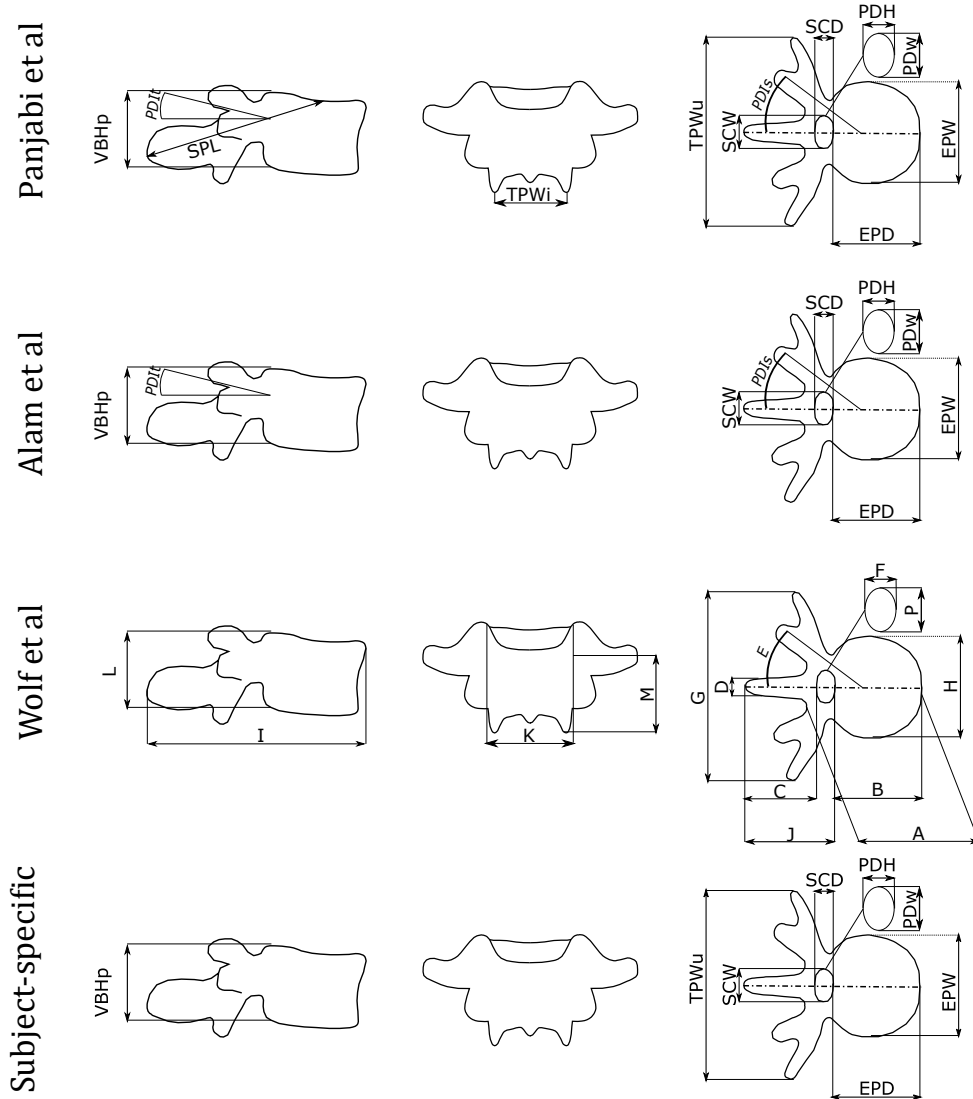
Figure 3.4: Comparison of all the dimensions evaluated in each study with the correspondent symbols. The suffixes s,i,l,r used in the tables of this chapter refer to superior, inferior, left and right dimensions and are not shown in this figure.

Table 3.2: Dimensions (in [mm]) collected by Alam et al. [43]. The dimensions have been divided between male and female at each level of the lumbar spine.

Acronyms	L1		L2		L3		L4		L5	
	m	f	m	f	m	f	m	f	m	f
VBHa	24.5	23.9	26.65	25.6	27.3	27.05	27.46	26.92	27.6	26.7
VBHp	28.2	25.6	29.23	26.69	28.55	27.47	27.1	26.21	24.84	23.9
EPWs	41.7	38.4	43.44	39.5	45.45	40.88	47.08	43.43	48.95	46.24
EPWi	42.5	38.9	44.69	40.7	45.39	42.35	46.91	43.51	47.04	44.9
EPDs	30.4	27.7	32.47	29.6	32.85	30	33.85	30	33.71	31.5
EPDi	31.7	29	32.99	29.86	33.01	30.01	33.85	31.77	33.03	31.91
PWr	6.4	5.6	7.29	6.38	10.54	9.56	10.54	9.56	13.53	12.19
PHr	13.5	12.8	13.4	12.31	12.03	11.71	12.03	11.71	11.53	10.94
PWl	6.1	5.9	7.29	6.37	10.64	9.67	10.64	9.67	13.53	12.71
PHl	13.2	12.6	13.46	11.9	12.38	11.36	12.38	11.36	10.26	10.84
PSr	3.7	4.4	3.95	4.61	4.68	4.9	4.68	4.9	4.06	4.21
PTr	13.11	14.13	13.86	13.94	16.15	17.55	16.15	17.55	22.47	20.13
PSt	3.8	4	4.21	4.28	4.52	4.81	4.52	4.81	3.84	4.79
PTt	13.2	14.8	13.91	14.4	16.77	17.37	16.77	17.37	23.08	21.77
SCD	17.7	16.7	16.26	16.28	15.48	15.31	14.77	14.28	15.25	13.76
SCW	24.2	23.5	24.34	23.46	24.13	22.36	24.48	23.81	28.43	25.96

phometry of the lumbar spine to evaluate the dimensions of interest in the surgical workspace in the case of lumbar pathologies, aiming to use statistical analysis on those dimensions also for implant design and modelling. The dimensions of 55 CT data scans (25 female and 30 male) were collected and the mean values and standard deviations were reported. The dimensions (Figure 3.5), stated in Table 3.3, were reported with another set of symbols and for clarity have been related to the acronyms used in this study.
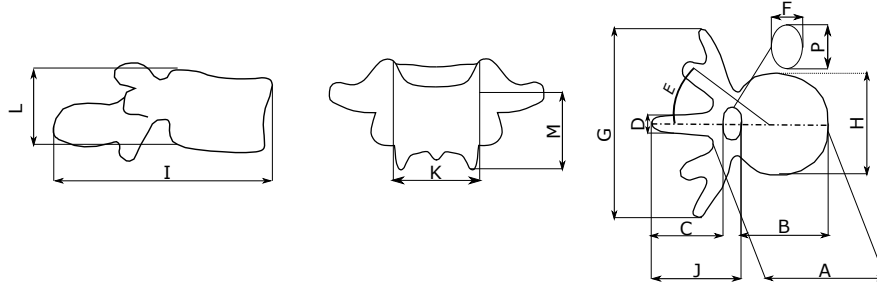
Figure 3.5: Dimensions measured by Wolf et al. [26]. The letters used in their paper and the acronyms of this Chapter are in Table 3.3. Some dimensions have not direct correspondence (A, D, K, J) while others can be evaluated like: SCD = J-C.

3.2.2 Subject-specific dataset (SSD)

The data-scans from new specimens were obtained from Imperial College London. The cadavers were obtained as part of another study, and scanned

Table 3.3: In the first column the symbols used in Wolf et al. [26] have been reported and referred to the acronyms used overall this chapter. The mean values, in [mm], and standard deviation are reported.

		L1		L2		L3		L4		L5	
Symbol	acronyms	mean	sd	mean	sd	mean	sd	mean	sd	mean	sd
A	-	44.8	2.8	46.9	3.6	47.6	3.7	47.6	4.4	46.6	5.3
B	EPDs	28.9	2.3	29.8	2.3	32.3	1.3	31.7	2.1	32.5	2.1
C	SPL	30	3.7	31.5	4.6	33.5	5.7	32.8	5.3	26	5.7
D	na	5	1.1	4.3	1.3	4.7	1.2	5.3	1.4	5.8	1.4
E	Pdi	11.8	1.3	11	1.7	12.8	2.2	14.1	2.1	18.5	3.9
F	PDW	5.6	1.3	7.7	1.5	8.9	1.9	11.4	1.8	13.7	2.2
G	TPW	81.8	5.1	80.4	4.6	89.4	5.5	90.5	5.7	93.7	5.9
H	EPWs	40.7	3.8	39.8	4.6	43.1	3.8	44.1	4.6	48.1	3.8
I	-	76	9	79.1	7	80.1	6.7	79.6	5	77.1	6.7
J	-	49.4	7.2	48.5	7	48.9	5.7	47.2	5	43.6	7.4
K	TPWs	37.5	5.5	36.9	2.9	39.8	2.7	43.9	3.6	53.5	5.3
L	VBH	24.9	2.4	25.4	1.1	25.6	1.6	26.5	0.6	28.6	1.3
M	-	11.5	2.5	10.8	3.2	11.8	2.8	11.4	3.5	11.2	3.7
N	-	22.4	2.5	21.6	3.4	19.4	5.4	23.2	7.6	21.6	4.9
P	PDH	15.1	1.9	14.8	1.6	14.5	1.9	14.8	2.1	15.6	2.3

with an IVIS SpectrumCT Imagining System (Caliper Life Sciences, Hopkinton, MA, USA, voxel size 0.15× 0.15×0.15 mm) at Imperial College London (supplied by N. Newell, ethical approval obtained from the Tissue Management Committee of the Imperial College Tissue Bank ethics committee: 12/WA/0196).

Scans from four specimens were provided (male subjects, between 22 to 58 years of age) of which one was excluded due to the low quality of the scan where the external surfaces were not well defined, not allowing measurements. Thus, in total three new specimens have been evaluated. To obtain coherent data, only male data scans were used, belonging to the same ethnic group (Caucasian). Moreover, no pathologies were reported on the lumbar spine and the cause of death was not linked to related pathologies.

The measurements were evaluated using 3D-Slicer (https://www.slicer.org/,[227]) from the scans (Figure 3.6), and the mean and standard deviation values are reported in Table 3.4. The dedicated measurement tool of 3D-Slicer was used to evaluate the dimensions stated in Table 3.4, according to a method identified elsewhere [228] to evaluate the vertebral body height and endplate width. A schematic of the dimensions evaluated is given in Figure 3.6. The number of specimens included in this study has not been used to evaluate any statistical analyses or obtain accurate correlation analyses. Instead, this dataset has been used only to evaluate the accuracy of the correlation analyses, obtained from the other studies, when compared to 'patient-specific' measurements; in essence, they are being used to answer the question: do generalised correlations hold true for an individual?
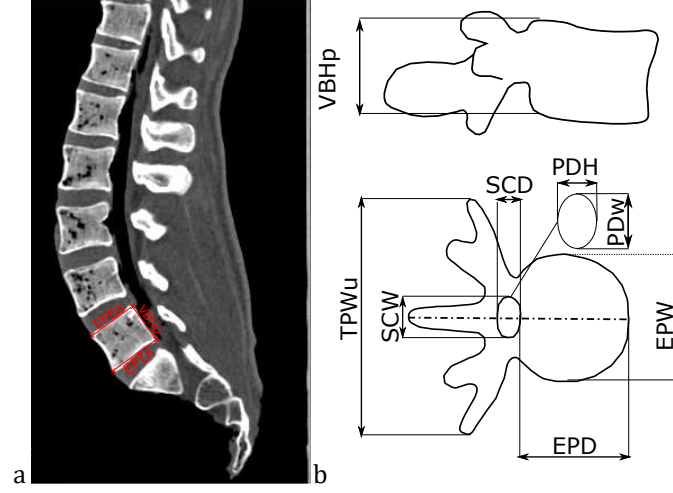
Figure 3.6: Evaluation of the subject-specific model from Slicer 3D.

Table 3.4: Dimensions (in [mm]) evaluated from the new specimens obtained from Imperial College London .

Dimension	L1		L2		L3		L4		L5	
	mean	std	mean	std	mean	std	mean	std	mean	std
VBHp	31.33	1.57	30.90	1.66	29.53	4.66	31.67	1.69	28.90	3.11
EPWs	47.57	4.23	50.80	4.53	51.80	3.15	52.80	3.85	55.43	4.95
EPWi	48.67	3.79	48.90	2.11	53.90	3.15	56.10	4.56	53.77	9.12
EPDs	34.47	1.82	36.17	2.00	38.27	1.80	39.27	3.51	37.20	2.91
EPDi	35.33	1.72	38.03	1.97	38.50	3.29	38.70	4.76	36.80	1.15
PDHl	20.27	3.40	20.67	4.72	21.37	5.94	20.73	3.87	20.97	3.98
PDWl	7.47	1.61	9.13	1.36	11.67	1.70	12.60	0.87	15.57	1.58
PDHr	21.07	5.73	21.03	5.11	20.63	4.76	17.80	3.06	18.27	3.44
PDWr	7.47	2.11	8.95	0.91	11.77	1.72	13.03	2.06	16.77	1.72
SCD	17.60	2.36	16.03	1.15	14.17	1.70	13.30	0.26	15.23	3.45
SCW	25.33	0.91	25.43	2.96	24.27	2.68	24.30	2.26	28.23	0.90
TPW	78.10	2.82	91.80	0.95	104.67	4.73	97.17	4.13	97.83	4.48

3.3 Correlation analyses

In the studies by Kunkel et al. [44] and Breglia [36], the correlations between the VBHp and the other dimensions characterising the vertebrae were evaluated. In this study, the same correlation analysis was performed on the datasets of Wolf et al. [26] and Alam et al. [43]. Linear and non-linear correlation analyses were implemented in Matlab, using the least-square optimization method, on the measurements of these two studies. Thus, establishing two sets of correlation functions for Israeli and Pakistani data-sets. Moreover, in the case of the dataset of Alam et al. [43], the analyses have been performed separately for male and female subjects. As evaluated by Kunkel et al. [44], polynomial curves of first (Equation 3.1), second (Equation 3.2) and third (Equation 3.3) order were assessed to fit each parameter in function of the posterior vertebral body height VBHp:

$$y = c_2 + c_1 x \tag{3.1}$$

$$y = c_3 + c_2 x + c_1 x^2 \tag{3.2}$$

$$y = c_4 + c_3 x + c_2 x^2 + c_1 x^3 \tag{3.3}$$

where y is the dimensions being evaluated, x the VBHp and c_1, c_2, c_3, and c_4 are the coefficients estimated for each equation, reported in Table 3.5 and Table 3.6. To assess the goodness of fit, minimum, maximum and mean values of R^2 for each study have been listed in Table 3.8.

3.3.1 Accuracy of the correlation analyses

The correlation analyses obtained in this study, based on Wolf et al. [26] and Alam et al. [43] section 3.3, and those of Kunkel et al. [44] and Breglia [36] have been compared. The results were also compared with the subject-specific datasets: the VHP model (introduced in chapter 2), whose dimensions were evaluated as in subsection 3.2.2, and the data collected from data scans SSD. The values of the VBHp obtained from the VHP, have been used to predict its anatomy from the correlation studies available (Alam, Wolf and SSD). In Table 3.7 the dimensions evaluated in each study are listed, and only the dimensions in common in all the studies (EPDs, EPWs, PDH and PDW) were compared. In the study of Kunkel et al. [44] and Alam et al. [43], the PDH and PDW dimensions were evaluated on the left and right side. Then, the average values for those measurements have been used to compare with the other studies, in which the axial-symmetry hypothesis has been adopted.

3.4 Results

The results are presented as follows:

Table 3.5: Correlation analysis evaluated on male and female subjects of the Alam et al. [43] dataset. The correlations have been performed with a 3rd order polynomial (Equation 3.3), 2nd order polynomial (Equation 3.2) and 1st order polynomial (Equation 3.1) where c_1, c_2, c_3 and c_4 are the coefficients of the equations and R^2 is the metrics to evaluate the goodness of fit.

	Parameter	Male					Female				
		c_1	c_2	c_3	c_4	R^2	c_1	c_2	c_3	c_4	R^2
3rd order	EPWu	0.42	-33.99	918.75	-8201.44	0.73	-1.05	82.26	-2141.00	18596.97	0.68
	EPWi	0.51	-41.22	1115.93	-9997.95	0.64	-0.94	73.73	-1919.55	16677.12	0.62
	EPDu	0.42	-34.51	933.83	-8368.88	0.56	-0.74	58.20	-1513.58	13129.49	0.88
	EPDi	0.31	-25.62	695.42	-6243.99	0.58	-0.64	49.51	-1279.94	11045.92	0.52
	PWr	0.05	-4.17	109.09	-924.69	0.68	-0.47	37.83	-1004.06	8874.87	0.67
	PHr	0.10	-7.75	205.95	-1796.81	0.64	-0.40	31.80	-849.95	7564.80	0.70
	PWl	-0.01	0.59	-16.86	168.33	0.56	0.22	-17.56	460.09	-4000.39	0.76
	PHl	0.09	-7.43	204.64	-1868.79	0.92	0.28	-21.81	568.95	-4928.51	0.73
	PDIsr	0.06	-4.62	127.60	-1168.01	0.24	-0.03	2.55	-65.29	559.81	0.75
	PDItr	-0.07	5.93	-175.04	1741.11	0.90	-0.15	12.48	-349.97	3265.92	0.64
	PSt	0.08	-6.30	172.27	-1563.84	0.41	-0.10	8.02	-210.26	1838.70	0.47
	PTt	-0.07	6.05	-177.18	1752.07	0.87	-0.18	15.03	-418.36	3880.05	0.81
	SCD	-0.31	25.36	-688.33	6226.49	0.45	0.38	-30.10	784.19	-6785.67	0.50
	SCW	-0.05	4.19	-124.38	1251.57	1.00	-0.38	29.37	-758.78	6556.56	1.00

	Parameter	Male				Female			
		c_1	c_2	c_3	R^2	c_1	c_2	c_3	R^2
2nd order	EPWu	0.04	-3.57	112.47	0.66	0.91	-47.96	673.65	0.58
	EPWi	0.01	-1.36	73.47	0.41	0.86	-44.75	622.69	0.47
	EPDu	0.04	-2.32	69.72	0.28	0.61	-31.80	440.57	0.60
	EPDi	-0.04	2.23	4.55	0.07	0.22	-11.63	185.06	0.29
	PWr	0.10	-6.72	119.22	0.68	1.17	-60.98	799.02	0.64
	PHr	0.10	-6.92	122.07	0.64	1.21	-62.75	823.78	0.68
	PWl	0.05	-2.12	35.53	0.56	-0.32	16.48	-201.64	0.67
	PHl	-0.10	6.07	-78.80	0.91	-0.30	15.72	-191.04	0.57
	PSr	-0.09	5.02	-63.06	0.20	0.00	0.31	-1.87	0.74
	PTr	0.47	-27.09	407.48	0.90	1.10	-57.03	757.42	0.64
	PSt	-0.06	3.19	-39.76	0.26	0.16	-7.96	106.32	0.40
	PTt	0.42	-24.78	378.32	0.87	1.18	-62.11	829.33	0.81
	SCD	0.05	-2.34	42.89	0.22	-0.36	18.98	-232.89	0.41
	SCW	0.37	-20.75	317.43	1.00	0.09	-5.40	105.11	0.92

	Parameter	Male			Female		
		c_1	c_2	R^2	c_1	c_2	R^2
1st order	EPWu	-1.36	82.80	0.66	-1.46	79.59	0.39
	EPWi	-0.70	64.49	0.41	-0.68	59.65	0.15
	EPDu	-0.42	44.31	0.27	-0.35	38.85	0.12
	EPDi	-0.11	35.96	0.06	-0.45	42.17	0.22
	PWr	-1.37	47.35	0.67	-0.86	31.06	0.19
	PHr	-1.38	47.65	0.64	-1.00	34.87	0.23
	PWl	0.38	1.89	0.55	0.22	6.09	0.18
	PHl	0.69	-6.62	0.88	0.14	8.02	0.08
	PSr	-0.01	4.46	0.00	0.19	-0.45	0.74
	PTr	-1.95	70.14	0.83	-0.92	40.52	0.22
	PSt	0.08	2.04	0.14	0.00	4.66	0.00
	PTt	-2.06	73.44	0.82	-1.42	54.02	0.42
	SCD	0.31	7.41	0.21	0.43	3.99	0.22
	SCW	-0.98	52.22	0.82	-0.93	48.05	0.91

Table 3.6: Correlation analysis evaluated on the female subjects of Wolf et al. [26]. The correlations have been performed with 3rd order polynomial (Equation 3.3), 2nd order polynomial (Equation 3.2) and 1st order polynomial (Equation 3.1), where c_1, c_2, c_3 and c_4 are the coefficients of the equations and R^2 is the metrics to evaluate the goodness of fit.

	Parameter		c_1	c_2	c_3	c_4	R^2
3rd order	B	EPDs	0.52	-42.05	1132.24	-10122.91	0.799
	C	SPL	0.39	-32.25	894.95	-8214.94	0.969
	E	PDi	-0.33	26.69	-712.10	6322.39	0.965
	F	PDW	0.07	-6.62	197.19	-1942.70	0.998
	G	TPW	-0.29	21.80	-542.15	4520.71	0.772
	H	EPWs	-0.25	20.20	-531.86	4684.29	0.903
	J	-	0.05	-4.18	112.64	-950.49	0.990
	K	-	-0.76	60.84	-1617.70	14321.21	0.987
	P	PDH	-0.14	11.32	-305.50	2758.22	0.962

	Parameter		c_1	c_2	c_3	R^2			Parameter		c_1	c_2	R^2
2nd order	B	EPDs	-0.51	28.14	-355.61	0.72		1st order	B	EPDs	0.79	10.42	0.51
	C	SPL	-1.45	76.46	-974.21	0.96			C	SPL	-1.41	67.76	0.48
	E	PDi	0.18	-7.59	89.92	0.96			E	PDi	1.97	-37.93	0.95
	F	PDW	-0.71	40.02	-552.27	1.00			F	PDW	2.05	-44.29	0.90
	G	TPW	-1.26	70.78	-901.54	0.77			G	TPW	3.25	2.09	0.68
	H	EPWs	-0.11	8.12	-92.55	0.90			H	EPWs	2.11	-12.25	0.90
	J	-	-0.12	4.83	3.26	0.99			J	-	-1.59	89.12	0.98
	K	-	0.20	-5.99	63.28	0.98			K	-	4.62	-78.62	0.98
	P	PDH	0.18	-9.53	139.89	0.88			P	PDH	0.20	9.71	0.49

Table 3.7: Comparison between the parameters evaluated in Kunkel et al. [44], Breglia [36], Wolf et al. [26] and Alam et al. [43]. The values not evaluated in each study are identified as - and with ∗ a value that can be evaluated from the others. Only four mutual dimensions can be identified, EPWs, EPDs, PDH and PDW.

Dimension	Kunkel [44]	Breglia [36]	Wolf [26]	Alam [43]
EPWs	√	√	√	√
EPWi	√	√	-	√
EPDs	√	√	√	√
EPDi	√	√	-	√
PDH	-	√	√	-
PDHl	√	-	-	√
PDHr	√	-	-	√
PDW	-	√	√	-
PDWl	√	-	-	√
PDWr	√	-	-	√
PS	-	√	√	-
PSl	√	-	-	√
PSr	√	-	-	√
PT	-	√	-	-
PTl	√	-	-	√
PTr	√	-	-	√
TPW	√	√	√	-
SCW	√	√	-	√
SCD	√	√	∗	√
SPL	√	√	√	-

1. evaluation of the correlation analyses (subsection 3.4.1);

2. comparison of the dimensions estimated from the correlation analyses with subject-specific datasets (SSD and VHP, subsection 3.4.2).

3.4.1 Correlation analyses evaluations

The range of goodness of fit of the linear and non-linear regression analyses, of the datasets of Alam et al. [43] and Wolf et al. [26], are reported in terms of minimum, maximum values and overall mean values (Table 3.8). In Alam

Table 3.8: *Range of R^2 values for all the dimensions evaluated in the two datasets.*

Polynomial order	R^2	Alam male	Alam female	Wolf
3rd	min	0.245	0.471	0.772
	max	1.000	0.995	0.998
	mean	0.657	0.695	0.910
2nd	min	0.075	0.295	0.717
	max	0.998	0.919	0.998
	mean	0.547	0.602	0.882
1st	min	0.001	0.000	0.480
	max	0.880	0.909	0.948
	mean	0.498	0.291	0.701

et al. [43], there is a noticeable difference between the R^2 obtained from male and female subjects. This difference is explained by a high variability in the VBHp of the original dataset in the male subjects (Figure 3.7), evaluated as the percentage difference in VBHp between the vertebrae taking the L1 vertebra as a reference, evaluated as:

$$d(L1, L_i) = \frac{L1 - L_i}{L1}\%$$ (3.4)

where L_i represents the other vertebrae levels (L2, L3, L4, L5) and the results are reported in Table 3.9. The correlation analyses were used to

Table 3.9: *Variability in the VHBp in the male and female datasets. The variations are evaluated as the percentage difference with the L1 vertebrae as in Equation 3.4.*

Dataset	$d(L1, L2)\%$	$d(L1, L3)\%$	$d(L1, L4)\%$	$d(L1, L5)\%$
Male	-3.65	-1.24	3.90	11.91
Female	-4.26	-7.30	-2.38	6.64

evaluate the vertebral dimensions, estimated with the different orders of polynomial curves. The dimensions were evaluated for the datasets of Alam
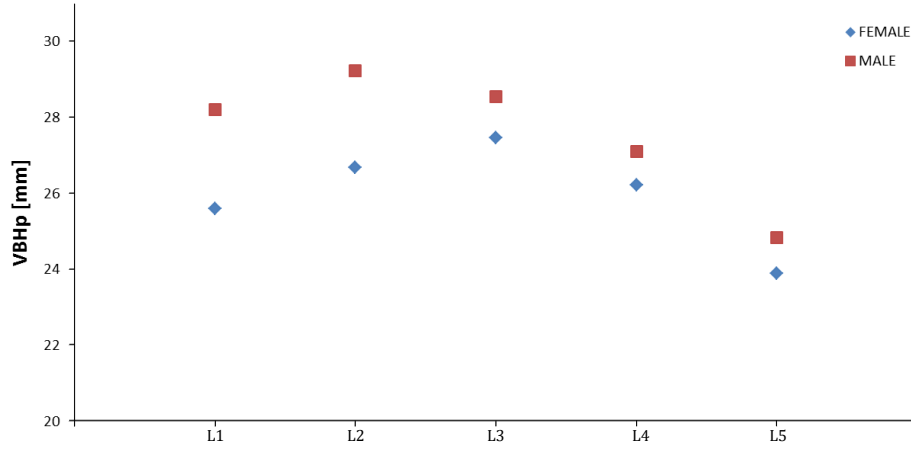
Figure 3.7: Values of the VHBp at each level of the lumbar spine for male and female datasets in the Alam et al. [43]'s dataset.

et al. [43] and Wolf et al. [26] (Figure 3.8 and Figure 3.9), and compared with the subject-specific datasets (VHP and the SSD). From the overall results, the R^2 values reported in Table 3.8, the 3rd order polynomials fit best the initial dataset, but it is evident in Figure 3.8 and Figure 3.9, that 2nd and 1st order polynomials best follow the subject-specific trends. The 3rd order polynomials are characterized by high changes in their curvatures, which vary between positive and negative values. This factor can strongly affect the estimation of the vertebral parameters, that would be valid only in the range of values in which the fitting has been done, then not obtaining a correlation able to fit a wide population.

The correlation analyses results obtained from Alam's dataset reported a mean R^2, varying from the 1st to the 3rd order polynomials, between 0.498 and 0.657, for male subjects, and between 0.291 and 0.695, for female subjects. In the case of Wolf, the R^2 values ranged from 1st to 3rd order polynomials between 0.701 and 0.910. The results can be described when evaluating the fitting as low, moderately and well correlated, when $R^2 < 0.5$, $R^2 > 0.5$ and $R^2 < 0.8$ and $R^2 > 0.8$, respectively.
Using such criteria for the male datasets [43], on a 3rd order polynomial, only the dimensions related to the spinal canal and the sagittal inclination of the pedicles (SCD, PDIsl and PDIsr) resulted in a low correlation ($R^2 < 0.5$). All the other dimensions were moderately correlated (EPWs, EPDs, EPWi, EPDi, PDWl and PDWr, PDHr, with $R^2 > 0.5$ and $R^2 < 0.8$) or well correlated (PDHl, SCW, PDItl and PDItr with $R^2 > 0.8$). Using 2nd and 1st order polynomials, the correlation of EPDs, EPWi, EPDi had a reduced R^2 value leading to a poor correlation. Evaluating the correlation analyses based on Wolf's dataset, using either the 3rd and 2nd order polynomials, most of the vertebral dimensions resulted well correlated (EPWs,

Table 3.10: R^2 *obtained for all the correlation analyses on each dataset,*
where for Alam only the male dataset was reported.

R^2	Kunkel [44] 3rd	Breglia [36] 1st	Wolf [26] 3rd	2nd	1st	Alam [43] 3rd	2nd	1st
EPWs	0.982	0.953	0.903	0.898	0.896	0.727	0.661	0.661
EPDs	0.981	0.923	0.799	0.717	0.515	0.563	0.276	0.273
EPWi	0.976	0.937	-	-	-	0.640	0.412	0.412
EPDi	0.981	0.887	-	-	-	0.584	0.075	0.060
PDW	-	0.461	0.998	0.998	0.897	- -	-	
PWl	0.590	-	-	-	-	0.558	0.558	0.546
PWr	0.537	-	-	-	-	0.678	0.677	0.672
PDH	-	0.767	0.962	0.875	0.495	- -	-	
PDl	0.853	-	-	-	-	0.924	0.908	0.880
PDr	0.879	-	-	-	-	0.645	0.641	0.636
SCW	0.964	0.104	-	-	-	0.999	0.998	0.824
SCD	0.811	0.024	-	-	-	0.447	0.221	0.213
SPL	0.882	0.774	0.969	0.956	0.480	-	-	-
TPW	0.616	0.400	0.772	0.770	0.675	-	-	
PTI	-	0.001	-	-	-	-	-	-
PDItl	0.693	-	-	-	-	0.873	0.872	0.820
PDItr	0.524	-	-	-	-	0.899	0.898	0.826
PDIs	-	0.440	0.965	0.956	0.948	-	-	-
PDIsl	0.524	-	-	-	-	0.411	0.264	0.143
PDIsr	0.669	-	-	-	-	0.245	0.197	0.001
mean	0.779	0.556	0.910	0.882	0.701	0.657	0.547	0.498
max	0.982	0.953	0.998	0.998	0.948	0.999	0.997	0.880
min	0.524	0.001	0.772	0.717	0.480	0.245	0.075	0.001

PDW, PDH, SPL, PDIs with R^2 >0.8) or moderately correlated (EPDs,
TPW with R^2 <0.5, R^2 >0.5), while in the 1st order fitting the fitness
quality decreased for the PDH and SPL measurements. Evaluating the 3rd
order fittings (*Group a: Alam, Wolf and Kunkel*), the correlation analysis on
Wolf dataset had the highest overall R^2 mean value (Kunkel mean R^2=0.779,
Wolf mean R^2=0.910 and Alam mean R^2= 0.657). The same trend is shown
for *Group b (Alam, Wolf and Breglia)* (Breglia mean R^2=0.556, Wolf mean
R^2=0.710 and Alam mean R^2= 0.498). If considering only the dimensions,
for *Group a*, the R^2 on the analysis of Wolf are higher than the Kunkel's,
except for the EPDs (Kunkel R^2=0.981, Wolf R^2=0.799). In the *Group b*,
the highest R^2 for the PDW, TPW and PDIs was found in the correlation
analysis of Wolf, while in the same analysis EPDs, EPWs, SPL and PD are
lower than in Breglia. In all the compared dimensions, the correlation based
on the dataset of Alam had the lowest R^2.

3.4.2 Correlation analyses accuracy

In Figure 3.10, the dimensions obtained from the correlation studies of Kunkel et al. [44] and Breglia [36] were compared with the results of the 1st order polynomial fitting obtained from the datasets of Alam et al. [43] and Wolf et al. [26]. Furthermore, the analyses have been compared with the dimensions of the VHP and the new measurements described in subsection 3.2.2.

Error values have been evaluated, comparing the dimensions obtained with the correlations of Alam et al. [43], Wolf et al. [26], Breglia [36] and Kunkel et al.[44], against the subject-specific dimensions of the VHP and the new dataset considered in this study. The differences, reported in Table 3.11, have been evaluated as

$$diff = \frac{dim_{ss} - dim_{corr}}{dim_{ss}} \qquad (3.5)$$

where dim_{ss} are the subject specific measurements (VHP or SSD) and dim_{corr} are the dimensions obtained with the correlation analyses (Kunkel, Breglia, Wolf or Alam).

In the range of VBHp considered, the correlation of Kunkel (obtained with 3rd order polynomials) predicted values outside the standard deviation of the subject-specific measurements and with high errors from the VHP as reported in Table 3.11. Moreover, in the case of PDH and PDW, the values estimated are negative, then predicting solutions not physically acceptable. The percentage differences, evaluated versus both the subject-specific datasets, confirmed these findings, which were included in the ranges 1-20% for the EPWs, 32-59% for the EPDs, 82-215% for the PDH and 80-240% for the PDW.

The linear estimations of Wolf et al. [26] and Breglia [36] follow similar trends to each other. The EPWs estimated values are included in the range of variation of the subject-specific measurements for the vertebrae L1, L2, L3 and L4, while at the L5 level the predictions are less accurate. Alam et al's [43] correlation follow the same trend, however, the estimations showed a higher difference from the subject-specific values. The percentage differences confirmed these results, with error values for Breglia [36] included in the range 1%-15% against both the subject specific datasets; Wolf et al. [26] led to differences such as between 2%-10% against the VHP and 2%-12% against the subject-specific dataset; measurements from Alam et al. [43] showed differences between 8% and 20% against VHP and 10%-22% against the subject-specific measurements.

The EPDs values estimated with Breglia's correlations follow the same trend as the VHP measures with error values less than 8%, and are included in the range of variability of the subject-specific measurements at the level L4 and L5 (differences <4%) and included in the range 6-16% at the other levels.

The values predicted with Wolf's [26] correlation, showed a similar trend, with errors less than 19% with the VHP dataset and less than 12% with the other subject-specific dataset. The evaluations based on the Alam et al. [43] correlations showed high error values with the VHP (between 12% and 29%), while improved results (7%-20%) were obtained from the comparison with the subject-specific dataset.

The evaluation of the PDH estimation, showed for Breglia et al's correlation analyses errors in the ranges 4%-16%, versus the VHP, and 3%-11%, versus the subject-specific dataset. Wolf's correlation analyses showed errors in the ranges 1%-10%, versus the VHP, and 18%-25%, versus the subject-specific dataset, and Alam et al's correlation analyses had errors in the ranges 34%-44% versus the VHP and 46%-54% versus the subject-specific dataset.

The highest error values, were obtained for the PDW for all the correlation analyses. The comparison of D.P.Breglia's correlation analyses with the VHP, showed an overestimation at the level L1 and L2, (47% and 39% respectively), a minimum error value at L3 (8%) and then underestimated at L4-L5 levels (18%-42%). Similar trends have been recorded in the comparison with the subject-specific dataset, where the errors are included in the range of -61% to 26%. Using estimates based on Wolf et al's data, the PDW is overestimated from the L1 to L4 levels, and underestimated at L5 with error values ranging between -122% and 27% versus the VHP and -115% to 6% versus the subject-specific dataset. As similar trend is shown in Alam et al. [43] estimations, with an initial overestimation of the PDW at the L1 level, and then underestimation at the other levels, with error values included in the ranges -24% to 50% versus the VHP and -36% to 36% versus the subject-specific dimensions.

Table 3.11: Error values evaluated as Equation 3.5 between the dimensions obtained with the correlation analyses and the subject specific dimensions (VHP and SSD)

Corr	Par	vs VHP					vs subjest-specific				
		L1	L2	L3	L4	L5	L1	L2	L3	L4	L5
Breglia	EPWU	-3%	-4%	-2%	7%	13%	-1%	-2%	3%	7%	15%
	EPDU	-8%	4%	4%	1%	-2%	-13%	-16%	-6%	-2%	-4%
	PDH	-16%	-20%	-9%	-4%	-5%	11%	6%	9%	3%	8%
	PDW	-47%	-39%	8%	18%	42%	-61%	-42%	-7%	4%	26%
Kunkel	EPWU	-20%	-21%	-20%	-9%	-1%	-18%	-19%	-14%	-9%	1%
	EPDU	-45%	-32%	-30%	-34%	-36%	-52%	-59%	-45%	-38%	-39%
	PDH	92%	215%	157%	127%	82%	94%	190%	147%	125%	84%
	PDW	84%	236%	145%	116%	84%	82%	240%	152%	119%	80%
Alam	EPWU	8%	20%	16%	21%	20%	10%	22%	21%	21%	22%
	EPDU	12%	29%	26%	21%	15%	7%	14%	18%	20%	14%
	PDH	34%	41%	43%	44%	39%	50%	54%	53%	48%	46%
	PDW	-24%	2%	30%	34%	50%	-36%	-1%	19%	23%	36%
Wolf	EPWU	-7%	-10%	-8%	2%	10%	-5%	-8%	-2%	3%	12%
	EPDU	7%	19%	19%	15%	12%	3%	2%	10%	13%	11%
	PDH	1%	1%	9%	13%	10%	25%	23%	24%	18%	21%
	PDW	-96%	-122%	-38%	-17%	27%	-115%	-128%	-60%	-37%	6%
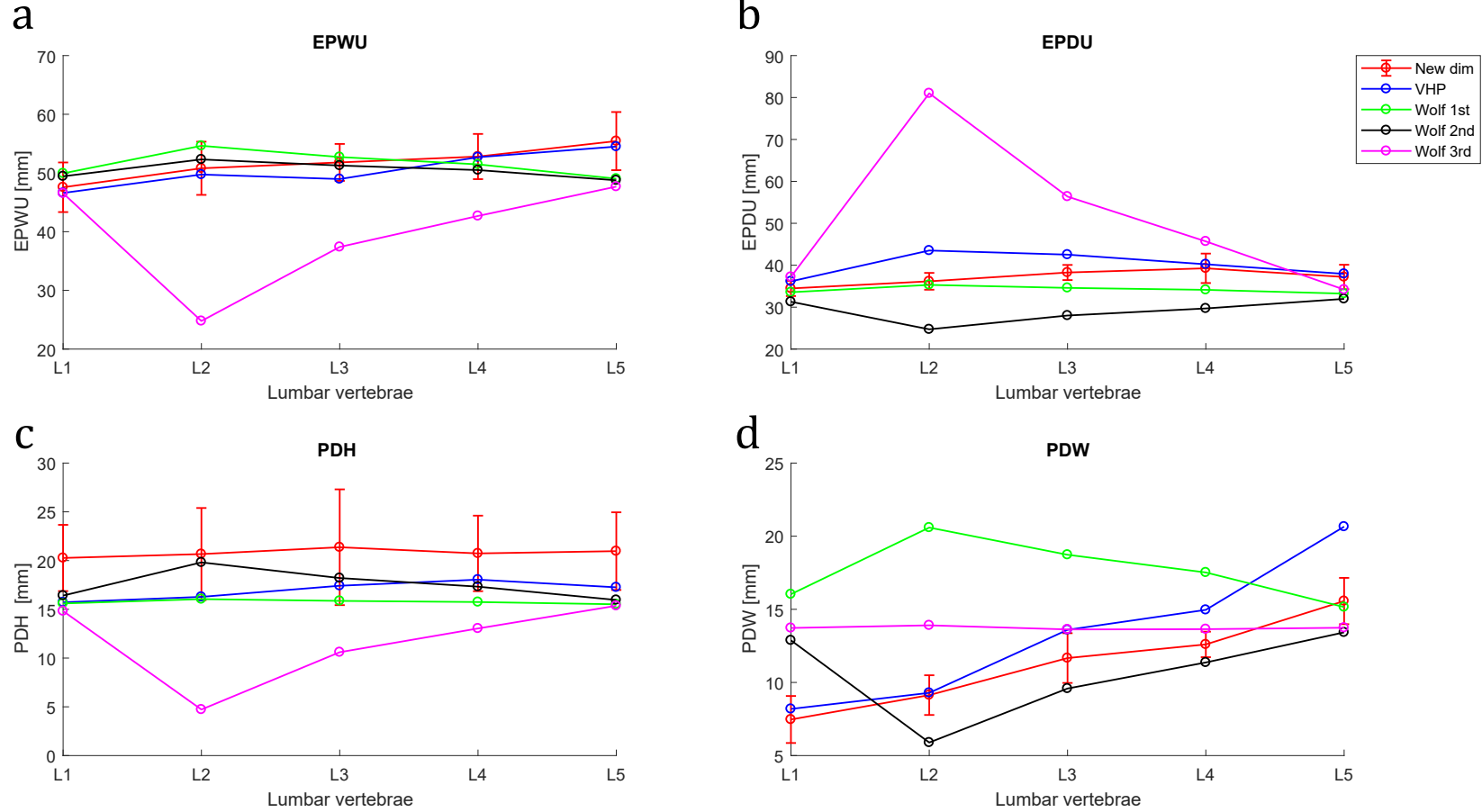
Figure 3.8: Evaluation of the correlations obtained from Wolf et al. [26] with 1st, 2nd and 3rd polynomials and comparison with the VHP and the subject-specific measurements (blue and red lines respectively). The anatomical parameters ((a) EPWu, (b) EPDu, (c) PDH and (d) PDW) were plotted in function of the vertebral level.
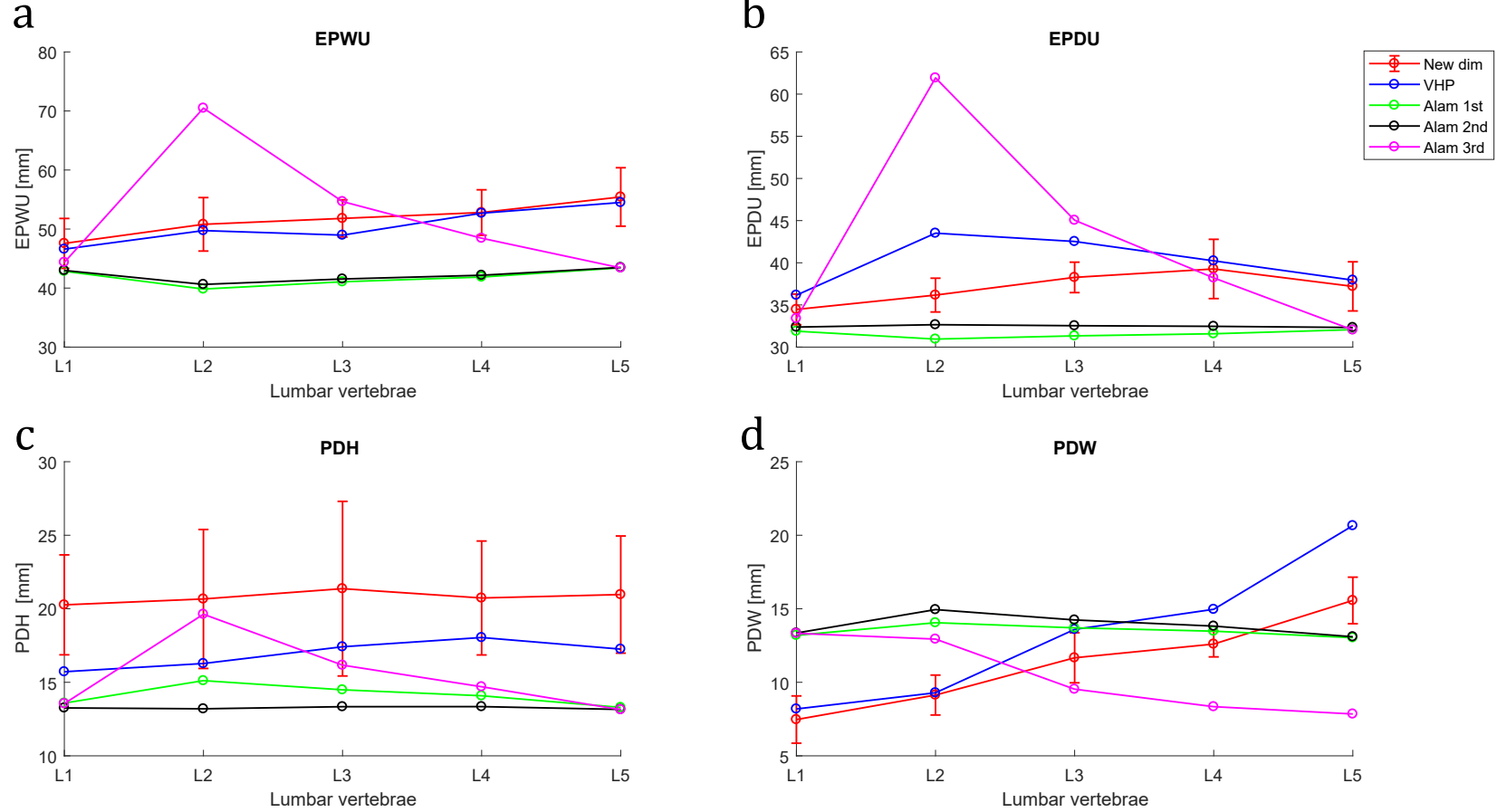
Figure 3.9: Evaluation of the correlations obtained from [43] with 1st, 2nd and 3rd polynomials and comparison with the VHP and the subject-specific measurements (blue and red lines respectively). The anatomical parameters ((a) EPWu, (b) EPDu, (c) PDH and (d) PDW) were plotted in function of the vertebral level.
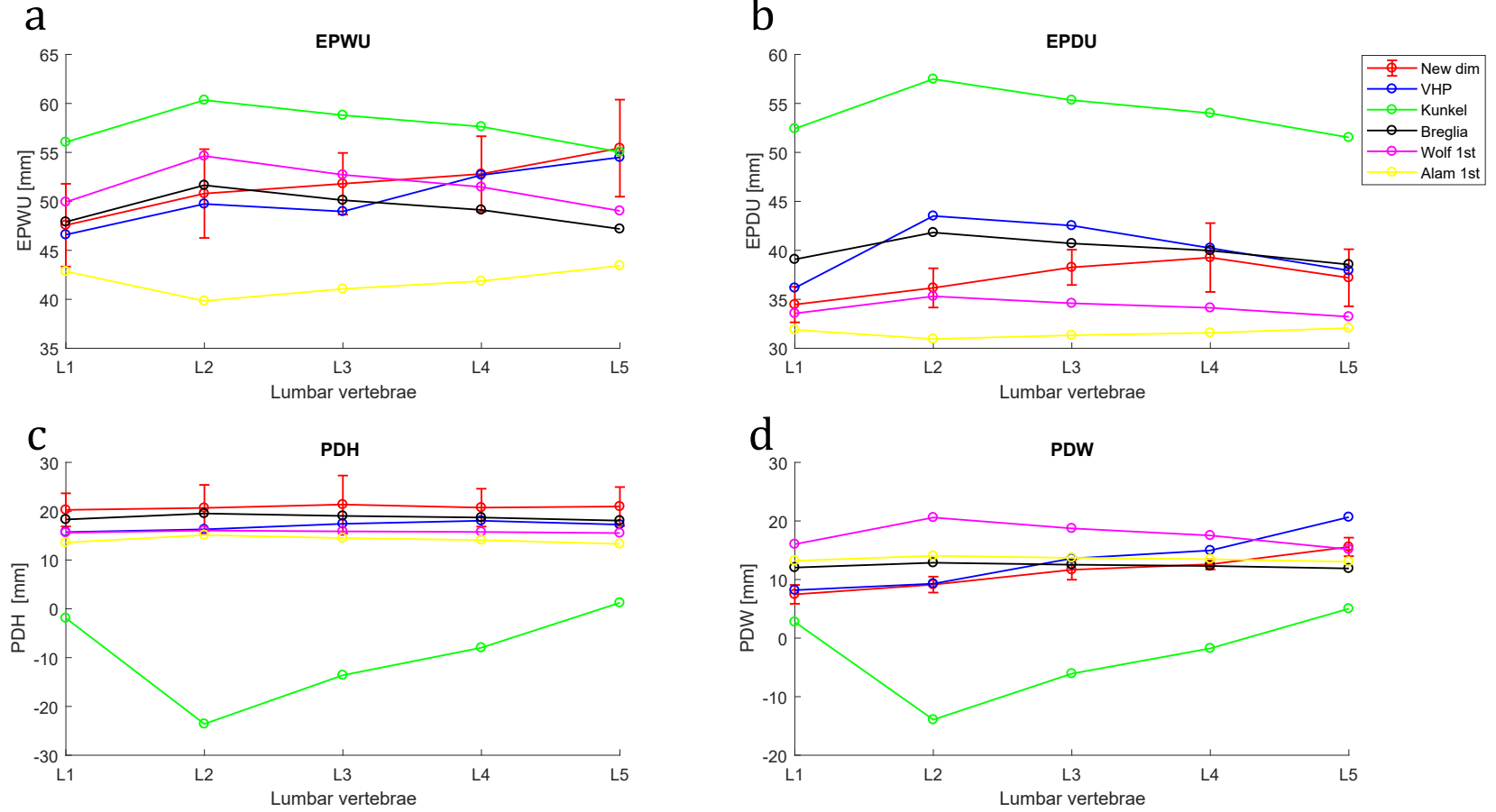
Figure 3.10: Comparison of the correlations obtained from Kunkel et al. [44],Breglia [36],Wolf et al. [26] and [43] and the dimensions of the VHP and the new measurements (blue and red lines respectively) with the correspondent error bars. The anatomical parameters ((a) EPWu, (b) EPDu, (c) PDH and (d) PDW)) were plotted in function of the vertebral level.

3.5   Discussion

The correlations between the posterior vertebral height and the dimensions characterizing the vertebrae have been analysed using the datasets available in the literature. The relationships between those parameters have been evaluated with first, second and third order polynomials, and the R^2 values have been reported to assess the goodness of fit. The correlation analyses have been used to estimate the dimensions of a person with the VBHp measured from the VHP dataset. The parameters in common in all the studies were compared (EPDs, EPWs, PDH and PDW) and the differences have been evaluated with the VHP measurements and the subject-specific dimensions.

It has been shown that a 3rd order polynomial is a poor predictor of the dimensions of the lumbar spine. Even though, this fitting curve led to the best R^2 values, the characteristic variability of the 3rd order polynomial curves lead to values which vary over an wide range and in some cases simply not physiological (e.g. negative dimensions). Moreover, in some cases such as for the pedicle depth and width, the range of validity of Kunkel's correlation analysis do not cover the possible variation of the VBHp (Figure 3.11). In fact, the 3rd order polynomials are characterized by a change in their curvature for values around 30 mm, which do lead to negative dimension (simply not a true physical representation). The same considerations are made for second order polynomials, in which the change of curvature can lead to non-valid values. Therefore, Kunkel et al's [44] correlation is valid for a narrow range of VBHp due to the nature of the fitting used (3rd order polynomials), limiting the application of its formulation, and overall it showed the highest error values (despite the better R^2 values). 1st order polynomials resulted more accurate and better followed the subject-specific trends. This emphasizes the need to compare generalised correlations with actual trends seen per individuals, to ensure that the two are comparable.

The predictions, obtained from all the correlation functions, were compared with subject-specific dimensions (VHP and SSD). The results showed that the evaluations based on Breglia [36] and Wolf et al. [26] functions are accurate (<20%) for the EPWs, EPDs and PDH. Focusing on the linear fitting results evaluated in this study (*Group b*), the dimensions based on Alam et al. [43] and Wolf et al. [26] correlations followed the subject-specific trends and the error values were higher against the VHP dataset, than the new dataset. It is worth noting that the VHP dimensions are for only one subject, whereas in the SSD the number of specimens was n=3 (i.e.: this new dataset includes anatomical variability between subjects for each dimension).

The main factors influencing the accuracy of the correlations are the ethnicity of the datasets evaluated, the number of subjects included in the subject-specific dataset and the gender.
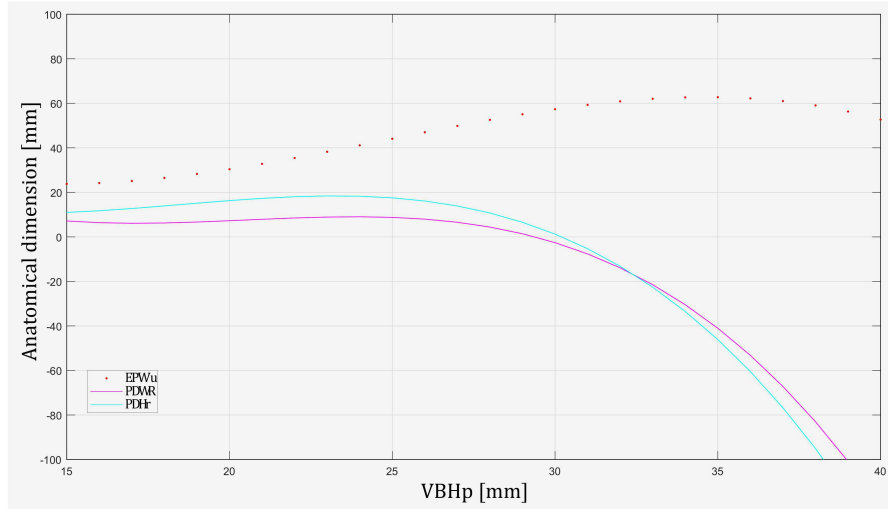
Figure 3.11: Variability of the 3rd order polynomial obtained from the correlations of Kunkel et al. [44], where the EPWs, PDWr and PDHr are plotted on varying the VBHp.

The ethnicity of the dataset included in this study are not consistent (caucasian, Israeli, Pakistani and unknown in the case of Panjabi [31]) and as stated by Alam et al. [43] there is an important difference on the morphology of subjects from different origins. Therefore, the error values are affected by the different ethnicity of the datasets evaluated which were compared with caucasian datasets (new dimensions) and Panjabi et al's [31] dataset, where the ethnicity was not specified. In order to obtain a more consistent study, the datasets should be categorized by ethnicity and the accuracy test should be evaluated with a control group with the same characteristics (gender, ethnicity).

The gender of the specimens affects the dimensions of the vertebrae, as demostrated from the Alam et al's [43] correlations, where different trends and variability between the lumbar levels are reported. Even though the gender of the study of Alam et al. [43] and the new subject-specific measurements were stated, it is not stated in the study of Panjabi [31] and Wolf et al. [26]. Thus, the correlations previously evaluated from Breglia [36] and Kunkel [44], and those of Wolf [26], are characterised by a range of variability due to the mixed gender of the datasets and the influence of the gender in those studies can not be estimated *a priori*. Hence, none of these studies evaluated sexual dimorphism, which would affect the shape of vertebrae [229, 27, 230]. The number of subjects affects considerably the statistics about the subject-specific dataset. Evaluating a numerous amount of specimens, more variability of the anatomical dimensions would be included in the study, and subsequently the correlation analyses would take in consideration a wide

anatomical description obtaining realistic and representative functions of the individuals. For this reason, the new dimensions have been used only to evaluate the accuracy of the correlation analyses obtained from the previous studies [43, 26, 36, 44]. Future studies would require the collection of high number of data-scans, dividing the dataset according to the following criteria:

- known sex, to differentiate the measurements according to the gender;

- ethnicity of the specimens to obtain coherent measurements;

- no pathologies to the lumbar spine reported for the subjects.

3.6 Conclusions

The linear correlation analyses evaluated in this study follow similar trends of the subject-specific datasets (VHP and new measurements). In particular, the correlation analyses evaluated by Breglia and those estimated from Wolf's datasets described well the parameters evaluated, obtaining error values less than 20% when compared with subject-specific datasets. However, more numerous datasets are required, to take into account the anatomical variability between subjects. Critically, collecting measurements including the gender of the specimens and the ethnicity, would be considerably beneficial as they influence the anatomical dimensions.

Currently, the dimensions collected in literature are reported accordingly with the final aim of each specific study and not all the dimensions which characterize the anatomy of the vertebrae are stated. The dimensions listed in Panjabi's dataset describe exhaustively the vertebral geometry and it should be followed when collecting new measurements. However, the description of method used in each study, in term of reference points adopted to furnish a repeatable strategy is required to identify and measure the characteristic dimensions.

In the development of a parametric and scalable model, that has been the focus of chapter 4, only Breglia et al's [36] dataset can be used (using the 1st order polynomial). It is currently the most accurate between the studies considered and, critically, contains the most complete set of dimensions to describe the vertebrae anatomy.
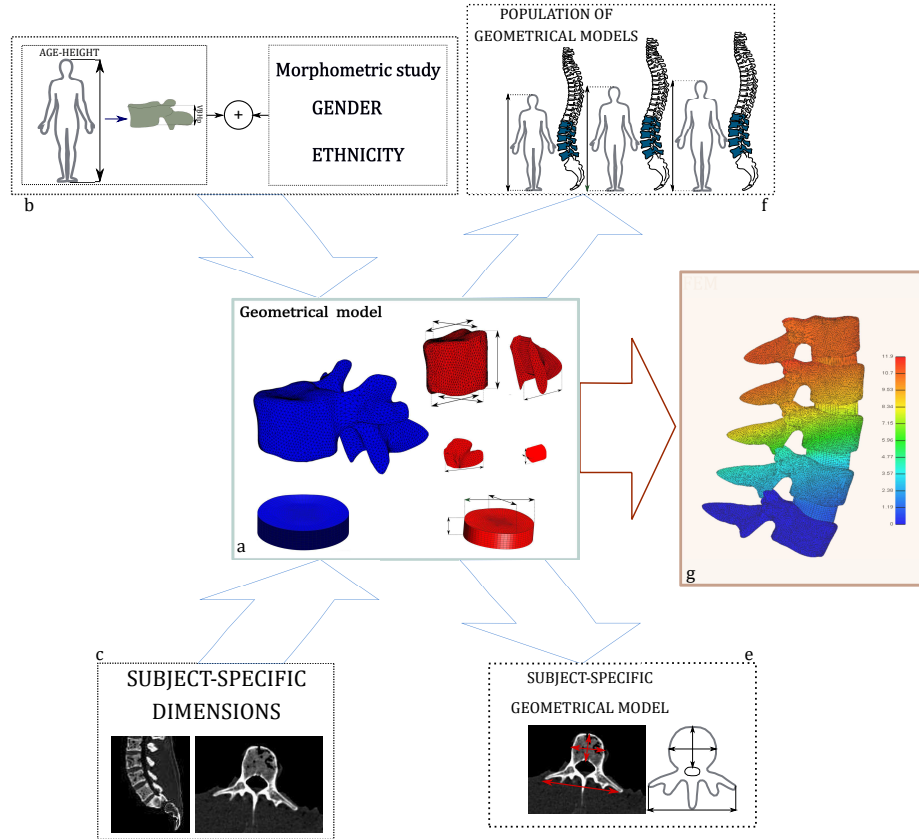
Figure 3.12: Future implementation of morphological studies in the LMG toolbox where a baseline model of the vertebrae and IVD (a) is parametrised based on dimensions evaluated through correlation analyses (b), based on the age and height of a patient, or on subject-specific dimensions measured from data scans (c). The parameterization creates either a population of geometrical model (f) or a subject-specific model (e) according to the initial input (respectively b and c). The FE model is the generated from the toolbox and solved in FEBio (g). Further explanations are given in chapter 4.

Chapter 4

The Lumbar Model Generator

4.1 Introduction

The development of new devices and the improvement of treatment techniques are needed in the care of LBP diseases. To meet design and regulatory requirements, a medical device is subjected to a review between each phase of the product design [231]. Each of these reviews introduces additional costs to the device development delaying its final release. New technologies, such as 3D printing, have assisted with this iterative design process, allowing for the rapid production of cost-effective prototypes. However, the design process of a medical device has to be evaluated in relation with the bodies and tissues with which it interfaces. These interactions can be simulated using finite element (FE) models and can be combined with iterative optimization of the design topology and mechanical properties.

Lumbar spine models available in literature are mostly subject-specific models based on magnetic resonance (MR) or computed tomography (CT) imaging [136, 96], or models based on averaged approximated dimensions which use relatively simplified geometries [232, 44, 36, 233, 234]. While models based on medical images precisely represent the subject-specific geometry, the process to generate these models is both time consuming and expensive. Moreover, to provide wider understanding, beyond a single individual, subject-specific models require a number of models to be solved, for statistical power [113]. However, idealised models based on average dimensions often lack the anatomical detail that is necessary to be of clinical value, with their geometries typically too simplistic. Further, several studies have highlighted the importance of anatomically representative geometry in simulations of the spine [114, 14] due to its effects on the intradiscal pressure, the range of motion and facet joint contact forces. Clearly, this is of relevance to any spinal device developed which use such geometry for the spine.

Recently, the Food and Drug Administration (FDA) and the Medical Device Innovation Consortium (MDIC) focused on the necessity of improving the regulatory system delivering new devices more quickly through the use of computer modelling and simulations [17, 14]. Accordingly, parametric and anatomically accurate models are needed to implement the range of combinations of geometrical features necessary to evaluate the huge variety of clinical cases that can be addressed using the designed device. This methodology would speed up the acceptance of new devices, reducing the risk of failure of the device.

The aim of this study was to develop an automated technique to obtain a population of anatomically representative models, which can be used to evaluate the effects of spinal implants on distinct anatomical features of the spine. In this study, a software toolbox named the Lumbar Model Generator (LMG) was developed and implemented using MATLAB. Using a parameterized baseline model, the LMG can be used to create a population of geometric models of the lumbar spine (from the L1 to L5 including the intervertebral discs), whose surfaces and solid regions are meshed allowing for direct use in FE models.

The parametric model generated by LMG, has an anatomically accurate geometry, as evaluated through a comparison with the male dataset of the Visible Human Project (VHP) [119], described in Section 4. The models can be reconstructed through the definition of 17 parameters. The parameter set is either determined directly from subject-specific measurements, or can be estimated from correlation analyses based on subject age and height (described in Section 3). Thus, geometric models are fully parametrized and scalable, so a range of anatomical geometries can be easily generated and replicated.

In this chapter the capabilities of the LMG toolbox are described, which includes: (i) the methodology for developing the geometry, (ii) the correlation analyses implemented to evaluate the anatomical dimensions, (iii) the process to obtain the meshed solid model ready to use in FE software. The innovative functionality, here introduced but object of further publications, is the automatic pre-processing of the solid meshed model and FE simulations. The material properties, boundary conditions and contact properties can be defined by the user and the simulation can be directly run from MATLAB, using FEBio (FEBio Software Suite). As far as the authors know, the LMG is the first toolbox which allows the accomplishment of the entire workflow (described in Figure 1) from the generation of a geometrical model, the pre-processing of the FE model and then obtaining the solution of the analysis. This chapter is based on the paper published on Interface, the Royal Society [110].

4.2   The Lumbar Model Generator (LMG) toolbox

4.2.1   General features of the toolbox

A LMG software toolbox that can generate the geometry for biomechanical models of the lumbar spine was developed and implemented in MATLAB (MATLAB, R2017a, 9.2.0.538062, The MathWorks Inc., Natick, MA, USA). The workflow of the toolbox is shown in Figure 4.1. The toolbox generates a complete lumbar spine model, including the five vertebral bodies (L1 to L5) and the four intervertebral discs (IVD) interposed between them. The main geometric features of the vertebrae and IVD follow recommendations from previous studies [44, 32]reported as linear and angular parameters used in the generated model (Figure 4.2). Models are parameterized such that they can be generated using two alternative techniques: (i) based on subject-specific dimensions (which can be directly inputted by the user) directly measured from subject-specific data (e.g. image data and scans), or (ii) using average dimensions derived from correlation analysis based on subject height and age (described further in section 4.3). Once the geometrical data has been generated, the triangulated surface geometries can be exported to a stereolithography (STL) file, which is compatible with computer aided design and finite element analysis software packages. Further, the surface model can be meshed and exported to FE software. Using FEBio to run the FE analysis, the meshed model can be pre-processed. Defining materials, boundary conditions and contact properties through MATLAB, the simulations can be requested as an output of the LMG.

4.2.2   Geometrical model

Vertebrae model

An STL file of a lumbar spine (50th percentile) was supplied by an industrial partner (*S14 Implants*, Pessac, France), used in a previous study [235]. This model was used as a template to reproduce the geometry of the lumbar vertebrae and the intervertebral discs. The two key assumptions were: (i) the geometry of the healthy spine is reproduced and (ii) the lateral symmetry, across the mid-sagittal plane, applies to both the vertebrae and IVD [233]. Each vertebra was divided into four regions: the vertebral body, the pedicles, the transverse processes and the spinous process (Figure 4.1B). The surfaces characterizing each region were identified and the best fitting polynomial curves were selected to be used to build an accurate and scalable model of the vertebrae. The solid model was parametrised, identifying the dimensions reported in literature for each region, to obtain a scalable model. The parameters identified (listed in Figure 4.2) can be independently scaled according to the dimensions obtained from the subject-specific scans or from
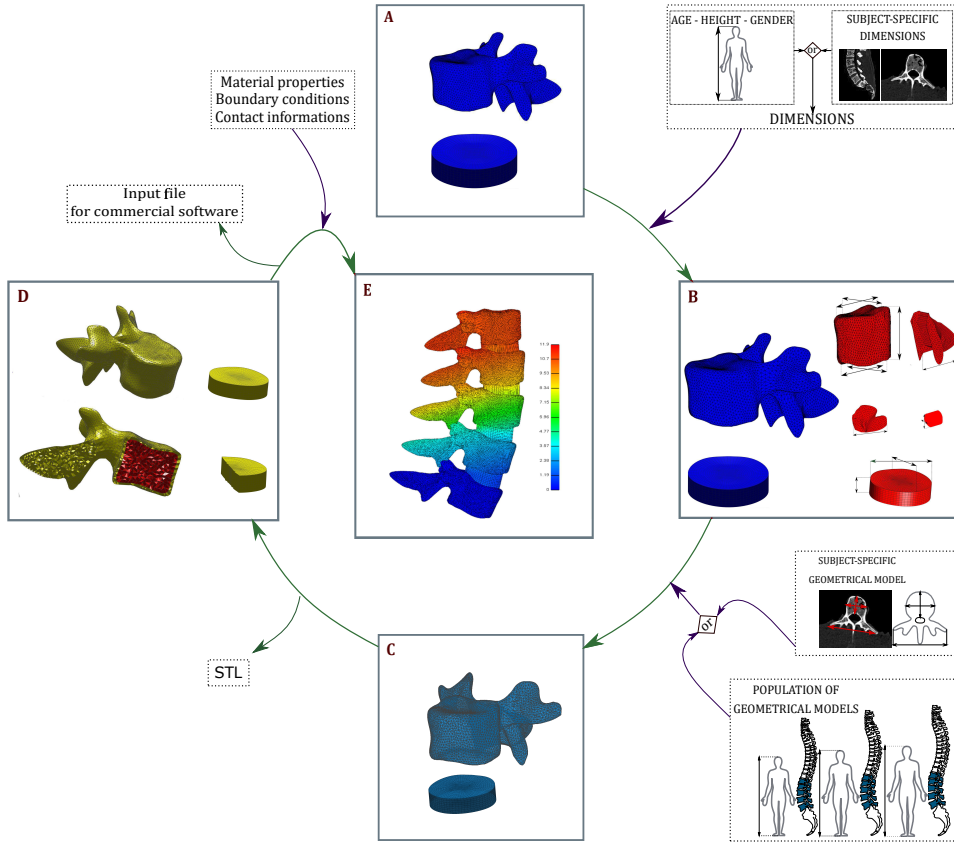
Figure 4.1: Workflow of the lumbar model generator, from the generation of the geometrical model to the solution of the FE simulation. The FE model is shown for the purpose of description and will be described in details in chapter 5. A. The inputs of the LMG are the baseline model previously generated and the dimensions, measured on subject-specific scans or average dimensions based on the height, age and gender of a patient. B. Parameterization of the geometrical model. The anatomical dimensions have been identified in each region of the vertebrae and IVD and then independently scaled. Accordingly with the input, the output of this step can be a population of geometrical models or a subject-specific model. C. Generation of a triangulated surface model and output of STL files. D. Solid meshing of the vertebrae (tetrahedral elements) and the IVD (hexahedral elements). The output of this step can be exported to commercial software. E. Preprocessing of the meshed model, defining the material properties, boundary conditions, contact properties and then run the simulations in FEBio.

C - T - L	Cervical Toracic Lumbar
VBHp	Vertebrae body height
EPW(u/i)	Endplate width (upper/inferior)
EPD(u/i)	Endplate depth (upper/inferior)
PDH	Pedicle height
PDW	Pedicle width
SCD	Spinal canal depth
SCW	Spinal canal width
TPWu	Transvers process width (upper)
TPWi	Transvers process width (inferior)
SPL	Spinous process length
IVDw	Intervertebral disc width
IVDd	Intervertebral disc depth
IVDh	Intervertebral disc height
α	Lumbar curvature
PDIs	Pedicle sagittal inclination
PDIt	Pedicle transverse inclination

Figure 4.2: The picture shows the input requested in the toolbox, in the first and simplest case only body height, age and gender are requested. In the second case, the dimensions identified have to be added as input.

the correlation analysis (described further in section 4.3). The following vertebral dimensions have been implemented:

- width of the upper and inferior endplates (EPWu, EPWi);

- depth of the upper and inferior endplates (EPDu, EPDi);

- pedicle height and width (PDH, PDW);

- spinal canal depth and width (SCD, SCW);

- width of the upper and inferior transverse process (TPWu, TPWi);

- spinous process length (SPL);

- vertebral posterior body height (VBHp);

- pedicle sagittal inclination (PDIs);

- pedicle transverse inclination (PDIt);

- intervertebral disc width and depth (IVDw, IVDd);

- intervertebral disc height (IVDh);

- lumbar curvature (α)

Intervertebral disc model

The key variable to describe the disc geometry is the IVD height [114, 14], thus only the superior and inferior surfaces have been reconstructed with the best fitting polynomial curves. The height is not constant throughout all the geometry, but it is characterized by different heights in the posterior and anterior aspects [236, 226]. However, the average height for the IVD has been used for the LMG, consistent with literature [237], and the anterior and posterior aspect were linearly scaled. Moreover, the perimeter of each endplate was simplified to be kidney-bean shaped [32, 235, 236]. The IVD was exported as composed of two different parts, the annulus fibrosus (AF) and the nucleus pulpous (NP). The volumetric percentage of the two bodies has been reported in the literature [235, 236, 44] and a proportion of 44% NP and 56% AF, corresponding to a healthy spine, was used to guide the model [235]. However, these values can be altered to simulate different pathologies. Disc degeneration affects the mechanical behaviour of the IVD, with changes in the composition of the AF and NP, and through structural changes of the disc. Thus, by implementing the volumetric fraction and the height and width of the disc as variables (further discussed in chapter 6), it is feasible to use the model developed to simulate the mechanical behaviour of degenerated discs [237].

4.2.3 3D orientation

The IVDs and vertebral bodies generated from the lumbar generator (Section 4.2) were arranged in $3D$ space (Figure 4.3). The lumbar section follows an arc of circumference [238] and in this study the value of $43.39°$ was used [239] listed as α in Figure 4.2. The centroid of each vertebral body and IVD bodies were evaluated and used to distribute the bodies in 3D space. The vertebrae have been rotated to follow the lumbar angle (α), aligned over the lumbar curvature and spaced using the IVD height at each level. The lumbar curvature is a further input parameter (α) which can be varied by the user if required for instance, to simulate pathological conditions.

4.3 Correlation analysis and evaluation of dimensions

The LMG includes a function which enables the automated generation of full vertebrae and discs based on the stature and age of a subject. This follows previous studies which have correlated these two parameters to vertebral dimensions [44, 36, 32, 237, 223, 45, 240]. According to Jason et al. [240], the combined length of the cervical, thoracic and lumbar spine (C-T-L) can
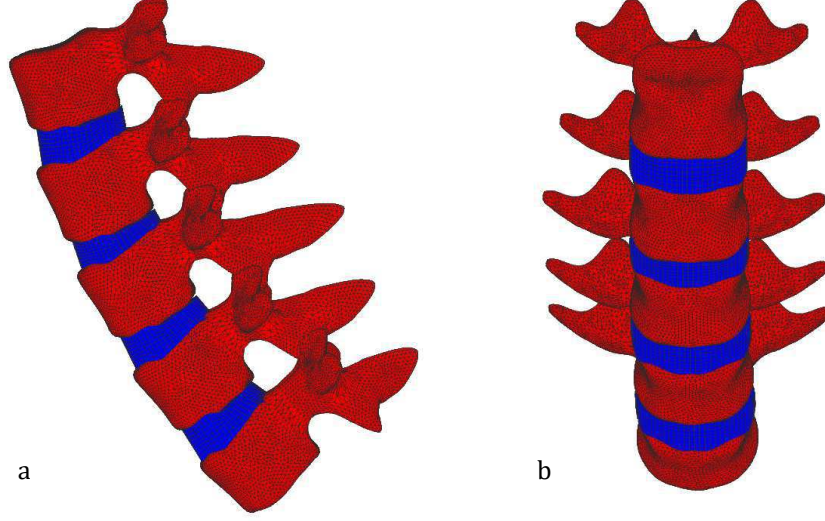
Figure 4.3: Lumbar spine model. (a. lateral, b. anterior posterior views) generated from subject-specific measurements obtained from the VHP and listed in Table 4.5 and Table 4.6.

be correlated with the stature of a subject according to Equation 4.1:

$$h = al_{CTL} + b \tag{4.1}$$

where a and b are the correlation coefficients, listed in 4.1, between the stature (h) of a person and the length of the cervical-thoracic-lumbar segments (l_{CTL}) of the spine (where CTL refers to cervical-thoracic-lumbar). Then, the posterior height for each vertebral body of the lumbar spine can be evaluated as a percentage of the total length, l_{CTL} (Table 4.2) [45]. Likewise, the IVD height is correlated with the age of the subject according to the Equation 4.2

$$h_{IVD} = cn_{age} + d \tag{4.2}$$

where h_{IVD} is the height of the IVD, n_{age} the age of a person and c and d the correlation coefficients listed in Table 4.3 (35).

The dimensions of the vertebra, described in Figure 4.2 have been correlated in previous studies to the vertebral posterior height (V_{BH_p}) [44, 36] based on datasets originally published by Panjabi [32]. Due to the axial symmetry hypotheses and to the more complete description of the anatomical features, as discussed in chapter 3, the correlation analysis used by Breglia [36] has been implemented in the LMG according to Equation 4.3

$$V_p ar = fV_{BPHp} + g \tag{4.3}$$

Table 4.1: Correlation analysis between the stature of a person and the spine segments, reported in Jason & Taylor 1995 [240]. The parameters a and b are the coefficients of the regression Equation 4.1, where a has no units and b is in [mm].

	Segment	a	b [mm]
White males	C-T-L	2.069	47.258
	Lumbar	4.058	95.562
White females	C-T-L	2.334	29.735
	Lumbar	4.375	82.367
Black males	C-T-L	2.420	29.395
	Lumbar	4.696	85.723
Black females	C-T-L	1.661	70.336
	Lumbar	3.926	91.507

Table 4.2: Percentage of the posterior height of the lumbar vertebrae, relative to the full length of the vertebral column [45].

Vertebrae	Male	Female
L1	5.55	5.59
L2	5.60	5.77
L3	5.66	5.89
L4	5.63	5.87
L5	5.71	5.91

where V_{BPHp} is the vertebral body posterior height, V_{par} identify the parameters identified in Figure 4.2, f and g are correlation coefficients shown in Equation 4.3. The entire sets of equations based on correlation analyses from literature, described above, were used to generate a full lumbar spine model. Once the age and the height of a patient were defined, these values were automatically evaluated in the script and sent as input parameters ready for use in the LMG (subsection 4.2.3).

4.4   Accuracy

The accuracy of the model generated through the LMG was assessed through comparison with the male dataset of the Visible Human Project (VHP) [119]. The male dataset was segmented from the axial cryosection photographs of a 38 year-old man, of height 180.34 cm. Two models were generated, importing the dimensions with the two procedures described above (section section 4.2):

1. The vertebral dimensions were generated following correlation analyses, importing only the age (38 years old) and height (180.34 cm) of

Table 4.3: Correlation coefficients (c and d) describing the relationship between height and age (see Equation 4.2). These equations are valid for male and female subjects between 20 and 69 years

IVD level	Male		Female	
	c [mm]	d [mm]	c [mm]	d [mm]
T12-L1	0.04903	5.19	0.04840	4.33
L1-L2	0.06201	6.80	0.04771	6.27
L2-L3	0.06687	8.32	0.04982	8.17
L3-L4	0.05455	11.05	0.05052	9.85
L4-L5	0.06952	10.76	0.05979	10.51
L5-S1	0.08630	9.73	0.08170	9.26

the VHP dataset

2. The vertebral dimensions were directly measured from a 3D reconstruction of the VHP (Table 4.5 and Table 4.6), and implemented directly into the LMG (i.e. following case-2 in section 4.2.

The accuracy of the generated vertebrae and IVD models were evaluated against the VHP model using CloudCompare (version 2.9, GPL software, retrieved from http://www.cloudcompare.org/). The Iterative Closest Point 265 algorithm was used to register the STL models and assess the RMS (Root Mean Square) error values. Moreover, the accuracy of the 3D orientation of the generated model, using the VHP dimensions, and the VH model has been examined, evaluating the RMS errors.

4.5   FE model pre-processing

4.5.1   Solid tetrahedral meshing

The geometrical model produced by the LMG is in the form of a point cloud and this section outlines the steps required to import the model into FEA software. In this section, the meshing procedures are described. Once a model has been created and meshed, the LMG allows the user to choose to work either with commercial or open source software in the model implementation. Alternatively the model can be prepared using the LMG toolbox and solved directly with FEBio. The pre-processing of the geometry developed (defined in section 4.2.2 and 5.2.2) for FEA was performed in two separate steps for the vertebrae and the IVD.

Vertebral bodies

The point cloud of each vertebra was meshed in MATLAB, using the GIBBON toolbox [241], and Tetgen [242]. In order to simulate the cortical shell

Table 4.4: Correlation coefficients of the lumbar vertebra with the posterior height of the vertebra

Linear parameters			
Parameters		f [-]	g [mm]
EPWu	Upper endplate width	1.684	-1.598
EPWi	Inferior endplate width	1.762	-0.765
EPDu	Upper endplate depth	1.233	2.838
EPDi	Inferior endplate depth	1.135	5.391
SPL	Spinous process length	2.002	13.823
PDH	Pedicle height	0.553	2.049
PDW	Pedicle width	0.368	1.218
TPW	Transvers process width	1.407	36.851
SCW	Spinal canal width	0.090	16.553
SCD	Spinal canal depth	0.121	17.777
SPL	Spinous process length	2.0017	13.823
Angular Parameters			
Parameters		f [mm]	g []
PDIs	Pedicle sagittal inclination	-1.246	46.075
PDIt	Pedicle transverse inclination	0.042	4.683

Table 4.5: Vertebral dimensions measured from the VHP.

Vertebrae Dimensions [mm]	L1	L2	L3	L4	L5
EPWu	46.60	49.74	48.97	52.69	54.50
EPDu	36.16	43.51	42.53	40.23	37.94
EPWi	48.85	50.47	52.19	53.44	54.19
EPDi	37.72	44.75	39.04	38.73	36.13
VBHp	29.40	31.63	30.72	30.13	28.98
PDH	15.72	16.28	17.42	18.05	17.26
PDW	8.19	9.29	13.60	14.96	15.00
SPL	36.06	38.58	42.63	36.72	36.00
PDIs	15.02	14.74	14.40	14.57	14.12
PDIt	5.73	5.74	5.75	5.74	5.76
SCD	18.00	16.90	16.04	17.00	17.00
SCW	22.27	22.24	22.56	24.00	25.00
TPWu	74.21	88.84	96.89	96.79	97.45
TPWi	24.97	22.43	26.80	31.25	42.14

in the vertebral bodies, during the meshing procedure, the internal cancellous core was selected and specific element indexes were assigned. The thickness of the cortical shell is either defined by the user or left at its default value and then different material properties can be assigned (Figure 4.4).

Table 4.6: Dimensions of the IVD measured from the VHP.

IVD dimensions [mm]	L1-L2	L2-L3	L3-L4	L4-L5
IVDh	9.07	11.11	12.91	11.07
IVDd	36.16	43.51	42.50	40.23
IVDw	46.60	49.74	48.97	52.50

Table 4.7: RMS error values of the accuracy test between the VHP model and the models obtained with the LMG toolbox using the two procedures: evaluating the dimensions on the VHP model and using the measurements obtained from the correlation analyses.

	VHP dimensions	Age and height correlation	IVD	VHP dimensions	Age and height correlation
	RMS [mm]	RMS [mm]		RMS [mm]	RMS [mm]
L1	1.51	1.68	L1-L2	1.11	3.19
L2	1.54	1.59	L2-L3	1.18	3.90
L3	2.13	2.39	L3-L4	1.31	3.38
L4	1.82	2.54	L4-L5	1.57	3.72
L5	2.94	4.30			
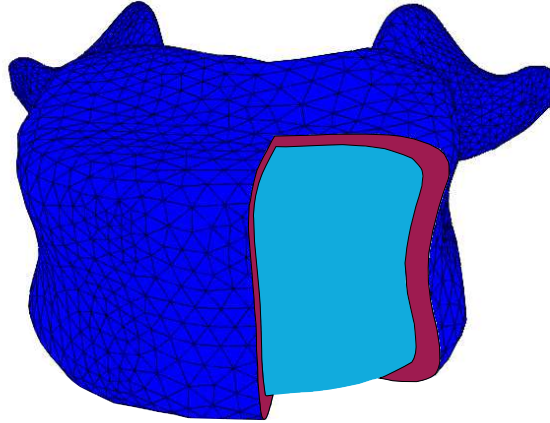
Figure 4.4: The vertebral body was divided into cancellous and cortical bone. The thickness of the cortical bone can be defined by the user in the toolbox

Intervertebral discs

The high complexity of the IVD microstructure, where collagen fibres are embedded in the ground substance, required the definition of a structured mesh. A custom algorithm was developed in MATLAB, using the Gibbon toolbox, to mesh the AF and the NP. The parameters to define the mesh size are the perimeter points of the AF (pp), the volumetric percentage (VP) of the IVD, the number of layers (nl) which will be implemented in

the AF and the number of elements in the axial direction (*nz*) (Figure 4.5). Initially, a 2D mesh structure was defined, which combined the concentric
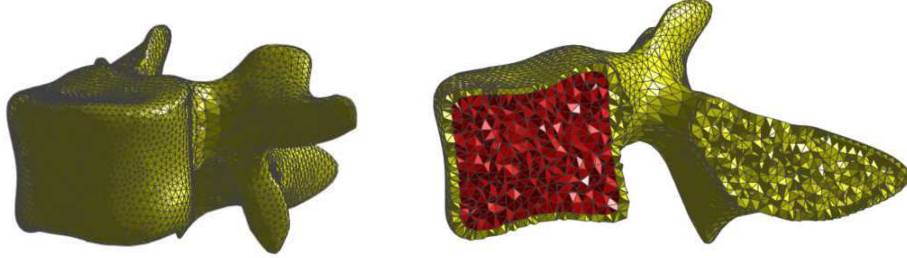
Figure 4.5: IVD mesh. (a) Representation of the surface, meshed by quadrangular elements, where in the AF they follow the external perimeter, arranged in nl layers. (b) Division between NP and AF, and the volumetric ratio (VP) is an input of the toolbox. (c) The number of elements nz can be defined to obtain a finer mesh.

alignment of the elements and an internal rectangular grid, subsequently smoothed with an elliptical perimeter to improve the mesh quality. The positions of the perimeter points are concentrically scaled and replicated *nl* times to reproduce the concentric alignment of the collagen fibres. The mesh element size depends on the VP, on the number of layers and on the number of points taken on the perimeter (Figure 4.6). The elements in the
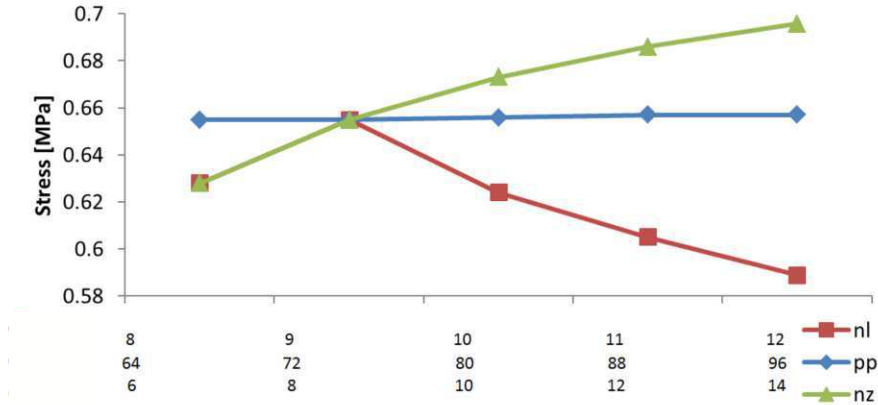
Figure 4.6: Mesh convergence test on varying the geometrical parameters (nl, pp, nz) for the IVD mesh.

AF were oriented following the perimeter and arranged in concentric layers, in order to mimic the layers of fibres of collagen and assign their material properties so as to represent fibre-orientation.

Mesh quality

In order to check the mesh quality in the generation of several models, the mesh quality was evaluated through a sensitivity analysis. In the case of the vertebral bodies, two cases were evaluated: 1. Different mesh dimensions were considered (1.2 to 2.2 mm); 2. Three models were generated based on different person heights (1.75 m, 1.80 m, and 1.82 m). The mesh quality criteria evaluated from TetGen included the aspect ratio, the face angles and the dihedral angles (the definitions are reported in Si [242]). The evaluation of the mesh quality does not have a unique definition, but it depends on the application [242, 243]. Consistent with previous studies, the mesh quality was judged satisfactory when at least 95% of the elements had an aspect ratio less than 4, and face angle less than $100°$ and dihedral angles were less than $130°$, consistent with existing literature [243, 244, 245, 246, 50]. A mesh convergence test was performed in FEBio for the L1 vertebra at different mesh sizes (1.4 mm, 1.6 mm, 1.8 mm, 2.0 mm, 2.2 mm), applying 1 MPa pressure over the superior surface. The difference in the stress between the model with the finest mesh and the others was evaluated and the results led to the selection of 1.6 mm with an error of less than 5% (as compared to subsequent mesh refinement). The frequency distribution of the quality criteria of the L1 vertebrae was then compared either with the distribution of the other vertebrae (L2 to L5) or the distribution of the models based on different body dimensions, through a quantile-quantile plot (QQ-plot).

The IVD mesh was evaluated through a sensitivity study on varying the parameters which influence the mesh size pp (64, 72, 80, 88, 96), nl (8, 9, 10, 11, 12) and nz (6, 8, 10, 12, 14), described above. A pressure of 0.5 MPa was applied to the upper surface with the lower surface fully constrained, further, neo-hookean material properties were assigned to both the AF and NP ($E_{AF} = 5$ MPa, $_{AF} = 0.3$; $E_{NP} = 3$ MPa, $_{NP} = 0.3$, where E_{AF} and E_{NP} are the Young's moduli and v_{AF} and v_{NP} the Poisson's ratio for the AF and NP [96]).

4.6 Model evaluation

4.6.1 Comparison between the LMG generated and the VHP

A comparison between the VHP spine and the generated models are shown in Figure 4.7, and the RMS values are reported in Table 4.7. The quantitative analysis highlighted the areas of the model which differ most from the VHP model. In particular, the largest differences have been identified in the posterior vertebral structures, where the superior and the inferior articular facets, lamina and pedicles of the generated geometry are less detailed. For all the vertebrae, the maximum RMS error for the models generated with the correlation analysis were higher than for the models generated using
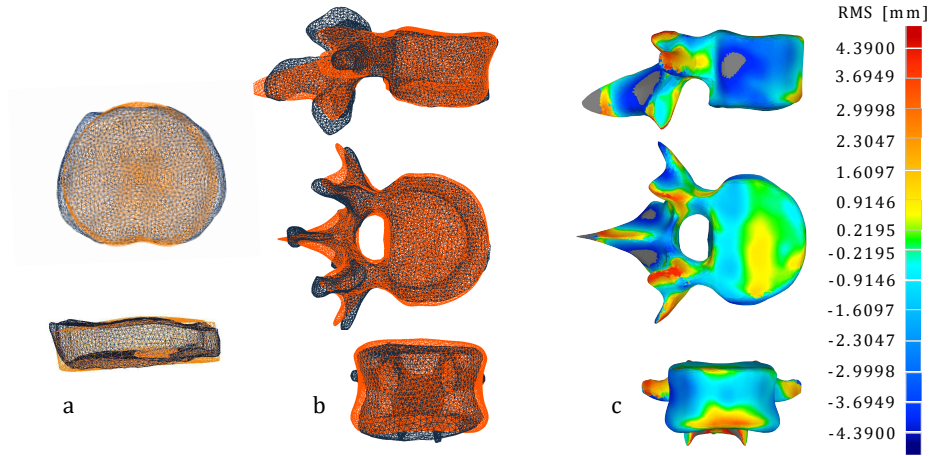
Figure 4.7: Accuracy evaluation. Qualitative evaluation of the accuracy between the VHP model in black and the generated model in orange a. IVD, b. vertebrae; c. quantitative evaluation of the accuracy through the RMS error values for the vertebrae.

the VHP dimensions. In both cases, the L5 vertebrae geometry showed the highest RMS values. Lower RMS values are shown when the dimensions are directly measured on the subject specific model and then imported into the algorithm. In fact, using the correlation analysis method based on previous studies [44, 36], the model is affected by the grade of correlation between the variables. High and moderate errors have been shown in the dimensions, which had low (R^2 less than 0.5: PDW, SCW, SCD, TPW, PDIt, PDIs) and moderate correlation coefficients (R^2 between 0.5 and 0.8: SPL, PDH), provided by [36]. Figure 4.8 shows the accuracy of the 3D orientation between the generated model and the VH model. Due to the supine position of the cadaveric specimen during the image acquisition, the curvature of the lumbar curve is reduced as compared to an upright position. Nevertheless, using CloudCompare a best fit registration has been performed, obtaining a mean RMS value of 2.73 mm.

4.6.2 Mesh quality evaluation

Assessment of mesh convergence demonstrated a suitable compromise between a mesh size (which preserves geometric precision) and variation in predicted results. In the case of vertebral bodies, the differences in stress from the finer model are less than 5%, where the fine model has a mesh size of 1.2 mm. The mesh convergence study on the IVD found that the differences in the stress values were less than 6% varying the *nl*, *nz* and *pp* parameters (Figure 4.6). A sensitivity analysis was performed to evaluate potential differences in the mesh quality throughout the vertebrae (L1-L5) or

Figure 4.8: Accuracy on the whole model. The VH model (black) has been overlapped on the model generated (orange), using the best fit registration in Cloudcompare. Due to the supine position of the cadaveric specimen, the lumbar curvature is lost in the VH model.

on varying the dimensions selecting different body heights of a patient. The mesh quality obtained in both approaches was checked through a QQ-plot where the vertebra L1 with element size of 1.6 mm, generated as average model based on a person of 1.75 m height, was taken as reference. The QQ-plots in Figure 4.9 demonstrate that there were no differences between the distributions on varying either the vertebrae considered (Figure 4.9a) and the dimensions of the specimens (Figure 4.9b). The sensitivity analysis on varying the geometrical dimensions, in both the IVD and vertebræ bodies, showed that there were no effects on the mesh quality. The mesh quality reported that more than 95% of elements had an aspect ratio of less than 4, more than 98% of elements had a face angle less than 100° and more than 95% of elements had a dihedral angle less than 130°, consistent with other
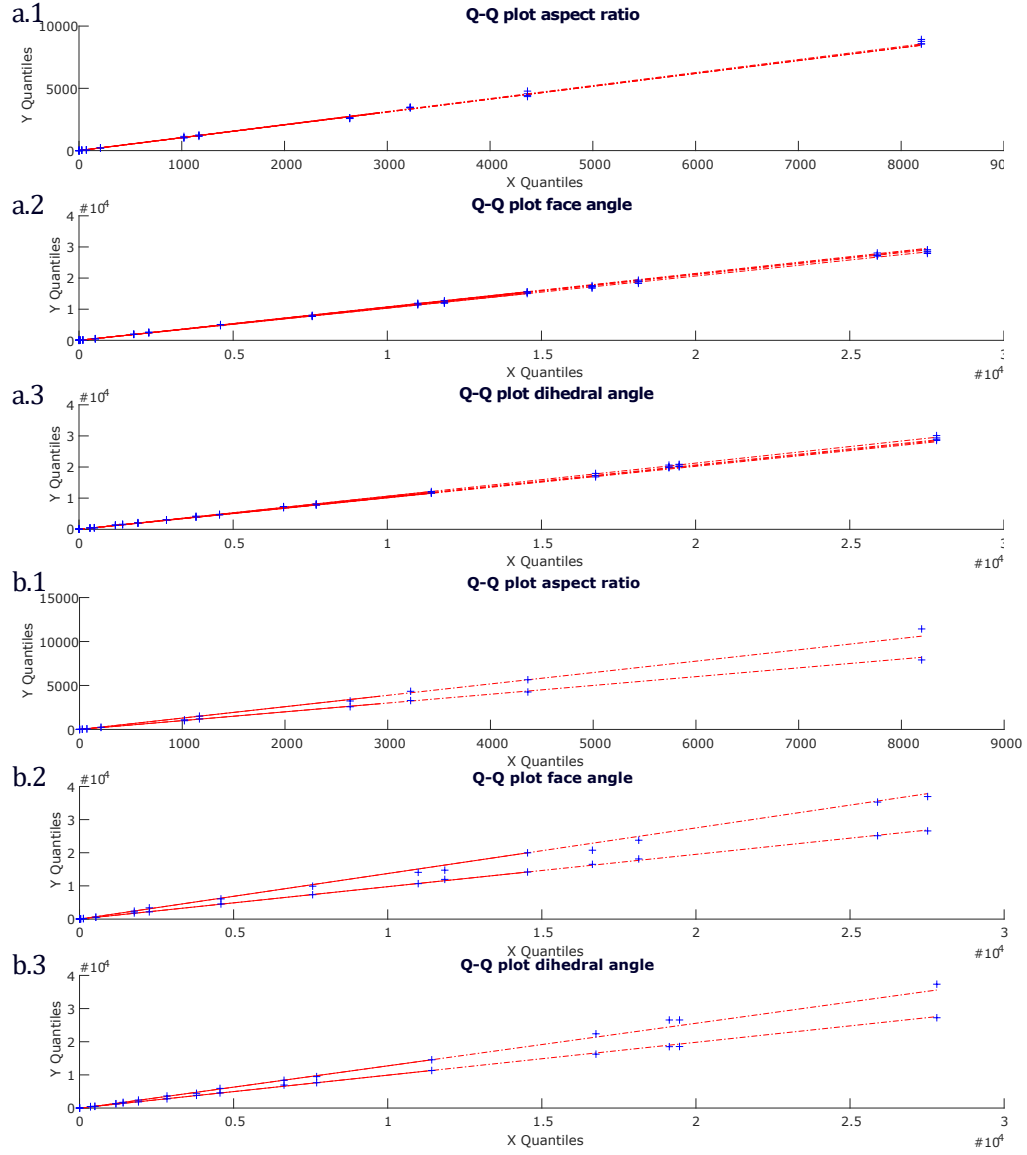
Figure 4.9: QQ plots between a. the L1 vertebrae and the other vertebrae at mesh size of 1.6 mm; (b) and between the geometrical model based on a person 1.75 m height and those ones at 1.80 m and 1.82 m. The three different criteria are showed: (a1 and b1) aspect ratio,(a.2 and b.2) face angle, (a.3 and b-3) dihedral angle.

studies [247]. Quantitative results of the distribution of the dihedral angle are shown in Figure 5.5, where the two histograms show the distribution of the maximum and minimum dihedral on the total number of elements.
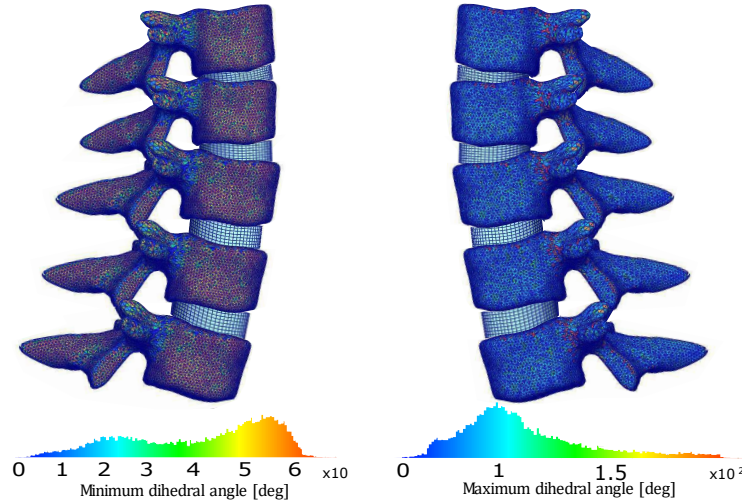
Figure 4.10: Qualitative analyses of the dihedral angles for the tetrahedral elements of the vertebral bodies. The minimum (a) and maximum (b) dihedral angles are shown and the colormaps refer to the histograms below.

4.7   Discussion

The Lumbar Model Generator (LMG) is a toolbox which allows the generation and simulation of finite element models (further described in chapter 5 and chapter 6) for the lumbar segment. It is possible to obtain averaged models, imported using as input only the height, age and gender of a patient, where the dimensions are evaluated from a subroutine based on the correlation analysis described above. Another option is to input the data evaluated from subject specific scans, or alternatively opting for a hybrid use of the tool, changing the dimensions desired from the averaged model. In the case of the former, it is not necessary to have clinical data available, and a population of models can be generated based on the gender, age and height of patients. The output can then be pre-processed in commercial software able to read STL file or input file for commercial software can be requested (e.g. Abaqus, Hyperworks). The main novelty is the possibility to obtain from the LMG, using as input a set of dimensions: 1. a geometrical model, based on dimensions obtained from subject-specific scans or on correlation analysis; 2. obtain a solid meshed model; 3. pre-process the model directly in MATLAB; 4. run the simulations using FEBio. The LMG could be seen as having two end-user applications: (i) clinical/industrial applications where

a device is assessed using FEA on a range of models; (ii) engineering science applications where multiple variables are assessed to determine the sensitivity of whole spine mechanics to these variables. Pathological conditions can be evaluated implementing models with different lumbar curvatures to compare to the averaged lumbar curvature, or changing the volumetric ratio between the NP and AF or varying their material properties [50].

Considering that the LMG was intended as an averaged model, which does not take into account the subject-specific anatomical variations, the models generated through the LMG toolbox are anatomically realistic. Moreover, subject-specific models are affected by errors due to the segmentation procedure. In fact, the accuracy of the geometry obtained from scans depends on the type of scan used (CT or MR), their respective resolutions (inter-slice resolution ranging between 0.6 mm to 2.5 mm), the technique used for the segmentation (mean RMS errors of around 1 mm) and the operator expertise (RMS errors ranging between 0.39 to 1.22 mm) [109][108]. Hence, the RMS errors obtained in this study are comparable to the range of accuracy of subject-specific models and is thus considered acceptable. The highest differences between the VPH model and the generated one have been highlighted in the accuracy test and they are principally localised in the posterior area of the vertebrae. The effect of the geometry of the spinous processes on the biomechanics of the spine has been evaluated [114, 14], however, no direct influence has been identified. Future studies would investigate the limitations due to the simplified geometry of spinous processes. The RMS error values, showed good agreement with the subject-specific model: the RMS values were less than 2.94 mm when the model was based on the VHP dimensions, and RMS values less than 4.30 mm when generated with correlation functions. In particular, greater difference has been highlighted at the L5 level (RMS values between L1 and L4 less than 2.54 mm while it is 4.30 mm at the L5 level). This is justified by assessing previous studies [44, 248, 249], which did not consider the L5 vertebrae in morphometric studies due to the high variability of its geometry. Moreover, the higher RMS values are related to the lumbar vertebrae obtained from the correlation analysis, which are affected by uncertainties, as reported in chapter 3.

Unfortunately, the measurements between the different correlation and morphometric studies could not be merged since those studies did not consider the same anatomical parameters, gender or ethnic group, which would affect the whole correlation analysis [43, 250]. Further studies are required to obtain more complete datasets of morphological measurements and to evaluate new correlation analyses, as described in chapter 3. Moreover, the fitting of the posterior part of the vertebrae shall be improved and further parameters (i.e.: thickness and height of the spinous processes) will be added to better describe their geometry.

The results on the mesh quality and its reproducibility on different geometries showed that the automated generation leads to valid meshed models. Using a fixed mesh size, according to the mesh convergence test, demonstrated that the mesh quality of the vertebrae was not sensitive to the variation of the vertebral dimensions. Hence, the FE model can be directly set up to run the simulations without further time-consuming actions.

Several models have been developed based on subject specific datasets [165, 178, 251, 252]. Subject specific models have the advantage to reproduce the anatomy of the patient accurately, with the possibility to include soft and hard tissue with high resolution. However, they reproduce the anatomy of an individual subject and reconstructing these individual models is time consuming. Further, they require extensive pre-processing. This final point is actually a barrier to clinical implementation because of the need to have someone dedicated to develop and solve the models. The LMG offers an anatomically representative alternative to such models, as it is scalable to average human dimensions, it does not require an extensive segmentation processes. Moreover, the pre-processing is accelerated further since the models can be directly meshed and the material properties, boundary and loading conditions can be imported in order to obtain a ready-to-solve FE model (described in chapter 5).

In the last decades several models have been created using average dimensions [253, 233, 234, 114] obtaining models to get quantitative analysis over the biomechanics of the lumbar spine. However, all of them have used approximations in the anatomy of the vertebrae. Campbell et al. [116] developed an automatic tool to reconstruct models from data scans without user intervention and with low computational cost. This enables highly detailed models from subject specific data. However, the limitation is that it requires having data from clinical studies. As far as the author knows, this current study is the first parametric model which generates a full finite element model and includes the potential for anatomical variability and the flexibility to input the dimensions of an individual subject. This model has been used to perform a preliminary sensitivity analysis (descibed in chapter 6), varying morphological parameters and material properties, and further studies will be performed varying the dimensions most subjected to change in the population. These models could be used in the design process of new devices, or to develop custom made implants and assess their performance, as recently recommended by the FDA and MDIC [17]. The biomechanics of the spine has been identified as being sensitive to parameters such as the lumbar curvature, the vertebral body height, IVD height and the width of transverse processes [182, 134]. Therefore, the evaluation of the functionalities of new devices and how they influence the biomechanics of the spine, in several anatomical configurations, will lead to the design optimization and

customization of new implants. The intention is to implement the lumbar model to assess the validity of devices such as BDyn (chapter 7), a posterior stabilization device produced by S14 Implants and described elsewhere [254], to assess the performance of the device and its effect on the spine. Further optimisation of posterior stabilization devices is of value because, unlike fusion, such devices retain motion at the spinal segment of interest.

The current study has focused on the concept of developing an anatomically accurate but automated model. Future releases of the toolbox would include the definition of the 1-D non-linear spring elements to simulate the action of ligaments [165, 80], which are placed in the corresponding anatomical location. The facet cartilage will be included, defined as a 1D element in between the anatomical location. In future development, facet joints and the definition of the facet contact properties, and the attachment points for the ligaments will be automatically implemented. The toolbox has been released on Zenodo [255] and the development version is freely available on GitHub.

4.8 Conclusion

The LMG toolbox has been developed with the intent of helping in the design optimization of spinal devices such as posterior stabilization devices as well as the development of custom devices. The developed toolbox enables an automated workflow which is user independent and fully compatible with open-source software (Octave, FEBio, Calculix). It constitutes a tool that can be used in clinical studies to improve the decision making process to select the best intervention. The clinicians, supported by engineers, using the GUI would be able to simulate and understand the effect on the biomechanics of the specific patient taking in to account the anatomical variation. In fact, it will enable the use of average dimensions or importing the dimensions measured from data-scans or evaluating a hybrid model where the dimensions of a desired structure can be altered, then evaluating the specific case to treat. This toolbox was released on an on-line platform with a user-friendly GUI, and chapter 5 describes the development and evaluation of a FE model. It can then be used to aid clinicians practice when assessing the biomechanics of the spine of their patients, and it could lead to improve the decision making process to select the best intervention.

Chapter 5

Automatic pre-processing of the lumbar model

5.1   Introduction

The Lumbar Model Generator (LMG) toolbox allows the generation of an accurate and parametric model of the lumbar spine. The geometry is generated according to subject-specific dimensions or dimensions based on correlation analysis (chapter 4, chapter 3) and the mesh is then generated for the vertebrae and the intervertertebral discs (IVD). The innovation of the LMG is the automation of the entire workflow, from the geometry generation to the meshed model and ready for pre-processing and FE analysis through a direct link to FEBio (FEBio Software Suite). The whole process is performed in Matlab (MATLAB, R2017a, 9.2.0.538062, The MathWorks Inc., Natick, MA, USA), where a Graphical User Interface (GUI) guides the user to assign the requested parameters.

Several FE models of the lumbar spine have been developed in the literature [165, 256, 257, 131], which are based on the reconstruction of the geometry from data-scans. The pre-processing of each model is done individually on those models, material properties are assigned, the mesh size is defined after a mesh convergence analysis, surfaces are manually identified and then loading and boundary conditions assigned to the model. However, pre-processing of the model is time consuming (it could require weeks between the segmentation and model setup) and a major obstacle in the translation of FE models to clinical practice. Automation of the pre-processing stage, would allow a real-time evaluation of spine biomechanics and the effect of different implants on a specific anatomy, could help clinicians in deciding the best treatment. At the same time, this process can be used in the evaluation and optimization of a new device on a population of anatomical models and eventually implementing custom features. In order to facilitate the use of lumbar spine models to investigate eventual treatments or, potentially, im-

plant design, and to evaluate the biomechanics of the spine, an automated pre-processing of the FE models has been implemented with the LMG toolbox.

In the previous chapter (chapter 4) the solid body and mesh generation was described, focusing on the entire workflow of the toolbox. In this chapter, instead, the automatic pre-processing of the Finite Element Model is presented. Once the geometry has been generated, the number of bodies required in the simulation can be selected, using one or more level lumbar spine units (two vertebrae and an IVD, referred as Functional Unit, FU) or the entire lumbar spine. The LMG toolbox generates scalable vertebrae and IVD bodies, and according to the anatomical dimensions considered, a mesh convergence analysis has to be performed, which is a time-consuming task. An innovative feature of this toolbox is the automated sensitivity analysis on the mesh size that is directly performed with the size chosen according to user's criteria (for the vertebrae and IVD). Subsequently, the material properties are assigned to the bodies involved in the model, and the geometrical features which define the boundary and loading conditions are identified. Once the loading features and the simulation control parameters have been defined and imported, the input file is directly written and exported to FEBio to run the simulations.

The aim of this study was to develop the automatic pre-processing for the lumbar spine, from the definition of the mesh size according to the convergence test, the material properties assignment and estabilishing the boundary and loading conditions. As proof-of-concept, a model of the entire lumbar spine was generated, demonstrating the functionalities of the toolbox. Then, a preliminary analysis of an L1-L2 FU was performed and the results compared with the state of the art as available in literature. Figure 5.1 provides an overview of the steps described in this chapter.

5.2 Automatic FE pre-processing

The LMG toolbox allows the pre-processing of vertebrae and IVD bodies to obtain a model ready to be run in FE software. Once the geometrical model has been generated, it is possible to define:

- the number of bodies to use for the FE simulation;

- the desired mesh size accordingly with a mesh convergence test (subsection 5.2.1);

- the material properties (subsection 5.2.2);

- the contact surfaces and properties (subsection 5.2.3);

- the boundary conditions, such as load to be applied (subsection 5.2.4).
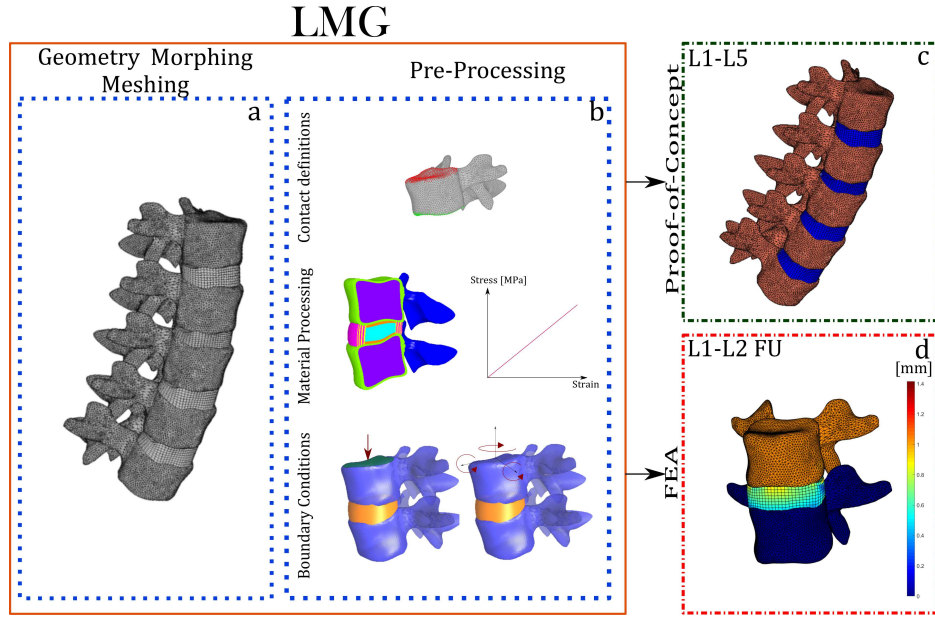
Figure 5.1: Starting from the model generation (a), described in chapter 4, in this chapter the automatic pre-processing is explained (b). An entire lumbar spine segment has been generated and pre-processed (c), while a Finite Element Model of the L1-L2 FU has been analysed(d).

These features are directly implemented in Matlab, and selected through a user-friendly GUI (Figure 5.2), where step by step the information required are added as inputs (Figure 5.1b). In this section, the inputs required to define the model and the default values are described.

5.2.1   Mesh definition and convergence test

The LMG toolbox is able to automatically mesh the vertebrae and IVD as shown in the previous chapter (chapter 4). A novel feature introduced in this toolbox is the possibility to automatically run a mesh sensitivity analysis of the model generated with the dimensions imported. The input required are related to the size of the mesh elements. In the case of the vertebrae, meshed with tetrahedral elements, the range of dimensions for the tetrahedral elements is required. In the case of the IVD, as described in chapter 4, dimensions of the hexahedral elements are described by three parameters: the number of layers of the AF nl, the number of points on the perimeter np, and the number of elements nz characterizing the height of the IVD. These parameters are linked to the IVD height and volumetric ratio and are displayed in Figure 5.3.

  Along with the element dimensions, the material properties, boundary and loading conditions are required to evaluate the mesh convergence analysis.
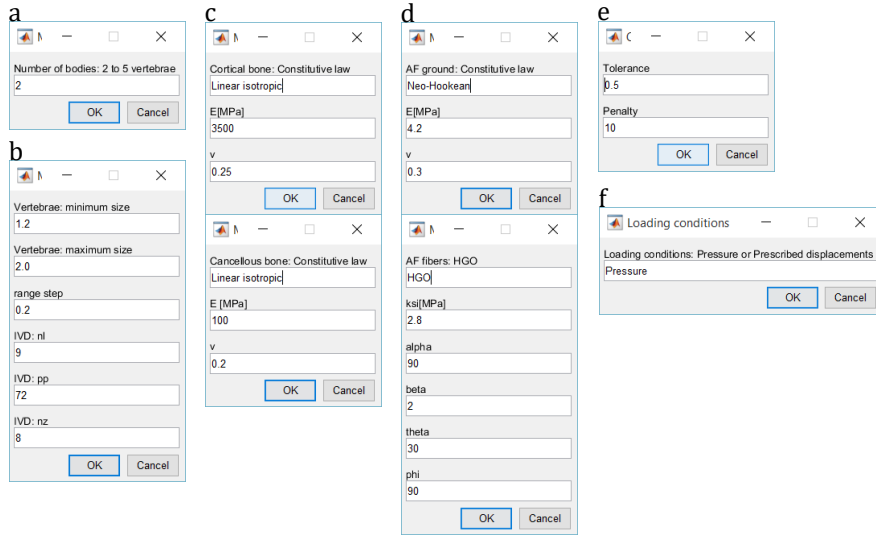
Figure 5.2: Sample of the graphic-user interface used to collect the required inputs: a. number of vertebrae involved in the model; b. mesh size for the vertebrae and IVD; c,d. Material properties to assign for individual components; e. Contacts conditions; f. type of loading condition.

Subsequently, an FEBio input file was written in Matlab through the Gibbon toolbox [241], to perform the simulations. There are no standardised methods for mesh convergence analysis, therefore, the default metrics implemented in the toolbox are based on a local evaluation of the maximum stress on a group of elements in the upper part of the body (vertebrae or IVD). Alternatively, the user can adopt the desired metrics, adding custom scripts or evaluating the results through the FEBio post-processing interface (PostView, FEBio Software suite). The described procedure is represented in Figure 5.4 taking the vertebrae as an example. The mesh quality of the bodies generated can be graphically evaluated in Pre-View (FEBio, Software suite), the standard pre-processing software associated with the FEBio package. This software includes the tools to evaluate the tetrahedral quality and the dihedral angle distributions for tetrahedral elements, and Jacobian value distribution for hexahedral elements (Figure 5.5) have already been implemented. Alternatively, during the mesh generation process, the user can request (chapter 4) the dihedral angle and aspect ratio distributions for the vertebral bodies. These parameters are retrieved from Tetgen and evaluated in Matlab through a dedicated script.

5.2.2 Material properties

The material properties of the bodies involved can be assigned to the model according to the regional material properties identified in previous studies
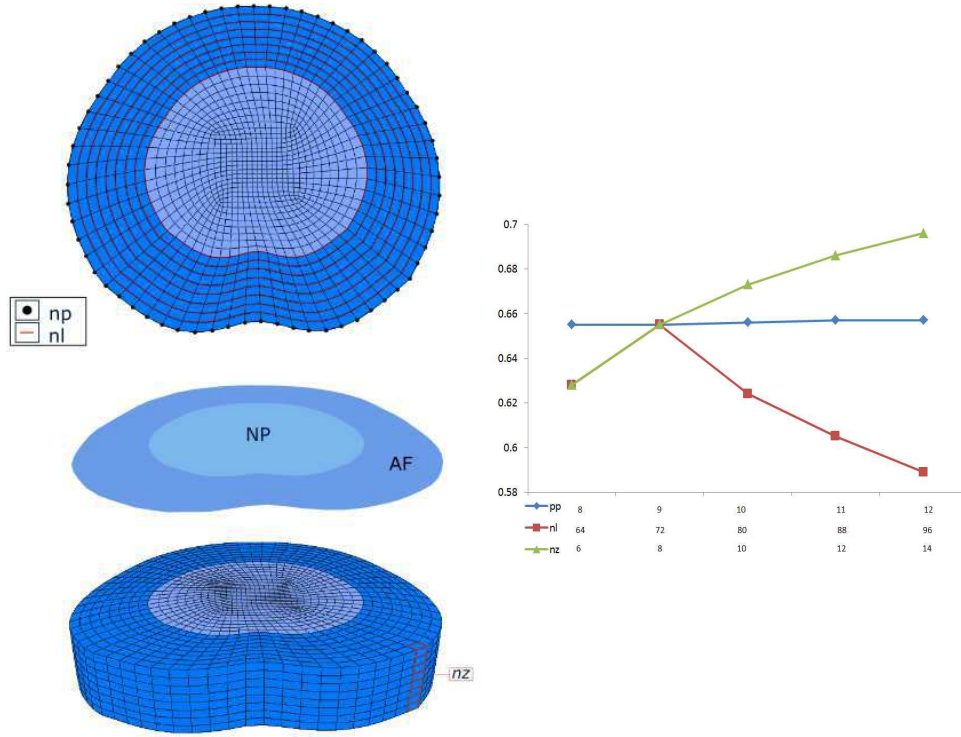
Figure 5.3: Parameters to define the IVD mesh convergence, where np is the number of points on the AF perimeter, nl is the number of layers on the AF and nz the number of elements on the height of the IVD.

[14, 95, 258, 259]. In the following sections the inputs required in the LMG toolbox, for the IVD and vertebrae, are described.

Vertebrae

The spine can be modelled as having vertebrae consisting of an inner cancellous core and a thin layer of cortical bone (see Figure 5.6) [95, 79, 14, 260, 261]. In the LMG model, the mechanical behaviour of the vertebrae is mimicked by assigning different material properties to the vertebrae in each area. To assign material properties to the corresponding elements, during the meshing procedure (chapter 4, subsection 4.5.1), the element indexes were identified according to their locations. In literature, linear isotropic and orthotropic material properties have been applied to the vertebrae [90, 262, 261], and the user can decide the preferred formulation in agreement with the FEBio User manual [263]. In the LMG, linear isotropic material properties are defined, and the user can add the coefficients as stated in Table 5.1, where E and ν are the Young's modulus and the Poisson's ratio respectively.
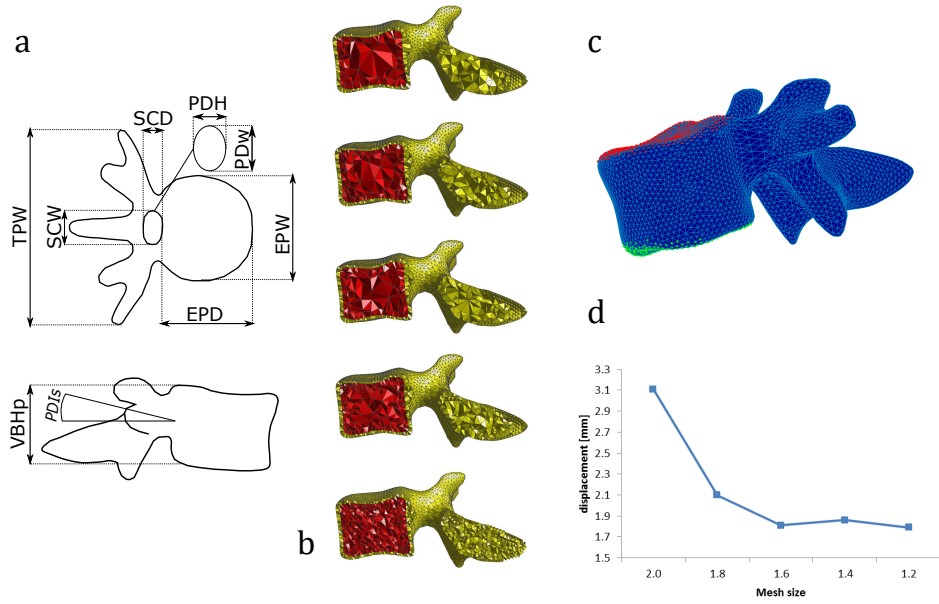
Figure 5.4: Workflow for the mesh convergence analysis. a. Definition of the anatomical dimensions; b. L1 vertebrae meshed with different mesh density; c. Definition of boundary and loading conditions, in red the upper vertices and in green the lower vertices; d. Mesh convergence results.

Table 5.1: Default material properties assigned to the vertebrae.

Material	Constitutive law	Coefficients
Cancellous bone	linear isotropic	E,ν
Cortical bone	linear isotropic	E,ν
Posterior elements	linear isotropic	E,ν

Intervertebral disc

In the IVD, two main volumes can be identified: the annulus fibrosus (AF), and the nucleus pulposus (NP). The structure of the AF can be described as a composite material, where concentric layers of collagen fibres are embedded in a ground substance (chapter 2, chapter 4). The IVD has been previously modelled as both time-independent or time-dependent in terms of its mechanical behaviour [137]. Several methods have been followed to assign the mechanical properties to the AF [14, 252, 168]: concentric layers have been identified and the ground substance material properties have been assigned either homogeneous over the entire AF or assigned by dividing the AF in to anterior, posterior and lateral regions. The IVD models generated

Tetrahedral quality

Minimum dihedral angle

Maximum dihedral angle
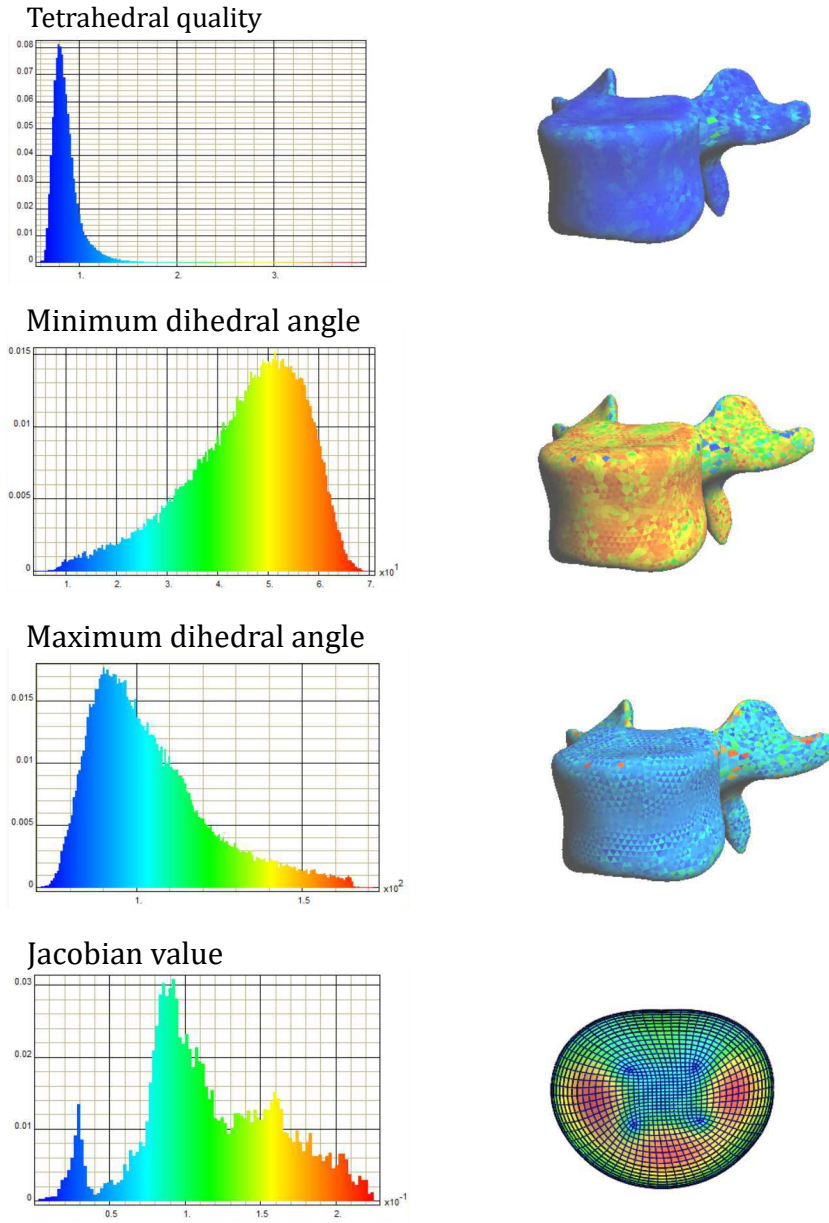
Jacobian value

Figure 5.5: Mesh quality evaluation in Pre-View. The criteria evaluated for tetrahedral (tetrahedral qulity, maximum and minumum dihedral angle) and hexahedral (Jacobian value) elements are shown.

from the LMG, have the hexahedral elements arranged in concentric layers (see Figure 5.7), as described in Table 5.2.2.

The element indexes are first of all differentiated for the elements belonging to the NP and the AF. Subsequently, two approaches to assign the material elements to the AF can be followed, so the user can decide to emulate meth-
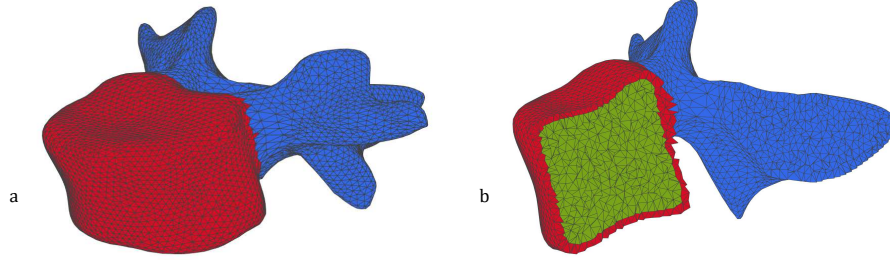
Figure 5.6: The colours identify the regions where different material properties are assigned, including: a cancellous core (green), the cortical layer (red) and the posterior elements (blue).
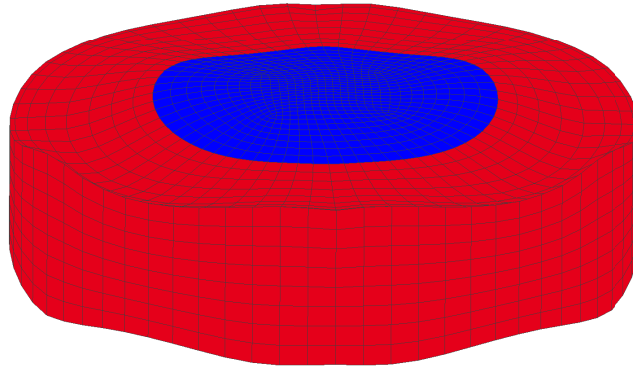
Figure 5.7: IVD geometry and mesh. The hexahedral elements are arranged in concentric layers.

ods described in the literature: i. different element indexes are assigned to each layer; ii. different element indexes assigned to each region of the AF (anterior, posterior, anterior-lateral, posterior-lateral). Local axis of coordinates for the elements of the AF have been defined (Figure 5.8), so fibers orientations can be assigned as shown in Figure 5.9.

To allow users to follow the preferred approach modelling the IVD, as well as allowing sensitivity analyses on varying the material properties formulations, the following combinations can be implemented in the LMG:

- same material properties for the ground substance and fibres for every layer (Figure 5.10 a);
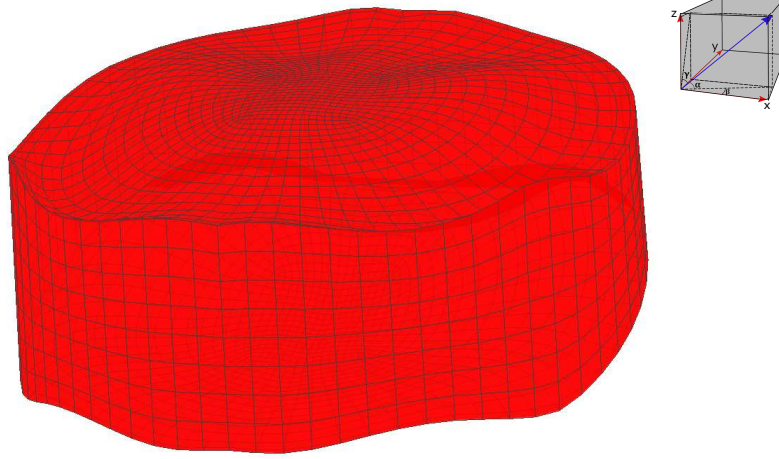
Figure 5.8: IVD geometry and mesh. The coordinate system of each of the elements is evaluated to define the fibre orientation.
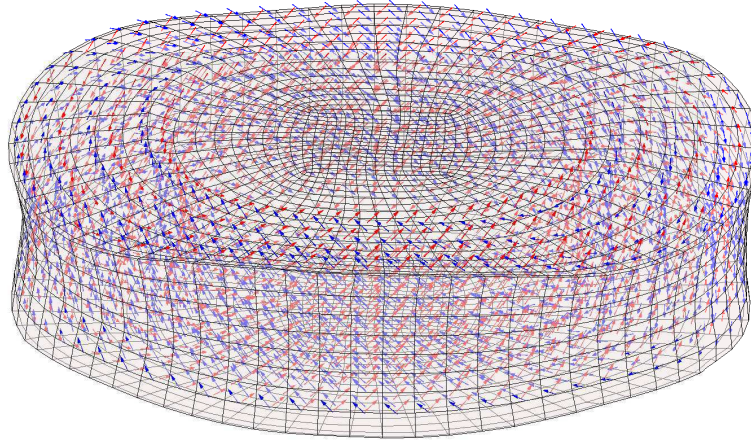
Figure 5.9: Disc with the fibers embedded in the AF layers

- same material properties for the ground substance and different fibres orientations at each layer;

- same material properties for the ground substance and different orientation and material properties for the fibres at each layer (Figure 5.10 b);

- different material properties according to the area of the IVD: anterior, posterior, anterior-lateral, and posterior-lateral, as shown in

Figure 5.10c .

The default material constitutive laws have been implemented in the LMG, and the fibre material properties have been assigned using the anisotropic formulation implemented by Holazpfel-Odgen-Gassen [127]; the default coefficients are described in Table 5.2.
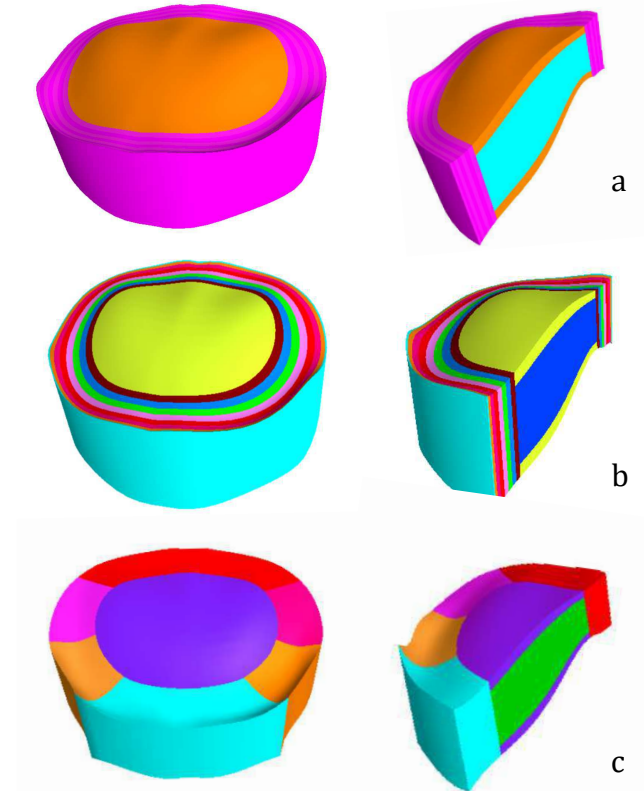
Figure 5.10: Possible combination of material properties to use in the AF: a. same material properties for all the layers; b. different material property for each layer; c. different material properties according to the region (anterior, posterior, anterior-lateral, posterior-lateral). Independently from these formulations, the fibre orientations can be defined, and a double layer of fibres is implemented for each lamella. In correspondence of the NP two layers of elements are identified, showed with different colours in each figure, and selected as cartilaginous material.

Cartilaginous endplates

The cartilaginous endplates (CEP) are cartilaginous cushions in-between the vertebrae bodies and the IVD (chapter 2), usually modelled with a thickness of 0.7 mm [264]. In the LMG toolbox, different material indices are assigned

to the upper and lower elements of the IVD which correspond to the NP [168] as shown in Figure 5.11. By default, the cartilaginous endplates have been modelled as linear isotropic materials and the coefficients required in the toolbox are listed in Table 5.2. However, the user can assign other constitutive laws, assigning for example biphasic material properties following the FEBio user's manual.
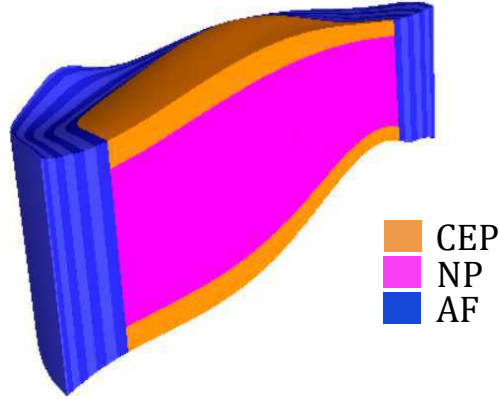
Figure 5.11: The CEP are selected as one layer of elements in corresponding to the upper and lower surfaces of the NP.

Table 5.2: Formulation of material properties for the AF and NP, available in the LMG toolbox for the FEBio pre-processing and described elsewhere Appendix A. The coefficients stated in the last column are related to the formulations described in the Maas et al. [263] for each material law formulation.

Material	Consitutive law	coefficients
AF Ground		
	Neo-Hookean	E, ν
	Mooney-Rivlin	c_1, c_1, k
AF fibers		
	Holazpfel-Odgen	$\xi, \alpha, \beta, \theta, \varphi$
NP		
	Isotropic elastic	E,ν
	Mooney-Rivlin	c_1, c_1, k
CEP		
	Isotropic elastic	E,ν

Ligaments

In the LMG, four set of ligaments (anterior ALL, posterior PLL, inter-spinous ISL, inter-transverse ITL ligaments) are defined. The attachment points are selected by a custom algorithm, freely accessible with the LMG toolbox, which evaluates the anatomical attachment points on each vertebrae. The points selected are displayed in Figure 5.12 and coupled with those of the adjacent vertebrae to simulate the ligament connections. The liga-
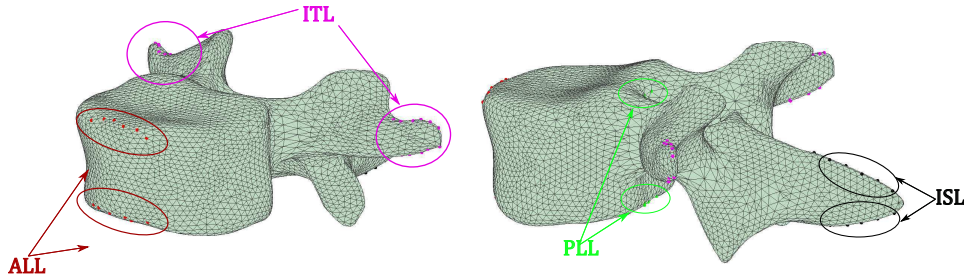
Figure 5.12: Attachment points for the ALL, PLL, ITL, ISL ligaments.

ments are defined as 1D springs, and their mechanical properties (described in chapter 2, subsection 2.1.2) can be described with a force-elongation curve which has an initial non-linear behaviour and then a high stiffness material response (chapter 2, Figure 5.13). The tension only behaviour of the ligaments can be simulated assigning the material as linear, thus, simulating only the stretching phase of the fibrils, or implementing non-linear material properties in which the stiffness is a function of the stretch level.

5.2.3   Identification of geometrical features

Once the number of bodies involved in the FE simulation are chosen, and the morphological and material features are defined, the final step to prepare the FE input file is the definition of the boundary and loading conditions. This step requires the identification of the surfaces involved in the contacts and boundary definitions and the related nodes. The upper and lower surfaces of the vertebrae and IVD are automatically selected by the algorithm, identifying the faces in correspondence of the upper and lower surfaces of the bodies. The external faces are identified using the indices of the boundary faces (section 2.5), then evaluating the normal versors at each face. In the case of the IVD, the faces on the external surfaces (superior, inferior, lateral) are almost aligned in each region. The normal versors have similar orientations, which are identified according to the versors components in the 3D space. Then the faces are selected evaluating a range of values, for each surface, for the versors' components. In the case of the vertebrae, the geometry is more complex. The surfaces are characterized by several variation of inclinations and the identification of the upper and lower surfaces,
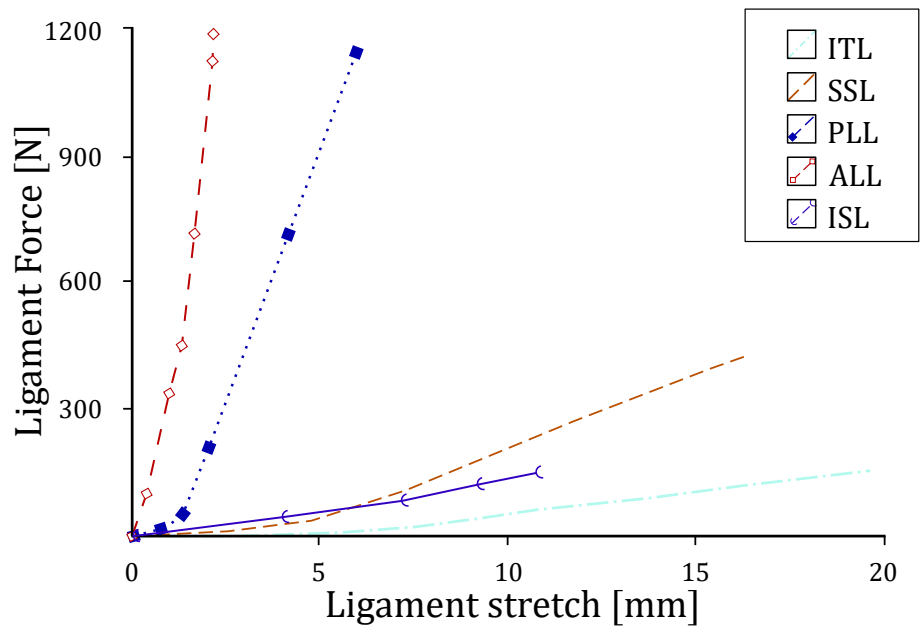
Figure 5.13: Force-elongation curves for Anterior Longitudinal Ligaments (ALL), Posterior Longitudinal Ligaments (PLL), Inter-Spinous Ligaments (ISL), Inter-Transverse Ligaments (ITL) and Super-Spinous Ligaments (SSL).
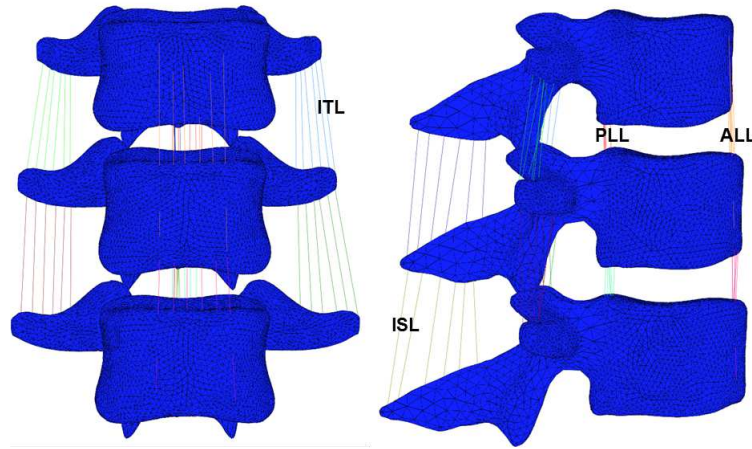
Figure 5.14: Model of the double level FU (L1-L3) where the IVD have been hidden and the vertebrae are vertically aligned.   The ALL, PLL, ITL, ISL ligaments have been included.

based on the normals at each face, lead to the identification of surfaces not belonging to the upper and lower endplates (Figure 5.15). For example, the selection of the upper surface of the first vertebrae to assign the loading condition, would also select elements belonging to the transverse process and lamina. Hence, it would lead to simulate different loading conditions than the requested ones (Figure 5.16). The information of the fitting parameters, described in chapter 4, have been used to identify the nodes and faces of the requested surfaces. The nodes obtained from the fitting equations of the surfaces, have been used to find the correspondent nodes on the meshed model and the connected faces. Using this method, the detection of the geometrical features leads to an accurate definition of the surfaces of interest as shown in Figure 5.16. In the toolbox, the information linked to the surfaces of interest are saved and subsequently used as follows:

- the nodes associated to the described surfaces are used in case of applying prescribed displacements to the model;

- the surfaces are used to define the boundary conditions and to assign the contact properties (Figure 5.17).

5.2.4   Boundary and loading conditions

The boundary conditions are meant to identify similar conditions of the body or to follow an experimental setup. The boundary conditions are defined selecting the surfaces or nodes to fix and those in which a degree of motion has to be applied (prescribed displacements, nodal forces or pressure forces). The loading conditions, applied to the upper surface of the first body, can
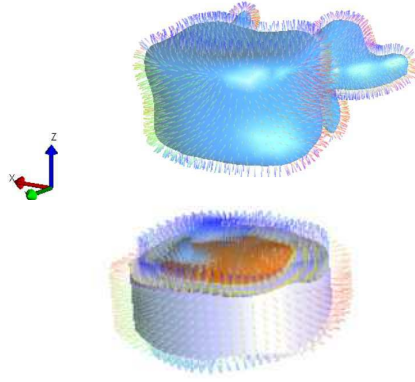
Figure 5.15: Normals on the external surfaces of the vertebrae and IVD.
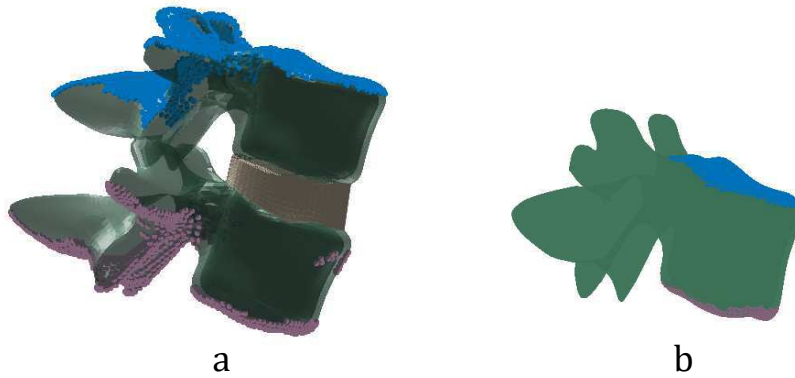
Figure 5.16: Surface recognition based on the normal orientations at each face (a), the blue and black dots are identified selecting the nodes attached to the selected faces. Faces not included in the upper and lower endplates are selected. Evaluating the fitting surface equations (b) only the upper and lower endplate surfaces are identified.
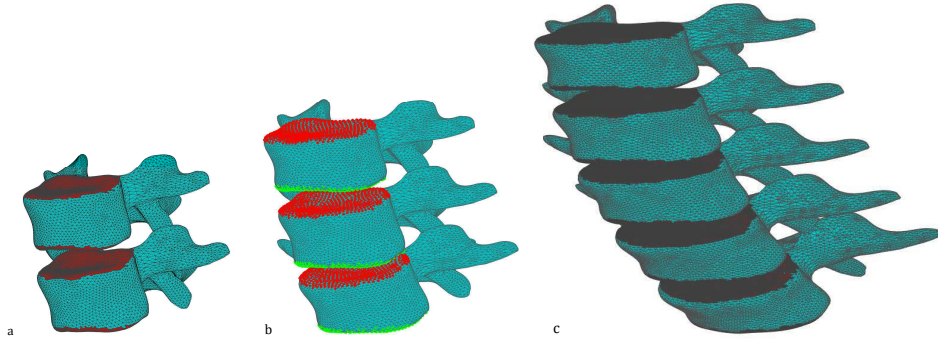
Figure 5.17: Surfaces identification on the L1-L2 model (a) and on L1-L5 FU (c), and nodes identification on the L1-L2-L3 FU (b). The upper and lower surfaces are showed in red. The boundary conditions are applied on the upper and lower surfaces of the first and last bodies involved in the FE model (ie: applying a load on the L1 upper surface and fixing the bottom surface of the L2).

be chosen between: i. prescribed displacement; ii. prescribed rotation; iii. pressure. In FEBio, it is not possible to apply pure moments on deformable bodies, but a rigid body can be connected by means of rigid constraints (with high stiffness) and then the moments are applied to the rigid body (as shown in Figure 5.18). In this first version of the *LMG*, the vertebrae are defined as deformable bodies and the application of a pure moment has not been implemented.

5.2.5 Contact properties

The boundary surfaces, previously identified in subsection 5.2.4, are used to define the contacts. The surfaces are classified as slave or master surfaces: master properties were assigned to the less deformable bodies and slave to the opposing surface. Thus, slave surfaces have been assigned to the IVD and master surfaces to the contacting vertebrae ([263, 265]). In this first release of the LMG, only the endplates of the vertebrae and IVD are selected, and the contacts for the facets are not included.

The vertebrae and the IVD were meshed with non-conforming meshes, for which only tied contacts can be used in FEBio. In FEBio, two parameters have to be defined for tied contacts: penalty and tolerance coefficients. The contact parameters reported in Table 5.3 are the adopted default values, which were evaluated through a sensitivity analysis. These values have to lie in a specific range to obtain a repulsion force which would allow contact to occur and avoid the penetration between the bodies. However, a range
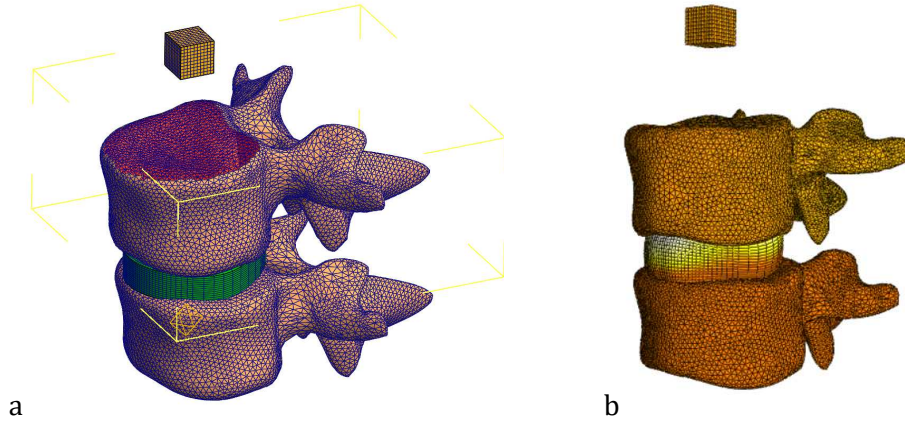
Figure 5.18: Definition of a rigid box in Preview. a. The selection of the surface to connect to the rigid body in Preview. b. Preliminary test on the L1-L2 FU, applying a prescribed displacement.

of combinations of tolerance and penalty factor could potentially lead to a valid physical solution.

Table 5.3: Contact formulation available for the LMG toolbox and parameters requested as input.

Contact formulation	Parameters	Default values
Tied interface	Penalty factor	10
	Tolerance	0.5

5.2.6   Control properties and output variables

The control parameters required by FEBio can be selected in the GUI and are reported in Table 5.4, and described elsewhere [263]. The output files requested in the LMG are listed in Table 5.4, and further outputs can be requested from the user. The solution of the FE model is achieved with an incremental-iterative approach, based on a quasi-Newton method (Broyden-Fletcher-Goldfarb-Shanno (BFGS) method [266]), as described in detail in the FEBio Theory manual [263] and introduced in chapter 2.

5.2.7   Post-processing

The LMG toolbox requests, as default, the evaluation of the displacements, deformation gradient tensor and stress components on the whole model. The evaluation of the outputs is distinct for each study, it depends on the features which the users wants to evaluate (i.e. displacements on the IVD, intradiscal

Table 5.4: Control parameters and output requested for the FEBio simulations from the LMG.

Control parameters	Numbers
Analysis type	Static, Steady-static, Dynamic
Step	Total number of steps
Auto-step	Enable the step-time adjustment
Time	Total time
Output variables	Cauchy stress matrix Nodal displacements Deformation gradient

pressure IDP in the inner elements of the NP or the average IDP through the whole NP). The displacements on the model are an automatic output from the LMG. Therefore, post-processing is left to the user given their specific needs, with the user able to either implement a custom script or evaluate the results using Post-View, the post-processing software to visualise the results obtained from FEBio.

Table 5.5: Default parameters

Mesh	Hexaedral	nl, pp, nz
	Tetrahedral	Mesh size range
Material properties	Cortical bone	Linear isotropic
	Cancellous bone	Linear isotropic
	Posterior bone	Linear isotropic
	CEP	Linear isotropic
	AF	HGO
	NP	Linear isotropic
Contact	Tolerance	0.5
	Penalty	10
Boundary condition	L5	fixed bottom surface
Loading condition	L1	Pressure on upper surface
Output	Node dataset	Displacements
	Element dataset	Cauchy stress matrix

5.3   L1-L5 model: proof of concept

An L1-L5 geometrical model has been developed to test the full model generation and the functionalities of the LMG toolbox (Figure 5.19). It has been developed using the correlation analysis method (described in chapter 4) for a 30 year old male, 180 cm in height and with a lumbar curvature

of 43.3°. These inputs have been arbitrarily selected to demonstrate that the model work and the arbitrary does not represent a limiting factor in demostrating proof-of-concept. The initial pre-processing was set up adopting
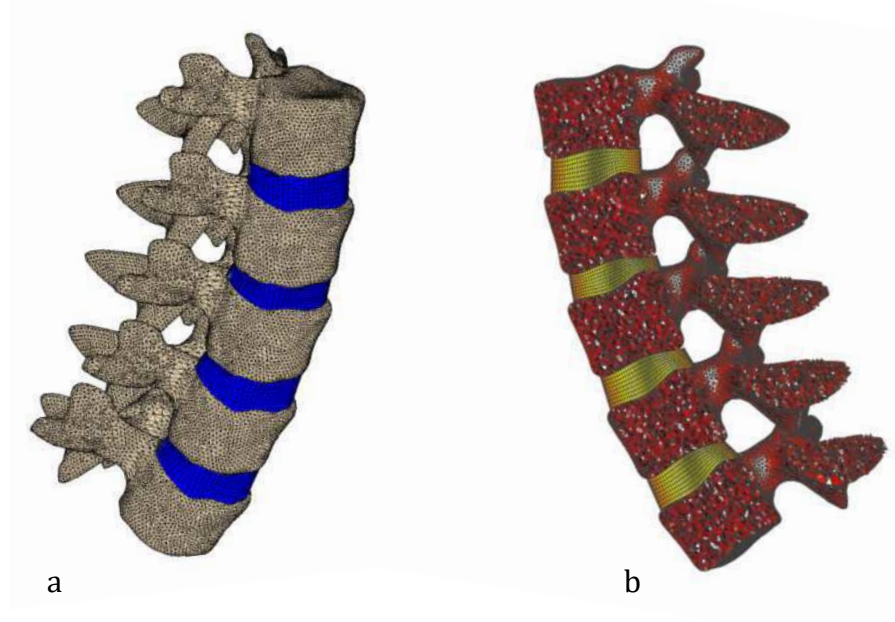
Figure 5.19: a. Model of the entire lumbar spine. b. Section view of the model

the default parameters provided in Table 5.5. The model was meshed with hexahedral elements for the IVD and tetrahedral elements for the vertebrae, and quality checked in Pre-view as described in chapter 4 and the results are shown in Figure 5.20. The boundary and contact surfaces are displayed in Figure 5.21, while the final steps (assigning loading conditions and control properties) of the pre-processing and the analysis of the model are left for future studies. In the next section, the full functionalities of the toolbox are shown for a single-level functional unit (L1-L2).

5.4   L1-L2 functional unit FE analysis

A FE model of a functional unit of the lumbar spine has been developed and solved. The geometry was based on the same dimensions used to develop the L1-L5 model (Section 5.3), with the VP used for the healthy disc case (46%,54% [238, 140]), and only the first FU (L1-L2) has been used to build the FE model (Figure 5.22), in which the ligaments have not been implemented. In this study a single FU was in depth analysed and compare the results with the data in the literature.
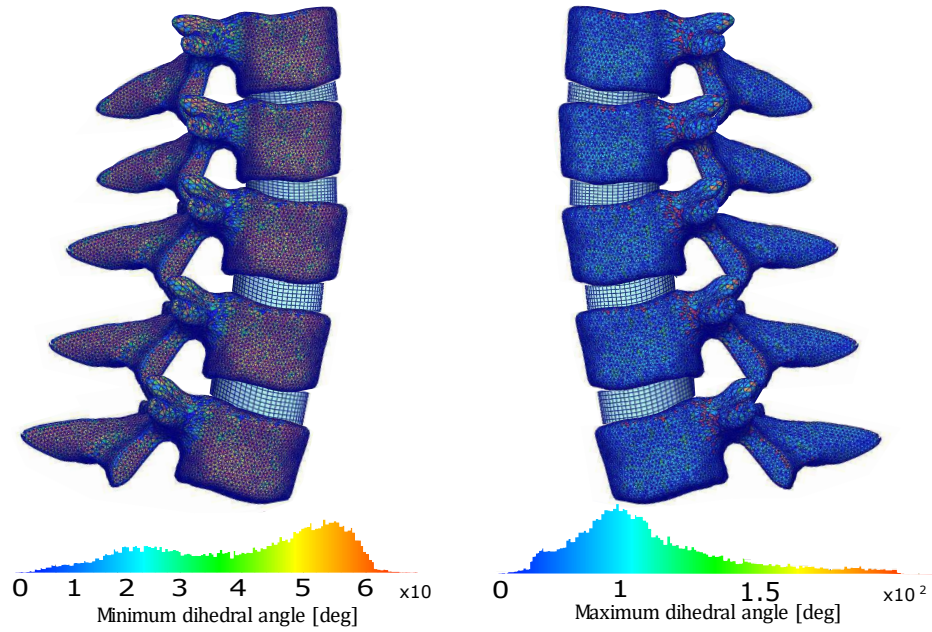
Figure 5.20: Mesh quality evaluated in Preview
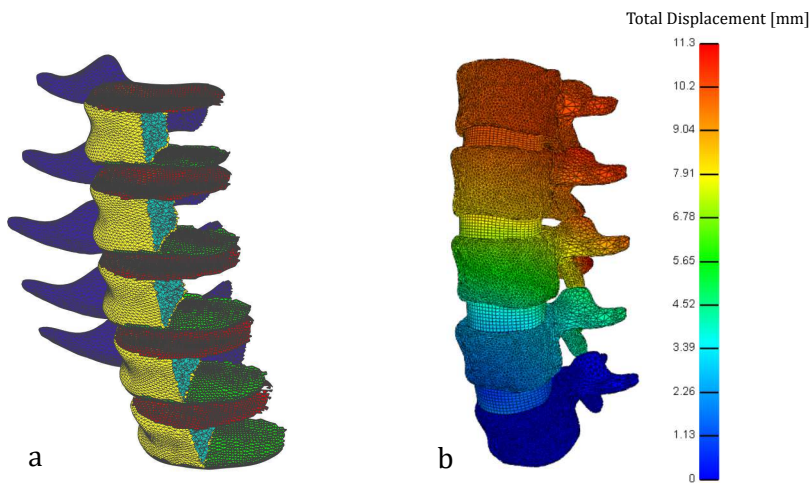
Figure 5.21: The lumbar spine model, including the vertebrae L1 to L5. a. The inferior and superior surfaces of the vertebrae are highlighted (red superior, green inferior). b. a solution of the entire lumbar spine is provided, showing the total displacements. The solution is shown as proof-of-concept and the detail of this model are not described because further analysis are required.
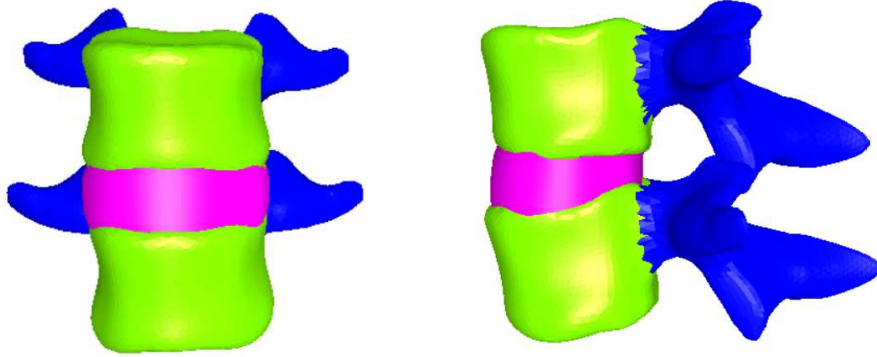
Figure 5.22: Model of the L1-L2 functional unit.

Tetrahedral and hexahedral mesh elements were used, respectively, for the vertebrae and IVD. The mesh sizes were chosen accordingly to the mesh convergence subroutine, as described in subsection 5.2.1. The mesh sizes for the vertebrae and the IVD were the results of a compromise between the computational time required and the precision of the results obtained. The sensitivity analysis on the mesh size was undertaken by applying fully constrained boundary conditions to the inferior surfaces of the IVD and vertebrae. A distributed load, corresponding to applying a pressure of 1 MPa, was applied on the upper surface. The results, shown in Figure 5.23, were considered accurate if the maximum axial stress did not differ by more than 5% from the model with the finer mesh. Tetrahedral elements of 1.6 mm and hexahedral elements characterized by $nl = 9$, $pp = 72$, and $nz = 8$ were used, obtaining a model with a total of 190,222 elements.

 The material properties were assigned to the bodies (Figure 5.24) in agreement with the studies in the literature, and the values are listed in Table 5.6 and Table 5.7. The IVD has been modelled considering its non-linear and anisotropic features: the Holazpfel-Gassen-Odgen [127] formulation was implemented, where the hyperelastic material property of the ground substance was combined with non-linear properties and 3D orientations were assigned to a double layer of fibers. In this study, the ground substance was modelled with Neo-Hookean material properties, eight layers of fibers are embedded. In each layer, the fibres are arranged in a criss-cross pattern, with an inclination of $\pm 30°$ respect to the horizontal axis [267]. The NP was modelled as a isotropic linear elastic material [268] and the material properties are reported in Table 5.7.

The boundary surfaces have been selected (Figure 5.25) from the algorithm and tied contacts have been defined between the vertebrae and IVD surfaces. Default values were used as described in Subsection 5.2.5 in Ta-
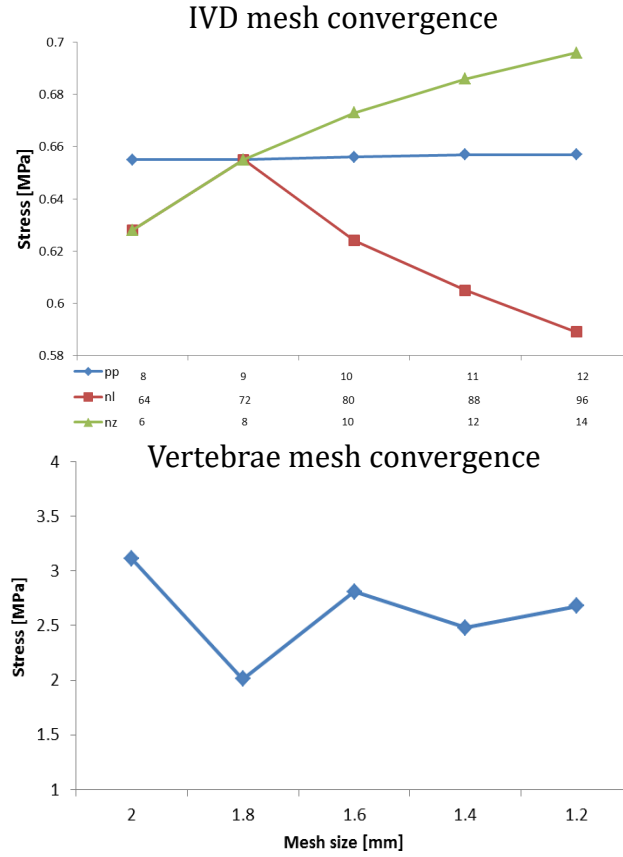
Figure 5.23: Mesh convergence result for the IVD and vertebrae. The parameters nl, pp and nz have been changed one at time.

ble 5.3. The inferior surface of the L2 vertebrae has been fully constrained (Figure 5.25) and consistent with the literature. A distributed load, which increased linearly to 1000 N [95], was applied on the faces of the upper end-plate of the L1. Finally, an FE static analysis was solved in FEBio. The axial displacement on the anterior-posterior cross-section (Figure 5.26) were evaluated. Moreover, the IDP was estimated in different areas of the IVD, as shown in Figure 6.7.

Table 5.6: Material properties for the vertebrae.

Bone material properties	Constitutive law	E[MPa]	ν	ref
Cancellous bone	linear isotropic	100	0.2	[90]
Cortical bone	linear isotropic	12000	0.3	[90]
Posterior elements	linear isotropic	3500	0.25	[269]

Table 5.7: Material properties for the IVD.

IVD material properties	Constitutive law	coefficients					ref
Anulus Fibrosus							
AF ground	Neo-Hookean	E	ν				
		4.2 MPa	0.3				[150]
AF fibres	HOG	ksi	α	β	θ	ϕ	
		2.8 MPa	90	2	±30	90	[259]
Nucleus Pulposus	Linear isotropic	E	ν				
		2 MPa	0.4				[89]
Cartilagineus Endplates	Linear isotropic	E	ν				
		23.8 MPa	0.4				[79]

5.5   Results: functional unit

The axial deformations on the anterior-posterior cross-section (Figure 5.26) of the IVD were evaluated in Matlab. The mean values have been evaluated identifying adjacent volumes of elements along the defined cross-section. These results were considered an estimation of the deformations over the volume of the cross-section, subsequently compared with experimental results. The axial deformations have been plotted in Figure 5.27, where the horizontal axis represents the y position (as in Figure 5.26a) on the cross-section (posterior to anterior). The results, reported at 500 N, 750 N and 1000 N showed a mean deformations, in correspondence of the centre of the NP, respectively of 1.28 mm, 1.57 mm and 1.75 mm.

The intervertebral disc pressure (IDP) was evaluated in Equation 5.1 as reported in Schmidt et al. [256]:

$$P = -\frac{tr\sigma}{3} \tag{5.1}$$
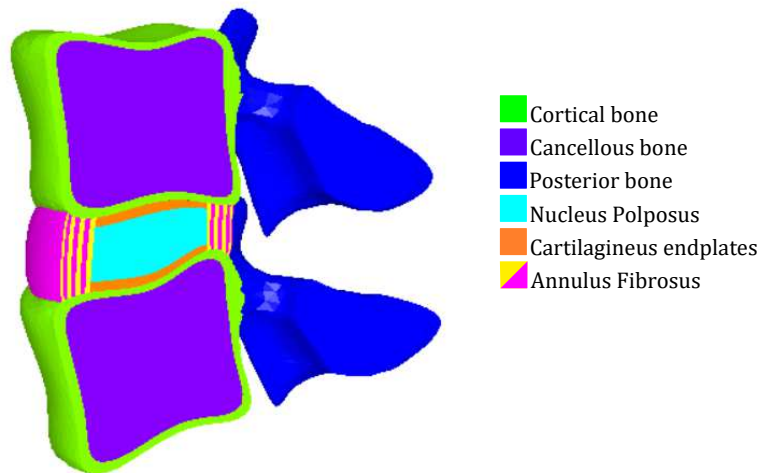
Figure 5.24: Model of the L1-L2 functional unit.
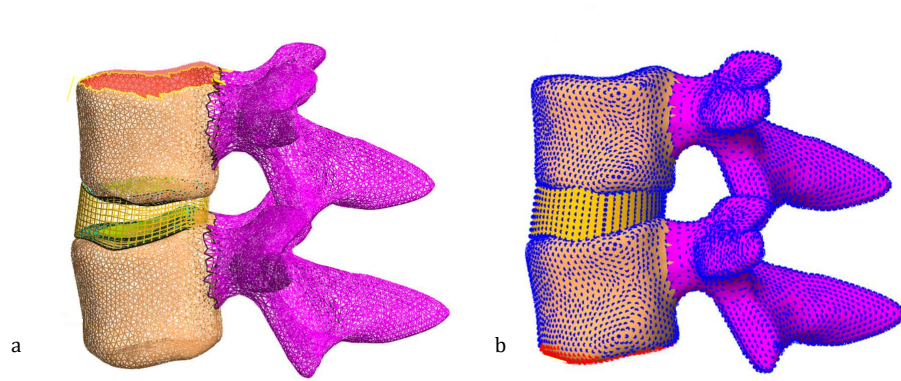
Figure 5.25: *L1-L2 functional unit where the superior faces of the L1 are selected (red) to apply the distributed load (a) and the inferior points of the L2 are identified to be constrained (b).*
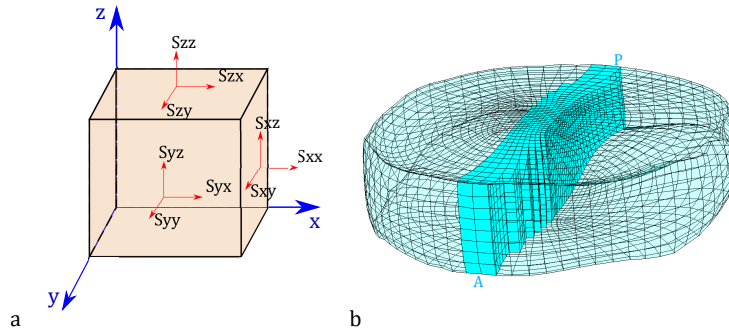
Figure 5.26: *(a) Reference system and stress directions identified; (b) Anterior-posterior cross-section.*

where *tr* is the trace of the Cauchy stress matrix (σ). The IDP was evaluated in volumes, identified around the mean height of the IVD, in the centre, anterior, posterior and lateral regions of the NP (Figure 6.7) and the anterior and posterior areas of the AF. All the results for the NP were reported for the posterior volume, where the standard deviation was always less than 0.1 but not reported in the graphs presented (e.g. Figure 5.29). In this region, the IDP was found to be 0.38 MPa, 0.60 MPa and 0.78 MPa respectively at 500 N, 750 N and 1000 N. In the AF, higher values were found on the posterior region (0.45 MPa, 0.70 MPa and 0.90 MPa) than in the anterior side (0.38 MPa, 0.62 MPa and 0.82 MPa), while in the whole AF average values between the anterior and posterior regions were found. In the AF, due to a bulging effect, the different material properties and fibers orientations at each layer, the stress and pressure values predicted include higher standard deviations. The mean values reflect an averaged mechanical behaviour, only
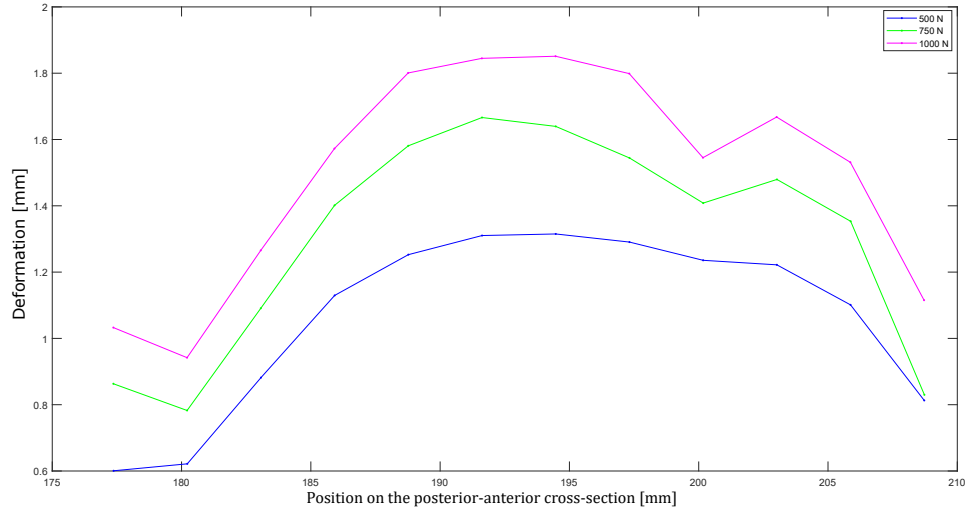
Figure 5.27: Axial deformations evaluated on the anterior-posterior cross-section at 500 N, 750 N and 1000 N.
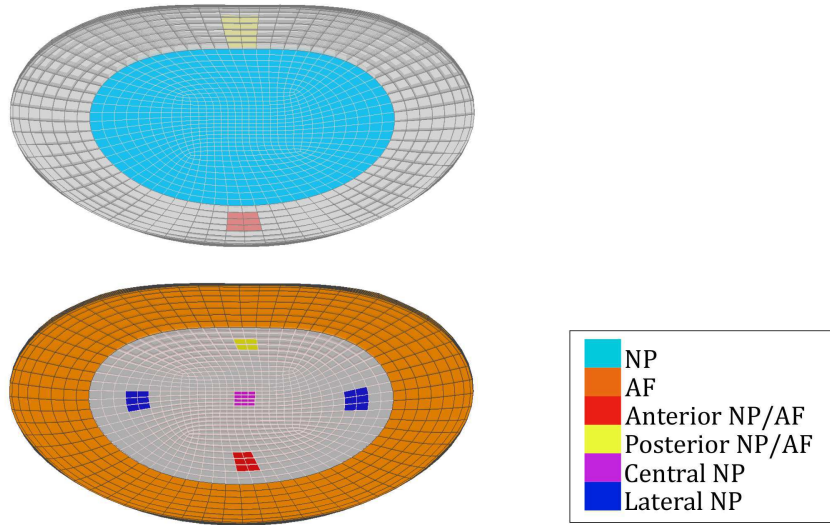
Figure 5.28: Volumes identified in the NP and AF to evaluate the pressure.

if small volumes of elements are considered. Thus, to obtain an overview of the AF behaviour, stress and pressure distribution were extracted from PostView (Figure 5.30). The pressure distributions on the AF at the different loads shows the same trend described above and reported in the bar plot Figure 5.29. The axial stress plots demonstrated an increasing compressive stress as the load increased. Due to the bulging effect the most external
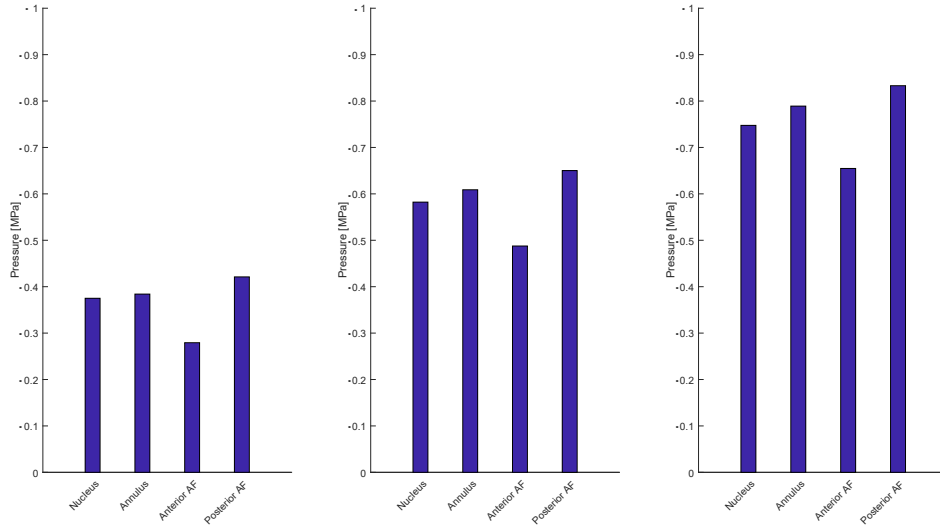
Figure 5.29: Pressure evaluated on the AF and NP at 500 N (a), 750 N (b) and 1000 N (c).

layer of the AF had a positive axial stress.

5.6   Discussion

The automatic pre-processing of the lumbar spine (L1-L5) has been presented, describing all the steps involved in the preparation of the FE model. The entire workflow, from the generation of the L1-L5 geometric model to the FE model ready to be solved, takes less than five minutes in the LMG toolbox. This toolbox has the potential to be used in clinical assessment as well as in the implant design optimization process, where population of anatomical models can be generated and evaluated in a reasonable amount of time.

The L1-L5 lumbar model has been implemented in section 5.3 to show the functionalities of the LMG toolbox. The geometrical model was generated and the pre-processing performed, using the default features earlier described. Furthermore, a L1-L2 FU was generated and the FE model solved and analysed.

The results of the L1-L2 have been analysed and the average axial deformations across the AP cross-section is shown in Figure 5.27. In the transition between NP to AF in both the posterior and anterior side, there is a drop of this value, due to the change of material properties. The axial deformations obtained for the IVD have been compared with experimental and computational results available in the literature (reported in Table 5.8). The average values, in correspondence of the NP region, obtained in the FE simulation
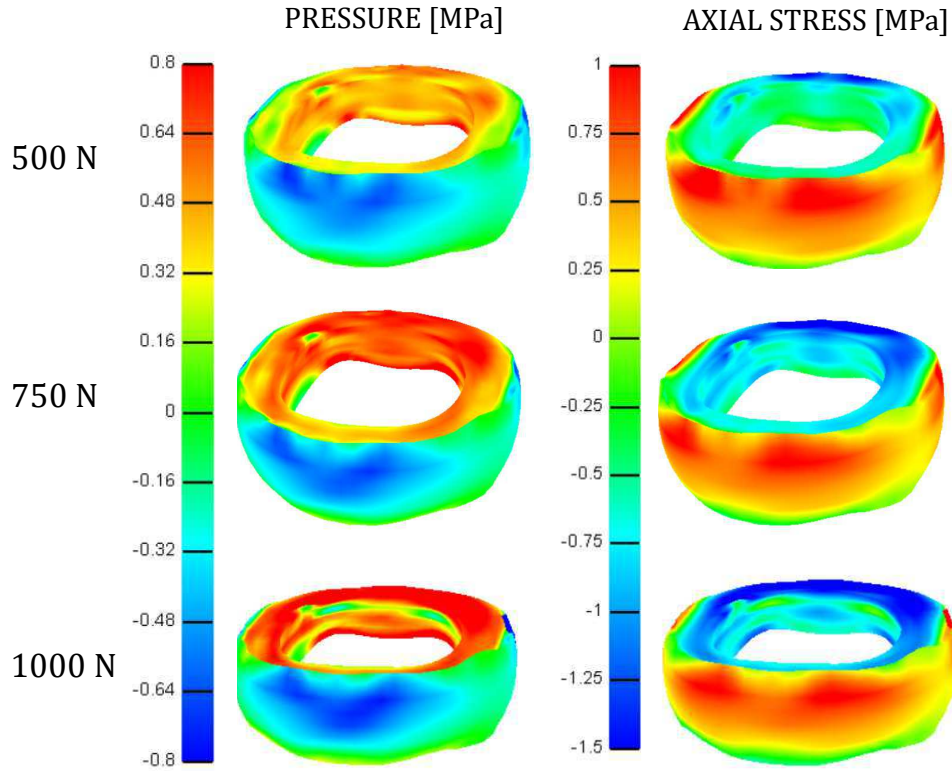
Figure 5.30: Qualitative evaluation of pressure and axial stress distributions on the AF.

are in agreement with the experimental data.

The IDP values obtained in the NP increased linearly from 0.38 MPa to 0.78 MPa at the different load considered according with Adams et al. [273]. The results have been compared with the results in the literature and are shown in Figure 5.31. Moreover, the results are compared with the exhaustive review of FE models of Dreischarf et al. [95] and the experimental results of Brinckmann et al. [274]. The IDP values obtained in this study (highlighted with orange dots in Figure 5.31), are in agreement with the previous experimental studies and FE analyses. The range of results obtained in previous FEA are included in the green area, while the median of the experimental results are illustrated with a red dotted line and the bars identify the range of variability of the results at the compression load considered [274]. These comparisons demonstrated the validity of the model used, paving the way for further improvements and applications.

There are several factors which influence the differences in the output of experimental tests [275]. The collection and storage of samples, the test setup, the preconditioning and loading conditions, healthy conditions of the disc and the lumbar level considered, all affect the test results. Furthermore, the

Table 5.8: *Maximum load and displacement evaluated in previous experimental studies on cadaver specimens (EXP) and FE models (FEM). The displacements of the experimental results were obtained as the average on the specimens evaluated in each study.*

Study	Max load [kN]	Displacement [mm]	Study
Hirsch et al. [270]	1.0	1.8	EXP
Markolf et al. [271]	4.4	1.6	EXP
Simon et al. [272]	0.5	1.5	FEM
Adams et al. [157]	1.3	1.7	EXP
Marini et al. [258]	1.0	0.9	FEM
	0.5	1.28	
Current study	0.75	1.57	
	1	1.75	
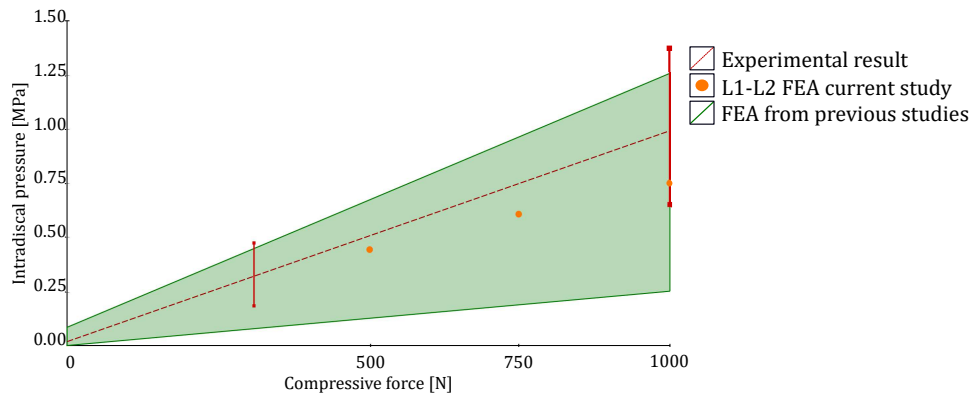
Figure 5.31: *The results of the IDP has been evaluated in several studies and the green area identifies the range of values obtained [165] which have been compared with the the median of in-vitro results (red dashed line) and their variability (red bar)[274, 273]. The orange dots identify the results of the current study at 500 N, 750 N and 1000 N.*

variability between the geometry and material properties of the FE models have to be taken into account. Recent studies using statistical methods (i.e.: Monte Carlo sampling, Taguchi method and factorial analysis), have evidenced the most influential set of parameters, or combination of parameters for FE models, which are the IVD height and the facets geometry [276, 87, 13, 100]. In the following chapter (chapter 6), a preliminary sensitivity study on anatomical and material variability is described, with the intention of identify influential parameters for the spine biomechanics.

Schmidt et al. [256] evaluated the effect of different loading conditions, and in particular the effect of the follower load on the IDP. The IDP ranged between 0.14 MPa to 0.35 MPa, applying pure moments in flexion, extension, axial rotation and lateral bending, and it increased by an average value

of 0.34 MPa when applying a follower load. It is reasonable to hypothesise that the offset obtained in the other loading modes could be addressed to the compression case, placing the current results in the range of values found in the literature. Ultimately, a follower load is applied to distribute the load along the lumbar curvature, and give more stability to the simulations miming the muscles effects. Toumanidou T. [141] evaluated muscles and swelling effects on the IDP, in flexion, lying and standing positions. In the standing position, without considering the effects of muscles and swelling of the IVD, the IDP at the L1-S1 levels ranged between 0.24 MPa and 0.31 MPa. A variation of the 25%-29% at all the levels when the muscles were not simulated was reported, thus strengthening the mentioned hypothesis for the compressive load.

The stress distribution along the layers of the IVD follow a similar trend to those identified in the literature [277, 278], with an increased tensile stress in the outermost layer, as shown in Figure 5.30. Furthermore, the pressure distributions have been evaluated in different regions (nucleus, anulus, AF anterior, AF posterior) for each loading step considered. The average value on the AF does not reflect the differences on its behaviour according to the different region. In fact, the posterior side of the AF is affected by higher pressure than the anterior side (Figure 5.30), which is in agreement with the results reported in literature [273][278].

It has been suggested [13] that more studies are needed to investigate the effect of morphometric variation and how it affects subsequent stress distribution. In fact, it is shown in Figure 5.32 that the contact surfaces are not plane, but characterized by the curvatures of the endplates. This feature could affect the stress and pressure distribution in the IVD particularly in the case of different volumetric ratio and height of the disc. The results here compared are in the range of variability of the experimental results and the FE analyses reported in the literature. In this study the ligaments and facet joints and follower loads have not been modelled, which affect the biomechanics of the FU [107]. Their influences have been investigated mainly applying pure moments, but it is expected that they exert an influence on the biomechanics (i.e.: higher IDP, as in case of facetomy [279]) also in pure compression [97]. In fact, load sharing between the anterior and posterior structures of the FU is affected by the action of facet joints and ligaments [280, 279] .

Future studies would implement a more complete set of loading conditions directly applied from the LMG toolbox. As stated in subsection 5.2.4, only compression and prescribed rotations are automatically implemented, limiting the evaluation of the FU biomechanics in this study.

The LMG toolbox represents a step forward to develop and evaluate FE models overcoming the time-consuming issue of subject-specific models, which enables intra-subjects variations to be considered. In fact, anatomical variations can be assessed (described in chapter 4) and the FEA workflow is
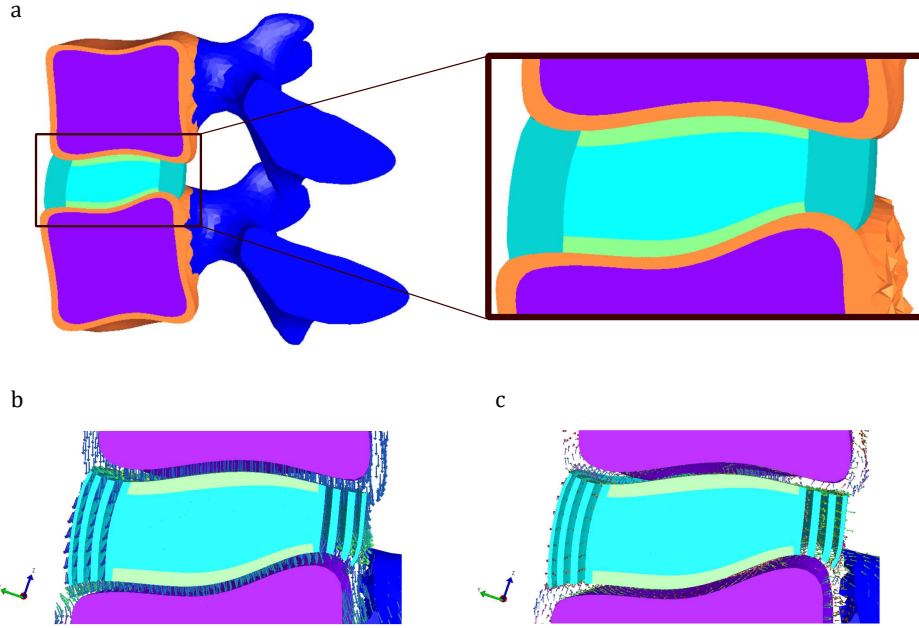
Figure 5.32: Morphometry of the bone endplates in contact with the IVD with an overview on the contact surfaces (a). The displacement (b) and first principal stress (c) distributions are displayed with vector plots, where the vector colors are referred to the orientation and the length is normalized. In the bottom figures the cortical bones and some of the AF layers have been hidden to show the vectors.

fastened by the automatic pre-processing. Moreover, the LMG generates the geometrical model in 20 s and the FE model is pre-processed and ready to perform the simulations in less than 5 minutes. Considering a longer-term aim of using this tool in clinical studies, this result represents an important achievement, as it provides a first major step in enabling quick evaluation for the decision making of treatments to adopt or to improve the design of devices. This parametric tool is particularly of interest given recent reports by international authorities and consortia (FDA and MDIC) [17]. To speed up the development of new devices, they suggest developing parametric models to evaluate variety of anatomy and pathological conditions, through the use of validated tools. The LMG requires the implementation of further structures (ligaments, facet joint contacts and follower loads) and functions to enable a wider range of biomechanical assessment. At the present it represents a first step toward the use in clinical studies.

5.7 Chapter summary

In this chapter the automatic pre-processing of the lumbar FE model has been described and a preliminary study on the L1-L2 FU has been evaluated.

The automatic pre-processing of the LMG toolbox (described in chapter 4) included: i. the mesh size assessment; ii. identifying the geometrical features to define boundary and contact surfaces; iii. assigning the material properties of all the structures involved in the FE model; iv. defining the required loading conditions. Currently, the LMG does not include all the possible conditions, only few loading conditions (compression, prescribed displacements and rotations) are directly applied. The definition of ligaments and facet joint surfaces is already implemented, but it has not been included in the preliminary model generated. In future studies, further loading conditions will be included in the toolbox, and rigid elements (i.e.: beam or spring) to simulate follower loads acting through the lumbar arch, will be included.

The whole toolbox, from the geometry generation to the FE model simulation, represents a novel approach to the computational modelling of the lumbar spine and has the potential to speed up its biomechanical evaluation. In particular, this process would be useful in the evaluation of the effects of implants on the range of motion of the spine and how the stress are distributed, assessing the effects with different anatomical features. Sensitivity analysis could be evaluated varying the geometrical features, the material constitutive laws of the structures involved in the lumbar spine, emulating healthy and degenerated conditions, as well as optimization of the design and materials properties of the devices.

The described workflow can be pursued with the methods already adopted in the literature [261], starting from the segmentation of subject-specific datasets and developing the FE model. The development of these models has a high computational cost, some stages are affected by inter-user variability and it does not allow the evaluation of sensitivity analysis on varying the anatomical morphology. This toolbox offers the generation of an accurate geometrical model, with a highly reduced computational time (the geometry is generated in less than 20 s), with the possibility to evaluate several morphological variations, anatomical deformity or degenerated conditions (chapter 4). Evaluating the same sensitivity analysis on subject-specific models would require weeks/months of extensive work for expert users: collecting and segmenting the subject-specific scans and then pre-process the obtained geometrical models. In which case, the model generations would rely on the availability of subject-specific scans which restrict the evaluation and optimization of the implants design to few particular cases.

The potentiality of the LMG toolbox is introduced in the preliminary study of the L1-L2 FU and the improvements required to obtain a more complete,

accurate FE model has been described in the dedicated discussion (Section 5.6). Focus of further studies would be the validation of complete osteo-ligamentous FE models with experimental results. Moreover, the automatic insertion of devices will be described and added in the toolbox, where a dedicated GUI allows the selection of the desired level.

In the next chapter, sensitivity analyses on the L1-L2 FU is presented, where the results of twenty-one models are compared. In particular, the effects of different morphologies and material properties are evaluated, considering the L1-L2 FU discussed in this chapter as reference.

Chapter 6

Sensitivity study

6.1 Introduction

Finite Element models are well recognized to predict the mechanical behaviour of biological structures [281, 282, 283]. However, the geometry (i.e. their anatomy) and material property of biological structures varies more than would be expected of standard mechanical systems, therefore, this variability requires assessment [100]. This chapter combines the generation of a scalable and parametric model of the spine (chapter 4) and the automatic pre-processing of the FE Model (chapter 5), to assess the variability of morphological and material properties to estimate the biomechanics of the spine under compression.

The material properties and the constitutive laws of soft connective tissues are not well known and they are affected by several factors such as the location within the body and pathological status [171, 284, 285]. Regarding FE models, variability associated with each component of the overall structure complicate the evaluation and estimation of biological structures. In literature, there is a huge variety of lumbar spine FE models differing in terms of constitutive laws and coefficients assigned to the bodies, and how the regions are identified when assigning material properties (chapter 2). The effects of the material properties used and their combinations has been evaluated previously, using statistical modelling techniques [102, 100], so as to quantify their role on the predicted biomechanics [13, 87]. For a functional unit of the lumbar spine, the disc morphology (disc height and the anatomical division between NP and AF) and material properties, have the greatest effects on the subsequent biomechanics of the spine, while less significant effects have been identified by varying the ligament material properties [13, 14]. While variability of material properties can be easily assessed in the models previously evaluated in the literature, assessing these for a range of morphologies require the availability of multiple anatomical models as well as the evaluation of mesh convergence. The LMG toolbox, described in chapter 4, allows

the generation of models varying the morphologies of the spinal bodies, and the automatic assignment of material properties as described in chapter 5.

The aim of this chapter was to evaluate the effects of the morphological variations and material properties on the L1-L2 FU. An overview of the variations evaluated is given in Figure 6.1. A reduced NP volume and disc height as well as a less organized structure of the lamellae in the AF, have been noted in degenerated conditions, resulting in a decreased range of motion. In this study, pathological conditions of the IVD have been evaluated, through assessing variations of the volumetric percentage (VP), material properties of the annulus fibrosus (AF), nucleus pulposus (NP) and cartilaginous endplates (CEP).
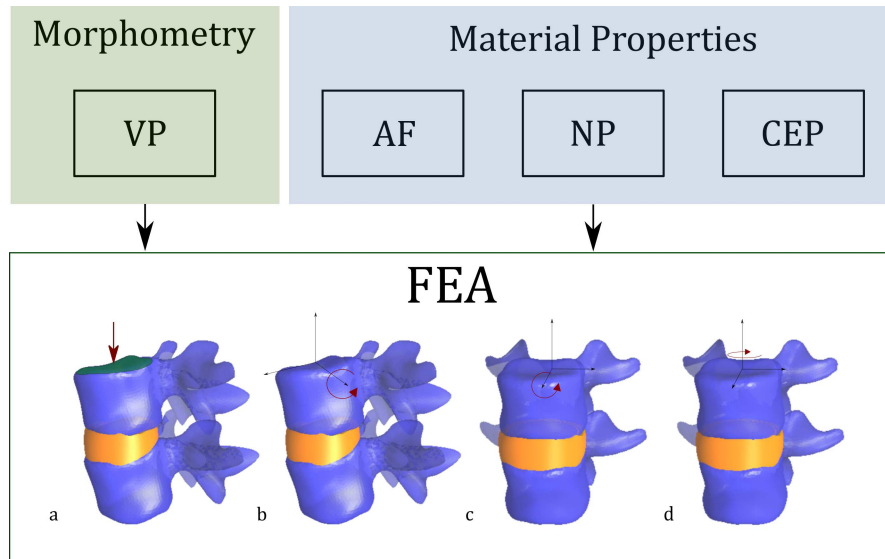
Figure 6.1: Overview of the sensitivity analyses evaluated in this study. Morphological and material properties variations were investigated through FE analyses.

The VP morphological variations have been simulated, obtaining eight different anatomical models, with a AF volume varying from 30% to 60% of the entire IVD volume. The AF has been modelled consistent with the previous simulations (chapter 5), with criss-crossed fibers embedded in each layer and the thickness of the layers is altered with the VP. The reinforcing fibers allow the transmission of the load from the IVD to the vertebral cortex [170]. As seen in chapter 2, the fibers arrangement and strength, as well as the material properties of the ground substance, vary between healthy and degenerated cases. Thus, the material properties of the fibers, their orientations and ground substance constitutive laws have been varied

in this analysis to evaluate the subsequent effects on the biomechanics of an
FU.

The NP and CEP material properties are affected by degenerated conditions,
due to a decreased water content, resulting stiffer in pathological conditions
or due to ageing [49, 286, 21, 47]. These variations were implemented by
evaluating the effects of different constitutive laws, and how the degenerate
conditions affect (simulated with high Young's modulus) the biomechanics.
These modifications jointly interest the conditions of the lumbar spine, and
the degenerated/pathological status are a result of a mixture of these effects.
In this study, the effects of each alteration to geometric components and
material composition have been investigated independently, to determine
relative contribution of each factor without considering the cross-dependence
between the parameters.

6.2 Materials and methods

6.2.1 Model geometry and material properties

An FE model of the L1-L2 functional unit has been generated from the LMG
toolbox using the average model generation method (chapter 5, section 4.3)
for a male subject of 30 years, 1.80 m height and with a lumbar curvature
of 43°. The vertebrae and IVD were meshed respectively by tetrahedral and
hexahedral elements and the details of the mesh, its size and convergence
have been explained in chapter 5, where a preliminary analysis has been
evaluated.

The material properties assigned to the vertebral bodies (Table 6.1), have
not been varied since they are subject to substantially lower strains than
the soft tissues [87].

Table 6.1: Material properties assigned to the vertebrae in all the simulations.

Vertebral bodies	Constitutive law	E[MPa]	ν	ref
Cancellous bone	linear isotropic	100	0.2	[90]
Cortical bone	linear isotropic	12000	0.3	[90]
Posterior elements	linear isotropic	3500	0.25	[269]

The effects of ligaments have been investigated extensively [87, 13], and
have, therefore, not been a focus of this study. This decision was taken:
a. to reduce redundancy in terms of results already well established within
literature, and b. to simplify the clarity of assessment of the results. Hence
in this chapter, the focus is on evaluating only the effects of the altered
morphological features of the IVD and the material properties of the IVD

and CEP, as follows:

1. morphological parameters of the IVD, varying the volumetric ratio between NP and AF between 30% to 60% in eight models;

2. eight different material properties of the AF, varying the stiffness and orientation of the fibers, the constitutive law and the material properties assigned to the ground substance;

3. three models with different material properties of the NP;

4. two models with different material properties of the CEP.

The range of variability of the morphological features and material properties for each component have been chosen accordingly to previous studies and described in the following sections.

Sensitivity analysis: volume percentage ratio

In this study, the volumetric percentage (VP) corresponds to the AF volumetric percentage (i.e. the 30% VP refers to 30% of AF and 70% of NP). Eight meshed models of the IVD were generated and included in the FU model, obtained with the following values of VP: 30%, 35%, 40%, 43%, 46%, 50%, 55%, 60% as shown in Figure 6.2, considering 46% as the average healthy model [238, 140] and previously used in chapter 5. The two outer limits values represent exaggerations to mimic degeneration, with higher AF volume (60%), and the intact AF (30%) [273]. Only morphometric changes
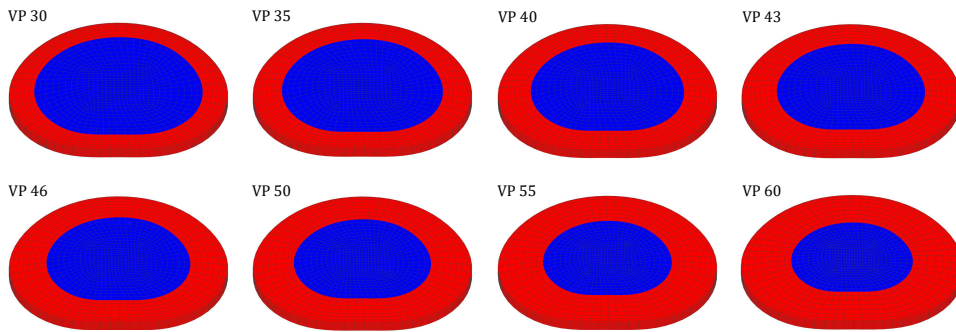
Figure 6.2: IVD models generated with different volumetric ratio.

have been implemented, using fixed material properties in all the cases (Table 6.2). The AF has been modelled following the Holazpfel-Gasser-Odgen (HGO) formulation (described in chapter 2) [127] of criss-crossed fibers, embedded in a ground substance.

Table 6.2: AF, NP and CEP material properties used in the VP sensitivity analysis. The Neo-Hookean material properties is reported in terms of Young's modulus and Poisson's ratio and directly converted into Lamé coefficient in FEBio.

Body	Constitutive law	coefficients						ref
AF ground	Neo-Hookean	E	ν					
		4.2 MPa	0.3					[150]
AF fibres	HGO	ksi	α	β	θ	ϕ		
		2.8 MPa	90	2	±30	90		[258, 287]
NP	Isotropic elastic	E	ν					
		2 MPa	0.499					[89]
CEP	Isotropic elastic	E	ν					
		23.8 MPa	0.4					[79]

Sensitivity analysis: material properties of the AF

The IVD model with a VP of 46% has been taken as the reference model as it is considered to be a healthy condition [238, 140]. The material properties of the other bodies were not varied (Table 6.1 and Table 6.3). Eight models have been implemented, assigning the material properties of the AF as stated in Table 6.4 and here described in detail:

- AF-Case 1: Mooney-Rivlin material properties and criss-crossed fibers at ±30 ° (regards to the orizontal plane of the IVD) in each layer;

- AF-Case 2: Neo-Hookean material properties and criss-crossed fibers at ±30 ° in each layer, which is the same model discussed in chapter 5;

- AF-Case 3: Neo-Hookean ground substance and fibers oriented at ±46° to simulate a degenerated condition;

- AF-Case 4: fibers strength (identified as *ksi*) multiplied for a weight factor w increasing from the inner ($w = 0.65$) to the outer layer ($w = 1$);

- AF-Case 5: fibers strength *ksi* multiplied for the lowest w value in all the layers;

- AF-Case 6: fibers strength assigned following the anterior, posterior, lateral (posterior and anterior) regions (Figure 6.3). In this evaluaton all the layers have the same fiber material properties and orientations;

- AF-Case 7: fiber orientations varying from ±46° in the outer layer to ±30° in the inner layer;

- AF-Case 8: fiber strength properties and orientations varying across the AF from the inner to the outer layer.
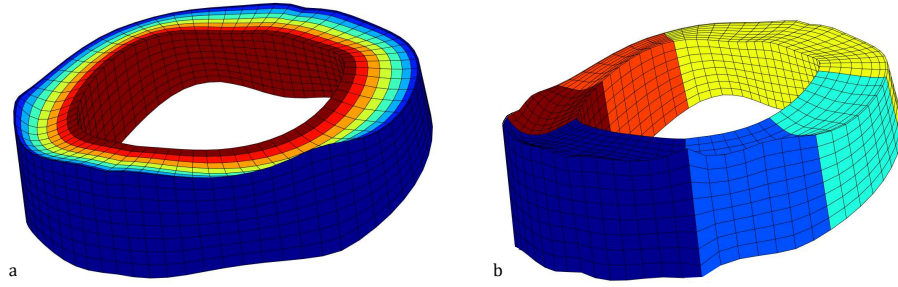
Figure 6.3: IVD models generated with a. different material properties assigned to each layer and b. for each region: anterior, posterior, anterior and posterior lateral (left and right).

Table 6.3: Material properties not varied in the AF sensitivity analysis.

Body	Constitutive law	coefficients	Ref
NP	Isotropic elastic	E ν	
		2 MPa 0.499	[89]
CEP	Isotropic elastic	E ν	
		23.8 MPa 0.4	[37]

Sensitivity analysis: material properties of the NP

The material properties of the NP were varied accordingly to constitutive laws (Neo-Hookean and Mooney-Rivlin) and values from the literature [252, 131]. Three different cases were implemented, varying the material properties as reported in Table 6.6. These variations were implemented to evaluate the effects of different constitutive laws, and how the degenerate conditions affect (simulated with high Young's modulus in NP-case 1) the biomechanics. The NP-case 1 represents the material properties used in the L1-L2 FU in chapter 5. The material properties of the AF and CEP were assigned as in the VP sensitivity analyses and are stated in Table 6.5.

Sensitivity analysis: material properties of the CEP

The material properties assigned to the CEP in previous studies [289][50] were evaluated. Two extreme values, which simulate the degenerate and healthy material properties, have been implemented as listed in Table 6.8. The CEP-case 1 has already been presented in chapter 5 and it has been used as a reference model for comparison. The AF and NP material properties, not varied in these simulations, are listed in Table 6.7.

Table 6.4: *Material properties varied for the AF sensitivity analysis. The symbol * identify the parameter varied in each simulation. The Neo-Hookean material properties is reported in term of Young's modulus and Poisson's ratio and directly converted into Lamé coefficients in FEBio*

Annulus Fibrosus				
AF cases	Property varied	coefficients	ref	
AF-Case 1	AF Ground	c1,c2	0.82,0	[287]
	Mooney-Rivlin*	ksi	2.8 MPa	[287]
		α	90	
		β	2	
		θ	$\pm30°$	
		ϕ	90	
AF-Case 2	AF Ground	E,ν	4.2 MPa,0.3	[150]
	Neo-Hookean*	ksi	2.8 MPa	
		α	90	
		β	2	
		θ	$\pm30°$	
		ϕ	90	
AF-Case 3	Fibres orientation	E,ν	4.2 MPa, 0.3	[150]
	$\theta = \pm46°$	ksi	2.8 MPa	
		α	90	
		β	2	
		θ *	$\pm46°$	
		ϕ	90	
AF-Case 4	ksi weighted	E, ν	4.2 MPa, 0.3	[150]
	layer $1-2$ $w=1$	ksi*	2.8 MPa	[256]
	layer $3-4$ $w=0.9$	α	90	
	layer $5-6$ $w=0.75$	β	2	
	layer $7-8$ $w=0.65$	θ	$\pm30°$	
		ϕ	90	
AF-Case 5	ksi weighted	E, ν	4.2 MPa, 0.3	[150]
	$w=0.65$	ksi*	2.8 MPa	
		α	90	
		β	2	
		θ	$\pm30°$	
		ϕ	90	
AF-Case 6	ksi regionally weighted	E, ν	4.2 MPa, 0.3	[150]
	A, AL, L, PL, P	ksi*	2.8 MPa	[252]
	$w = [1, 0.71, 0.5, 0.68, 0.7]$	α	90	
		β	2	
		θ	$\pm30°$	
		ϕ	90	
AF-Case 7	θ weighted	E, ν	4.2 MPa, 0.3	[150]
	$25° - 46°$	ksi	2.8 MPa	[252]
		α	90	
		β	2	
		θ *	$\pm(25° - 46°)$	
		ϕ	90	
AF-Case 8	$\theta and ksi$ weighted	E, ν	4.2 MPa, 0.3	[150]
	$\theta = 25° - 46°$	ksi*	2.8 MPa	[252]
	$w = 1 - 0.65$	α	90	
		β	2	
		θ *	$\pm(25° - 46°)$	
		ϕ	90	

Table 6.5: *AF and CEP material properties assigned in the NP sensitivity analysis. The Neo-Hookean material properties is reported in terms of Young's modulus and Poisson ratio and directly converted into Lamé coefficients in FEBio.*

Body	Constitutive law	coefficients		ref
AF Ground	Neo-Hookean	E, ν	4.2 MPa, 0.3	[288]
AF fibres	HGO	ksi	2.8 MPa	[252]
		α	90	
		β	2	
		θ	± 30 °	
		ϕ	90	
CEP	Isotropic elastic	E, ν	23.8 MPa 0.4	[79]

Table 6.6: *NP material properties assigned in the NP sensitivity analysis.*

Nucleus Pulposus	Constitutive law	coefficients		ref
NP-case 1	Isotropic elastic	E,ν	2 MPa,0.499	[89]
NP-case 2	Isotropic elastic	E,ν	1 MPa,0.499	[131, 135]
NP-case 3	Mooney-Rivlin	c1,c2	0.12,0.03	[131]

Table 6.7: *Material properties not varied in the CEP sensitivity analysis. The Neo-Hookean material properties is reported in term of Young's modulus and Poisson's ratio and directly converted in Lamé coefficient in FEBio.*

Body	Constitutive law	coefficients		ref
AF Ground	Neo-Hookean	E, ν	4.2 MPa, 0.3	[288]
AF fibres	HGO	ksi	2.8 MPa	[252]
		α	90	
		β	2	
		θ	± 30 °	
		ϕ	90	
NP	Isotropic elastic	E ν	2 MPa 0.499	[89]

Table 6.8: Material properties for the CEP sensitivity analysis.

CEP	Constitutive law	coefficients		ref
CEP-case 1	Isotropic elastic	E, ν	5 MPa,0.4	[289, 290]
CEP-case 2	Isotropic elastic	E, ν	23.8 MPa,0.4	[79]

6.2.2 FE models and analyses

Twenty-one models have been defined with the material properties described in subsection 6.2.1. To compare these results, the same boundary and loading conditions were applied to all the models. The FU has been fully constrained at the lower surface of the L2 and pure compression and pure moments (around the three axis) have been applied on the upper surface of the L1 (see Figure 6.4). A compressive load of 500 N was applied as a distributed load on the upper surface of the L1, and extension, lateral bending and axial rotation have been applied as prescribed displacements, where the displacement in the three directions (x, y, z) are evaluated according to the rotation applied (described below). In the last loading case, an initial axial displacement of 1 mm was applied to enforce the contacts and 3D displacement are applied to simulate extension, lateral bending and axial rotation. The axial-symmetry hypothesis has been adopted and only left lateral bending and axial rotation with a positive angle around the z-axis (as shown in Figure 6.4) have been considered. Coombs et al. [87] showed that the rotation values corresponding to 10 N m is equal to apply a rotation of 8.66° in flexion, 5.92° in extension, 6.01° for lateral bending and 1.75° for axial rotation. The displacement d to apply in the three dimensions, to obtain the final position after imposing the described rotation, have been calculated through Equation 6.1 and Equation 6.2,

$$d = coord'_{x,y,z} - coord_{x,y,z} \tag{6.1}$$

$$coord'_{x,y,z} = coord_{x,y,z}R \tag{6.2}$$

where *coord* and *coord'* are, respectively, the initial and final coordinates of the nodes of the L1 vertebrae and R is the rotation matrix R (Equation 6.3), evaluated as a combination of the rotation matrices around the three axes (Equation 6.4).

$$R = R_x R_y R_z \tag{6.3}$$

$$R_x = \begin{bmatrix} 1 & 0 & 0 \\ 0 & cos\alpha & -sin\alpha \\ 0 & sin\alpha & cos\alpha \end{bmatrix} ; R_y = \begin{bmatrix} cos\beta & 0 & sin\beta \\ 0 & 1 & 0 \\ -sin\beta & 0 & cos\beta \end{bmatrix} ; R_z = \begin{bmatrix} cos\gamma & -sin\gamma & 0 \\ sin\gamma & cos\gamma & 0 \\ 0 & 0 & 1 \end{bmatrix} \tag{6.4}$$
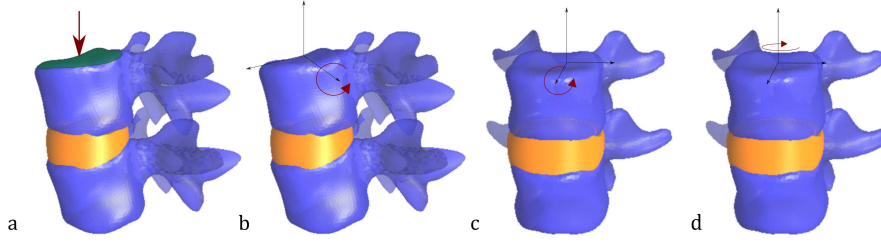
Figure 6.4: Loading conditions: a. compression; b. extension; c. lateral bending; d. axial rotation.

In each group of simulations (varying the VP, AF, NP or CEP material properties) a reference model has been used, which corresponds with the model described in chapter 5.

The results of the sensitivity analyses simulations were reported in terms of displacements, pressure on the NP (Intradiscal Pressure IDP) and axial stress. The post-processing has been performed in Matlab, importing the output files obtained from FEBio.
In order to evaluate the displacement on the IVD, the Anterior-Posterior (AP) cross-section was taken in consideration (Figure 6.5). Then, the mean values of the axial displacement on the IVD elements (excluding the cartilaginous endplates elements) were evaluated.
The IDP was evaluated as in Equation 6.5 [37], in volumes identified around the mean height of the IVD in the centre, anterior, posterior and lateral regions of the NP and anterior and posterior side of the AF (Figure 6.7).

$$P = -\frac{1}{3}tr(\sigma) \tag{6.5}$$

where tr is the trace of the Cauchy stress matrix σ. The NP was modelled with solid elements, which differs from other studies in the literature [90, 291, 134] where fluid-like elements were used and the pressure did not vary within its volume. Using solid elements, the pressure distribution was not constant throughout the NP, and it was evaluated at different regions. All the results were reported for the posterior volume, where the standard deviation was always within 0.1 but for simplicity it has not been reported in the results plotted. Moreover, the results followed the similar trend in all the volumes, as shown in Figure 6.6 for the VP sensitivity, with an increasing IDP in the models with higher values of AF volumetric percentage.   In the AF, the stress and pressure values were affected by higher standard deviations and the mean values reflect an average behaviour within the small volume of elements considered (Figure 6.7). This greater variation is due to the
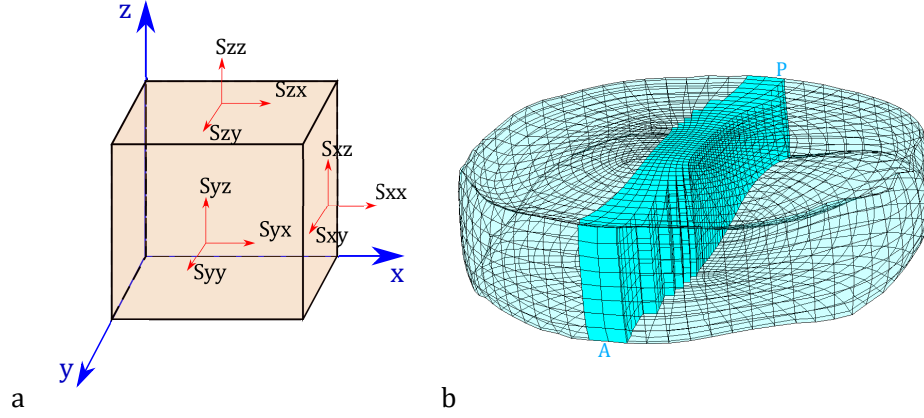
Figure 6.5: The picture shows the reference coordinate axes and the direction of the Cauchy stresses (a) and the Anterior-Posterior (AP) cross-section where the results have been evaluated (b).
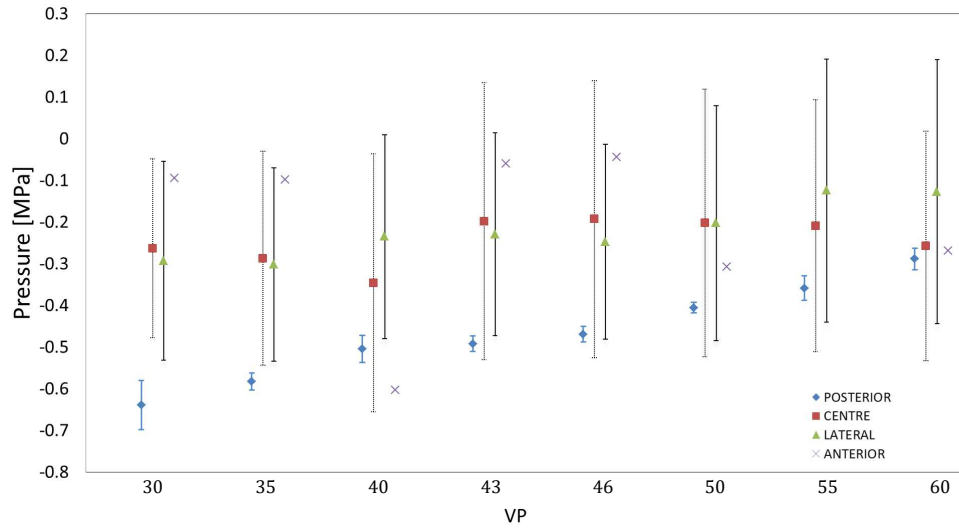
Figure 6.6: Pressure on varying the VP in the different volumes (posterior, anterior, centre, lateral). It is shown that in the posterior side the standard deviation is lower than in the other case, but a common trend is evident in all the volumes.

bulging effect, the different material properties and fiber orientation within each layer. In order to obtain an overview of the AF behaviour, stress and pressure distribution were extracted from PostView, a post-processing FEBio tool.
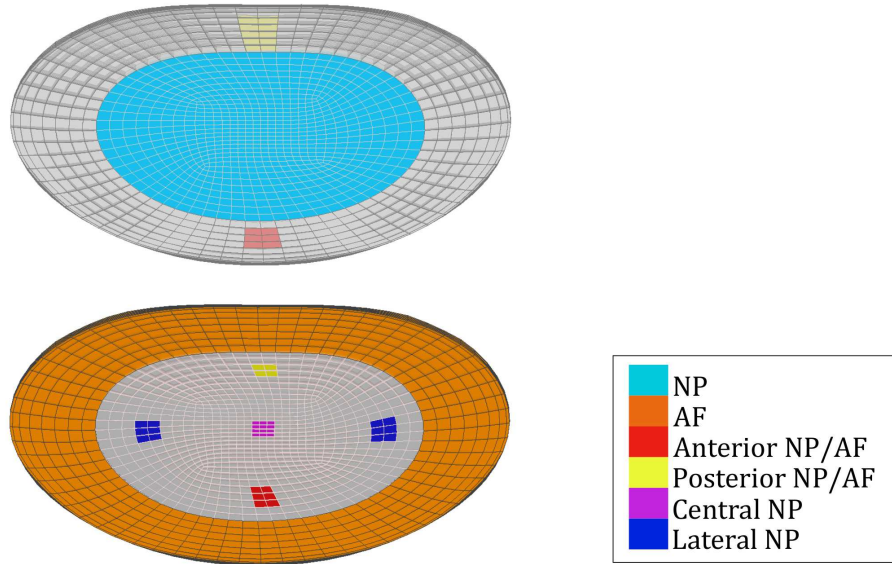
Figure 6.7: Volumes identified in the NP and AF to evaluate the pressure.

6.3 Results

The results are reported according with the sensitivity studies described in the previous sections: morphological variations (VP), and material properties of NP, AF and CEP.

Sensitivity: on varying the VP

The effect on the displacement under compression, varying the VP (30%, 35%, 40%, 43%, 46%, 50%, 55%, 60%), over the AP cross-section, is shown in Figure 6.8. The displacement increases with increasing NP volume. Displacement ranged from 1.2 mm to 1.4 mm, where the maximum values are related to higher NP volumes, in correspondence of the simulated healthy model. In Figure 6.9 the pressure distributions on the IVD along the AP cross-section (Figure 6.9a) and the cross-section passing by the mid-line of the IVD (Figure 6.9b) are displayed. From these figures, a decrease in pressure is observed as the AF volume increases. The same trend is evident in Figure 6.10, where the pressure on the NP and AF has been reported for
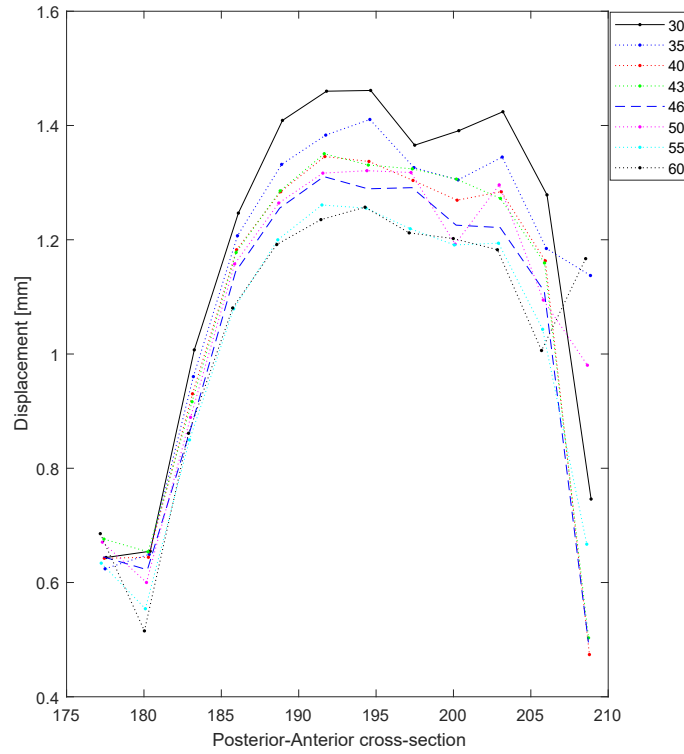
Figure 6.8: Displacements on the IVD evaluated along an anterior-posterior cross-section. The results are reported at different VP (30%, 35%, 40%, 43%, 46%, 50%, 55%, 60%) and the x-axis reports the positions of the IVD, from the posterior to the anterior side.

a small volume of elements. With a decreasing AF volume, the pressure in the NP increases, however, an opposite trend is observed for the pressure in the AF. The overall pressure on the AF increments when the NP volume decreases, and it is evident that there is an increasing pressure on the posterior side of the AF. The stress on the axial direction (S_z as shown in Figure 6.5) and the pressure distributions on the AF are shown in Figure 6.11 for a VP of 30%, 46% and 60%, which represent extreme conditions (thin AF, and degenerated condition) and an average healthy condition. It is evident that in the case of high VP values, the axial stress and pressure distributions affect more the AF volume. It is noticeable that for a VP of 30% on the posterior side and anterior outer surface there is a higher pressure as compared to a VP of 60%. The axial stress present the same features, with a more distributed stress over all the AF and low stress values on the outer layers increasing the VP.

The 60% model, which represents the degenerated condition, should experience higher stress and pressure than the other VP cases. However, in this
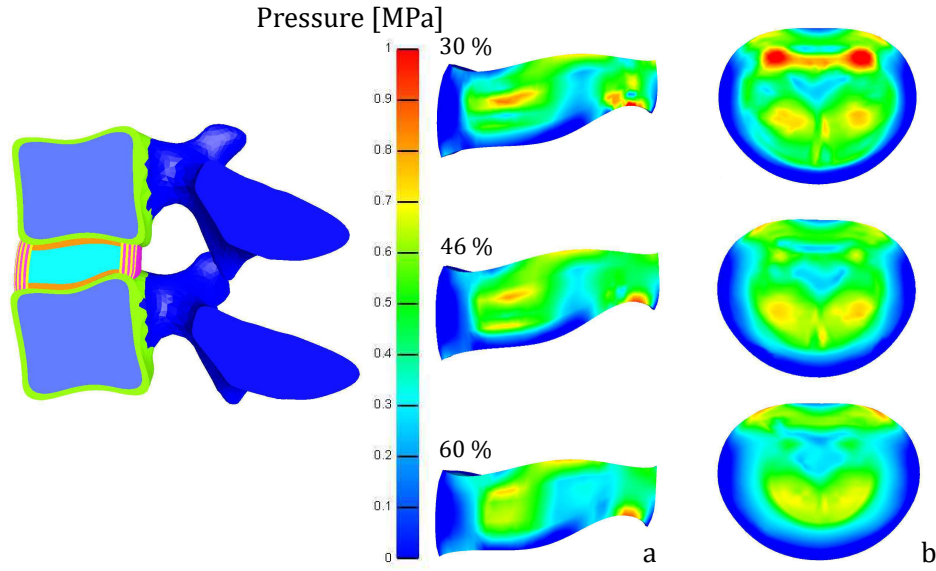
Figure 6.9: Pressure distribution on the AP cross-section (a) and on the transverse plane at the average height of the IVD (b). The results are shown for three VP (30%, 46%, 60%), representing the two extreme conditions and the average healthy conditions.
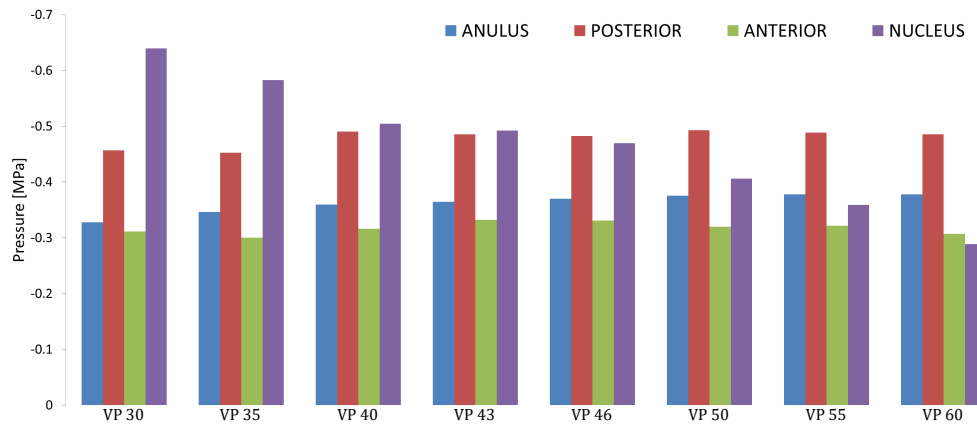
Figure 6.10: Pressure evaluated in volumes defined in the centre of the NP and anterior and posterior area of the AF.

simulation the change of material properties in the degenerated conditions have not been taken into consideration, then the VP 60% has a thicker AF structure than the VP 30%, which better bear the loads. The results of
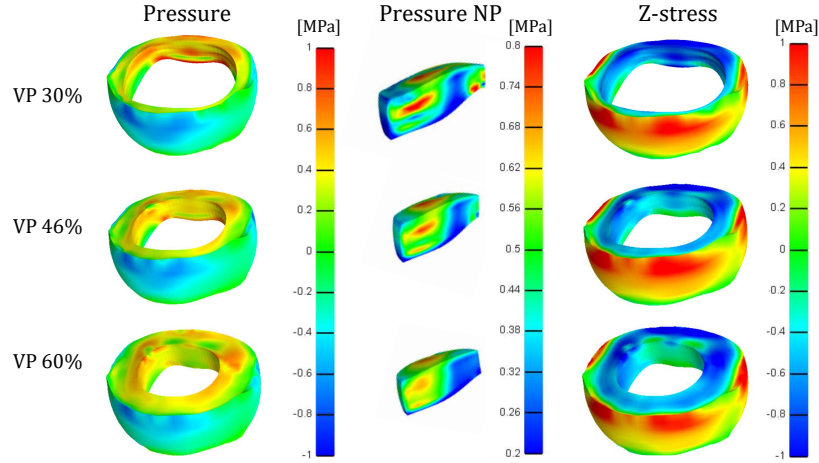
Figure 6.11: Stress distributions along z-direction and pressure distributions on the AF for the model at 30%, 46% and 60% VP. The pressure and stress in both AF and NP are higher in the model with thinner AF.

applying the lateral bending, axial rotation and extension movements on the FU are shown in Figure 6.12. The results follow the same trend as the compression simulations, the load is better distributed on the AF volume as this volume is increased. This is a result of a better load sharing due to a wider area with higher material properties, and lower pressure in the NP.

Sensitivity: on varying the AF

The displacements, over the AP cross-section identified above (Figure 6.13), do not show high variations on varying the fiber properties which showed a mean value on the NP of around 1.2 mm. When varying the material properties of the AF ground substance (AF-case 1), the mean value of the axial displacement was around 1.6 mm in correspondence of the NP, and it was around 1.35 mm when the fibre strength was assigned according to the different region of the AF (AF-case 6). Thus, higher axial displacement was recorded when the material properties of the ground substance were varied (see Figure 6.3) as compared to the other cases (AF-case 2,3,4,5,7,8). The results from varying the material properties of the ground substance are confirmed by Figure 6.14 where the stress and pressure distributions on the AF are displayed. In Figure 6.15 the mean values on the volumes identified in the NP, AF and on the anterior and posterior side of the AF have been compared. In compression, it has been shown that AF-case 1 predicts the
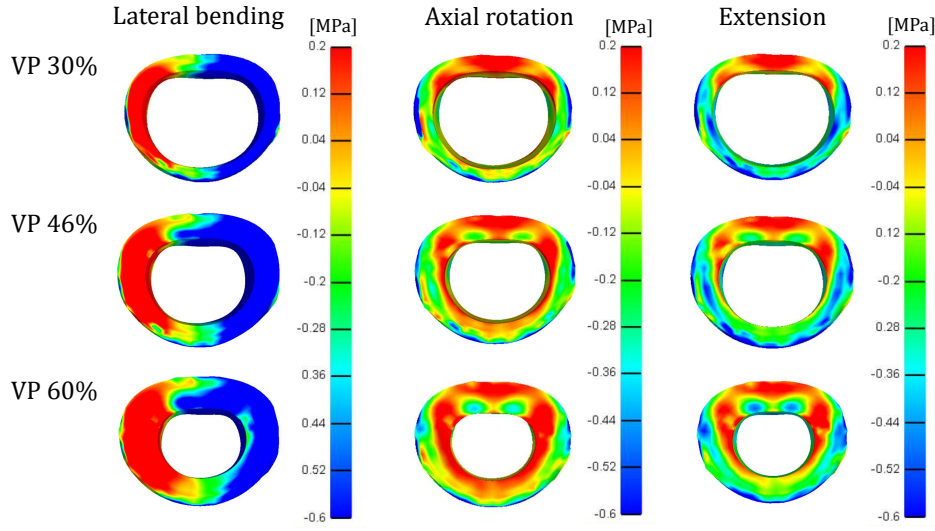
Figure 6.12: Pressure distribution on the IVD for different VP (30%, 46%, 60%) for the different loading conditions: lateral bending, axial rotation and extension.

lowest value of stress and pressure on the AF, but as confirmed by the high displacements in the NP, there is a peak value of pressure in the NP (-0.68 MPa). This results in a more even distribution of pressure across the NP (Figure 6.14). In the other cases, the IDP in the NP is around -0.45 MPa while differences are better shown in Figure 6.14. Higher stress concentrations are observable on the external layers of the AF, particularly in cases 3 and 4. From varying the fiber orientations between the two extreme values evaluated (± 30 ° and ± 46 °) reported in AF-Case 2 and AF-Case 3 (respectively), it is evident that this leads to a higher stress and pressure on the AF outer layer of the model with a high fiber angle (Figure 6.14).

Predictions following the application of moments over the three axes (lateral bending, axial rotation, extension) are shown in Figure 6.17 and Figure 6.16. In all the cases a non-symmetric pattern of the results (both in stress and pressure distributions) is noted, during these loading conditions. The key-results can be evaluated by comparing the following cases:

- AF-case 1 and AF-case 2, which differ in the AF ground substance: there are not major differences in pressure or stress distributions in the NP, while higher pressure and stress are visible on the outermost layer of AF-case 2;

- AF-case 2 and AF-case 3, where the same material properties are implemented, and the fibers are arranged respectively at ± 30 ° and ± 46 °: a slightly higher IDP is recorded for the AF-case 3 in the lateral bending loading condition: -0.22 MPa versus -0.13 MPa in AF-case 2,
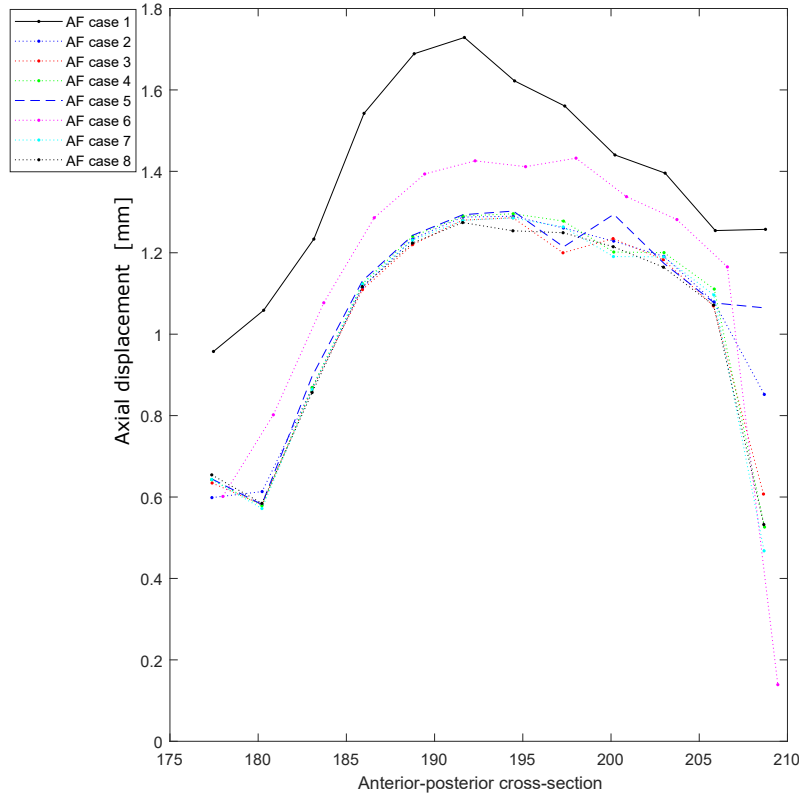
Figure 6.13: Displacements on the anterior-posterior cross-section.

as well as increasing pressure and stress in the AF external layer;

- AF-case 4 and AF-case 5, where the difference is linked to the fiber stiffness (ksi), differences can be noted for extension and axial rotation. For instance, AF-case 4 has fiber stiffness varied per layers, and leads to a higher IDP (-0.39 MPa AF-case 4) when compared to AF-case 5 (-0.34 MPa) in extension; in axial rotation higher IDP was recorded for AF-case 5 (-0.18 MPa) than AF-case 4 (-0.11 MPa);

- AF-case 6 predicts the highest value of IDP in extension (-0.55 MPa), due to the different fiber properties of the AF;

- AF-case 7 and AF-case 8 have the same material properties for the AF ground substance, but a lower IDP is predicted under extension loading mode in AF-case 8 (-0.35 MPa vs -0.46 MPa) due the variation of the fibers strength in between the layers. In fact, in AF-case 8 the fibers have a variable strength, with the lowest value in the inner layer and the highest in the outer one.
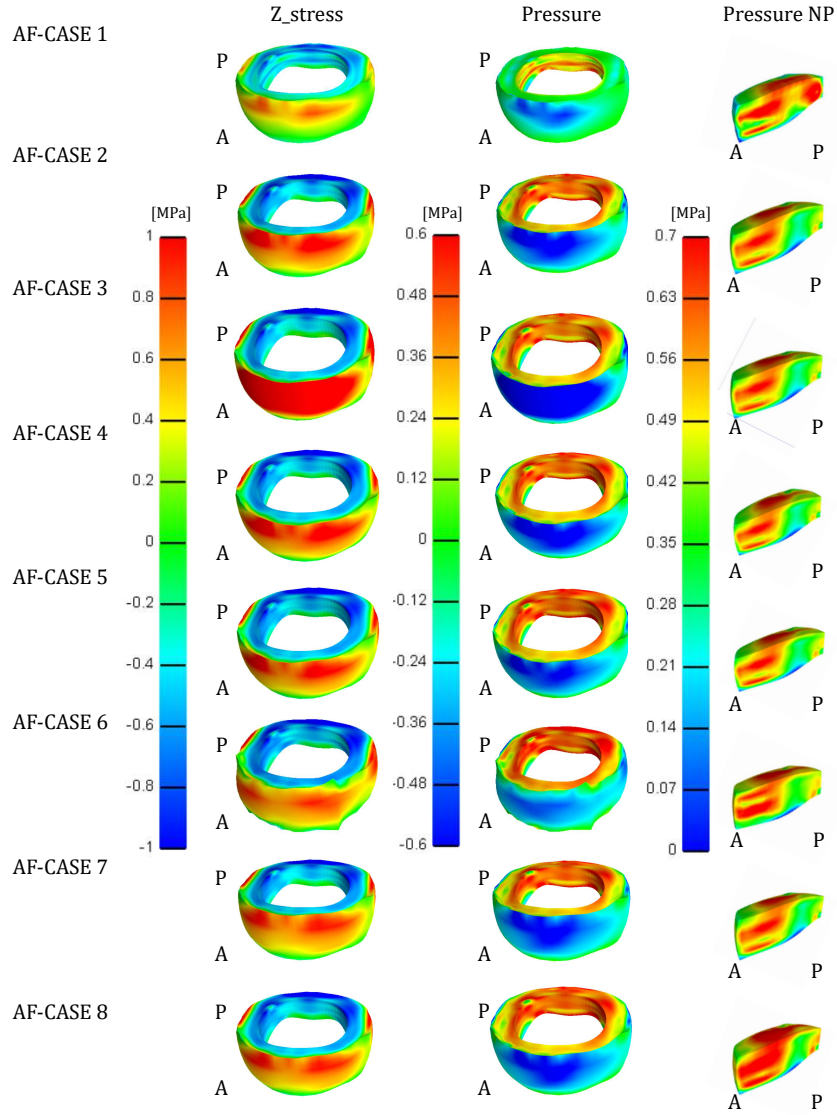
Figure 6.14: Stress on the vertical direction and pressure distributions for all the cases listed in Table 6.4. The letters A and P correspond to Anterior and Posterior.
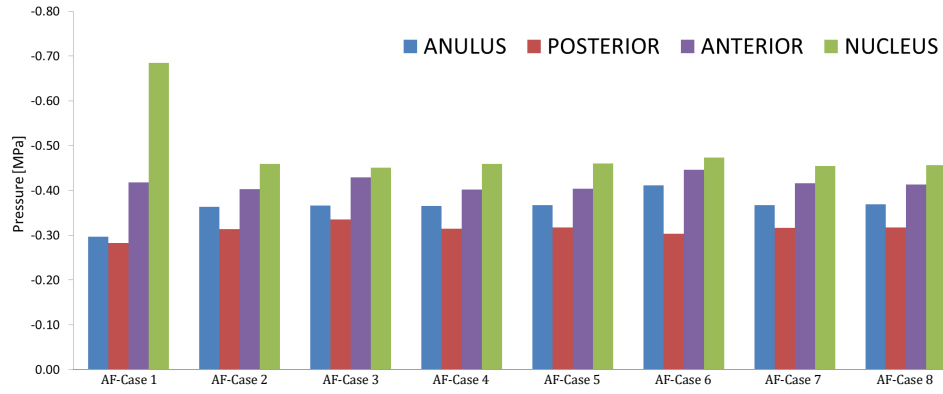
Figure 6.15: Pressure evaluated on the entire AF and on the volumes defined in the anterior-posterior cross-section in correspondence of the anterior and posterior AF and in inner volume of the NP.
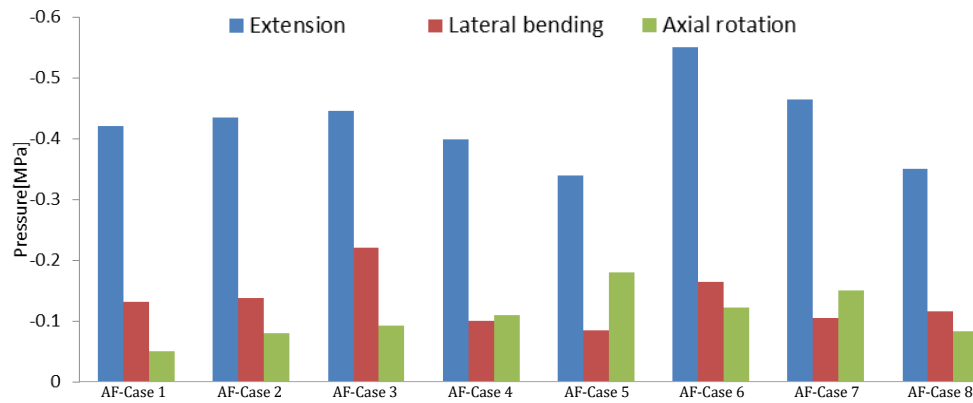
Figure 6.16: IDP evaluated in the three loading mode: extension, lateral bending and axial rotation.
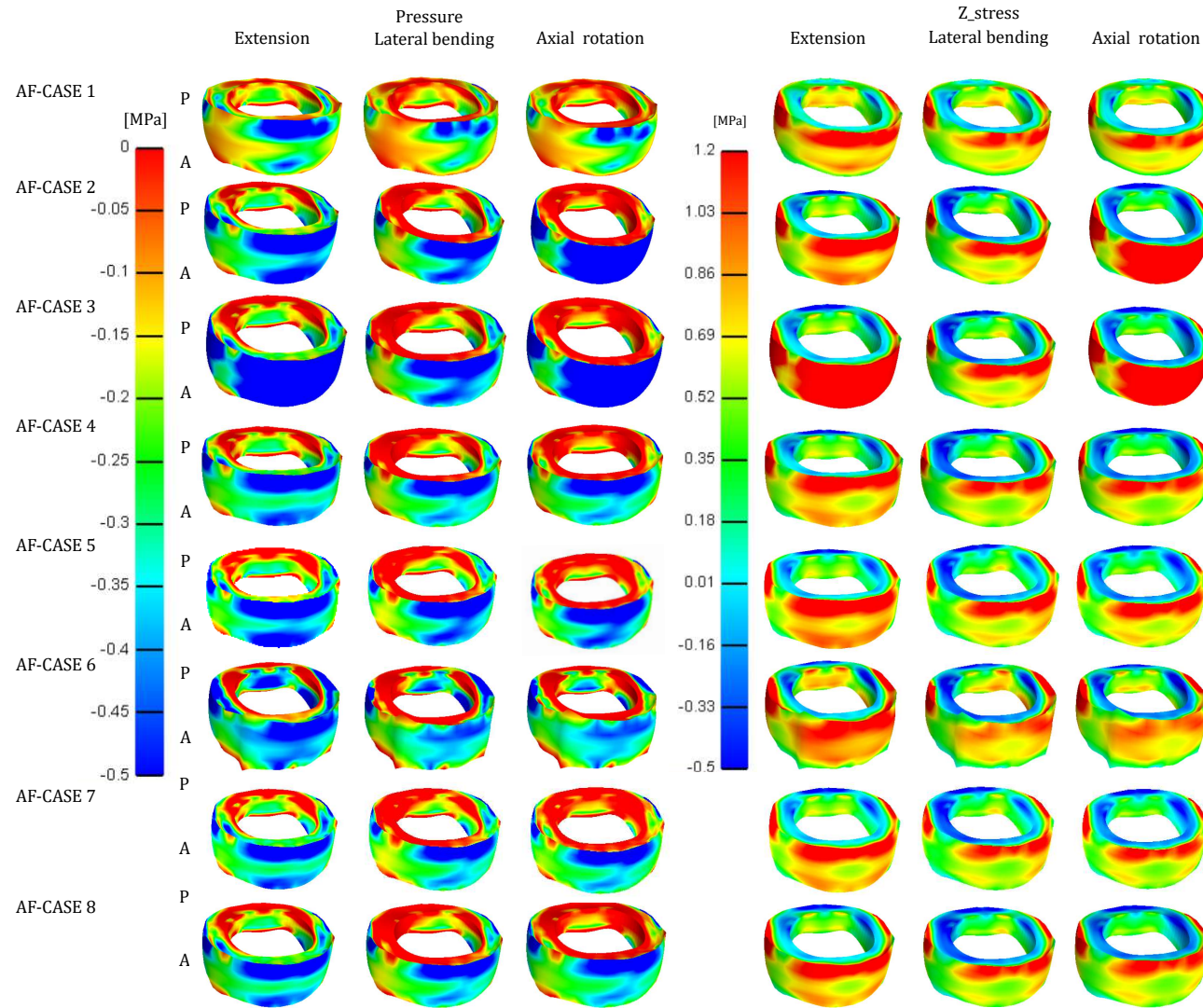
Figure 6.17: Stress in the vertical direction and pressure distributions for the cases listed in table 6.4. The letters A and P correspond to Anterior and Posterior.

Sensitivity: on varying the CEP

The displacements over the two cross-sections were reported in Figure 6.18. In correspondence of the highest Young's modulus (CEP-Case 2), the axial displacement on the two cross-sections has a mean value around 1.4 mm in correspondence of the NP, while in CEP-Case 1 it was around 1.23 mm.

In Figure 6.19 the pressure and stress distribution are displayed and the
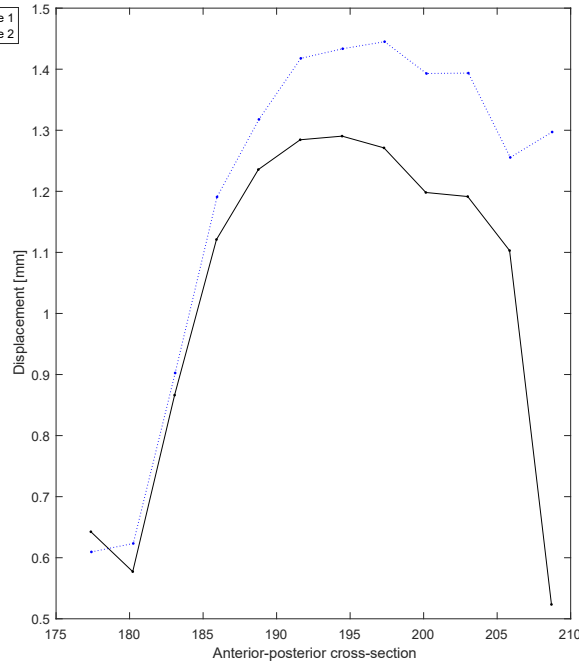
Figure 6.18: Displacements on varying the CEP material properties

mean values on the AF and NP are reported in the histogram in Figure 6.20. It is particularly evident that in CEP-Case 2, the NP is subjected to a higher pressure (-0.39 MPa) than in the CEP-case 1 (-0.29 MPa). The pressure and stress distributions following the application of moments about all the three axes, are displayed in Figure 6.22. From this figure, it can be observed that there is higher stress and pressure on both the AF external layer and NP under all the loading conditions. The mean IDP in the volume selected in the NP is shown in Figure 6.21.

Sensitivity: on varying the NP

The displacement on the AP cross-section is shown in Figure 6.23. Both cases 1 and 2, were evaluated with Neo-Hookean material properties. Higher displacements are shown for the NP region with a low Young's modulus. This behaviour is confirmed by a higher pressure on the NP-Case 1 as shown
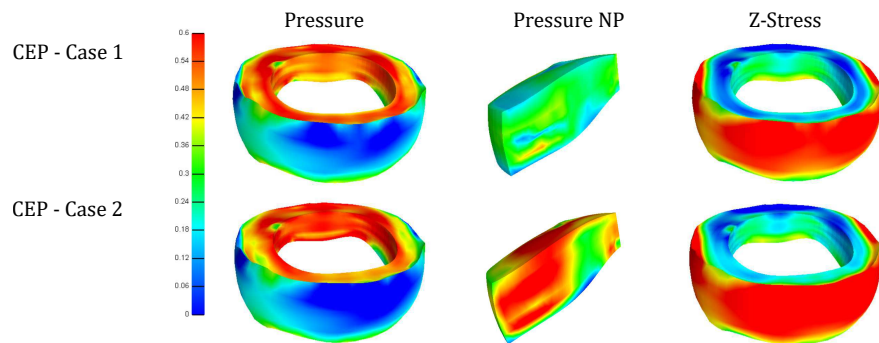
Figure 6.19: Pressure and stress distribution on the AF and NP on varying the CEP material properties
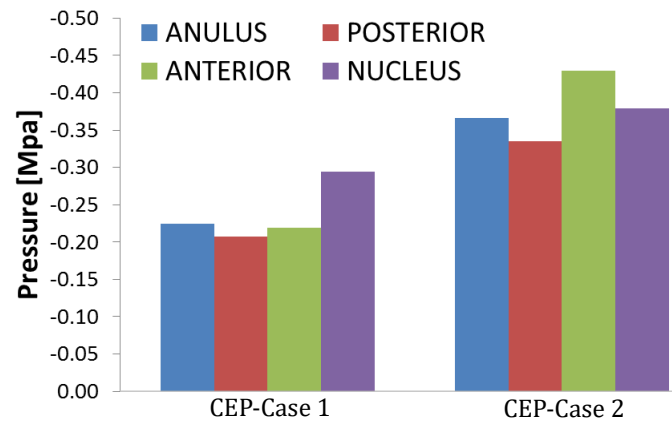
Figure 6.20: Pressure on the IVD varying the CEP material properties
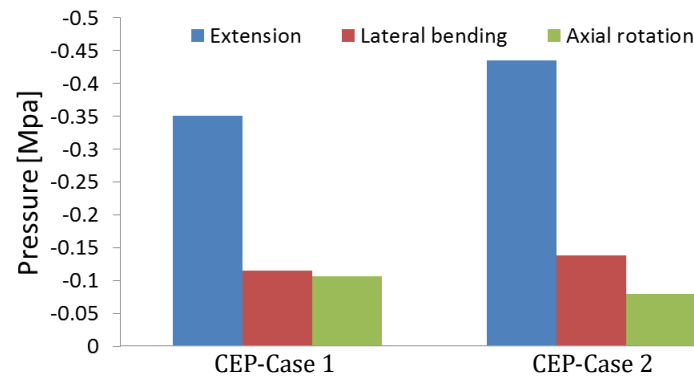
Figure 6.21: Pressure on the NP varying the CEP material properties in extension, lateral bending and axial rotation.
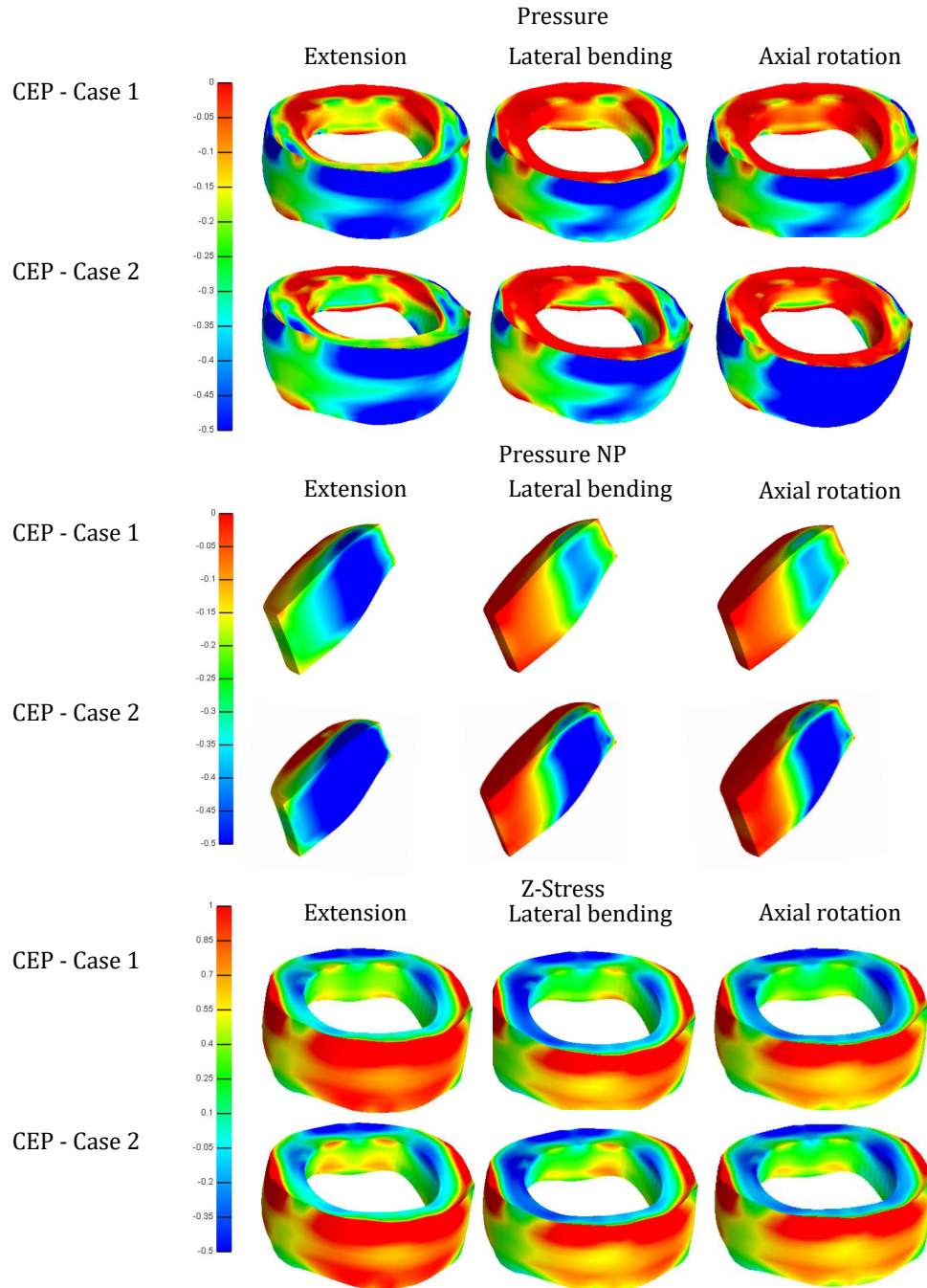
Figure 6.22: Pressure and stress distributions on the NP and AF when extension, lateral bending and axial rotation are applied.

in Figure 6.24. However, in NP-Case 1, higher pressure is reported in the posterior side of the AF (Figure 6.24). In NP-Case 3, stress and pressure have inferior values than the previous cases, but the displacement are comparable with those of the NP-Case 2.
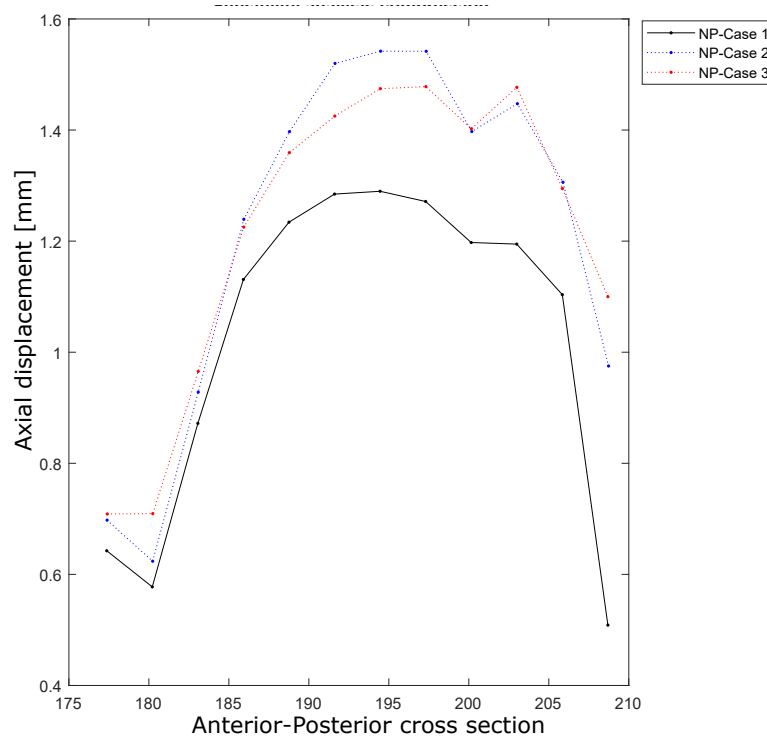
Figure 6.23: Displacement on the Anterior-Posterior cross-section.
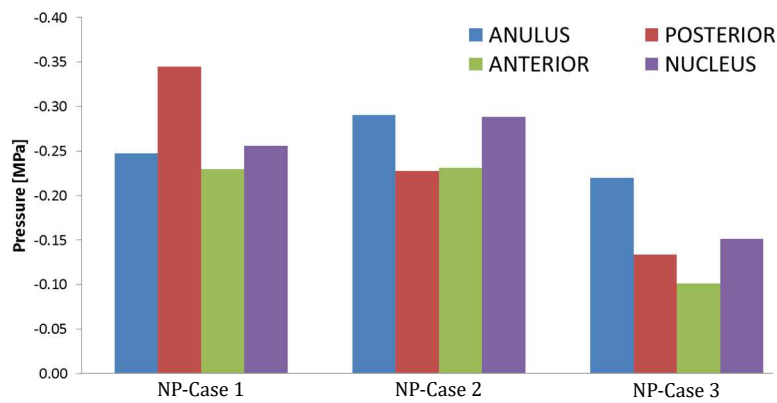
Figure 6.24: Pressure on the whole AF and the selected volumes, and on the NP internal volume.
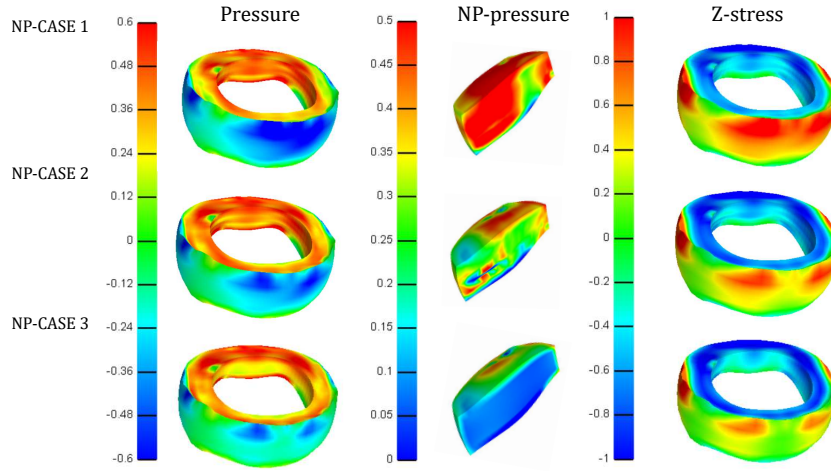
Figure 6.25: Pressure and stress distribution on the AF and VP.

6.4 Discussion

This chapter has identified the material and morphological parameters which influence the biomechanics of the spine the most. Considering the numerous variables involved in the anatomy of the spine, singular variations have been evaluated, to identify the most influential parameters and implement further studies in the future with statistical methods (i.e.: Taguchi, Monte Carlo). In this study the functionalities of the LMG toolbox have been demonstrated, showing the possible combinations that can be implemented and the further improvements required to develop more accurate models. To develop a toolbox which can be used in clinics, all these aspects have to be taken into account and validated with subject-specific datasets. The sensitivity analyses performed in this chapter, focused on determining the effects of each parameter varied. The most influential parameters which affect the stress distributions and the range of motion of the lumbar spine, are:

- the volumetric ratio in the IVD affects the axial displacements and IDP and stress distribution. However, further studies are required to combine morphological and material properties effects.

- The constitutive law assigned to the AF ground substance and how the material properties are assigned. In compression, Mooney Rivlin and Neo-Hookean material properties showed the highest and lowest axial displacement, respectively.

- The fiber stiffness and orientations and their distribution on the AF affect the IDP and stress distribution when moments are applied.

- High Young's modulus of the CEP causes an increase of the axial displacement and IDP in the NP;

- Low Young's modulus of the NP caused an increase of the axial displacement and IDP in the NP. Moreover, assigning a hyperelastic formulation the IDP showed a more even distribution in the NP.

The physical meaning of these parameters have been described previously (section 6.1), and the effects of each variation are discussed further below. The results on the sensitivity analyses on varying the VP showed that having thicker (60% VP) or thinner (30%) AF influences the FE biomechanics, where a thinner annulus corresponds to a healthy situation, and a thicker AF corresponds to a degenerated disc [273, 292, 293]. Degenerated models are characterized by less mobility, due to a limited NP volume, which allows the movements of the FU and the spine, with high Young's modulus and decreasing the Poisson's ratio [294, 90, 155]. The results obtained confirmed these findings, in fact higher displacements were measured for thin AF. In the case of these simulations, the findings were due to the increased volume of AF with stiffer material properties than the NP. In previous studies [155, 90], the degenerated conditions have been simulated reducing the disc heights of 20%, 40% and 60% respectively obtaining mildly, moderated and highly degenerated disc and varying the compressibility of the NP from 0.0005 mm^2/N to 0.15 mm^2/N, where the stiffer material properties corresponds to the degenerated NP. It has been assumed that the AF material properties remained unvaried [295], even though the lamellae become irregular with the fibers disorganized [52]. In previous studies [50, 286, 296], a variation of the material properties has been considered, with more compliant material properties and different disc heights in the degenerated condition. These two factors would result in an increasing stress and pressure distribution on the AF, which could lead to posterior bulging. In the current study, the effects of each factor have been explored, and further investigations are required to evaluate their joint effects on the biomechanics of the spine. In future studies, degenerated conditions would be simulated assigning, along with VP variations, different material properties to the NP, as well as varying the height of the disc. Moreover, degenerated conditions in the fiber distributions can be simulated, varying their orientation according to the region or varying the density of fibers.
The IDP decreased with an increasing VP, in agreement with experimental studies [273, 278, 293]. Moreover, the results obtained are in the range of the computational and experimental results reported by Dreischarf et al. [165], as also shown in chapter 5, where a VP of 46 % has been evaluated. The results in compression on varying the material properties of the AF, showed notable differences on varying the constitutive law of the ground substance and on varying the way of assigning the material properties to the AF.
The effect of varying the fiber orientations is more evident applying the pure
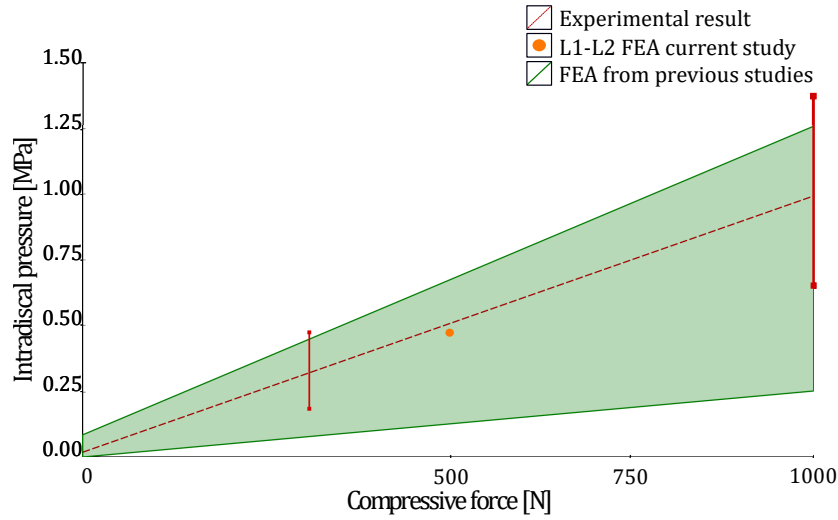
Figure 6.26: The IDP at VP = 46% was compared with previous FE results and experimental results. The red bars identify the standard deviation of the experimental study [165].

moments. The model with fibers uniformly oriented with high angles (± 46 °, AF-Case 3) showed higher IDP values than the one at ± 30 ° (AF-Case 2). The stiffness of the fibers plays another important role, in fact in the model with low stiffness (AF-Case 5) the IDP was less than in the one with stiffness varied at each layer (AF-Case 4). Another difference is shown when the fiber orientations are varied on each layer with a constant strength all over the AF layers (AF-Case 7) or varying the strength at each layer (AF-Case 8), which results in a lower IDP in the second case, due to a more deformable structure around the IVD.

Experimental studies have demonstrated the differences on the fiber orientations and strength at each layer of the AF [297, 298, 299], and this study has highlighted the effects on the biomechanics and on the simulation results of these variations.

In literature, the NP has been modelled mainly with fluid-elements [90, 134, 154, 131, 142] which are characterized by hydrostatic pressure, not varying with the direction or location inside the NP. However, other studies have implemented it with solid elements, applying linear elastic or hyperelastic material properties [300, 238, 140]. In the former, the IDP is usually evaluated in an inner volume of the NP, but it is not stated where this volume is taken and if there is a variation with the surrounding areas. In this study, several volumes have been evaluated (anterior, central, left-lateral, right-lateral and posterior regions). The results of the mean value of the IDP showed a high standard deviation, due to the distribution of the pressure. This finding depends on the elements used as well as the loading conditions

and particularly the morphology of the vertebrae. In many studies this morphology is highly simplified, not taking into account the concavity of the vertebral endplates. The contact surfaces are not plane (Figure 6.27), further, varying the VP reducing the AF, which plays a structural role, influence the load distributions and the pressure distribution inside the NP.
Varying the CEP material properties affect the pressure on the NP. In par-
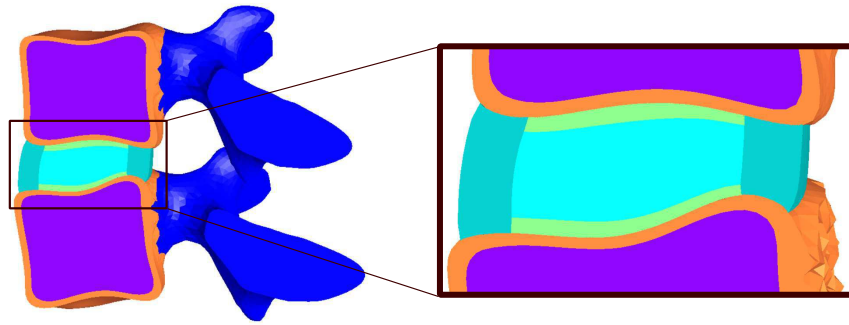
Figure 6.27: Morphometry of the bone endplates in contact with the IVD with an overview on the contact surfaces.

ticular, stiffer CEP material properties resulted in an increased IDP. The evaluation of a model with a higher Young's modulus for the CEP corresponds to a material with a low water content, thus, degenerated. Therefore, it would result in a higher pressure on the NP [49]. In this model, linear elastic material properties were assigned to the CEP, omitting their viscoelastic and porous characteristic which could affect the biomechanics of the spine [290, 301].

Previous studies have evaluated the effect of several material properties of the AF. Such studies have varied the material formulations or evaluated the effects of changing the incompressibility of the AF [290, 98, 87], which could affect the sensitivity of the AF fibers [107, 302]. As stated by Zander et al. [13], the sensitivity to morphological parameters has not been evaluated yet. The main reason is the mesh convergence and the pre-processing of several models which is time consuming. The LMG toolbox is able to provide a population of models where the material properties and morphological parameters can be varied and a mesh convergence directly run, avoiding time-consuming actions around setting up multiple independent models.

6.4.1 Limitations and Future Work

In this study, a simplified functional model of the lumbar spine has been evaluated. The ligaments and the facet joints cartilagineus surfaces have not been modelled, reducing the range of validity of this model. However,

this study evaluated the effects on the spine biomechanics of varying each material property and the morphological features of the IVD individually. The aforementioned soft tissues have not been implemented to reduce the complexity of the results, nonetheless, this provides limitations for the evaluation of the range of motion. These anatomical structures can be included in further studies, in order to obtain a more complete evaluation of the effects on the biomechanics. However, the current study has reported an evaluation which is not addressed in depth in literature, unlike the ligaments and soft tissues material properties [87, 13]. In fact, this is the first study where the effect of volume percentage variations have been investigated.

In the evaluated models, the NP occupied the same relative position with the AF, but it has been shown that it is slightly displaced in the posterior side than the central area [292], with a resulting thinner posterior AF. This factor would be useful to investigate and include in degenerated models. In future studies the NP position would be varied to evaluate the effects on the stress distribution on the AF, then evaluating the correspondent bulging which in the posterior side is one of the causes of back pain.

Pure moments have been applied as prescribed displacements in this study, by applying the range of motions calculated in previous studies. Usually, the range of motion is one of the outputs from FE analysis of the spine, which is also used for the validation with experimental results. However, in this study the range of motion has been applied as prescribed displacement; thus, it could not be considered as an output of the model. In future studies, pure moments would be applied as described in chapter 5 to evaluate how the range of motion is affected by variation in material properties.

Further future developements include making material properties available in the LMG toolbox, to evaluate time-dependent effects such as viscoelastic and biphasic properties assigned to CEP, NP and AF. It would increase the toolbox functionality, covering a wider range of effects to evaluate, and investigate the time-dependent effects on loading the spine biomechanics [137], obtaining a more accurate model for the evaluation of the biomechanics. However, the geometry obtained from the LMG toolbox represents an average geometry of the spine, which can not take in consideration the subject-specific anatomical details. Then, the evaluation of pathological cases affecting the anatomy of the vertebrae and eventual anatomical deformity need further studies. This is the first application of the LMG toolbox and static analyses have been performed, comparing them with previous studies and place this model at the state of the art level. Further studies would investigate combinations of material properties and loading conditions to explore new frontiers.

Statistical, more structured studies with a high number of models to evaluate cross-variations between the parameters identified in this study (ie. morphological features along with degenerated material properties) are needed. Future work would focus in the generation of an accessory GUI where the

level of degeneration can be chosen, evaluating a combination of the previous conditions. For example, assigning a grade of degeneration (0 to 5), the height and VP of the IVD would be automatically setup and the material properties of the AF, NP and CEP assigned according to the range found in the literature Figure 6.28.
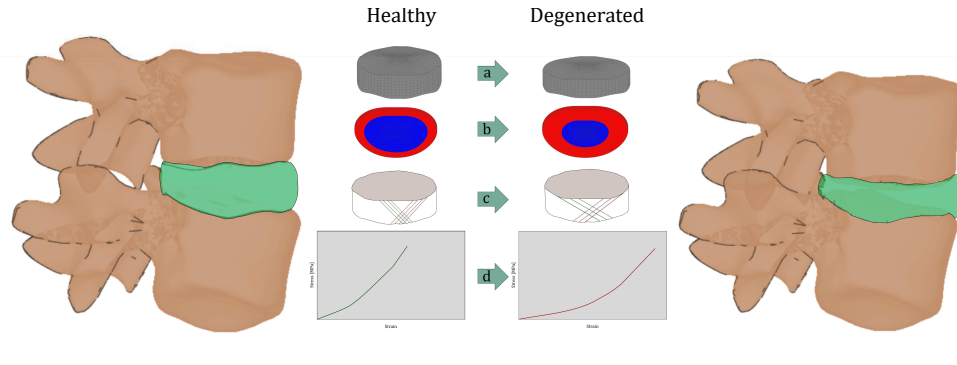
Figure 6.28: The degeneration level can be chosen varying: a. IVD height, b. volumetric ratio, c. fiber orientations, d. AF, NP and CEP material properties.

6.5 Conclusion

The IVD volumetric percentage and the material properties of its structures (NP, AF, CEP) affect the biomechanics of the FSU. All these parameters resulted in having important effects on the range of motion, in terms of axial displacements, and stress and pressure distribution. The VP and the constitutive law assigned to the AF ground substance, NP and CEP affect the IDP and axial displacement, while the effect of fiber stiffness and orientation are more evident when moments are applied. These properties are connected with subject-specific pathological conditions which should be considered and implemented in the evaluation of the biomechanics and evaluated according with the purpose of the study (e.g. evaluate the effects of fiber orientation when bending moments are applied).

The variation of material and morphometric parameters have focused on a healthy range of values (low VP, low NP and CEP material properties and AF with compliant fibers) and degenerated conditions (high VP, high NP and CEP material conditions and stiffer fibers in the AF). Mapping the effect of each parameter of the IVD, would lead to the estimation of the unknown material properties between healthy and degenerated conditions. An exhaustive description of the IVD material properties, and the development, in the LMG toolbox, of a dedicated subroutine to implement the

variety of anatomical and possible pathological conditions, would be beneficial in the optimization of new implants and their assessment over a range of pathological states.

Chapter 7

Dynamic posterior stabilization device: Finite Element Modelling, validation and application

7.1 Introduction

Fusion is the current gold standard, for pain related discopathy. However, several studies have asserted that fusion, due to load-bearing effects, induces the degeneration of the adjacent level intervertebral discs [6, 7, 8]. Moreover, the fusion system, fixes two adjacent vertebrae, which reduces the range of motion of the spine (chapter 2, section 2.3).

Many studies have focused on the development of new devices to overcome the disadvantages of fusion. One possible alternative is represented by dynamic stabilization devices, previously described in Chapter 2,section 2.3. Posterior stabilization devices (PSD) are designed to enable some form of motion, unlike fusion. There is some initial evidence that PSDs also reduce and better distribute the stresses on the IVD and preserve the inter-segmental range of motion [303, 304, 305]. In between this category of devices, this study focused on the BDyn, a bilateral pedicle screw device, developed by $S14$ $Implants$ (Pessac, Bordeaux).

The BDyn is a dynamic device, where a mobile rod has a relative motion with respect to the other components; two elastomer components allow higher displacements, than the titanium rod, due to their greater compliance. The BDyn device was designed to treat back pain diseases (further described in chapter 2); however, its design and the elastomer components, are well suited to be used in combination with other devices. For instance, it is expected that the BDyn device would improve the range of motion, and give more flexibility to implants. One possible application, in the spinal

surgery, would be the combination with a GsDyn device. This is a growing-rod device designed for the Early On-set Scoliosis in paediatric patients. Currently, treating severe cases of scoliosis in paediatric patients is challenging, since the devices must be used during the growth of the patients. The target is improved quality of life through minimally invasive surgery. Moreover, two issues have been reported in the growing-rod devices on the market: wear and breakage [306, 307, 308].

The performance evaluation of the BDyn was required to understand how it affects the behaviour of the Functional Spinal Unit (FSU). The studies performed on the BDyn so far, included experimental tests on the device [254] and *in-vitro* studies with cadaveric spines [309] with *ex-vivo* studies under way on devices ex-planted from patients [310]. However, these studies do not allow the evaluation of the effects on the biomechanics of the spine with distinct pathological conditions or anatomical features. Finite Element analyses could be implemented to evaluate the different setups, varying the anatomy and studying the worst loading condition scenarios, as a direct application of the LMG toolbox chapter 4. FE models would enable assessment of its mechanical behaviour which could not be undertaken *in vivo*. The results of such analyses can be directly used for the optimization of the design and material properties that could lead to the development of improved devices, as well as assessing stress distribution following use of the BDyn device.

The aim of this chapter was to develop a dynamic FE model of the BDyn which could be applied to a range of future studies on the performance of the device, and on its influence on an FSU. Dynamic simulations have been compared with experimental tests, with FE model predictions further compared, qualitatively, with deformations of *ex-vivo* devices. A preliminary evaluation of the mechanics of the combined device, BDyn and GsDyn, has been carried out, assessing whether there would be any potential benefits in combining the BDyn device with this scoliotic device (GsDyn).

In this chapter, the development of a BDyn Finite Element (FE) model, along with validation with dynamic data, is presented (Figure 7.1). Two separate mechanical tests were carried out; a compression test (subsection 7.3.1) and Dynamic Mechanical Analysis (DMA) (Figure 7.3.1), performed as part of a separate study [311]. The results from the first set of tests were used to obtain the constitutive laws describing the mechanical behaviour of the elastomeric components. Subsequently, FEA was performed using Abaqus (Abaqus CAE/Implicit, version 6.14, Dassault Systmes, Providence, RI, USA) with the same DMA boundary conditions subsection 7.3.2. The ensuing results were compared with experimental data from the second set of tests to validate the FE model. The evaluation of the BDyn through the experimental DMA and the dynamic FE analysis, is essential due to its dynamic features and applications in the human body.

A qualitative comparison of the plastic deformation on the explanted de-
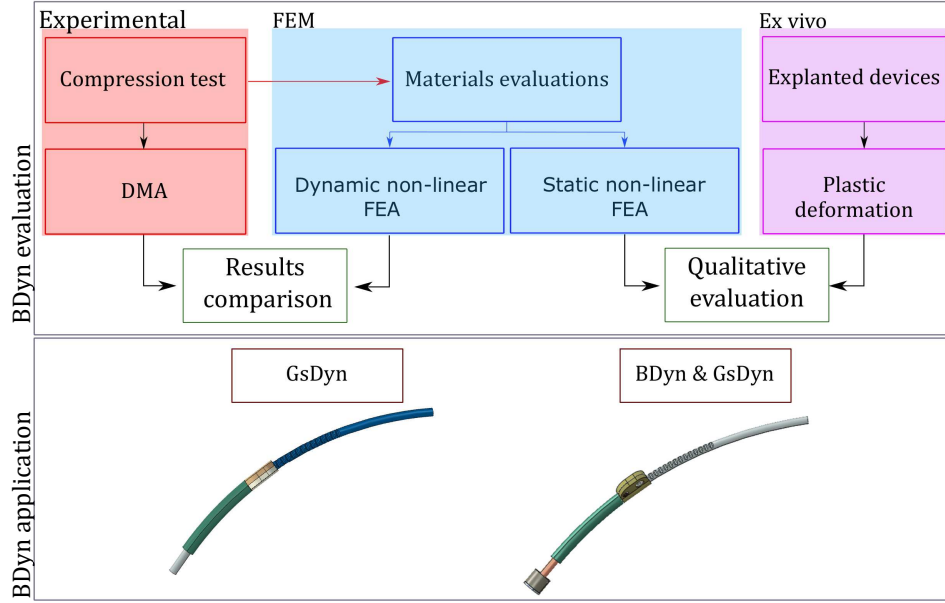
Figure 7.1: Outline of this chapter. Two separate experimental tests were performed. The results of the compression test was used to evaluate the material properties of the BDyn components. Then a dynamic non-linear analysis was simulate in the FE software, applying the same boundary and loading conditions, and the results were compared with the experimental ones. The deformations obtained from static analyses were compared with the plastic deformations found on explanted devices. An application of the BDyn has been evaluated coupling the device with the GsDyn, a device to treat the scoliosis.

vices and the deformation on the FE models has been performed. Static FE simulations have been performed, applying compressive and tensile loading conditions. The results have been compared qualitatively to ex-planted BDyn devices evaluated as part of a separate study [310]. Those devices were removed due to clinical complications/failure of the implants, and presented plastic deformation of the elastomer components.

In this study, an initial evaluation of the effects of the combined use of BDyn and GsDyn was performed in section 7.5. Two FE models have been developed and analysed: the GsDyn as single device, and a combined BDyn-GsDyn device. The FE analyses have been performed to understand the differences in terms of range of motion and stress distributions, and to evaluate the effect of the elastomer components in the device.

7.2 BDyn device

The BDyn, a posterior stabilization device (PSD) developed by S14 Implants (Pessac, France), was designed to reduce the intradiscal pressure and the loading on the facet joints. This device also allows the relative motion between the components and the preservation of the intersegmental range of motion. The BDyn device is inserted bilaterally, on both the sides of the vertebrae, on one spinal unit, which consist of two vertebrae and an intervertebral disc, or on multiple levels. The BDyn is attached to the vertebrae through two titanium alloy (Ti6Al4V) pedicle screws, which are connected to the mobile rod and a fixed rod (as shown in Figure 7.2). Two elastomeric components are embedded in the BDyn, silicone MED-4770 and Thermoplastic Polycarbonate Polyurethane (PCU) DSM Biomedical Bionate 80A PCU.
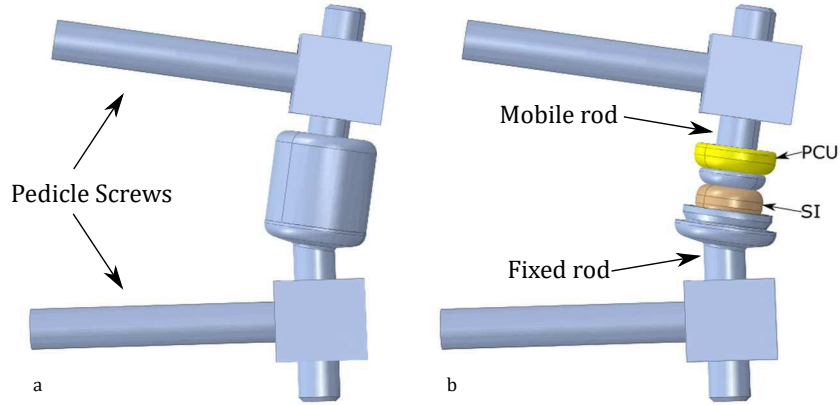
Figure 7.2: a. Overview of the BDyn device; b. the titanium cover has been hidden and the internal elastomer components are visible.

7.3 BDyn: material properties and Finite Element Models

The development of the FE model of the BDyn device required the evaluation of the material formulation of its elastomer components, starting from the results of experimental tests. The model was then validated against independent experimental data. The mechanical tests used in this study have been performed by a collaborator and described elsewhere [254, 311]. This section is divided as follows:

1. Experimental test (subsection 7.3.1)

   - Compression tests on the elastomers (subsection 7.3.1);

- Dynamic Mechanical Analysis on the BDyn (Figure 7.3.1).

2. Computational modelling (subsection 7.3.2)

   - evaluation of the material formulations to characterize the elastomer components (subsection 7.3.2);

   - FE dynamic analyses and validation of the BDyn device (Figure 7.3.2);

   - FE static analyses and qualitative comparison with *ex-vivo* devices (Figure 7.3.2).

7.3.1 Experimental tests on the BDyn

The experimental tests were performed by Lawless and described in detail elsewhere [254]. These tests have been used to evaluate the material properties for the FE model and to validate their results, and for this reason, a brief outline, only, of the mechanical setup is presented.

Compression test

Three BDyn single level devices were supplied by S14 Implants (Pessac, France). The devices were tested using a MTS Landmark Servo-Hydraulic Test System with FlexTest 40 Station Manager Version 5.3B software (MTS Corp., MN, USA). A custom procedure was developed with the MTS Multi-Purpose Testware (MPT) to perform compressive and tensile loadings. The devices were clamped in the machine through MTS 647 hydraulic wedge grips and MTS 647.02B jaws to fix the moveable and fixed rods (Figure 7.3). The tests were performed in air, at room temperature, and the following steps were implemented in the custom routine:

- a compressive ramp load until -1250 N was applied at a displacement rate of 0.02 mm/s;

- the actuator was moved to -1 mm at a rate of 0.5 mm/s;

- a tension ramp load until 1750 N at a displacement rate of 0.02 mm/s was applied;

- the actuator was repositioned to 0 mm at 0.5 mm/s, ending the test.

The data available of these tests regarded only the loading phases of the two elastomers, and no data were obtained during the unloading phases.

Figure 7.3: BDyn experimental test setup in the MTS Landmark Servo-Hydraulic Test System. The fixed and mobile rods were clamped through custom-designed grips.

Dynamic Mechanical Analysis (DMA)

A Bose ElectroForce 3200 testing machine, running BoseWinTest4.1 DMA software (Bose Corporation,Electroforce Systems Group,Minnesota,USA) was used to estimate the viscoelastic properties of the BDyn. This method has been used extensively in literature to evaluate the mechanical behaviour of biological tissues and polymers [312, 313, 314].
Customized grips were used to clamp the mobile and fixed rods of the BDyn device as shown in (Figure 7.4) and were used to load the device axially. Six BDyn devices were tested with the following procedure: sinusoidal loads, with an amplitude of 20 N for twenty frequencies (from 0.01 Hz to 30 Hz), were applied to the mobile rod. The range of load chosen, allowed the evaluation of the two elastomers, performing both tension and compression tests. The experimental test was performed with a temperature controlled chamber, to keep the device at body temperature (37 °C). Further information regarding the experimental tests are available in Lawless et al. [254].

7.3.2   Computational modelling

Materials evaluation

The evaluation of the material properties to use in the FE model, were obtained using the material evaluation tool in Abaqus. This tool determines the coefficients for a given material definition from the stress-strain curves obtained from the following mechanical testing: uniaxial, equibiaxial, planar and volumetric compression test (Abaqus 6.14 Documentation, Dassault Systémes, Providence, RI, USA). In this study, the evaluation was based on the uniaxial compression test only, obtaining an initial estimation of the material properties valid only under these loading conditions. In the case of defining the hyperelastic behaviour of a viscoelastic material, further information is required to define the strain-rate dependent behaviour and the loading-unloading characteristics. If the loading-unloading data are not fully provided, in Abaqus a linear behaviour is followed in the unloading

Figure 7.4: BDyn DMA experimental test setup. The fixed and mobile rods were clamped through custom-designed grips.

phase (Figure 7.5). In this study, only the data of the loading phases (PCU
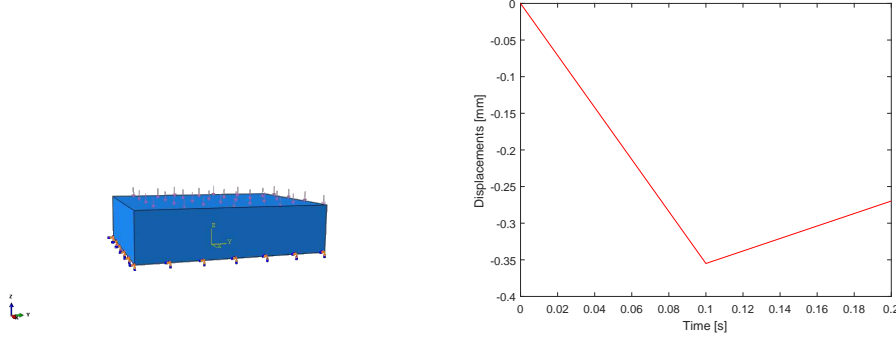
Figure 7.5: Example of a loading-unloading simulation of a hyperelastic material, where the unloading behaviour of the material is not defined. The displacement in the loading and unloading phases followed a different slope.

and silicone) were available. The stress and strain curves obtained from the compression tests were used to evaluate the constitutive laws which best simulate the material properties of the PCU and silicone in each loading phase. Two assumptions were made: (i) the materials were not strain-rate dependent (time-dependent effects were not implemented), (ii) the materials were incompressible. Thus, the viscoelastic material properties were ignored and volumetric changes neglected.

The material evaluation tool of Abaqus has been used only to obtain an

initial evaluation, for polynomial, Mooney-Rivlin and Neo-Hookean descriptions for the silicone and Neo-Hookean and Mooney-Rivlin for the PCU. Once the best material model was identified from this initial evaluation, an optimization subroutine was implemented to better define the coefficients of the best fitting constitutive laws.

The material characterisation was performed using a simple geometric model: a cube of unit height and the same boundary conditions as the compression test (subsection 7.3.1) were simulated: the lower surface was fully constrained and a ramp load, with the same maximum load of the experimental test, was applied on the upper surface. The coefficients used for the polyno-
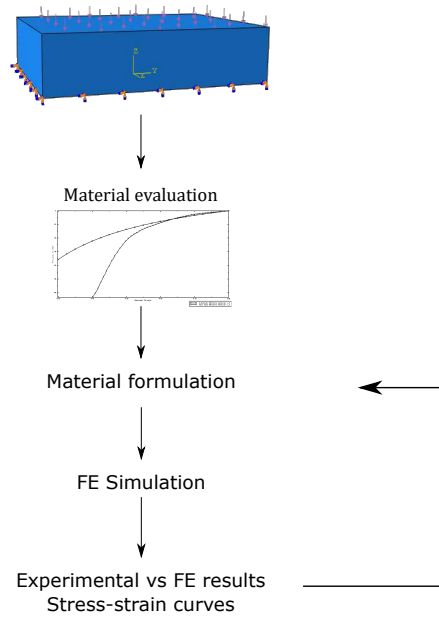
Figure 7.6: *Calibration workflow. In the first material evaluation, performed in Abaqus, the constitutive laws have been selected, then the parameters have been varied and the simulations performed again until the stress-strain curves from the experimental test and simulations reached a good fit (evaluated through the R^2).*

mial, Neo-Hookean and Mooney-Rivlin hyperelastic constitutive laws were iteratively changed in between the ranges reported in Table 7.1 and the stress-strain curves obtained from the FE analysis are shown in Figure 7.7 and Figure 7.8. The implemented optimization sub-routine to evaluate the material properties which obtained the best fit stress-strain curve to the experimental data is shown in Figure 7.6.

The stress-strain curves obtained from the FEA are shown in Figure 7.9a and Figure 7.9b and the constitutive laws were chosen according to the R^2 with the experimental stress-strain curves. Mooney-Rivlin ($R^2 = 0.998$) and

polynomial ($R^2 = 0.997$) constitutive law were chosen respectively for the PCU and silicone and the coefficients are reported in Table 7.2.

Table 7.1: Ranges of values evaluated for the coefficients of the constitutive laws.

Component	Constitutive law	Coefficient	Range
PCU	Mooney-Rivlin	C10	0.7 - 4
	Neo-Hookean	C10	0.5 - 8
Silicone	Mooney-Rivlin	C10	1 - 6
	Neo-Hookean	C10	0.5 - 9
		C10	0.1 - 6
	Polynomial	C11	0-1
		C20	0-2
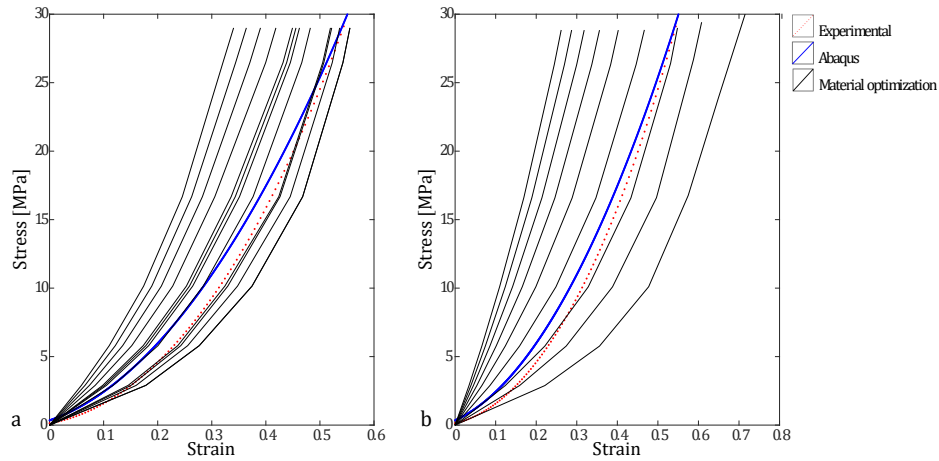
Figure 7.7: PCU material properties evaluations: a. Mooney-Rivlin, b. Neo-Hookean.

Table 7.2: Material properties of the BDyn components.

Component	Constitutive law	Coefficients
Titanium	Linear Elastic	$E = 105$ GPa, $\nu = 0.3$
PCU	Mooney-Rivlin	$C10 = 1, C01 = 0.6030, D1 = 0$
Sil	2nd order Polynomial	$C10 = 3, C01 = 1, C11 = 1,$ $C02 = 0, C20 = 2, D1 = D2 = 0$
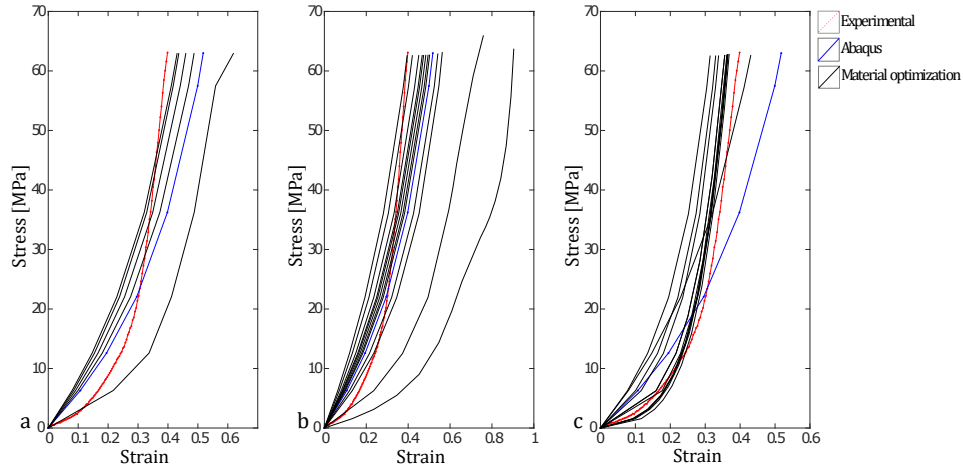
Figure 7.8: Silicone material properties evaluations: a. Mooney-Rivlin, b. Neo-Hookean, c. Polynomial.

BDyn FE model

The FE model, based on the CAD file supplied by S14 Implants, was pre-processed in Abaqus. The material properties identified, following the procedure described in subsection 7.3.2, were assigned to the elastomer components, and the complete material properties are listed in Table 7.2. Furthermore, the density was assigned to each material (Titanium 4.43 g/cm^3, PCU 1.19 g/cm^3, silicone $1.10g/cm^3$), according to their datasheets.

To reduce the computational time of the simulation, and in agreement with the experimental setup, a simplified geometry of the BDyn was used. The fixed titanium rod, which was fully constrained in the mechanical test, was removed from the geometry in the FE model (Figure 7.10). Hexahedral elements were used to mesh each component of the device. The mesh size of the components were evaluated through a convergence test, where each component was evaluated applying loads accordingly to the loading conditions of the simulation. The model with mesh density which showed a difference on the stress within the 5%, with the finer model, was chosen for each component. Mesh sizes were optimised for each individual component to reduce the computational time. The meshed device is shown in Figure 7.11. A total of 60042 hexahedral elements have been used to mesh the model and the number of elements for each component are listed in Table 7.3.

Surface-to-surface frictionless contacts were defined between the surfaces, enabling only normal movements between the components and, therefore, tangential sliding was neglected. In the normal direction, separation between the PCU and silicone from the mobile rod was enabled through a dedicated
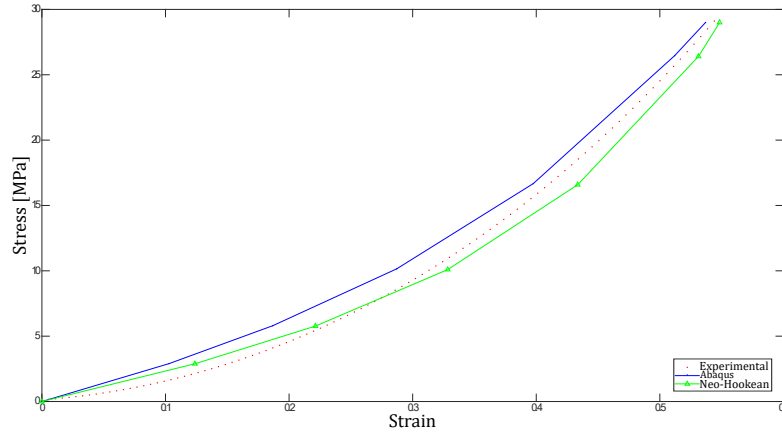
(a) PCU
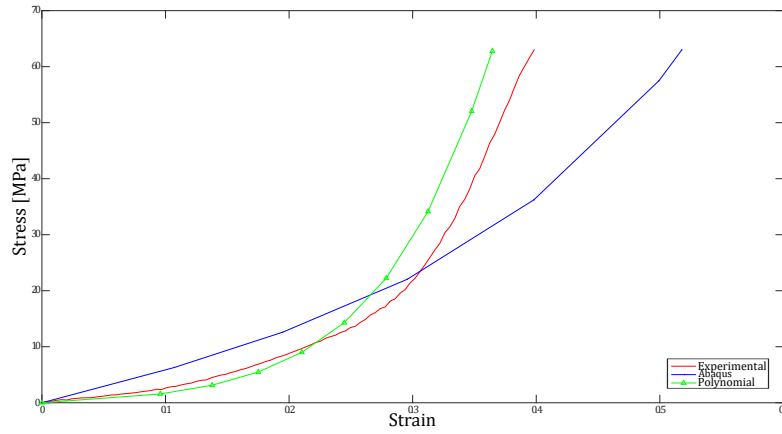
(b) Silicone

Figure 7.9: Material evaluation of the PCU (Figure 7.9a) and silicone (Figure 7.9b). The stress-strain curves obtained from the experimental test (in red), the Abaqus evaluation tool (in blue) and the material optimization (green) sub-routine are shown.

option in Abaqus to emulate the real conditions.

BDyn dynamic FE analysis

The inferior surface of the device was fully constrained and a sinusoidal distributed force varying between 20 N and -20 N, was applied at six frequencies (1, 3, 5, 10, 15 and 20 Hz) corresponding to the range of vibration of the human body [315, 316], to the upper surface of the mobile titanium
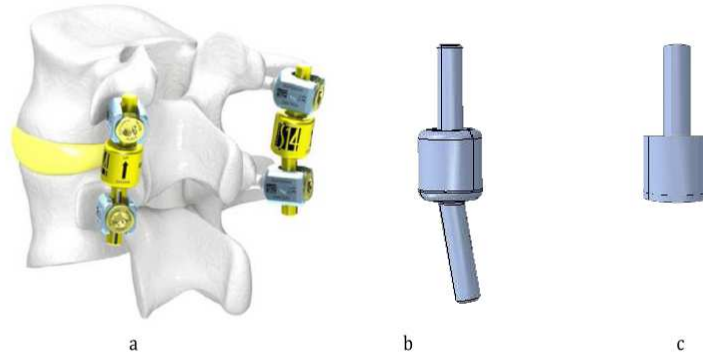
Figure 7.10: a. BDyn original geometry, including the screw to connect to the FSU; b. BDyn geometry used in the experimental study; c. simplified geometry of the BDyn. The inferior rod, of the BDyn is fixed in the mechanical test and it has been removed in the FE model to reduce the computational time, as well as some design details such as external fillets.

Table 7.3: Number of elements and mesh size of the BDyn components.

Component	Number of elements	Mesh size [mm]
Mobile rod	13488	0.28
Base	11516	0.28
Cover	1976	0.8
Silicone	23000	0.2
PCU	10062	0.28
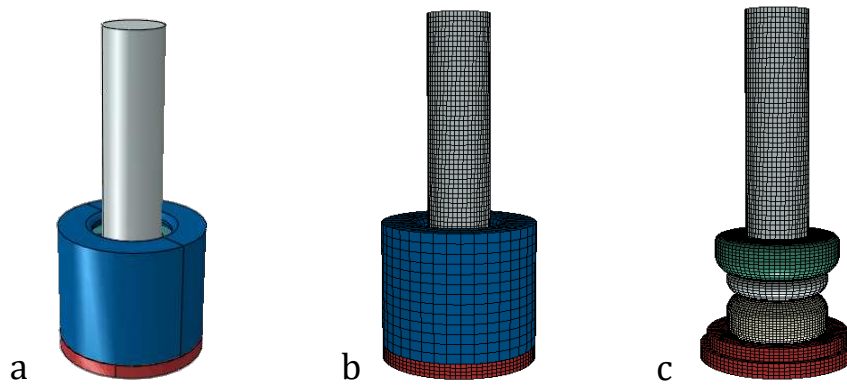
Figure 7.11: a. BDyn model simplified, b. model meshed, c. model meshed with the titanium cover removed.

rod.

Implicit dynamic simulations were run in Abaqus, with the time-step varying per frequency. Small time-steps were required for high frequencies to sample the displacement results, obtaining the same resolution of displacement data per loading cycle. The displacement of the device were measured from the upper surface of the mobile rod and compared with those obtained from the DMA tests on six specimens.

BDyn static FE analysis

A static analysis was performed to evaluate the effect of high loading conditions in compression and tension. The same boundary conditions of Figure 7.3.2 were applied, fully constraining the inferior surface. Distributed compressive and tensile loads, corresponding to applying pressure of 1 MPa, 10 MPa and 15 MPa have been applied on the upper surface of the mobile rod. These results have been used to qualitatively evaluate the deformation effects on the materials and compare the results with those of the explanted devices.

7.4 BDyn FEA outcomes

The material properties of the elastomer components of the BDyn device were evaluated in subsection 7.3.2. Mooney-Rivlin and 2nd order polynomial formulations were chosen for PCU and Sil respectively. The material coefficients have been evaluated and selected according with the best R^2, which in both cases were around 0.99.

The displacements of the upper nodes of the mobile rod were evaluated and reported in Figure 7.12, where either the single curves and the average mean values were shown. The differences peak to peak, represented in Figure 7.13, were evaluated as in Equation 7.1 and Equation 7.2:

$$diff_{min} = \frac{(min_{FEA} - min_{EXP})}{min_{FEA}} \tag{7.1}$$

$$diff_{max} = \frac{(max_{FEA} - max_{EXP})}{max_{FEA}} \tag{7.2}$$

where min_{FEA}, max_{FEA} and min_{EXP} and max_{EXP} are the average peak values on the FEA results and on the experimental data, respectively. The percentage differences are listed in Table 7.4. A decreasing trend has been shown on the percentage differences with increasing frequency. The results showed that this model replicated the dynamic response of the BDyn in between the range 10 Hz to 20 Hz with an error less than 10% (Figure 7.14). The percentage differences were 13% at 5 Hz (both PCU and Sil), and > 15% for low frequencies (1 Hz, 3 Hz).
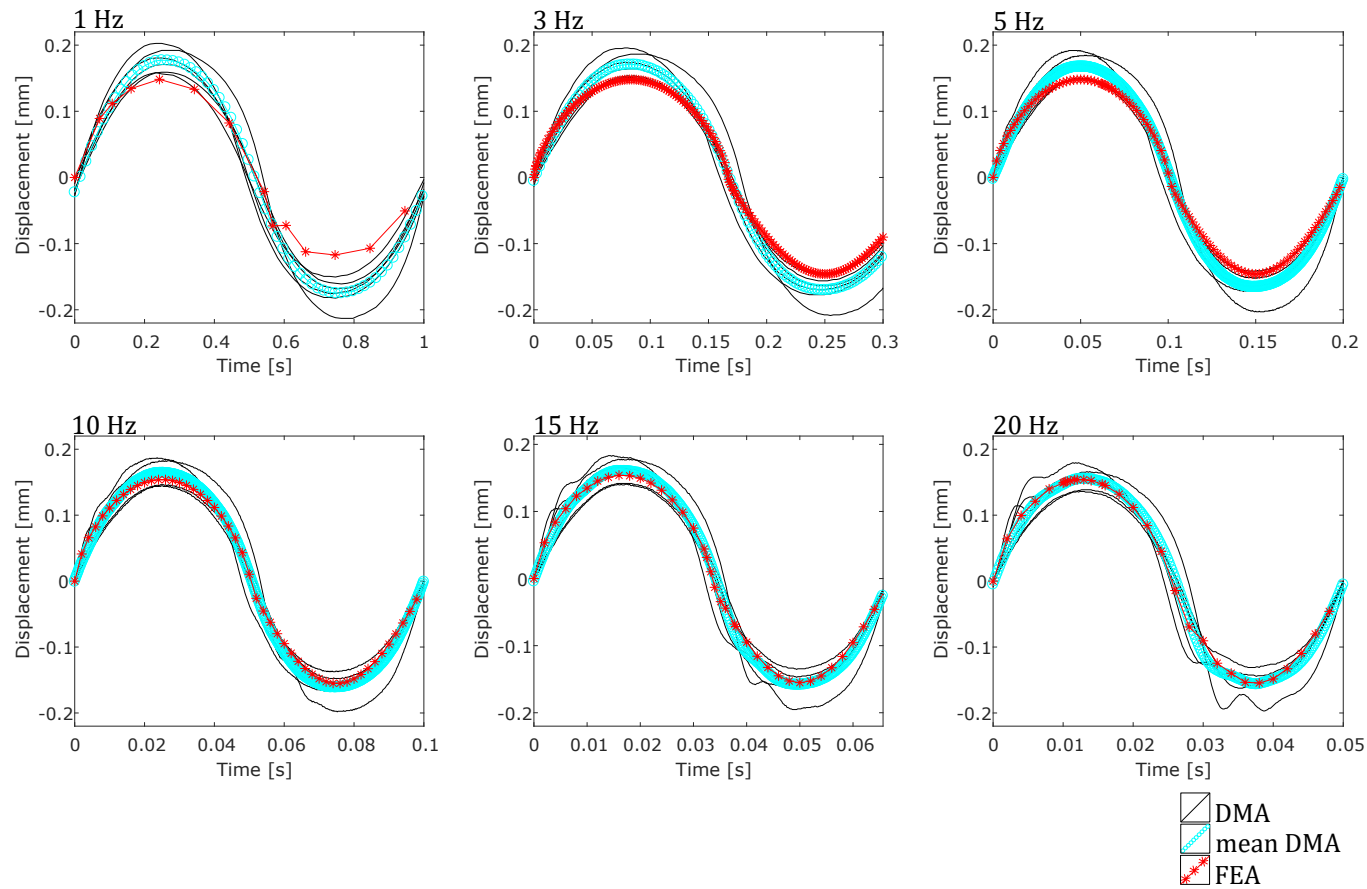
Figure 7.12: Comparison between the displacement curves obtained from the FE analyses (in red), the experimental DMA for the six specimens (in black) and the mean values of them (in light blue) at the frequencies evaluated (1 Hz, 3 Hz, 5 Hz, 10 Hz, 15 Hz, 20 Hz), plotted at different time scales.

Table 7.4: The table shows the percentage differences between the mean peak values of the experimental and FEA curves, evaluated as in Equation 7.2 and Equation 7.1. The differences have been evaluated between the curves in correspondences of the PCU and silicone peaks has shown in Figure 7.13.

% Differences	Frequencies					
	1 Hz	3 Hz	5 Hz	10 Hz	15 Hz	20 Hz
Silicone	20.0	15.0	13.0	7.0	4.0	1.2
PCU	50.0	17.0	13.0	4.0	2.0	1.0
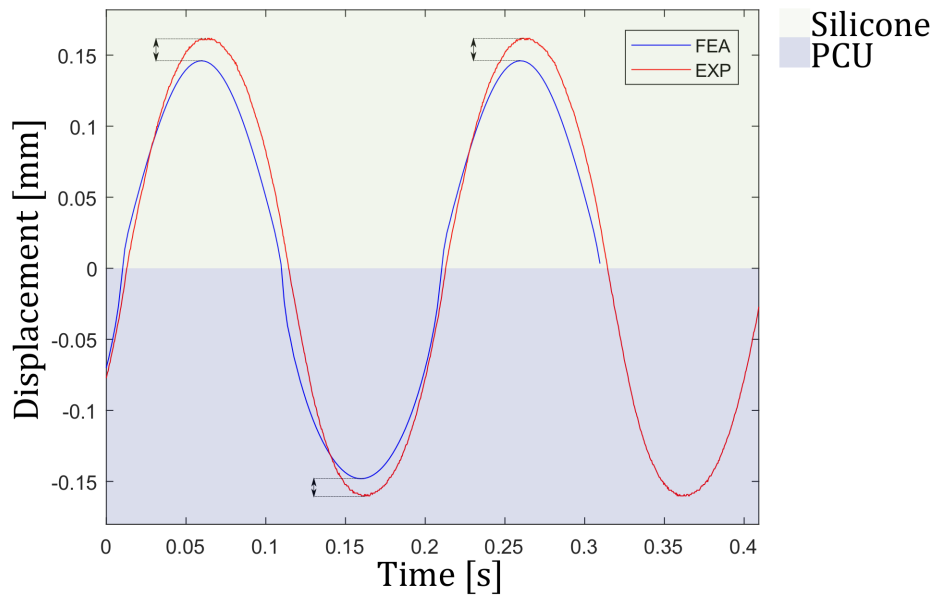
Figure 7.13: The peak to peak differences (illustrated with the black arrows) have been evaluated in correspondence of the compression silicone and tension (PCU) phases.

The static compression analyses on the PCU and Sil have been analysed through qualitative evaluations of the resulting deformations on the elastomer components. In Figure 7.15, an overview is given on the effects on the shape of the PCU, loaded in compression with an applied pressure of 1 MPa, 10 MPa and 15 MPa (20 N, 200 N and 300 N respectively). The displacement distributions on the PCU and silicone are reported in Figure 7.16 and Figure 7.17. In Figure 7.18 and Figure 7.19, the plastic deformations of the Silicone and PCU are directly compared with the results of the FE models. The silicone, deformed at the superior surface, where there is contact with the mobile titanium rod. The PCU, plastically deformed around the open side of the titanium cover when a tensile load is applied to the BDyn.

The explants, coated in gold to perform further studies not evaluated in this thesis, presented plastic deformations in the same area highlighted above and seen in the FE models.
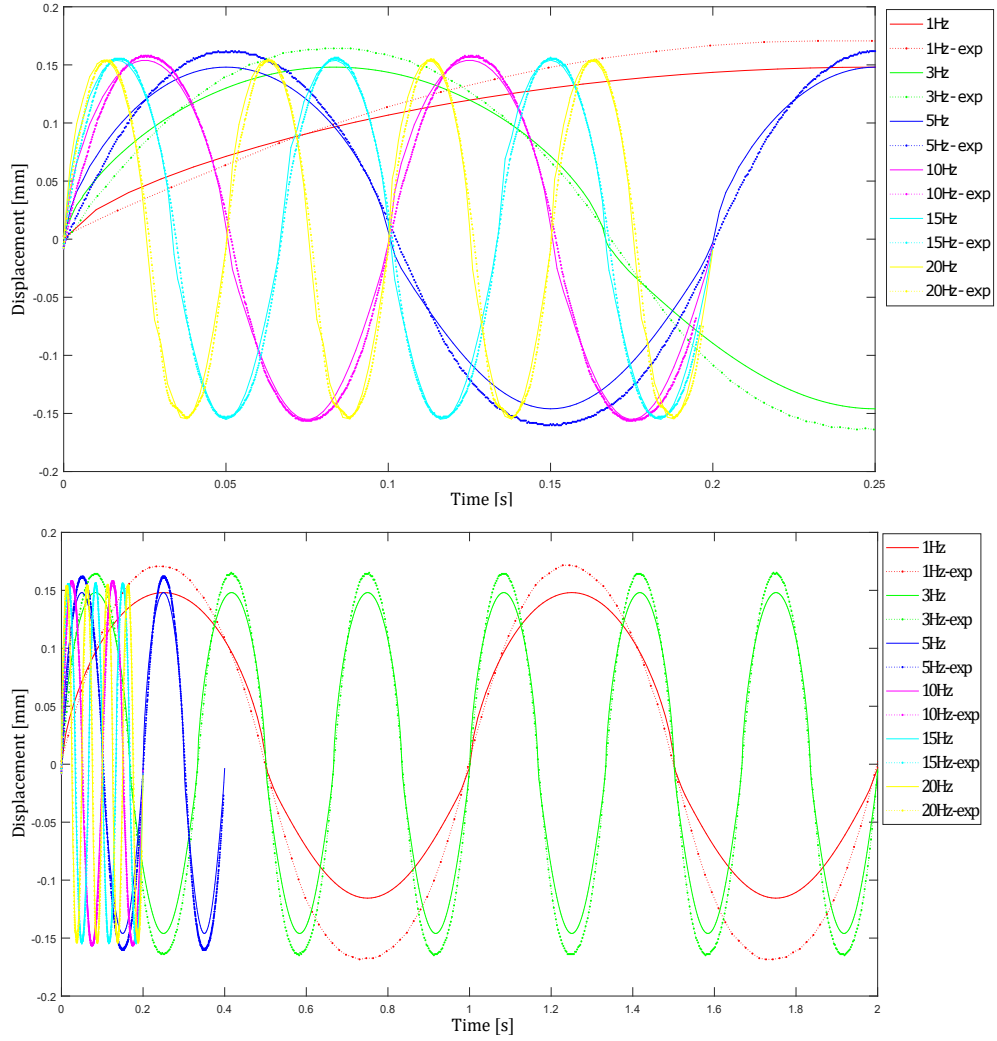
Figure 7.14: Displacements curves represented in time windows of 0.25 s (a) and 2 s (b). The curves with the continuous lines refer to the FE results, while the dotted lines refer to the mean value of the experimental results. The positive displacements refer to the compression loading phase, then the compression of the silicone, while the negative parts refer to the PCU compression.
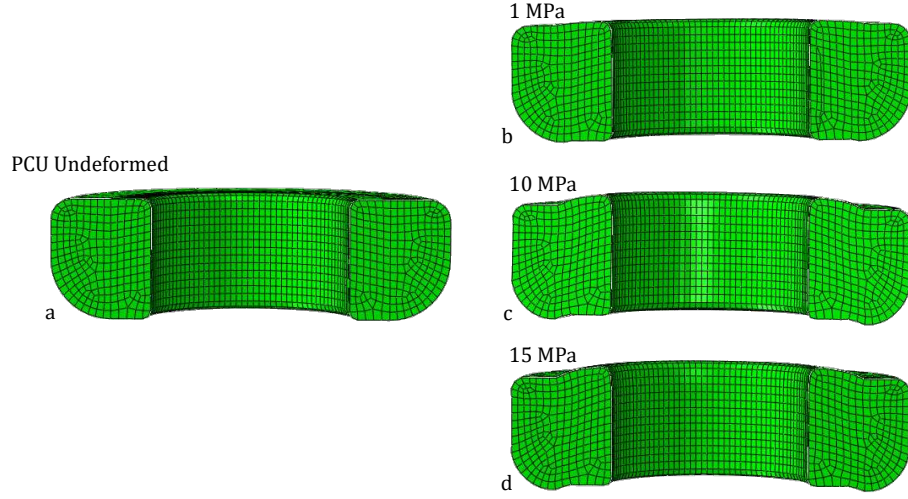
Figure 7.15: Undeformed model (a), deformed model on the right respectively at 1 MPa (b), 10 MPa (c) and 15 MPa (d).
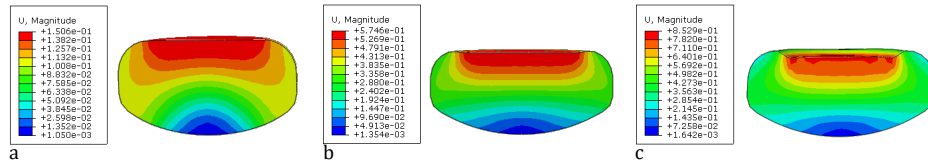
Figure 7.16: Displacement magnitude (in [mm]) at 1 MPa (a), 10 MPa (b) and 15 MPa.
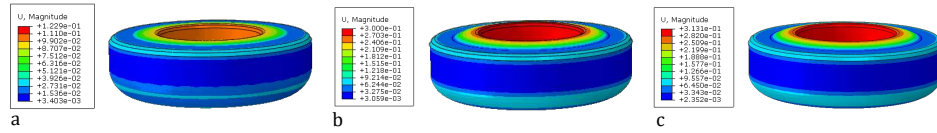
Figure 7.17: Displacement magnitude (in [mm]) on the PCU (in [MPa]) at 1 MPa (a), 10 MPa (b) and 15 MPa.

Figure 7.18: Silicone explanted and compared to the FE model.

Figure 7.19: PCU explanted and compared to the FE model.

7.5 BDyn application in combination with a new GsDyn scoliotic device

As stated in section 7.2, the BDyn device has been designed to restore the original range of motion in degenerated spinal unit and reduce the load applied to the IVD and facet joints. The BDyn range of motion can be used in combined applications with other devices. The BDyn device has been combined with the GsDyn (a device to treat the Early Onset Scoliosis (EOS)) device in an FE model, to investigate the effects on the mechanics of the GsDyn when a dynamic device is connected to it. Two FE models, pre-processed in Abaqus, are presented in this section: (i) a model of the GsDyn and (ii) a FE model of the combined device (BDyn-GsDyn). Subsequently, the results are analysed and compared to evaluate the effects introduced by these elastomeric components.

7.5.1 GsDyn

The GsDyn device, has been designed for the EOS treatment, based on surgical requirements by Gonzalez and the design concept details can be found elsewhere [18]. This type of device to treat the EOS, requires continuous follow-up surgery to adapt to the child growth and spinal curvature correction.

The GsDyn is an extendible device, composed of following parts (Figure 7.20):

i lower rod, attached by a screw to a lumbar verterbae;

ii body, it represents the fixed component of the device, with an hollow cavity to accomodate the mobile rack;

iii mobile rack, with toothed surface to move against the gear;

iv gear mechanism to allow the elongation of the device;

v lock system which keeps the device in the designed position chosen by the surgeon;

vi cover cases, which cover the gear and locking mechanism.

The elongation of the device during the surgery is allowed by the gear-rack system, and then fixed in a static condition with the locking mechanism. More details about this device, the design concept and evaluations of its functionality can be found elsewhere [18].

In this study, an initial evaluation of the GsDyn device was performed, then the FE model of the coupled device BDyn-GsDyn have been developed and analysed to study the influence on the mechanics of the elastomer components.
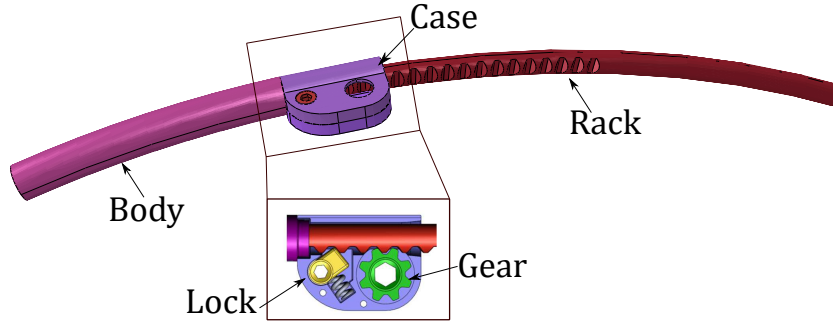
Figure 7.20: GsDyn components.

7.5.2 GsDyn FE model

The FE model of the GsDyn has been developed starting from the geometry shown in Figure 7.20, where the gear was not included. This simplification on the geometry has been used since the static condition was considered as the worst case scenario: the rack fully elongated with the locking pin in contact to the rack to avoid movement. The GsDyn components are composed of a Titanium alloy (Ti6Al4V), with Young's modulus and Poisson's ratio of 105000 MPa and 0.3 respectively.

The Gsdyn device has been meshed with tetrahedral elements, and in the area subjected to high stress concentration (locking pin and rack contact surfaces) the mesh was refined. Mesh convergence analyses have been performed on the components of the GsDyn, evaluating the mesh density of the single components, applying the loads correspondingly with the loading conditions subsequently applied in the FE simulation.

The mesh size was chosen by evaluating the differences on the stress varying the mesh size and evaluating the computational time required. The mesh size selected demonstrated less than 5% of difference in the stress as compared to a finer mesh model. To reduce the computational cost, larger mesh sizes (which resulted in error values >5%) were accepted for the body and rack components. The body is not directly involved in the contact between the locking pin and the rack, while in the rack component mesh refinement was implemented in the contact area to increase the resolution of the model. In Table 7.5 the mesh size and number of elements used are listed for each part.

Table 7.5: Number of elements and mesh size of the GsDyn components.

Component	Number of elements	Mesh size [mm]
Body	3 713	1.5
Lower case	9 498	0.9
Upper case	9 919	0.9
Lock	46 463	0.25
Rack	21 794	1.0

The contact properties between the GsDyn parts have been defined as follows:

- tied contact properties between the welded parts: upper and lower cases, lower rod and body;

- tied contact properties between the body and the rack, considering the rack in a fixed position and not allowing motion, as well as for case and locking pin;

- sliding contact properties between the locking pin and the correspondent rack tooth.

Boundary and loading conditions have been applied to replicate the implanted condition as shown in Figure 7.21, where the two extremities are connected by screws or hooks to the rib cage and the vertebrae. The device, which is meant to correct the excessive curvature of the spine, is inserted inclined with respect to the coronal plane (Figure 7.22). Thus, the load is applied with a variable angle. The angle of application depends on the stage of the treatment and on how it has been connected in the body. The
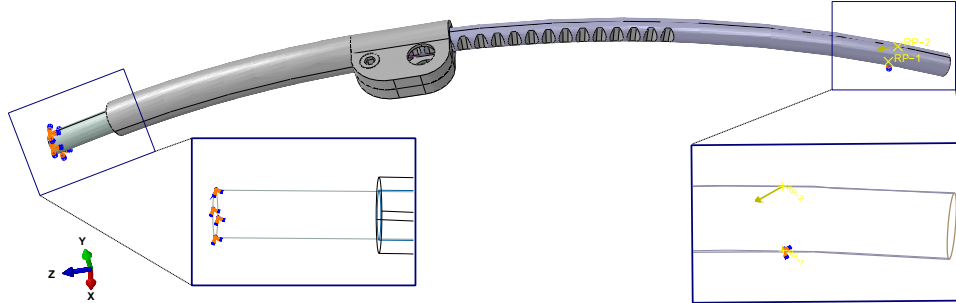
Figure 7.21: Load and boundary conditions applied to the GsDyn.

opposite side the device has been fixed, at the bottom surface, with a fully constrained boundary conditions. The nodes of the inferior surface of the rod were fully constrained, and 100 N load was applied to the rack in correspondence of the reference point shown in Figure 7.21 with the described direction (along the z-axis, as defined in the figure). A static simulation has been solved and the displacement and stress distribution evaluated.
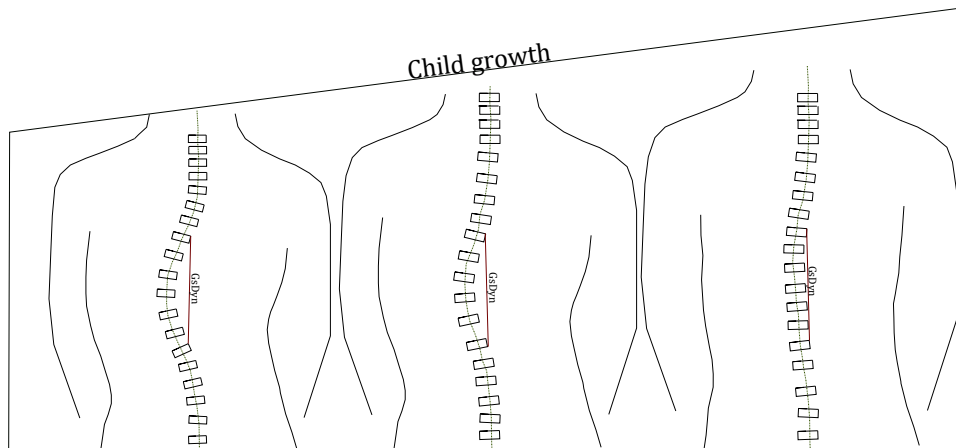
Figure 7.22: The inclination of the device changes accordingly with the patient growth and the treatment of the scoliosis.

The BDyn-GsDyn device was obtained connecting the BDyn at the inferior surface of the GsDyn, where the lower rod has been substituted by the mobile rod of the BDyn; further, the welding contacts between the two devices have been replicated by means of a tied contact. The pre-processing (mesh size, material and contact properties) described above in the previous sections (Figure 7.3.2) have been applied in this simulation.

The inferior surface of the BDyn has been fully constrained and the loading condition applied on the GsDyn FE model (100 N subsection 7.5.2) has been applied. A static simulation has been run and the displacements and stresses were analysed and compared with the results of the GsDyn simulation (solo device).
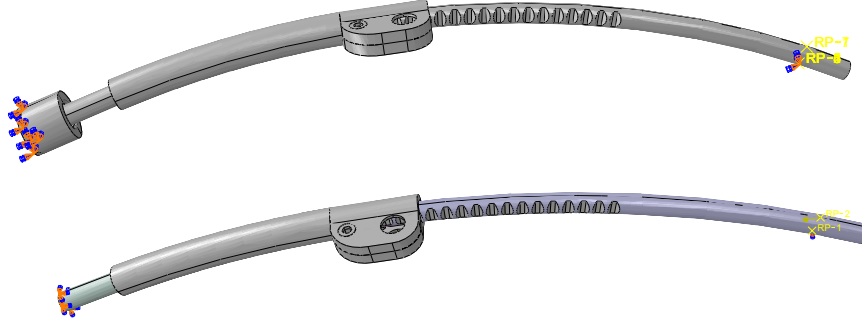
Figure 7.23: Boundary and loading conditions for the GsDyn and the combined BDyn-GsDyn device.

7.5.3 GsDyn & BDyn-GsDyn FE results

The displacements over the GsDyn and the combined device (BDyn-GsDyn) have been evaluated and the results are shown in Figure 7.24. For the
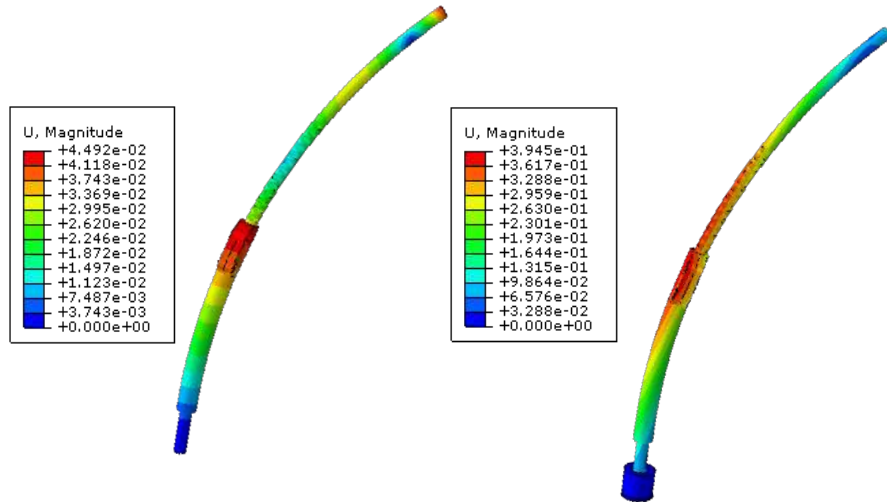
Figure 7.24: Displacements on the GsDyn (a) and the combined device BDyn-GsDyn (b). The magnitude of the displacements is shown (in mm).

GsDyn device, the displacements on the structure are limited, due to the high stiffness of the device. The elastomer components of the BDyn device gave more freedom to the structure, leading to a maximum displacement of 0.39 mm.

The stress distributions, evaluated as Von Mises distribution in Figure 7.26a
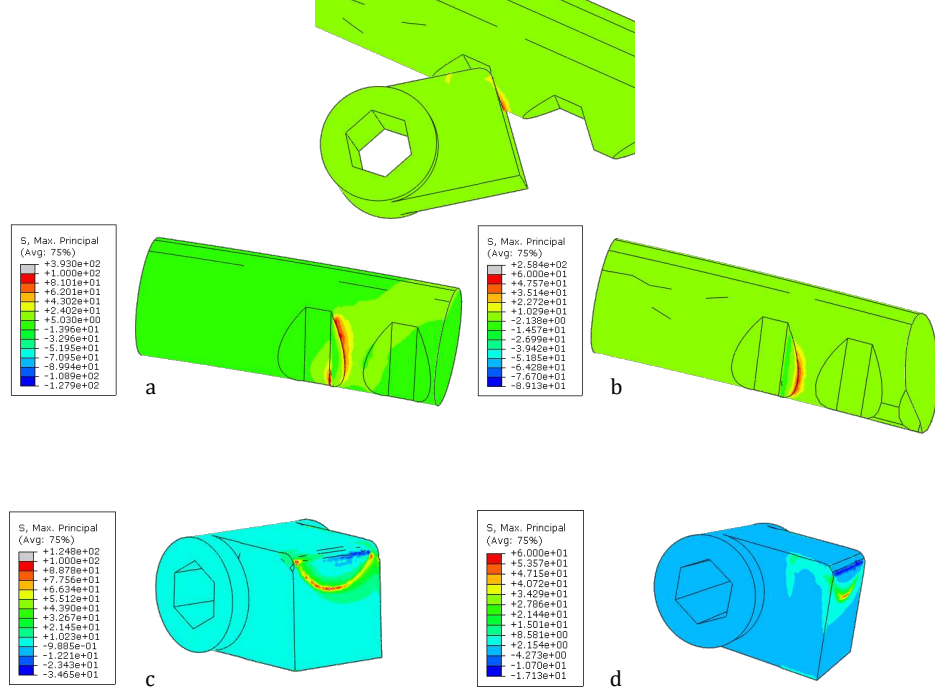
Figure 7.25: Stress distributions on the locking pin and rack in the GsDyn model (a and c) and in the combined device (b and d). The maximum principal stress are shown (MPa).

and Figure 7.26b, showed in both cases a peak value on the locking system, in correspondence of the contact area with the rack. The maximum stress values were 238.4 MPa in the case of the GsDyn device (Figure 7.26a), and 62.9 MPa for the combined device (Figure 7.26b); a four-fold reduction in peak stress.

7.6 Discussion

In this study, the material property formulations for the elastomer components have been determined and used for FE modelling of the BDyn device. The BDyn FE model has been validated against data from dynamic loading conditions. The model predictions were particularly accurate in the range between 10 and 20 Hz (percentage differences with the mean value of the experimental results were <10%), and at 5 Hz (percentage difference was
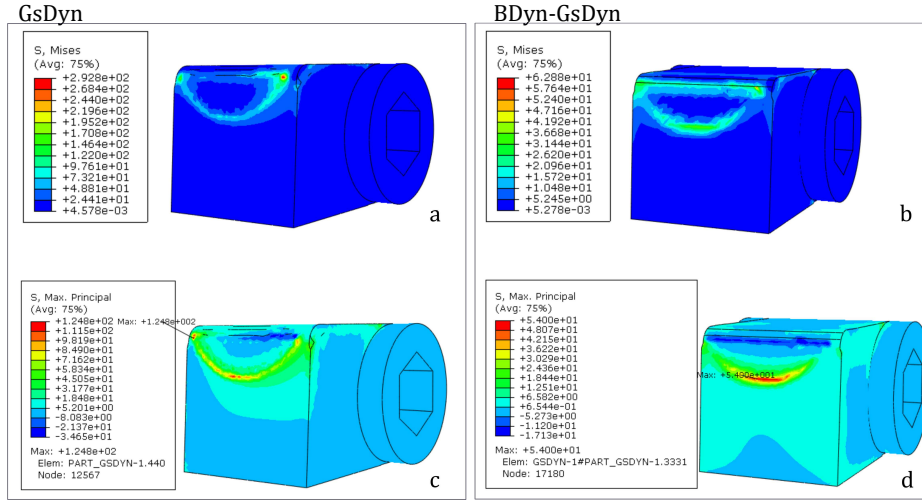
Figure 7.26: Stress distribution on the locking pin of the GsDyn. On the first row, the Von Mises stress is shown and in the second the maximum principal stress in MPa.

<15%) which includes the physiological range of vibrations [315, 316]. The percentage differences for the PCU and silicone were less accurate at 1 and 3 Hz (15%, 20% for the silicone, 17%, 50% PCU, respectively). Despite these differences, particularly accentuated for the PCU at 1 Hz, the FEA displacement results are included in the range of variability covered by the experimental test.

Critically, though, the stress distributions on the static models predicted high-stress in correspondence to the regions of failure on explanted devices. The simulation was performed in only compression, yet it has made some excellent predictions for explants loaded in the body and subjected to different loading conditions. Moreover, an application of the BDyn device as applied to a new device to help correct scoliosis (the GsDyn device) has been evaluated, with the key finding that inclusion of the BDyn device on to this novel scoliotic device reduces peak stresses by a factor of around 4.

The results of the dynamic analyses agreed with Lawless et al. [254], at high frequencies the material properties of the BDyn are characterized by higher stiffness, while at low frequencies (1 Hz, 3 Hz) the materials showed higher displacements. However, in the FE analyses, the viscoelastic properties have not been implemented, therefore, the time-dependency is not included in the model. Thus, the FE results did not include differences in the displacement amplitude under sinusoidal loading; unlike the experimental results. It is expected that discrepancies at lower frequencies may be a result of a greater energy dissipating capability of the components of the BDyn device, which is the component not modelled in this study. Differences in the loading and

unloading slopes were evident in the FE model at lower frequencies (1, 3, 5 Hz), where the mass of the bodies have more influence on the dynamics of the device as explained from the dynamics formulation, while it is not so evident at higher frequencies. This is likely due to the undefined unloading properties (subsection 7.3.1), a change in the slope of the sinusoids (both in the negative and positive parts of the sinusoids) were expected in correspondence of the unloading phase. In Figure 7.12, it is noticeable a change in the slope of the sinusoid in the PCU loading phase, which increases at low frequencies (ie.:1,3 Hz). These results are justified by the difference in density of the two materials and further emphasized at low frequencies according to the formulation of the dynamics (Equation 7.3):

$$m\frac{d^2x}{d^2t} + c\frac{dx}{dt} + kx = Fsin(\omega t) \tag{7.3}$$

Equation 7.3, describes the motion of a system where m is the mass of the body, k the elastic constant, c the damping coefficient, F the external force applied to the system at a frequency w. Its solution, in the forced and undamped condition, lead to the following displacement functions:
case 1. $\omega \neq \omega_0$

$$x(t) = Rcos(\omega_0 t - \delta) + \frac{F}{\omega_0^2 - \omega^2}cos(wt)) \tag{7.4}$$

case 2. $\omega = \omega_0$

$$x(t) = Rcos(\omega_0 t - \delta) + \frac{F}{2m\omega_0^2}cos(wt)) \tag{7.5}$$

where R is a coefficient of the specific solution of the differential equation and ω_0 the natural frequency, defined as:

$$\omega_0 = \sqrt{\frac{k}{m}} \tag{7.6}$$

As stated by Lawless et al. [254], in the range of frequencies simulated there are not resonant peaks. In both the loading phases (PCU and silicone), at low frequencies the density of the bodies has a dominant effect. In Table 7.4, the percentage differences between the experimental tests and computational simulations are >10% at low frequencies in correspondence of both the PCU and silicone peaks, where the FE results are more affected by its inertial properties (Figure 7.14). In particular, the differences were more accentuated in correspondence of the PCU loading phase, which has higher density than the silicone. These results showed that the FE model is able to accurately replicate the behaviour of the BDyn device only in the range of frequencies between 5 Hz and 20 Hz, where the errors between the

displacements is less than 10%. Nevertheless, despite the described limitations, this model is able to simulate the device behaviour across a range of frequencies which correspond with the physiological range [315, 316], as well as replicate the device behaviour under static loading.

The stress distributions and displacement, obtained from the FE simulations, were qualitatively coherent with the deformation of *ex-vivo* implants. High displacement is registered in the PCU around the surfaces in contact with the mobile rod. In particular, the upper internal corners are characterized by the highest values for displacement. In the silicone, the upper surface in contact with the titanium rod is affected by the highest deformation.

The combination of the BDyn device with the GsDyn implant resulted in a four-fold reduction in peak-stresses predicted, which would likely result in improved durability of the device. The stress distribution analyses have been principally focused on the contact between the locking system and the rack, which is anticipated as the weakest part of the device, and could lead to failure. The combined device resulted more compliant, with more flexibility given to the patient, and reducing the stress concentration in the locking mechanism. This coupled device represents one possible application of the BDyn. In fact, its design concept could be used in other devices to reduce the failure risk and obtain more flexible devices.

7.6.1 Limitations and future work

The material properties of the PCU and silicone have been evaluated as hyperelastic materials. To obtain an accurate estimation of the material formulations, more than one experimental test is recommended, particularly in case of non-linear materials properties. Although, the evaluation is also possible with only one experimental dataset, it provides an estimation valid only under those same loading condition. The materials have been hypothesised as incompressible, due to the lack of volumetric test and this hypothesis is widely accepted in case of elastomers [317, 318, 319, 320]. Another limitation from this estimate is the lack of the data related to the unloading phases of the mechanical tests. In fact, elastomers are characterized by different behaviours during different loading conditions and loading/unloading phases, and if the unloading formulation is not stated in Abaqus, it follows a linear behaviour. For this reason, a change on the sinusoid slopes was expected in the results. However, in this range of loads the obtained strains are in the initial part of the material's stress-strain curves, approximately linear. To obtain more complete characterization of the elastomers and a mechanical estimation valid for a wide range of load, more experimental test are required. In future studies, further experimental tests are required to fully characterize the mechanical behaviour of the elastomers, either as time-independent and time-dependent. Particularly, in the last case, the

description of the viscoelastic features needs creep test data and at least one between shear or volumetric test data.

A preliminary study [304, 305], on a generic lumbar model of the L4-L5 has been developed (Figure 7.27), obtaining as expected a decreasing pressure on the intervertebral disc and increasing the range of motion. Further studies would investigate the mechanics of the BDyn and its effects on the spine, using different morphologies, various degenerated conditions and loadings. These studies will be developed using the Lumbar Model Generator toolbox, described in chapter 4, where anatomical differences as well as healthy and degenerate conditions can be implemented to evaluate the effect of the Bdyn on the biomechanics of the spine.
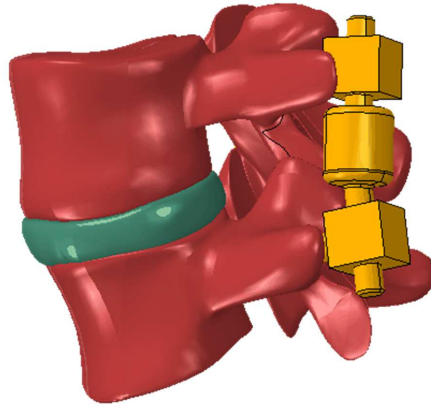
Figure 7.27: Functional unit obtained from previous studies [305] with an embedded BDyn device.

7.7 Conclusions

An FE model of the BDyn has been implemented and validated against experimental data and the model resulted accurate in the range between 5 and 20 Hz. The validated model could be used in combination with spinal models to predict the effects of the BDyn device on the spinal biomechanics, in particular under degenerated conditions.

Further, the BDyn model predicted deformations which qualitatively matched those of a retrieved implant, this level of agreement is impressive given that the BDyn device was simply modelled under compression, as opposed to an implant undergoing the full range of loading experienced within true physiological conditions. Coupling the Bdyn device with the GsDyn, resulted in four-fold reduction in induced stresses within the locking system. Thus, a reduced failure risk could be expected in that area of the device. Further, this demonstrated that the functionalities and design concept of the BDyn can be used in the development of new devices, reducing the risk of failure

of existing and new spinal implants.

Chapter 8

Overall discussion and conclusions

The aim of this thesis was to provide a Finite Element model of the lumbar spine to assess the design and the effects of implants in the biomechanics of the spine as well as providing a tool for the clinical evaluation of treatments in degenerated conditions. In order to fulfil this objective, the FE model has to provide generalised solutions valid for a population of subjects, as well as evaluate subject-specific conditions.

Anatomical dimensions of the lumbar spine were collected from literature and subject-specific datasets and subsequently used to evaluate correlation analyses available in literature. The morphological study which showed the best correlation with subject-specific datasets has been implemented in the development of the parametric and scalable geometrical model of the lumbar spine. The geometrical model can be generated either following the correlation analyses implemented, based on the age, height and gender of a subject, or importing the subject-specific measurements from data-scan. The generation of the geometry and the development of the FE model, performing the mesh generation and evaluation, pre-processing the meshed model, assigning material properties and defining contacts boundary and loading conditions, is implemented in a toolbox, the LMG (Lumbar Model Generator), developed in Matlab. Finally, the FE model is sent to solve to FEBio, an open-source software, through the LMG toolbox. The LMG performs all the steps, from the geometry generation to the preparation of the FE model, connecting internally to the FE solutor and analysing the results, avoiding time-consuming actions and transferring files from one software to another. An entire lumbar model has been generated as proof-of-concept, and a FE model of a L1-L2 functional unit has been analysed. The intervertebral disc pressure and the displacement on the nucleus pulposus (NP) were investigated at different compressive loads (500 N, 750 N, 1000 N) and were compared with experimental results and computational studies avail-

able in literature [273, 165]. The results were in agreement with the previous studies, thus showing the validity of the model generated.

The automation of the entire process allows the evaluation of different geometries and/or eventual anatomical deformity, as well as evaluating the effects of different material properties. Sensitivity analyses have been performed, evaluating scenarios (i.e.: morphological variation in the IVD) that usual model generation methods would require the use of several models and a considerable amount of time for the setup of the models. The sensitivity analyses showed that combined morphological and material properties variations are required to evaluate degenerated conditions. The constitutive material properties of the annulus fibrosus affect the displacement and IDP on the NP under compressive loads, while fiber orientations and stiffness influence the biomechanics when bending moments are applied. Moreover, the effects of sensitivity analyses on the NP and cartilaginous endplates material properties have been evaluated, demonstrating the effects on the axial displacement and IDP.

A dynamic, non-linear FE-model of the Bdyn was developed and validated against experimental results. Subsequently, the BDyn has been included in the design of a device for the treatment of scoliosis in paediatric patients (GsDyn) to evaluate the effects of deformable components. In the combined device, the stress on the locking system of the GsDyn resulted four-fold reduced, which would improve the durability of the device.

Correlation analyses evaluated in the literature have been assessed [226, 36] and compared with correlation analyses performed in this thesis, based on morphometric studies available in the literature [43, 26]. The complex anatomy of the vertebrae requires the measurements of several dimensions on each vertebrae, however general method to measure them has not been defined and the mentioned studies reported a different list of dimensions, allowing the comparison only on four dimensions (Endplate Depth EPD, Endplate Width EPW, Pedicle Height PDH, Pedicle Width PDW). A study by Alam et al. [43], demonstrated the importance of evaluating correlation studies from consistent groups, accounting for ethnicity and gender. Dividing correlation analyses according to the ethnicity and gender would allow the development of accurate correlation analyses and a dedicated section of the LMG toolbox (chapter 4).

The application of FE model of the lumbar spine in the development of new devices and in the evaluation of the possible clinical treatments is not yet a routine process and it is due to:

- Issues with solving subject-specific FE model in real-time;

- Uncertainty in material properties;

- A lack of validated protocols.

Subject-specific models are affected by a high computational cost, related to the acquisition of a scan, segmentation and pre-processing; all these steps require an expert and skilled technician, and long hours of work. Material properties remain unknown, and are affected by high variability between subjects and even intra-subject variability depending on the pathological conditions. A real-time procedure, requires the validation against an extensive data-set, in order to prove the reliability of that system; and, thus, the predictions of the model.
The LMG toolbox represents a possible solution to the underlined issues. It allows the generation of the geometry of a lumbar spine (given the dimensions from either subject-specific dimensions and correlation analyses) and the pre-processing of a FE model in less than 20 seconds. The accuracy of the LMG geometry has been ascertained against the Visual Human Project model, reproducing this subject-specific anatomy. Moreover, the material proprieties can be selected and assigned according to the pathological status or a range of values can be assigned. Potentially, enabling the evaluation of the possible effects of an implant on patients with different tissue degenerations. Further studies would map the combination of material and morphological changes to identify different degenerated status and directly select these using a GUI. However, the LMG toolbox generates average models and the subject-specific anatomical details can not be automatically included. Even evaluating an extensive data-set to map morphological and material properties variations between healthy and degenerated conditions, they would result as an approximation of the real morphologies and material properties.

The LMG toolbox allows the pre-processing of the generated lumbar geometry. All the bodies are meshed according to the automated convergence analyses, and the material properties are assigned. The geometrical features (i.e.: surfaces) are selected and contact properties and boundary conditions directly applied. The functionalities and potentiality of the toolbox are described in this thesis, as well as two applications, the generation of a L1-L5 FE model and the generation and analysis of a L1-L2 FE model. Further studies are required to improve the toolbox, adding a wide range of loading conditions to simulate the physiological range of motion, and adding the effects of ligaments and the follower load. Despite the mentioned limitations, the results of the L1-L2 model were in agreement with available experimental and computational studies, demonstrating the validity of the toolbox.

One of the advantages of a parametrised and scalable model, embedded in an automatic toolbox for the FE model generation, is that it allows the evaluation of sensitivity studies on either morphological parameters and

material properties. In the study presented in chapter 6, a range of volumetric ratio between the Anulus Fibrosus (AF) and Nucleus Pulposus (NP) and various material properties for the AF, NP, and cartilagineus endplates (CEP) have been evaluated. These variations represent the alteration of the mechanical properties in case of degenerated conditions. The VP sensitivity study showed how the mechanics change, in terms of IDP and axial displacements, on varying the thickness of the AF. However, in this study the morphological variations have not been paired with the respective material property changes, which is demanded to obtain realistic estimations. The material properties of the CEP, VP and AF have important effects on the biomechanics of the FU in both compressive and bending loadings. Instead, the effects of varying fiber orientations and fiber strengths were more influential only in bending loading conditions.

The evaluation of the effects of an implant on the biomechanics of the spine requires the use of an accurate and validate model of the device itself. Hence, a FE model of the BDyn was developed, where the material properties of the deformable bodies (PCU and Sil) were obtained from mechanical tests. Hyperelastic formulations have been evaluated and the best-fit constitutive laws assigned to the PCU and Sil. The model was evaluated under dynamic conditions, implementing a sinusoidal load across a frequency-sweep. The model was validated with data obtained from Dynamic Mechanical Analysis. The model was particularly accurate in the range of frequencies between 10 and 20 Hz, which correspond to a physiological range of vibration of the human body. The model was further validated comparing the deformations, obtained in static analyses at different load, with the deformations found on explanted devices. This qualitative comparison showed similar deformations between the simulations and experimental tests. This result provides further research paths that can be followed to optimize the material used and the design of the components. In fact, FE models allow evaluations that in reality are not possible to assess on the inner components of the device when implanted in a spine, unless explanted and opened up. The FE model of the BDyn device in combination with the GsDyn predicted a factor of 4 reduction in the peak stresses of the locking system. The combined device resulted in a more compliant and less constrained device, demonstrating the functionalities of the BDyn and in general of its concept. In fact, this design concept, of coupling elastomeric components with stiff materials (i.e.: Titanium) can be used in other applications developing more flexible devices and reducing the stress distribution in points where there is high risk of failure.

Finally, the LMG toolbox allows the generation and evaluation of accurate anatomical model of the lumbar spine, in a reduced time compared with previous studies. At the current stage, the toolbox can already be

used in the design of new implants, evaluating the effects either on different anatomies and different pathological stages, which can be simulated with material properties and morphological variations. Further developments are required to use it in clinical applications. A more user-friendly and intuitive graphical interface can be developed as well as simulating automatically the application of devices at different levels. These features can help the decision of the best treatment for a particular degenerated condition during the clinical assessment: assigning the stage of degeneration at each level of the spine and/or adding information about anatomical deformity, a subject-specific condition can be evaluated and the effects of each device analysed. According to this last application, the BDyn device is validated and ready to be imported in the toolbox.

8.0.1   Conclusions

Correlation analyses available in literature have been evaluated and compared with others obtained in this study, based on data from morphological studies. Above all, first order polynomial correlations have been found to better describe the geometrical relationship of the spine and further studies are required on a wide range of specimens.

A parametric and scalable geometrical model of the lumbar spine has been developed and implemented in a toolbox, the LMG (Lumbar Model Generator) developed in Matlab. This toolbox has been implemented to generate averaged models, where the anatomical dimensions are based on either subject-specific dimensions obtained from data-scans or correlation analyses. The correlation analysis chosen has been implemented in the LMG to reproduce the lumbar spine anatomy based on the age, height and gender of a subject. The toolbox allows the automatic preparation of FE models, performing the mesh generation and evaluation, assigning material properties, boundary conditions and analysing the results. The LMG generates models with a geometrical accuracy to within the tolerances of techniques used for generating subject-specific models, but within a timeframe orders of magnitude faster and compatible with translation into clinical practice (i.e. 20 seconds to generate the geometrical model and less than five minutes to obtain the pre-processed model).

A L1-L5 model has been generated as proof-of-concept and a functional unit (L1-L2) has been analysed and the results are in agreement with experimental studies and previous FE analyses.

One advantages of the LMG is the generation and pre-processing of population of models, allowing the evaluation of morphological and material properties variations of the bodies involved. Hence, sensitivity analyses were performed on morphological parameters and material properties, identifying how they influence the biomechanics. This preliminary study highlighted the

parameters to further investigate.

The FE model of a posterior stabilization device (BDyn) was developed and validated with experimental data. It can be integrated in the FE model of the lumbar spine to evaluate the effects on the biomechanics and eventually improving the design. Furthermore, the combination of the BDyn with the GsDyn, a device designed for Early Onset Scoliosis (EOS) treatment, has been implemented to evaluate the effects of elastomeric component on the device. Coupling these devices resulted in a reduction of the peak stresses within the locking system and it could reduce the failure risk of the GsDyn.

Appendix A

Material properties description

In this appendix, the constitutive laws of the materials used in this thesis are reported. In case of hyperelastic materials, the stress tensor can be obtained relating the free energy of a material to the deformation gradient or the three invariants of the strain tensor [321]:

$$W = U(I_1, I_2, I_3) \tag{A.1}$$

where I_1,I_2 are the strain invariants, defined as:

$$I_1 = \lambda_{xx} + \lambda_{yy} + \lambda_{zz} \tag{A.2}$$

$$I_2 = \lambda_{xx}\lambda_{yy} + \lambda_{yy}\lambda_{zz} + \lambda_{zz}\lambda_{xx} - \lambda_{xy}^2 - \lambda_{yz}^2 - \lambda_{zx}^2 \tag{A.3}$$

$$I_3 = \lambda_{xx}\lambda_{yy}\lambda_{zz} + 2\lambda_{xy}\lambda_{yz}\lambda_{zx} - \lambda_{xx}\lambda_{yz}^2 - \lambda_{yy}\lambda_{zx}^2 - \lambda_{zz}\lambda_{xy}^2 \tag{A.4}$$

where λ_{ij} are the stretch/extension ratios in the 3D dimensions.

A.1 Linear elasticity

In the linear elasticity theory, the stress σ is a linear function of the strain ϵ. This theory is valid for small strain and the constitutive equation is described by the Hooke's law:

$$\sigma_{ij} = D_{ijkl}\epsilon kl \tag{A.5}$$

where D is the elastic stiffness tensor.

A.2 Hyperelasticity

A.2.1 Neo-Hookean

$$W = C_1(\bar{I}_1 - 3 - 2\ln J) + D_1(\ln J)^2 \tag{A.6}$$

$$C_1 = \frac{\mu}{2}; D_1 = \frac{\lambda}{2} \tag{A.7}$$

In case of incompressible materials, it can be simplified as:

$$W = \frac{\mu}{2}(\bar{I}_1 - 3) \tag{A.8}$$

where μ and λ are the Lamé constants from linear elasticity and I_1 is the invariant of the deviatoric part of the right Chauchy-Green deformation tensor.

A.2.2 Mooney-Rivlin

The hyperelastic formulation of Mooney-Rivlin is described through the following strain energy equation (W):

$$W = c_1(\bar{I}_1 - 3) + c_2(\bar{I}_2 - 3) \tag{A.9}$$

where c_1 and c_2 are the Mooney-Rivlin material properties, I_1 and I_2 are the invariant of the deviatoric part of the right Cauchy-Green deformation tensor.

A.2.3 Polynomial

$$W = \sum_{i+j=1}^{N} C_{ij}(\bar{I}_1 - 3)^i(\bar{I}_2 - 3)^j \tag{A.10}$$

where C_{ij} are the material property coefficients, I_1 and I_2 are the invariant of the deviatoric part of the right Cauchy-Green deformation tensor.

A.2.4 Odgen

$$W = \sum_{k=1}^{N} \frac{\mu_k}{a_k}(\bar{\lambda}_1^{-\alpha_k} + \bar{\lambda}_2^{-\alpha_k} + \bar{\lambda}_3^{-\alpha_k} - 3) \tag{A.11}$$

where λ_1, λ_2 and λ_3 are the deviatoric principal streches and μ_k and α_k the material property coefficients.

A.2.5 Holazpfel-Gassen-Odgen

$$W_{matrix} = C_{10}(\bar{I}_1 - 3) + \frac{1}{D}(\frac{J^2 - 1}{2} - \ln J) \tag{A.12}$$

$$W_{fiber} = \frac{K_1}{2K_2} \sum_{\alpha=1}^{N}(exp(K_2(\bar{E}_\alpha^2 - 1))) \tag{A.13}$$

where $\bar{E}_\alpha$

$$\bar{E}_\alpha = \kappa(\bar{I}_1 - 3) + (1 - 3\kappa)(\bar{I}_{4(\alpha\alpha)-1}) \tag{A.14}$$

The entire strain energy equation is:

$$W = C_{10}(\bar{I}_1 - 3) + \frac{K_1}{2K_2} \sum_{\alpha=1}^{N}(exp(K_2(\bar{E}_\alpha^2 - 1))) \tag{A.15}$$

A.3 Hypoelasticity

Hypoelastic materials are characterized by linear elasticity, with the ability of return to the original shape when deformed, and non-linear stress strain behaviour for small strains. It is described through the tangent to the stress-strain curve [170]

$$d\sigma = D^{el} : d\epsilon^{el} \tag{A.16}$$

where d^{el} is the tangent elasticity matrix and $d\sigma$ and $d\epsilon$ are the rate of change of stress and strain respectively.

Permeability

Permeability characteristics have been assigned in previous studies to spine materials [322][290]. The mechanical formulation adopted is [146, 152]:

$$\kappa = \kappa_0 (\frac{e(1 + e_0))}{e_0(1 + e)})^2 e^{M(\frac{1+e}{1+e_0} - 1)} \tag{A.17}$$

where κ is the strain-dependent permeability, with κ_0 the initial permeability, e the void ratio dependent on the tissue deformation and its initial value e_0, and M is an empirical material constant.

References

[1] Damian Hoy et al. "The global burden of low back pain: estimates from the Global Burden of Disease 2010 study". In: *Annals of the Rheumatic Diseases* 73.6 (2014), pp. 968–974. DOI: `10.1136/annrheumdis-2013-204428`.

[2] Vinothan Sivasubramaniam et al. "Trends in hospital admissions and surgical procedures for degenerative lumbar spine disease in England: a 15-year time-series study." In: *BMJ open* 5.12 (2015), e009011. DOI: `10.1136/bmjopen-2015-009011`.

[3] Sean S. Rajaee et al. "Spinal Fusion in the United States". In: *Spine* 37.1 (2012), pp. 67–76. DOI: `10.1097/BRS.0b013e31820cccfb`.

[4] Eckardt Johanning. "Evaluation and management of occupational low back disorders". In: *American Journal of Industrial Medicine* 37.1 (2000), pp. 94–111. DOI: `10.1002/(SICI)1097-0274(200001)37:1<94::AID-AJIM8>3.0.CO;2-X`.

[5] N. J. Hallab. *Intervertebral disc joint replacement technology*. Ed. by P. A. Revell. Woodhead Publishing, 2014, Chapter 21. DOI: `10.1533/9780857098474.4.531`.

[6] D H Chow et al. "Effects of short anterior lumbar interbody fusion on biomechanics of neighboring unfused segments." In: *Spine* 21.5 (Mar. 1996), pp. 549–55.

[7] Malhar Kumar et al. "Correlation between sagittal plane changes and adjacent segment degeneration following lumbar spine fusion". In: *European Spine Journal* 10.4 (2001), pp. 314–319. DOI: `10.1007/s005860000239`.

[8] Hassan Serhan et al. "Motion-preserving technologies for degenerative lumbar spine: The past, present, and future horizons". In: *SAS Journal* 5.3 (2011), pp. 75–89. DOI: `10.1016/j.esas.2011.05.001`.

[9] Glenn R. Buttermann et al. "Interbody device endplate engagement effects on motion segment biomechanics". In: *The Spine Journal* 9.7 (July 2009), pp. 564–573. DOI: `10.1016/j.spinee.2009.03.014`.

[10] Hua-Zi Xu et al. "Biomechanical evaluation of a dynamic pedicle screw fixation device". In: *Clinical biomechanics (Bristol, Avon)* 21.4 (2006), pp. 330–336. DOI: `10.1016/j.clinbiomech.2005.12.004`.

[11] Ugur M. Ayturk et al. "Parametric convergence sensitivity and validation of a finite element model of the human lumbar spine". In: *Computer Methods in Biomechanics and Biomedical Engineering* 14.8 (2011), pp. 695–705. DOI: `10.1080/10255842.2010.493517`.

[12] Nikolai. Bogduk et al. *Clinical and radiological anatomy of the lumbar spine*. Elsevier/Churchill Livingstone, 2012, p. 260. ISBN: 9780702051661.

[13] Thomas Zander et al. "Impact of material and morphological parameters on the mechanical response of the lumbar spine. A finite element sensitivity study". In: *Journal of Biomechanics* 53 (2017), pp. 185–190. DOI: `10.1016/j.jbiomech.2016.12.014`.

[14] Jérôme Noailly et al. "How does the geometry affect the internal biomechanics of a lumbar spine bi-segment finite element model? Consequences on the validation process". In: *Journal of Biomechanics* 40.11 (2007), pp. 2414–2425. DOI: `10.1016/j.jbiomech.2006.11.021`.

[15] A Laville et al. "Parametric and subject-specific finite element modelling of the lower cervical spine. Influence of geometrical parameters on the motion patterns." In: *Journal of biomechanics* 42.10 (July 2009), pp. 1409–15. DOI: `10.1016/j.jbiomech.2009.04.007`.

[16] Pras Pathmanathan et al. "Applicability Analysis of Validation Evidence for Biomedical Computational Models". In: *Journal of Verification, Validation and Uncertainty Quantification* 2.2 (2017), p. 021005. DOI: `10.1115/1.4037671`.

[17] Owen Faris et al. "An FDA Viewpoint on Unique Considerations for Medical-Device Clinical Trials". In: *New England Journal of Medicine* 376.14 (2017), pp. 1350–1357. DOI: `10.1056/NEJMra1512592`.

[18] Alba Gonzalez. "Design, Manufacturing and Mechanical evaluation of a novel dynamic growing rod for the treatment of Early Onset Scoliosis". In: *Under preparation* (2018).

[19] Erling Asmussen et al. "Form and Function of the Erect Human Spine : Clinical Orthopaedics and Related Research". In: *Clinical Orthopaedics and Related Research* Volume 25 (1962), pp. 55–63.

[20] Ardiyansyah Syahrom et al. "Mechanical and microarchitectural analyses of cancellous bone through experiment and computer simulation." In: *Medical & biological engineering & computing* 49.12 (Dec. 2011), pp. 1393–403. DOI: `10.1007/s11517-011-0833-0`.

[21]   Alf Nachemson. "Lumbar Intradiscal Pressure: Experimental Studies on Post-Mortem Material". In: *Acta Orthopaedica* 31.S43 (1960), pp. 1–104. DOI: `10.3109/ort.1960.31.suppl-43.01`.

[22]   David R Eyre. "Collagens and Cartilage Matrix Homeostasis". In: *Clinical Orthopaedics and Related Research* 427 (Oct. 2004), S118–S122. DOI: `10.1097/01.blo.0000144855.48640.b9`.

[23]   T K Kobayashi et al. "Proteoglycans-collagen interactions in human costal cartilage." In: *Biochimica et biophysica acta* 303.1 (Mar. 1973), pp. 148–60.

[24]   A Shirazi-Adl et al. "Mechanical response of a lumbar motion segment in axial torque alone and combined with compression." In: *Spine* 11.9 (Nov. 1986), pp. 914–27.

[25]   Hukins D. W. et al. *Fibre reinforcing in articular joints. Material Properties and Stress Analysis in Biomechanics.* Engineering in Medicine, 1989.

[26]   A Wolf et al. "Morphometric study of the human lumbar spine for operation-workspace specifications." In: *Spine* 26.22 (Nov. 2001), pp. 2472–7.

[27]   Jeannie F. Bailey et al. "Morphological and postural sexual dimorphism of the lumbar spine facilitates greater lordosis in females". In: *Journal of Anatomy* 229.1 (2016), pp. 82–91. DOI: `10.1111/joa.12451`.

[28]   Lorin M. Benneker et al. "Correlation of radiographic and MRI parameters to morphological and biochemical assessment of intervertebral disc degeneration". In: *European Spine Journal* 14.1 (2005), pp. 27–35. DOI: `10.1007/s00586-004-0759-4`.

[29]   Youssef Masharawi et al. "A morphological adaptation of the thoracic and lumbar vertebrae to lumbar hyperlordosis in young and adult females". In: *European Spine Journal* 19.5 (2010), pp. 768–773. DOI: `10.1007/s00586-009-1256-6`.

[30]   C.D. Castro-Reyes et al. "Morphometric characteristics of lumbar vertebral pedicles in mexican population. Implications for transpedicular lumbar fusion surgery". In: *Journal of Morphological Sciences* 32.1 (2015), pp. 37–42. DOI: `10.4322/jms.072014`.

[31]   Manohar M Panjabi. "Human Lumbar Vertebrae: Quantitative Three-Dimensional Anatomy." In: *Spine* Volume 17.Issue 3 (1991).

[32]   M M Panjabi et al. "Human lumbar vertebrae. Quantitative three-dimensional anatomy." In: *Spine* 17.3 (Mar. 1992), pp. 299–306.

[33] M M Panjabi et al. "Articular facets of the human spine. Quantitative three-dimensional anatomy." In: *Spine* 18.10 (Aug. 1993), pp. 1298–310.

[34] M. M. Panjabi et al. "Complexity of the thoracic spine pedicle anatomy". In: *European Spine Journal* 6.1 (1997), pp. 19–24. DOI: `10.1007/BF01676570`.

[35] M. Kunkel. "A statistical approach to predict subject- specific morphometry of the human thoracic and lumbar spine from radiographic images". In: *PhD Thesis* (2011).

[36] Douglas P. Breglia. "Generation of a 3-D Parametric Solid Model of the Human Spine Using Anthropomorphic Parameters". In: *Master thesis* June (2006).

[37] Hendrik Schmidt et al. "Intradiscal pressure, shear strain, and fiber strain in the intervertebral disc under combined loading." In: *Spine* 32.7 (2007), pp. 748–55. DOI: `10.1097/01.brs.0000259059.90430.c2`.

[38] Byeong Sam Kim. "A follower load as a muscle control mechanism to stabilize the lumbar spine". In: *PhD Thesis, University of Iowa* (2011).

[39] Shankar Acharya et al. "Lower dorsal and lumbar pedicle morphometry in Indian population: a study of four hundred fifty vertebrae." In: *Spine* 35.10 (2010), E378–E384. DOI: `10.1097/BRS.0b013e3181cb7f2b`.

[40] Seema et al. "Morphometric Study of Pedicles of the Lumbar Vertebrae in Adult Punjabi Males". In: *International Journal of Anatomy and Research* 4.2 (2016), pp. 2401–2404. DOI: `10.16965/ijar.2016.209`.

[41] Bharatpur Hospital et al. "A Morphometric Study of Lumbar Spine Pedicles in Nepalese Population". In: *Journal of College of Medical Sciences-Nepal* 10.4 (2015), p. 2015.

[42] J M Olsewski et al. "Morphometry of the lumbar spine: anatomical perspectives related to transpedicular fixation." In: *The Journal of bone and joint surgery. American volume* 72.4 (Apr. 1990), pp. 541–9.

[43] Muhammad M. Alam et al. "Lumbar morphometry: A study of lumbar vertebrae from a Pakistani population using computed tomography scans". In: *Asian Spine Journal* 8.4 (2014), pp. 421–426. DOI: `10.4184/asj.2014.8.4.421`.

[44] Maria E Kunkel et al. "Prediction equations for human thoracic and lumbar vertebral morphometry." In: *Journal of anatomy* 216.3 (Mar. 2010), pp. 320–8. DOI: `10.1111/j.1469-7580.2009.01187.x`.

[45]   G L Tibbetts. "Estimation of stature from the vertebral column in American Blacks." In: *Journal of forensic sciences* 26.4 (Oct. 1981), pp. 715–23.

[46]   Wade Johannessen et al. "Effects of degeneration on the biphasic material properties of human nucleus pulposus in confined compression." In: *Spine* 30.24 (Dec. 2005), E724–9.

[47]   Benjamin R. Whatley et al. "Intervertebral disc (IVD): Structure, degeneration, repair and regeneration". In: *Materials Science and Engineering C* 32.2 (2012), pp. 61–77. DOI: 10.1016/j.msec.2011.10.011.

[48]   M. P. Grant et al. "Human cartilaginous endplate degeneration is induced by calcium and the extracellular calcium-sensing receptor in the intervertebral disc". In: *European Cells and Materials* 32.514 (2016), pp. 137–151. DOI: 10.22203/eCM.v032a09.

[49]   John F. DeLucca et al. "Human cartilage endplate permeability varies with degeneration and intervertebral disc site". In: *Journal of Biomechanics* 49.4 (2016), pp. 550–557. DOI: 10.1016/j.jbiomech.2016.01.007.

[50]   Andrea Malandrino et al. "On the Relative Relevance of Subject-Specific Geometries and Degeneration-Specific Mechanical Properties for the Study of Cell Death in Human Intervertebral Disk Models". In: *Frontiers in Bioengineering and Biotechnology* 3.February (2015), pp. 1–15. DOI: 10.3389/fbioe.2015.00005.

[51]   M A Adams et al. "The stages of disc degeneration as revealed by discograms." In: *The Journal of bone and joint surgery British volume* 68.1 (1986), pp. 36–41.

[52]   Jill P G Urban et al. "Degeneration of the intervertebral disc." In: *Arthritis research & therapy* 5.3 (2003), pp. 120–130. DOI: 10.1186/ar629.

[53]   Adams MA. "Biomechanics of back pain". In: *Acupuncture in Medicine* 22.4 (2004), pp. 178–188. DOI: 10.1136/aim.22.4.178.

[54]   Riaz Akhtar et al. "Mechanical Properties of Aging Soft Tissues". In: *Mechanical Properties of Aging Soft Tissues* (2015), pp. 7–35. DOI: 10.1007/978-3-319-03970-1.

[55]   N Aruna et al. "Transmission of the weight through the neural arch of lumbar vertebrae in man". In: *J Anat. Soc. India* 52.2 (2003), pp. 128–131.

[56] Themis Toumanidou et al. "Musculoskeletal Modeling of the Lumbar Spine to Explore Functional Interactions between Back Muscle Loads and Intervertebral Disk Multiphysics." In: *Frontiers in bioengineering and biotechnology* 3.August (Jan. 2015), p. 111. DOI: `10.3389/fbioe.2015.00111`.

[57] Sébastien Demers et al. "Analytical evaluation of stresses and displacements of an intervertebral disc". In: *Journal of Biomechanical Science and Engineering* 12.3 (2017), pp. 16–00675–16–00675. DOI: `10.1299/jbse.16-00675`.

[58] Tuncay Kaner et al. "Comparison of disc and body volumes in degenerated and nondegenerated lumbar discs: A stereological study". In: *Turkish Journal of Medical Sciences* 44.2 (2014), pp. 237–242. DOI: `10.3906/sag-1208-45`.

[59] Thomas R. Oxland. "Fundamental biomechanics of the spine-What we have learned in the past 25 years and future directions". In: *Journal of Biomechanics* 49.6 (2015), pp. 817–832. DOI: `10.1016/j.jbiomech.2015.10.035`.

[60] Augustus A. White et al. *Clinical biomechanics of the spine.* Lippincott, 1978, p. 534. ISBN: 0397503881.

[61] J R Meakin et al. "Replacing the nucleus pulposus of the intervertebral disk : prediction of suitable properties of a replacement material using finite element analysis". In: *Journal of Materials Science: materials in medicine* 2 (2001), pp. 207–213.

[62] M H Krag et al. "Internal displacement distribution from in vitro loading of human thoracic and lumbar spinal motion segments: experimental results and theoretical predictions." In: *Spine* 12.10 (Dec. 1987), pp. 1001–7.

[63] H.L. Guerin et al. "Quantifying the Contributions of Structure to Annulus Fibrosus Mechanical Function Using a Nonlinear, Anisotropic, Hyperelastic Model". In: *Journal of orthopaedic research* 11.4 (2006), pp. 1609–1612. DOI: `10.1002/jor.20324`. arXiv: 85.

[64] Uta Lange et al. "Anterior vertebral body replacement with a titanium implant of adjustable height: A prospective clinical study". In: *European Spine Journal* (2007). DOI: `10.1007/s00586-005-0015-6`.

[65] Karin D. van den Eerenbeemt et al. "Total disc replacement surgery for symptomatic degenerative lumbar disc disease: a systematic review of the literature". In: *European Spine Journal* 19.8 (Aug. 2010), pp. 1262–1280. DOI: `10.1007/s00586-010-1445-3`.

[66] C. Schizas et al. "Disc degeneration: current surgical options". In: *European Cells and Materials* 20 (2010), pp. 306–315. DOI: `10.22203/eCM.v020a25`.

[67] P. E. Moreau et al. "Radiologic adjacent segment degeneration 2 years after lumbar fusion for degenerative spondylolisthesis". In: *Orthopaedics and Traumatology: Surgery and Research* 102.6 (2016), pp. 759–763. DOI: 10.1016/j.otsr.2016.03.012.

[68] Amir Abbas Ghasemi. "Adjacent segment degeneration after posterior lumbar fusion: An analysis of possible risk factors". In: *Clinical Neurology and Neurosurgery* 143 (2016), pp. 15–18. DOI: 10.1016/j.clineuro.2016.02.004.

[69] Paul Willems et al. "Clinical decision making in spinal fusion for chronic low back pain. Results of a nationwide survey among spine surgeons." In: *BMJ open* 1.2 (Jan. 2011), e000391. DOI: 10.1136/bmjopen-2011-000391.

[70] J N Gibson et al. "The Cochrane review of surgery for lumbar disc prolapse and degenerative lumbar spondylosis." In: *Spine* 24.17 (Sept. 1999), pp. 1820–32.

[71] Ulrich Berlemann et al. "An injectable nucleus replacement as an adjunct to microdiscectomy: 2 year follow-up in a pilot clinical study." In: *European spine journal : official publication of the European Spine Society, the European Spinal Deformity Society, and the European Section of the Cervical Spine Research Society* 18.11 (Nov. 2009), pp. 1706–12. DOI: 10.1007/s00586-009-1136-0.

[72] Peter M Klara et al. "Artificial nucleus replacement: clinical experience." In: *Spine* 27.12 (June 2002), pp. 1374–7.

[73] Rick C. Sasso et al. "Prospective, Randomized Trial of Metal-on-Metal Artificial Lumbar Disc Replacement". In: *Spine* 33.2 (Jan. 2008), pp. 123–131. DOI: 10.1097/BRS.0b013e31816043af.

[74] Jianjiang Pan et al. "Coexistence of intervertebral disc herniation with intradural schwannoma in a lumbar segment: a case report." In: *World journal of surgical oncology* 14 (Apr. 2016), p. 113. DOI: 10.1186/s12957-016-0864-y.

[75] A Landi. "Interspinous posterior devices: What is the real surgical indication?" In: *World Journal of Clinical Cases* 2.9 (2014), p. 402. DOI: 10.12998/wjcc.v2.i9.402.

[76] Roberto Gazzeri et al. "Controversies about Interspinous Process Devices in the Treatment of Degenerative Lumbar Spine Diseases : Past , Present , and Future". In: *BioMed Research International* 2014 (2014).

[77] G Bonaldi et al. "Minimally-invasive posterior lumbar stabilization for degenerative low back pain and sciatica. A review". In: *European Journal of Radiology* 84 (2015), pp. 789–798. DOI: 10.1016/j.ejrad.2014.04.012.

[78] Rui Zhu et al. "Considerations when loading spinal finite element models with predicted muscle forces from inverse static analyses". In: *Journal of Biomechanics* 46.7 (2013), pp. 1376–1378. DOI: 10.1016/j.jbiomech.2013.03.003.

[79] Hendrik Schmidt et al. "Application of a new calibration method for a three-dimensional finite element model of a human lumbar annulus fibrosus". In: *Clinical Biomechanics* 21.4 (2006), pp. 337–344. DOI: 10.1016/j.clinbiomech.2005.12.001.

[80] Hendrik Schmidt et al. "Effect of multilevel lumbar disc arthroplasty on spine kinematics and facet joint loads in flexion and extension: A finite element analysis". In: *European Spine Journal* 21.SUPPL. 5 (2012). DOI: 10.1007/s00586-010-1382-1.

[81] Mohammad Ali Rajaee et al. "Comparative evaluation of six quantitative lifting tools to estimate spine loads during static activities". In: *Applied Ergonomics* 48 (2015), pp. 22–32. DOI: 10.1016/j.apergo.2014.11.002.

[82] Frank Heuer et al. "The relation between intervertebral disc bulging and annular fiber associated strains for simple and complex loading". In: 41 (2008), pp. 1086–1094. DOI: 10.1016/j.jbiomech.2007.11.019.

[83] Marco Viceconti et al. "Extracting clinically relevant data from finite element simulations." In: *Clinical biomechanics (Bristol, Avon)* 20.5 (June 2005), pp. 451–4. DOI: 10.1016/j.clinbiomech.2005.01.010.

[84] O C Zienkiewicz et al. "The Finite Element Method Volume 1 : The Basis". In: *Methods* 1 (2000), p. 708.

[85] Steve A. Maas et al. "FEBio: Finite Elements for Biomechanics". In: *Journal of Biomechanical Engineering* 134.1 (2012), p. 011005. DOI: 10.1115/1.4005694.

[86] T. Belytschko et al. "Finite element stress analysis of an intervertebral disc". In: *Journal of Biomechanics* 7 (1974), pp. 277–285. DOI: 10.1016/0021-9290(74)90019-0.

[87] Dana J. Coombs et al. "Efficient probabilistic finite element analysis of a lumbar motion segment". In: *Journal of Biomechanics* 61 (2017), pp. 65–74. DOI: 10.1016/j.jbiomech.2017.07.002.

[88] Ruoxun Fan et al. "Effects of resting modes on human lumbar spines with different levels of degenerated intervertebral discs: a finite element investigation." In: *BMC musculoskeletal disorders* 16.1 (2015), p. 221. DOI: 10.1186/s12891-015-0686-z.

[89] Narjes Momeni Shahraki et al. "On the Use of Biaxial Properties in Modeling Annulus as a Holzapfel Gasser Ogden Material". In: *Frontiers in Bioengineering and Biotechnology* 3.June (2015), pp. 1–9. DOI: 10.3389/fbioe.2015.00069.

[90] Won Man Park et al. "Effects of degenerated intervertebral discs on intersegmental rotations, intradiscal pressures, and facet joint forces of the whole lumbar spine". In: *Computers in Biology and Medicine* 43.9 (2013), pp. 1234–1240. DOI: 10.1016/j.compbiomed.2013.06.011.

[91] DJ Coombs et al. "Stepwise validated finite element model of the human lumbar spine". In: *Simulia Customer Conference* Ddd (2012), pp. 1–15.

[92] Susan M. Renner et al. "Novel model to analyze the effect of a large compressive follower pre-load on range of motions in a lumbar spine". In: *Journal of Biomechanics* 40.6 (2007), pp. 1326–1332. DOI: 10.1016/j.jbiomech.2006.05.019.

[93] Francisco Ezquerro et al. "Combination of finite element modeling and optimization for the study of lumbar spine biomechanics considering the 3D thorax-pelvis orientation". In: *Medical Engineering and Physics* 26.1 (2004), pp. 11–22. DOI: 10.1016/S1350-4533(03)00128-0.

[94] Antonius Rohlmann et al. "Comparison of the effects of bilateral posterior dynamic and rigid fixation devices on the loads in the lumbar spine: A finite element analysis". In: *European Spine Journal* 16.8 (2007), pp. 1223–1231. DOI: 10.1007/s00586-006-0292-8.

[95] M. Dreischarf et al. "Comparison of eight published static finite element models of the intact lumbar spine: Predictive power of models improves when combined together". In: *Journal of Biomechanics* 47.8 (2014), pp. 1757–1766. DOI: 10.1016/j.jbiomech.2014.04.002.

[96] Chin-chun Lan et al. "Finite element analysis of biomechanical behavior of whole thoraco-lumbar spine with ligamentous effect". In: *The Changhua Journal of Medicine* 11 (2013), pp. 26–41.

[97] R N Natarajan et al. "Modeling the annular incision in a herniated lumbar intervertebral disk to study its effect on disk stability". In: 64 (1997).

[98] S Kumaresan et al. "Finite element analysis of the cervical spine: a material property sensitivity study." In: *Clinical biomechanics (Bristol, Avon)* 14.1 (Jan. 1999), pp. 41–53.

[99]   M.M. Rahman A.Zulkifli A.K. Ariffin. "Probabilistic finite element analysis of vertebrae of the lumbar spine under hyperextension loading". In: *International Journal of Automotive andMechanical Engineering (IJAME)* 3.June (2011), pp. 256–264.

[100] Fazilat H Dar et al. "Statistical methods in finite element analysis." In: *Journal of biomechanics* 35.9 (Sept. 2002), pp. 1155–61.

[101] Peter J. Laz et al. "Incorporating uncertainty in mechanical properties for finite element-based evaluation of bone mechanics". In: *Journal of Biomechanics* 40.13 (2007), pp. 2831–2836. DOI: `10.1016/j.jbiomech.2007.03.013`.

[102] Daniel M. Espino et al. "Stochastic finite element analysis of biological systems: Comparison of a simple intervertebral disc model with experimental results". In: *Computer Methods in Biomechanics and Biomedical Engineering* 6.4 (2003), pp. 243–248. DOI: `10.1080/10255840310001606071`.

[103] A Rohlmann et al. "Comparison of intradiscal pressures and spinal fixator loads for different body positions and exercises". In: *Ergonomics* 44.8 (2001), pp. 781–794. DOI: `10.1080/00140130120943`.

[104] J Noailly et al. *Computational modelling of spinal implants*. Woodhead Publishing Limited, 2014, pp. 447–484. ISBN: 9780857096739.

[105] Hung Ming Lin et al. "Biomechanical comparison of the K-ROD and Dynesys dynamic spinal fixator systems-A finite element analysis". In: *Bio-Medical Materials and Engineering* 23.6 (2013), pp. 495–505. DOI: `10.3233/BME-130766`.

[106] Chiara Maria Bellini et al. "Biomechanics of the Lumbar Spine After Dynamic Stabilization". In: *Journal of Spinal Disorders & Techniques* 20.6 (2007), pp. 423–429. DOI: `10.1097/BSD.0b013e318031af6f`.

[107] Alison C Jones et al. "Finite element analysis of the spine: towards a framework of verification, validation and sensitivity analysis." In: *Medical engineering & physics* 30.10 (Dec. 2008), pp. 1287–304. DOI: `10.1016/j.medengphy.2008.09.006`.

[108] Daniel J. Cook et al. "Variability of manual lumbar spine segmentation". In: *International Journal of Spine Surgery* 6.1 (2012), pp. 167–173. DOI: `10.1016/j.ijsp.2012.04.002`.

[109] Marco Pereanez et al. "Accurate Segmentation of Vertebral Bodies and Processes Using Statistical Shape Decomposition and Conditional Models". In: *IEEE Transactions on Medical Imaging* 34.8 (2015), pp. 1627–1639. DOI: `10.1109/TMI.2015.2396774`.

[110] C. E. Lavecchia et al. "Lumbar model generator: a tool for the automated generation of a parametric scalable model of the lumbar spine". In: *Journal of The Royal Society Interface* 15.138 (2018), p. 20170829. DOI: 10.1098/rsif.2017.0829.

[111] Kathryn B. Higgins et al. "Biomechanical Alterations in Intact Osteoporotic Spine Due to Synthetic Augmentation: Finite Element Investigation". In: *Journal of Biomechanical Engineering* 129.4 (Aug. 2007), p. 575. DOI: 10.1115/1.2746379.

[112] Cari M. Whyne et al. "Burst Fracture in the Metastatically Involved Spine". In: *Spine* 28.7 (Apr. 2003), pp. 652–660. DOI: 10.1097/01.BRS.0000051910.97211.BA.

[113] David Jean Biau et al. "Statistics in brief: The importance of sample size in the planning and interpretation of medical research". In: *Clinical Orthopaedics and Related Research* 466.9 (2008), pp. 2282–2288. DOI: 10.1007/s11999-008-0346-9.

[114] Frank Niemeyer et al. "Geometry strongly influences the response of numerical models of the lumbar spine–a probabilistic finite element analysis." In: *Journal of biomechanics* 45.8 (May 2012), pp. 1414–23. DOI: 10.1016/j.jbiomech.2012.02.021.

[115] J.Q. Campbell et al. "Automated Finite Element Meshing of the Lumbar Spine: Verification and Validation with 18 Specimen-Specific Models". In: *Journal of Biomechanics* 49 (2016), pp. 2669–2676. DOI: 10.1016/j.jbiomech.2016.05.025.

[116] J.Q. Campbell et al. "Automated Finite Element Modeling of the Lumbar Spine: Using a Statistical Shape Model to Generate a Virtual Population of Models". In: *Journal of Biomechanics* 49.13 (2016), pp. 1–7. DOI: 10.1016/j.jbiomech.2016.05.013.

[117] Vincent Pomero et al. "Fast accurate stereoradiographic 3D-reconstruction of the spine using a combined geometric and statistic model". In: *Clinical Biomechanics* 19.3 (2004), pp. 240–247. DOI: 10.1016/j.clinbiomech.2003.11.014.

[118] L. Humbert et al. "3D reconstruction of the spine from biplanar X-rays using parametric models based on transversal and longitudinal inferences". In: *Medical Engineering and Physics* 31.6 (2009), pp. 681–687. DOI: 10.1016/j.medengphy.2009.01.003.

[119] Victor M. Spitzer et al. "The visible human dataset: The anatomical platform for human simulation". In: *Anatomical Record* 253.2 (1998), pp. 49–57. DOI: 10.1002/(SICI)1097-0185(199804)253:2<49::AID-AR8>3.0.CO;2-9.

[120] Amir A. Zadpoor. "Mechanics of biological tissues and biomaterials: Current trends". In: *Materials* 8.7 (2015), pp. 4505–4511. DOI: `10.3390/ma8074505`.

[121] Anders Odgaard et al. "Fabric and elastic principal directions of cancellous bone are closely related". In: *Journal of Biomechanics* 30.5 (1997), pp. 487–495.

[122] Km Quapp et al. "Material characterization of human medial collateral ligament." In: *Journal of biomechanical engineering* 120.6 (1998), pp. 757–63. DOI: `10.1115/1.2834890`.

[123] Fabio Galbusera et al. "Material models and properties in the finite element analysis of knee ligaments: a literature review." In: *Frontiers in bioengineering and biotechnology* 2.November (2014), p. 54. DOI: `10.3389/fbioe.2014.00054`.

[124] Maoz Shemesh et al. "Viscoelastic properties of a synthetic meniscus implant". In: *Journal of the Mechanical Behavior of Biomedical Materials* 29 (2014), pp. 42–55. DOI: `10.1016/j.jmbbm.2013.08.021`.

[125] Aviad Sasson et al. "Hyperelastic mechanical behavior of chitosan hydrogels for nucleus pulposus replacement-Experimental testing and constitutive modeling". In: *Journal of the Mechanical Behavior of Biomedical Materials* 8 (2012), pp. 143–153. DOI: `10.1016/j.jmbbm.2011.12.008`.

[126] Deok-Kee Choi. "Mechanical characterization of biological tissues: Experimental methods based on mathematical modeling". In: *Biomedical Engineering Letters* 6.3 (2016), pp. 181–195. DOI: `10.1007/s13534-016-0222-6`.

[127] Gerhard A. Holzapfel et al. "A New Constitutive Framework for Arterial Wall Mechanics and a Comparative Study of Material Models". In: *Journal of Elasticity* 61.1/3 (2000), pp. 1–48. DOI: `10.1023/A:1010835316564`.

[128] T. C. Gasser et al. "Hyperelastic modelling of arterial layers with distributed collagen fibre orientations". In: *Journal of The Royal Society Interface* 3.6 (2006), pp. 15–35. DOI: `10.1098/rsif.2005.0073`. arXiv: `0312002v1 [arXiv:q-bio]`.

[129] G. Chagnon et al. "Hyperelastic Energy Densities for Soft Biological Tissues: A Review". In: *Journal of Elasticity* 120.2 (2015), pp. 129–160. DOI: `10.1007/s10659-014-9508-z`.

[130] Benedikt Helgason et al. "Mathematical relationships between bone density and mechanical properties: A literature review". In: *Clinical Biomechanics* 23.2 (2008), pp. 135–146.

[131]   A. Shirazi-Adl et al. "Spinal muscle forces, internal loads and sta-
        bility in standing under various postures and loads - Application
        of kinematics-based algorithm". In: *European Spine Journal* 14.4
        (2005), pp. 381–392. DOI: 10.1007/s00586-004-0779-0.

[132]   V K Goel et al. *Applications of the finite element method to thora-
        columbar spinal research–past, present, and future.* 1995.

[133]   S D Boden et al. "Orientation of the lumbar facet joints: association
        with degenerative disc disease." In: *The Journal of bone and joint
        surgery. American volume* 78.3 (1996), pp. 403–411.

[134]   J P Little et al. "Geometric sensitivity of patient-specific finite ele-
        ment models of the spine to variability in user-selected anatomical
        landmarks." In: *Computer methods in biomechanics and biomedical
        engineering* 5842.September 2014 (2013), pp. 37–41. DOI: 10.1080/
        10255842.2013.843673.

[135]   Mehrdad Shahmohammadi et al. "Finite element simulation of an
        artificial intervertebral disk using fiber reinforced laminated com-
        posite model". In: *Tissue and Cell* 46.5 (2014), pp. 299–303. DOI:
        10.1016/j.tice.2014.05.008.

[136]   Hendrik Schmidt et al. "Response analysis of the lumbar spine dur-
        ing regular daily activities–a finite element analysis." In: *Journal
        of biomechanics* 43.10 (July 2010), pp. 1849–56. DOI: 10.1016/j.
        jbiomech.2010.03.035.

[137]   Maren Freutel et al. "Finite element modeling of soft tissues: Material
        models, tissue interaction and challenges". In: *Clinical Biomechanics*
        29.4 (2014), pp. 363–372. DOI: 10.1016/j.clinbiomech.2014.01.
        006.

[138]   Gloria Casaroli et al. "A novel finite element model of the ovine lum-
        bar intervertebral disc with anisotropic hyperelastic material proper-
        ties". In: *PLoS ONE* 12.5 (2017), pp. 1–18. DOI: 10.1371/journal.
        pone.0177088.

[139]   R. Eberlein et al. "An Anisotropic Model for Annulus Tissue and
        Enhanced Finite Element Analyses of Intact Lumbar Disc Bodies".
        In: *Computer Methods in Biomechanics and Biomedical Engineering*
        4.3 (2001), pp. 209–229. DOI: 10.1080/10255840108908005.

[140]   Eric Wagnac et al. "Finite element analysis of the influence of load-
        ing rate on a model of the full lumbar spine under dynamic loading
        conditions". In: *Medical & Biological Engineering & Computing* 50.9
        (2012), pp. 903–915. DOI: 10.1007/s11517-012-0908-6.

[141]   Toumanidou T. "Finite element simulation of the healthy and degen-
        erated lumbar spine Themis Toumanidou". In: *PhD Thesis, Univer-
        sitat Politecnica de Catalunya* (2016).

[142] Antonius Rohlmann et al. "Analysis of the influence of disc degeneration on the mechanical behaviour of a lumbar motion segment using the finite element method". In: *Journal of Biomechanics* 39.13 (2006), pp. 2484–2490. DOI: 10.1016/j.jbiomech.2005.07.026.

[143] Vijay K. Goel et al. "Computational Modeling and Finite Element Analysis". In: *Spine* 41.7 (2016), S6–S7. DOI: 10.1097/BRS.0000000000001421.

[144] A N Natali et al. "Nonlinear Analysis of Intervertebral Disk Under Dynamic Load". In: *J. Biomech.* 112.August 1990 (1990), pp. 358–363.

[145] A A Rao et al. "Influence of material properties on the mechanical behaviour of the L & intervertebral disc in compression : a nonlinear finite element study". In: 13 (1991), pp. 139–151.

[146] Hendrik Schmidt et al. "Computational biomechanics of a lumbar motion segment in pure and combined shear loads". In: *Journal of Biomechanics* 46.14 (2013), pp. 2513–2521. DOI: 10.1016/j.jbiomech.2013.06.038.

[147] a Shirazi-Adl et al. "A finite element study of a lumbar motion segment subjected to pure sagittal plane moments." In: *Journal of biomechanics* 19.4 (Jan. 1986), pp. 331–50.

[148] Antonius Rohlmann et al. "Effect of an artificial disc on lumbar spine biomechanics: A probabilistic finite element study". In: *European Spine Journal* 18.1 (2009), pp. 89–97. DOI: 10.1007/s00586-008-0836-1.

[149] Shih Hao Chen et al. "Biomechanical comparison between lumbar disc arthroplasty and fusion". In: *Medical Engineering and Physics* 31.2 (2009), pp. 244–253. DOI: 10.1016/j.medengphy.2008.07.007.

[150] Srirangam Kumaresan et al. "Contribution of disc degeneration to osteophyte formation in the cervical spine: A biomechanical inverstigation". In: *Journal of Orthopaedic Research* 19.5 (2001), pp. 977–984. DOI: 10.1016/S0736-0266(01)00010-9.

[151] A. Rohlmann et al. "Applying a follower load delivers realistic results for simulating standing". In: *Journal of Biomechanics* 42.10 (2009), pp. 1520–1526. DOI: 10.1016/j.jbiomech.2009.03.048. arXiv: arXiv:1011.1669v3.

[152] M. Argoubi et al. "Poroelastic creep response analysis of a lumbar motion segment in compression". In: *Journal of Biomechanics* 29.10 (1996), pp. 1331–1339. DOI: 10.1016/0021-9290(96)00035-8.

[153] J P Little et al. "The effect of soft tissue properties on spinal flexibility in scoliosis: biomechanical simulation of fulcrum bending". In: *Spine (Phila Pa 1976)* 34.2 (2009), E76–82. DOI: 10.1097/BRS.0b013e31818ad584.

[154] Chen-Sheng Chen et al. "Stress analysis of the disc adjacent to inter-body fusion in lumbar spine." In: *Medical engineering {&} physics* 23.7 (2001), pp. 483–491. DOI: 10.1016/S1350-4533(01)00076-5.

[155] Antonius Rohlmann et al. "Determination of trunk muscle forces for flexion and extension by using a validated finite element model of the lumbar spine and measured in vivo data". In: *Journal of Biomechanics* 39.6 (2006), pp. 981–989. DOI: 10.1016/j.jbiomech.2005.02.019.

[156] Frank A. Pintar et al. "Biomechanical properties of human lumbar spine ligaments". In: *Journal of Biomechanics* 25.11 (1992), pp. 1351–1356. DOI: 10.1016/0021-9290(92)90290-H.

[157] M A Adams et al. "The resistance to flexion of the lumbar interver-tebral joint." In: *Spine* 5.3 (), pp. 245–53.

[158] J Chazal et al. "Biomechanical properties of spinal ligaments and a histological study of the supraspinal ligament in traction." In: *Journal of biomechanics* 18.3 (1985), pp. 167–76.

[159] S. Naserkhaki et al. "Effects of eight different ligament property datasets on biomechanics of a lumbar L4-L5 finite element model". In: *Journal of Biomechanics* (2017). DOI: 10.1016/j.jbiomech.2017.05.003.

[160] Divya V. Ambati et al. "Bilateral pedicle screw fixation provides su-perior biomechanical stability in transforaminal lumbar interbody fu-sion: A finite element study". In: *Spine Journal* 15.8 (2015), pp. 1812–1822. DOI: 10.1016/j.spinee.2014.06.015.

[161] Nadine Lalonde et al. "Method to geometrically personalize a de-tailed finite element model of the spine To cite this version : Method to geometrically personalize a detailed finite element model of the spine". In: (2013).

[162] Sadegh Naserkhaki et al. "On the load-sharing along the ligamentous lumbosacral spine in flexed and extended postures: Finite element study". In: *Journal of Biomechanics* 49.6 (2016), pp. 974–982. DOI: 10.1016/j.jbiomech.2015.09.050.

[163] Pierre Roussouly et al. "Classification of the normal variation in the sagittal alignment of the human lumbar spine and pelvis in the stand-ing position." In: *Spine* 30.3 (2005), pp. 346–353. DOI: 10.1097/01.brs.0000152379.54463.65.

[164] Tobias Heimann et al. "Statistical shape models for 3D medical im-age segmentation: A review". In: *Medical Image Analysis* 13.4 (2009), pp. 543–563. DOI: 10.1016/j.media.2009.05.004. arXiv: NIHMS150003.

[165] Marcel Dreischarf et al. "Is it possible to estimate the compressive force in the lumbar spine from intradiscal pressure measurements? A finite element evaluation". In: *Medical Engineering and Physics* 35.9 (2013), pp. 1385–1390. DOI: 10.1016/j.medengphy.2013.03.007.

[166] J L Wang et al. "Viscoelastic finite-element analysis of a lumbar motion segment in combined compression and sagittal flexion. Effect of loading rate." In: *Spine* 25.3 (Feb. 2000), pp. 310–8.

[167] C E Aubin et al. "Morphometric evaluations of personalised 3D reconstructions and geometric models of the human spine." In: *Medical & biological engineering & computing* 35.6 (Nov. 1997), pp. 611–8.

[168] Daniel H. Cortes et al. "Elastic, permeability and swelling properties of human intervertebral disc tissues: A benchmark for tissue engineering". In: *Journal of Biomechanics* 47.9 (2014), pp. 2088–2094. DOI: 10.1016/j.jbiomech.2013.12.021.

[169] John M. Peloquin et al. "A comparison of stress in cracked fibrous tissue specimens with varied crack location, loading, and orientation using finite element analysis". In: *Journal of the Mechanical Behavior of Biomedical Materials* 57 (2016), pp. 260–268. DOI: 10.1016/j.jmbbm.2015.12.004.

[170] Jérôme Noailly et al. "Finite element modelling of the spine". In: *Biomaterials for Spinal Surgery* (2012), pp. 144–232. DOI: 10.1016/B978-1-84569-986-4.50005-2.

[171] Jérôme Noailly et al. "On the collagen criss-cross angles in the annuli fibrosi of lumbar spine finite element models". In: *Biomechanics and Modeling in Mechanobiology* 10.2 (2011), pp. 203–219. DOI: 10.1007/s10237-010-0227-5.

[172] Marek Pawlikowski et al. "Advanced finite element analysis of L4-L5 implanted spine segment". In: *Continuum Mechanics and Thermodynamics* (2014), pp. 1–12. DOI: 10.1007/s00161-014-0342-0.

[173] Tito Bassani et al. "Validation of the AnyBody full body musculoskeletal model in computing lumbar spine loads at L4L5 level". In: *Journal of Biomechanics* 58 (2017), pp. 89–96. DOI: 10.1016/j.jbiomech.2017.04.025.

[174] Miguel Christophy et al. "A Musculoskeletal model for the lumbar spine". In: *Biomechanics and Modeling in Mechanobiology* 11.1-2 (2012), pp. 19–34. DOI: 10.1007/s10237-011-0290-6.

[175] Marcel Dreischarf et al. "Different arm positions and the shape of the thoracic spine can explain contradictory results in the literature about spinal loads for sitting and standing". In: *Spine* 35.22 (2010), pp. 2015–2021. DOI: 10.1097/BRS.0b013e3181d55d52.

[176] H. J. Wilke et al. "Testing criteria for spinal implants: Recommendations for the standardization of in vitro stability testing of spinal implants". In: *European Spine Journal* 7.2 (1998), pp. 148–154. DOI: 10.1007/s005860050045.

[177] Marcel Dreischarf et al. "Optimised loads for the simulation of axial rotation in the lumbar spine". In: (2011). DOI: 10.1016/j.jbiomech.2011.05.040.

[178] Ugur M Ayturk et al. "Parametric convergence sensitivity and validation of a finite element model of the human lumbar spine." In: *Computer methods in biomechanics and biomedical engineering* 14.March 2015 (2011), pp. 695–705. DOI: 10.1080/10255842.2010.493517.

[179] Thomas Zander et al. "Influence of different artificial disc kinematics on spine biomechanics". In: *Clinical Biomechanics* 24.2 (2009), pp. 135–142. DOI: 10.1016/j.clinbiomech.2008.11.008.

[180] A. Shirazi-Adl et al. "Load-bearing and stress analysis of the human spine under a novel wrapping compression loading". In: *Clinical Biomechanics* 15.10 (2000), pp. 718–725. DOI: 10.1016/S0268-0033(00)00045-0.

[181] J. P. Little et al. "Are coupled rotations in the lumbar spine largely due to the osseo-ligamentous anatomy? A modeling study". In: *Computer Methods in Biomechanics and Biomedical Engineering* 11.1 (Feb. 2008), pp. 95–103. DOI: 10.1080/10255840701552143.

[182] Michael Putzer et al. "Sensitivity of lumbar spine loading to anatomical parameters". In: *Journal of Biomechanics* 49.6 (2016), pp. 953–958. DOI: 10.1016/j.jbiomech.2015.11.003.

[183] M J Fagan et al. "Patient-specific spine models. Part 1: Finite element analysis of the lumbar intervertebral disc - A material sensitivity study". In: *Proceedings of the Institution of Mechanical Engineers, Part H: Journal of Engineering in Medicine* 216 (2002), pp. 299–314. DOI: 10.1243/09544110260216577.

[184] Y E Kim et al. "Effect of disc degeneration at one level on the adjacent level in axial mode." In: *Spine* 16.3 (Mar. 1991), pp. 331–5.

[185] N Inoue et al. "Biomechanics of Intervertebral Disc Degeneration". In: *Orthop Clin North Am* 42.4 (2011), pp. 487–499. DOI: 10.1016/j.ocl.2011.07.001.Biomechanics.

[186] Raghu N. Natarajan et al. "Modeling Changes in Intervertebral Disc Mechanics with Degeneration". In: *The Journal of Bone and Joint Surgery (American)* 88.suppl_2 (Apr. 2006), p. 36. DOI: 10.2106/JBJS.F.00002.

[187] J. Cegoñino et al. "A constitutive model for the annulus of human intervertebral disc (IVD): implications for developing a degeneration model and its influence on lumbar spine functioning". In: *Journal of Applied Mathematics* 2014.April 2014 (2014). DOI: `10.1155/2014/658719`.

[188] James C. Iatridis et al. "Mechanisms for mechanical damage in the intervertebral disc annulus fibrosus". In: *Journal of Biomechanics* 37.8 (2004), pp. 1165–1175. DOI: `10.1016/j.jbiomech.2003.12.026`.

[189] Marco Viceconti et al. "Automatic generation of accurate subject-specific bone finite element models to be used in clinical studies". In: *Journal of Biomechanics* 37.10 (2004), pp. 1597–1605.

[190] A Nachemson. "Towards a better understanding of low-back pain: a review of the mechanics of the lumbar disc." In: *Rheumatology and rehabilitation* 14.3 (Aug. 1975), pp. 129–43.

[191] A L Nachemson. "Disc pressure measurements." In: *Spine* 6.1 (), pp. 93–7.

[192] A Nachemson et al. "In vivo measurements of intradiscal pressure. Discometry, a method for the determination of pressure in the lower lumbar discs". In: *The Journal of bone and joint surgery. American volume* 46 (July 1964), pp. 1077–92.

[193] Hans-Joachim Wilke et al. "Intradiscal pressure together with anthropometric data a data set for the validation of models". In: *Clinical Biomechanics* 16, Supple.1 (2001), S111–S126. DOI: `10.1016/S0268-0033(00)00103-0`.

[194] David J Polga et al. "Measurement of in vivo intradiscal pressure in healthy thoracic intervertebral discs." In: *Spine* 29.12 (June 2004), pp. 1320–4.

[195] Marcel Dreischarf et al. "Estimation of loads on human lumbar spine: A review of in vivo and computational model studies". In: *Journal of Biomechanics* 49.6 (2016), pp. 833–845. DOI: `10.1016/j.jbiomech.2015.12.038`.

[196] N. Arjmand et al. "Predictive equations to estimate spinal loads in symmetric lifting tasks". In: *Journal of Biomechanics* 44.1 (2011), pp. 84–91. DOI: `10.1016/j.jbiomech.2010.08.028`.

[197] Yuichi Kasai et al. "Biomechanical study of the lumbar spine using a unilateral pedicle screw fixation system". In: 3 (), pp. 364–367. DOI: `10.1016/j.jocn.2009.06.017`.

[198] Sabrina A. Gonzalez-Blohm et al. "The current testing protocols for biomechanical evaluation of lumbar spinal implants in laboratory setting: A review of the literature". In: *BioMed Research International* 2015 (2015). DOI: 10.1155/2015/506181.

[199] E. C. Bass et al. "Biaxial testing of human annulus fibrosus and its implications for a constitutive formulation". In: *Annals of Biomedical Engineering* 32.9 (2004), pp. 1231–1242. DOI: 10.1114/B:ABME. 0000039357.70905.94.

[200] O'Connell, Grace D. and Sen, Sounok and Elliott, Dawn M. "Human annulus fibrosus material properties from biaxial testing and constitutive modeling are altered with degeneration". In: *Biomechanics and Modeling in Mechanobiology* 11.3-4 (2012), pp. 493–503. DOI: 10.1007/s10237-011-0328-9. arXiv: NIHMS150003.

[201] Balkan Cakir et al. "Resect or not to resect: The role of posterior longitudinal ligament in lumbar total disc replacement". In: *European Spine Journal* 21.SUPPL. 5 (2012), pp. 592–598. DOI: 10.1007/ s00586-009-1193-4.

[202] Yuichi Kasai et al. "Biomechanical study of the lumbar spine using a unilateral pedicle screw fixation system". In: *Journal of Clinical Neuroscience* 17.3 (Mar. 2010), pp. 364–367. DOI: 10.1016/j.jocn. 2009.06.017.

[203] Angela D. Melnyk et al. "An In Vitro Model of Degenerative Lumbar Spondylolisthesis". In: *Spine* 38.14 (June 2013), E870–E877. DOI: 10. 1097/BRS.0b013e3182945897.

[204] Avraam Ploumis et al. "Revision of transforaminal lumbar interbody fusion using anterior lumbar interbody fusion: a biomechanical study in nonosteoporotic bone". In: *Journal of Neurosurgery: Spine* 12.1 (Jan. 2010), pp. 82–87. DOI: 10.3171/2009.7.SPINE0921.

[205] Selvon St. Clair et al. "Oblique Lumbar Interbody Fixation". In: *Journal of Spinal Disorders & Techniques* 25.4 (June 2012), pp. 183– 189. DOI: 10.1097/BSD.0b013e318211fc6b.

[206] Xiujun Zheng et al. "Biomechanical evaluation of an expandable meshed bag augmented with pedicle or facet screws for percutaneous lumbar interbody fusion". In: *The Spine Journal* 10.11 (Nov. 2010), pp. 987–993. DOI: 10.1016/j.spinee.2010.08.016.

[207] Yang Zhang et al. "Comparison of the Dynesys Dynamic Stabilization System and Posterior Lumbar Interbody Fusion for Lumbar Degenerative Disease." In: *PloS one* 11.1 (2016), e0148071. DOI: 10.1371/ journal.pone.0148071.

[208] Viktor Bartanusz et al. "Spinal Instrumentation after Complete Resection of the Last Lumbar Vertebra". In: *Spine* 36.13 (June 2011), pp. 1017–1021. DOI: 10.1097/BRS.0b013e3181e92458.

[209] Sergiu Botolin et al. "Facet Joint Biomechanics at the Treated and Adjacent Levels After Total Disc Replacement". In: *Spine* 36.1 (Jan. 2011), E27–E32. DOI: 10.1097/BRS.0b013e3181d2d071.

[210] Hakan Bozkus et al. "Dynamic lumbar pedicle screw-rod stabilization: in vitro biomechanical comparison with standard rigid pedicle screw-rod stabilization". In: *Journal of Neurosurgery: Spine* 12.2 (Feb. 2010), pp. 183–189. DOI: 10.3171/2009.9.SPINE0951.

[211] Mario J. Cardoso et al. "Does Superior-Segment Facet Violation or Laminectomy Destabilize the Adjacent Level in Lumbar Transpedicular Fixation?" In: *Spine* 33.26 (Dec. 2008), pp. 2868–2873. DOI: 10.1097/BRS.0b013e31818c63d3.

[212] Neil R. Crawford et al. "In Vitro Biomechanical Analysis of a New Lumbar Low-Profile Locking Screw-Plate Construct Versus a Standard Top-Loading Cantilevered Pedicle Screw-Rod Construct". In: *Neurosurgery* 66.2 (Feb. 2010), E404–E406. DOI: 10.1227/01.NEU.0000363701.76835.BF.

[213] Bryan W. Cunningham et al. "Revision strategies for single- and two-level total disc arthroplasty procedures: a biomechanical perspective". In: *The Spine Journal* 9.9 (Sept. 2009), pp. 735–743. DOI: 10.1016/j.spinee.2009.03.011.

[214] Karl-Stefan Delank et al. "How does spinal canal decompression and dorsal stabilization affect segmental mobility? A biomechanical study". In: *Archives of Orthopaedic and Trauma Surgery* 130.2 (Feb. 2010), pp. 285–292. DOI: 10.1007/s00402-009-1002-x.

[215] Karl-Stefan Delank et al. "How does spinal canal decompression and dorsal stabilization affect segmental mobility? A biomechanical study". In: *Archives of Orthopaedic and Trauma Surgery* 130.2 (Feb. 2010), pp. 285–292. DOI: 10.1007/s00402-009-1002-x.

[216] Serkan Erkan et al. "Biomechanical comparison of a two-level Maverick disc replacement with a hybrid one-level disc replacement and one-level anterior lumbar interbody fusion". In: *The Spine Journal* 9.10 (Oct. 2009), pp. 830–835. DOI: 10.1016/j.spinee.2009.04.014.

[217] Yoshi Fujita et al. "Radial Tensile Properties". In: *Bioengineering* (1997), pp. 814–819.

[218] S M Klisch et al. "Application of a fiber-reinforced continuum theory to multiple deformations of the annulus fibrosus." In: *Journal of biomechanics* 32.10 (Oct. 1999), pp. 1027–36.

[219] Lachlan J. Smith et al. "The elastic fibre network of the human lumbar anulus fibrosus: Architecture, mechanical function and potential role in the progression of intervertebral disc degeneration". In: *European Spine Journal* 18.4 (2009), pp. 439–448. DOI: `10.1007/s00586-009-0918-8`.

[220] Diane R. Wagner et al. "Theoretical model and experimental results for the nonlinear elastic behavior of human annulus fibrosus". In: *Journal of Orthopaedic Research* 22.4 (2004), pp. 901–909. DOI: `10.1016/j.orthres.2003.12.012`.

[221] M M Panjabi et al. "Cervical human vertebrae. Quantitative three-dimensional anatomy of the middle and lower regions." In: *Spine* 16.8 (Aug. 1991), pp. 861–9.

[222] Roop Singh et al. "Morphometric measurements of cadaveric thoracic spine in Indian population and its clinical applications." In: *Asian spine journal* 5.1 (Mar. 2011), pp. 20–34. DOI: `10.4184/asj.2011.5.1.20`.

[223] Yasufumi Hayashi et al. "Measurement of vertebral body dimensions of the thoracic and lumbar spines of 242 healthy women". In: *Journal of bone and mineral metabolism* 16 (1998), pp. 27–33.

[224] Disco Vertebral et al. "Evaluation of Lumbar Vertebral Body and Disc : A Stereological Morphometric Study". In: 28.3 (2010), pp. 841–847.

[225] Sajal R Mitra et al. "Morphometric study of the lumbar pedicle in the Indian population as related to pedicular screw fixation." In: *Spine* 27.5 (2002), pp. 453–459. DOI: `10.1097/00007632-200203010-00004`.

[226] Maria E. Kunkel et al. "Prediction of the human thoracic and lumbar articular facet joint morphometry from radiographic images". In: *Journal of Anatomy* 218.2 (2011), pp. 191–201. DOI: `10.1111/j.1469-7580.2010.01323.x`.

[227] Ron Kikinis et al. "3D Slicer: A Platform for Subject-Specific Image Analysis, Visualization, and Clinical Support". In: *Intraoperative Imaging and Image-Guided Therapy*. New York, NY: Springer New York, 2014, pp. 277–289. DOI: `10.1007/978-1-4614-7657-3_19`.

[228] Nicolas Newell et al. "A comparison of four techniques to measure anterior and posterior vertebral body heights and sagittal plane wedge angles in adolescent idiopathic scoliosis". In: *Medical and Biological Engineering and Computing* 55.4 (2017), pp. 561–572. DOI: `10.1007/s11517-016-1520-y`.

[229] Markus Bastir et al. "Three-dimensional analysis of sexual dimorphism in human thoracic vertebrae: Implications for the respiratory system and spine morphology". In: *American Journal of Physical Anthropology* 155.4 (2014), pp. 513–521. DOI: 10.1002/ajpa.22604.

[230] L. T. TWOMEY J. R. TAYLOR. "Sexual dimorphism in human vertebral body shape". In: *Journal of Anatomy* (1984). DOI: PMC1164068.

[231] G A Aitchison et al. "A Review of the Design Process for Implantable Orthopedic Medical Devices". In: *The Open Biomedical Engineering Journal* 3 (2009), pp. 21–27. DOI: 10.2174/1874120700903010021.

[232] J. Paige Little et al. "Parametric equations to represent the profile of the human intervertebral disc in the transverse plane". In: *Medical and Biological Engineering and Computing* 45.10 (2007), pp. 939–945. DOI: 10.1007/s11517-007-0242-6.

[233] Nicola Cappetti et al. "Parametric model of lumbar vertebra". In: *Journal of Industrial Design and Engineering Graphics* 5.2 (2010), pp. 15–18.

[234] F Lavaste et al. "Three-dimensional geometrical and mechanical modelling of the lumbar spine." In: *Journal of biomechanics* 25.10 (Oct. 1992), pp. 1153–64.

[235] L Monède-Hocquard et al. "An optimisation approach of a new dynamic spinal device". In: *Computer Methods in Biomechanics and Biomedical Engineering* 15.sup1 (2012), pp. 321–323. DOI: 10.1080/10255842.2012.713647.

[236] Chang Hwa Hong et al. "Measurement of the normal lumbar intervertebral disc space". In: *Asian spine journal* 4.1 (June 2010), pp. 1–6. DOI: 10.4184/asj.2010.4.1.1.

[237] S H Zhou et al. "Geometrical dimensions of the lower lumbar vertebrae–analysis of data from digitised CT images." In: *European spine journal : official publication of the European Spine Society, the European Spinal Deformity Society, and the European Section of the Cervical Spine Research Society* 9.3 (June 2000), pp. 242–8.

[238] Marwan El-Rich et al. "Finite element investigation of the loading rate effect on the spinal load-sharing changes under impact conditions". In: *Journal of Biomechanics* 42.9 (2009), pp. 1252–1262. DOI: 10.1016/j.jbiomech.2009.03.036.

[239] J. M. Peloquin et al. "A model for intervertebral disc shape variation in a population including the effect of degeneration". In: *2012 38th Annual Northeast Bioengineering Conference, NEBEC 2012* (2012), pp. 283–284. DOI: 10.1109/NEBC.2012.6207075.

[240] D R Jason et al. "Estimation of stature from the length of the cervical, thoracic, and lumbar segments of the spine in American whites and blacks." In: *Journal of forensic sciences* 40.1 (Jan. 1995), pp. 59–62.

[241] Kevin Mattheus Moerman. "GIBBON (Hylobates Lar)". In: (Jan. 2017). DOI: `10.5281/ZENODO.44404`.

[242] H Si. "A quality tetrahedral mesh generator and a 3d delaunay triangulator". In: *UR L http://tetgen. berlios. de* 13 (2010).

[243] Jonathan Richard Shewchuk. "What is a Good Linear Element ? Interpolation , Conditioning , and Quality Measures". In: *Eleventh International Meshing Roundtable* (2002), pp. 115–126. DOI: `10.1.1.68.8538`.

[244] Michael Holst Zhanheng Gao, Zeyun Yu. "Quality tetrahedral mesh smoothing via Boundary-Optimized Delaunay Triangulation". In: *Comput Aided Geom Des* 9.1 (2012), pp. 707–721. DOI: `10.3816/CLM.2009.n.003.Novel`. arXiv: `NIHMS150003`.

[245] Jun Wang et al. "Feature-sensitive tetrahedral mesh generation with guaranteed quality". In: *Comput Aided Geom Des* 44.5 (2012), pp. 400–412. DOI: `10.1016/j.immuni.2010.12.017.Two-stage`. arXiv: `NIHMS150003`.

[246] Dana Müller-Hoeppe. "Comparison of Tetrahedral and Brick Elements for Linear Elastic Analysis". In: *ASEN 5367* (2006).

[247] Zengwu Shao et al. "Radiographic changes in the lumbar intervertebral discs and lumbar vertebrae with age." In: *Spine* 27.3 (Feb. 2002), pp. 263–8.

[248] Ella Been et al. "Geometry of the vertebral bodies and the intervertebral discs in lumbar segments adjacent to spondylolysis and spondylolisthesis: pilot study". In: *Eur Spine J* (2011). DOI: `10.1007/s00586-010-1660-y`.

[249] G P Konin et al. "Lumbosacral Transitional Vertebrae: Classification, Imaging Findings, and Clinical Relevance". In: *Americal Journal of Neuroradiology* 31 (2010). DOI: `10.3174/ajnr.A2036`.

[250] Masaaki Chazono et al. "Ethnic differences in pedicle and bony spinal canal dimensions calculated from computed tomography of the cervical spine: A review of the English-language literature". In: *European Spine Journal* 21.8 (2012), pp. 1451–1458. DOI: `10.1007/s00586-012-2295-y`.

[251] K. K. Lee et al. "Finite-Element Analysis for Lumbar Interbody Fusion under Axial Loading". In: *IEEE Transactions on Biomedical Engineering* 51.3 (2004), pp. 393–400. DOI: `10.1109/TBME.2003.820994`.

[252] Hector E Jaramillo et al. "A finite element model of the L4-L5-S1 human spine segment including the heterogeneity and anisotropy of the discs." In: *Acta of bioengineering and biomechanics / Wroclaw University of Technology* 17.2 (2015), pp. 15–24.

[253] N Maurel et al. "A three-dimensional parameterized Finite Element Model of the lower cervical spine. Study of the influence of the posterior articular facets". In: *Journal of Biomechanics* 30.9 (1997), pp. 921–931.

[254] Bernard M. Lawless et al. "Viscoelastic properties of a spinal posterior dynamic stabilisation device". In: *Journal of the Mechanical Behavior of Biomedical Materials* 59 (2016), pp. 519–526. DOI: `10.1016/j.jmbbm.2016.03.011`.

[255] Carolina Lavecchia et al. "Celavecchia/Lmg: Lumbar Model Generator First Release". In: (Jan. 2017). DOI: `10.5281/ZENODO.835879`.

[256] Hendrik Schmidt et al. "Intradiscal Pressure, Shear Strain, and Fiber Strain in the Intervertebral Disc Under Combined Loading". In: *Spine* 32.7 (2007), pp. 748–755. DOI: `10.1097/01.brs.0000259059.90430.c2`.

[257] Antonius Rohlmann et al. "Influence of a Follower Load on Intradiscal Pressure and Intersegmental Rotation of the Lumbar Spine". In: *Spine (Phila Pa 1976)* 26.24 (2001), E557–E561. DOI: `10.1097/00007632-200112150-00014`.

[258] Giacomo Marini et al. "Geometrical aspects of patient-specific modelling of the intervertebral disc: collagen fibre orientation and residual stress distribution". In: *Biomechanics and Modeling in Mechanobiology* 15.3 (2015), pp. 543–560. DOI: `10.1007/s10237-015-0709-6`.

[259] Nathan T. Jacobs et al. "Validation and application of an intervertebral disc finite element model utilizing independently constructed tissue-level constitutive formulations that are nonlinear, anisotropic, and time-dependent". In: *Journal of Biomechanics* 47.11 (2014), pp. 2540–2546. DOI: `10.1016/j.jbiomech.2014.06.008`.

[260] Antonius Rohlmann et al. "Effect of total disc replacement with ProDisc on intersegmental rotation of the lumbar spine." In: *Spine* 30.7 (2005), pp. 738–43. DOI: `10.1097/01.brs.0000157413.72276.c4`.

[261] Ruth K. Wilcox et al. "A Dynamic Study of Thoracolumbar Burst Fractures". In: *The Journal of bone and joint surgery. American volume* 85-A (2003), pp. 2184–2189.

[262] Daniel J Woldtvedt et al. "Finite Element Lumbar Spine Facet Contact Parameter Predictions are Affected by the Cartilage Thickness Distribution and Initial Joint Gap Size". In: 133.June 2011 (2015), pp. 1–7. DOI: `10.1115/1.4004287`.

[263] Steve Maas et al. "FEBio User's Manual". In: (2007), pp. 0–52.

[264] Sung M. Moon et al. "Evaluation of intervertebral disc cartilaginous endplate structure using magnetic resonance imaging". In: *European Spine Journal* 22.8 (2013), pp. 1820–1828. DOI: `10.1007/s00586-013-2798-1`.

[265] Gentaro Hirota et al. "An improved finite-element contact model for anatomical simulations". In: *Visual Computer* 19.5 (2003), pp. 291–309. DOI: `10.1007/s00371-002-0188-5`.

[266] Hermann Matthies et al. "The solution of nonlinear finite element equations". In: *International Journal for Numerical Methods in Engineering* 14.11 (Jan. 1979), pp. 1613–1626. DOI: `10.1002/nme.1620141104`.

[267] Wei Fan et al. "Influence of different frequencies of axial cyclic loading on time-domain vibration response of the lumbar spine: A finite element study". In: *Computers in Biology and Medicine* 86.3 (2017), pp. 75–81. DOI: `10.1016/j.compbiomed.2017.05.004`.

[268] R. N. Natarajan J. R. Williams et al. "Inclusion of Regional Poroelastic Material Properties Better Predicts Biomechanical Behavior of Lumbar Discs Subjected to Dynamic Loading". In: 40.9 (2007), pp. 1981–1987. DOI: `10.1016/j.jbiomech.2006.09.022.Inclusion`.

[269] Y.M. M Lu et al. *Do bending, twisting, and diurnal fluid changes in the disc affect the propensity to prolapse? A viscoelastic finite element model.* 1996. DOI: `10.1097/00007632-199611150-00006`.

[270] C Hirsch et al. "New observations on the mechanical behavior of lumbar discs." In: *Acta Orthopaedica Scandinavica* 23.4 (1954), pp. 254–283. DOI: `10.3109/17453675408991217`.

[271] Keith L Markolf et al. "The Structural Components of the Intervertebral Disc". In: *The Journal of Bone & Joint Surgery* 56.4 (1974), pp. 675–687.

[272] B R Simon et al. "Structural models for human spinal motion segments based on a poroelastic view of the intervertebral disk." In: *Journal of biomechanical engineering* 107.4 (Nov. 1985), pp. 327–35.

[273] M A Adams et al. "Mechanical initiation of intervertebral disc degeneration". In: *Spine (Phila Pa 1976)* 25.13 (2000), pp. 1625–1636. DOI: `10.1097/00007632-200007010-00005`.

[274] P Brinckmann et al. "Change of disc height, radial disc bulge, and intradiscal pressure from discectomy. An in vitro investigation on human lumbar discs." In: *Spine* 16.6 (June 1991), pp. 641–6.

[275] N Newell et al. "Biomechanics of the human intervertebral disc: a review of testing techniques and results". In: *Journal of the Mechanical Behavior of Biomedical Materials* 69.August 2016 (2017), pp. 420–434. DOI: 10.1016/j.jmbbm.2017.01.037.

[276] N. Cappetti et al. "Finite elements/Taguchi method based procedure for the identification of the geometrical parameters significantly affecting the biomechanical behavior of a lumbar disc". In: *Computer Methods in Biomechanics and Biomedical Engineering* 5842.June (2015), pp. 1–8. DOI: 10.1080/10255842.2015.1128529.

[277] Patricia Dolan et al. "Recent advances in lumbar spinal mechanics and their significance for modelling". In: *Clinical Biomechanics* 1.1 (2001), pp. 8–16.

[278] M. A. Adams et al. "'Stress' distributions inside intervertebral discs. The effects of age and degeneration." In: *The Journal of bone and joint surgery. British volume* 78.6 (1996), pp. 965–972. DOI: 10.1302/0301-620X78B6.1287.

[279] Alireza Abouhossein et al. "A multibody modelling approach to determine load sharing between passive elements of the lumbar spine". In: *Computer Methods in Biomechanics and Biomedical Engineering* 14.6 (2011), pp. 527–537. DOI: 10.1080/10255842.2010.485568.

[280] F Azari et al. "A combined passive and active musculoskeletal model study to estimate L4-L5 load sharing". In: *Journal of Biomechanics* (2017). DOI: 10.1016/j.jbiomech.2017.04.026.

[281] Enrico Schileo et al. "Subject-specific finite element models can accurately predict strain levels in long bones". In: *Journal of Biomechanics* 40.13 (2007), pp. 2982–2989.

[282] Lorenzo Grassi et al. "How accurately can subject-specific finite element models predict strains and strength of human femora? Investigation using full-field measurements". In: *Journal of Biomechanics* 49.5 (Mar. 2016), pp. 802–806. DOI: 10.1016/J.JBIOMECH.2016.02.032.

[283] G. L. Niebur et al. "Convergence Behavior of High-Resolution Finite Element Models of Trabecular Bone". In: *Journal of Biomechanical Engineering* 121.6 (Dec. 1999), p. 629. DOI: 10.1115/1.2800865.

[284] James C. Iatridis et al. "Degeneration affects the anisotropic and nonlinear behaviors of human anulus fibrosus in compression". In: *Journal of Biomechanics* 31.6 (1998), pp. 535–544. DOI: 10.1016/S0021-9290(98)00046-3.

[285] Norimasa Nakamura et al. "The location-specific healing response of damaged articular cartilage after ACL reconstruction: short-term follow-up". In: *Knee Surgery, Sports Traumatology, Arthroscopy* 16.9 (Sept. 2008), pp. 843–848. DOI: 10.1007/s00167-008-0565-3.

[286] Andrea Malandrino et al. "Poroelastic modeling of the intervertebral disc: A path toward integrated studies of tissue biophysics and organ degeneration". In: *MRS Bulletin* 40.04 (2015), pp. 324–332. DOI: 10.1557/mrs.2015.68.

[287] O'Connell, Grace D. and Johannessen, Wade and Vresilovic, Edward J. and Elliott, Dawn M. "Human Internal Disc Strains in Axial Compression Measured Noninvasively Using Magnetic Resonance Imaging". In: *Spine* 32.25 (2007), pp. 2860–2868. DOI: 10.1097/BRS.0b013e31815b75fb.

[288] H. A L Guerin et al. "Degeneration affects the fiber reorientation of human annulus fibrosus under tensile load". In: *Journal of Biomechanics* 39.8 (2006), pp. 1410–1418. DOI: 10.1016/j.jbiomech.2005.04.007.

[289] Arin M. Ellingson et al. "Comparative role of disc degeneration and ligament failure on functional mechanics of the lumbar spine". In: *Computer Methods in Biomechanics and Biomedical Engineering* 5842.September (2015), pp. 1–10. DOI: 10.1080/10255842.2015.1088524. arXiv: 15334406.

[290] Andrea Malandrino et al. "Statistical factorial analysis on the poroelastic material properties sensitivity of the lumbar intervertebral disc under compression , flexion and axial rotation". In: *Journal of Biomechanics* 42.16 (2009), pp. 2780–2788. DOI: 10.1016/j.jbiomech.2009.07.039.

[291] Zheng-Cheng Zhong et al. "Finite element analysis of the lumbar spine with a new cage using a topology optimization method." In: *Medical engineering & physics* 28.1 (Jan. 2006), pp. 90–8. DOI: 10.1016/j.medengphy.2005.03.007.

[292] Michael A. Adams et al. "Intervertebral disc degeneration: Evidence for two distinct phenotypes". In: *Journal of Anatomy* 221.6 (2012), pp. 497–506. DOI: 10.1111/j.1469-7580.2012.01551.x.

[293] K Sato et al. "In vivo intradiscal pressure measurement in healthy individuals and in patients with ongoing back problems." In: *Spine* 24.23 (1999), pp. 2468–2474. DOI: 10.1097/00007632-199912010-00008.

[294] Márta Kurutz and László Oroszváry. "Finite Element Modeling and Simulation of Healthy and Degenerated Human Lumbar Spine". In: (2006).

[295] G. A. Holzapfel et al. "Single lamellar mechanics of the human lumbar anulus fibrosus". In: *Biomechanics and Modeling in Mechanobiology* 3.3 (2005), pp. 125–140. DOI: 10.1007/s10237-004-0053-8.

[296] John M. Peloquin et al. "Human L3L4 intervertebral disc mean 3D shape, modes of variation, and their relationship to degeneration". In: *Journal of Biomechanics* 47.10 (2014), pp. 2452–2459. DOI: 10.1016/j.jbiomech.2014.04.014. arXiv: NIHMS150003.

[297] Claudio Vergari et al. "Lamellar and fibre bundle mechanics of the annulus fibrosus in bovine intervertebral disc". In: *Acta Biomaterialia* 37 (2016), pp. 14–20. DOI: 10.1016/j.actbio.2016.04.002.

[298] Marlène Mengoni et al. "Derivation of inter-lamellar behaviour of the intervertebral disc annulus". In: *Journal of the Mechanical Behavior of Biomedical Materials* 48 (2015), pp. 164–172. DOI: 10.1016/j.jmbbm.2015.03.028.

[299] D. Ambard et al. "Mechanical behavior of annulus fibrosus: A microstructural model of fibers reorientation". In: *Annals of Biomedical Engineering* 37.11 (2009), pp. 2256–2265. DOI: 10.1007/s10439-009-9761-7.

[300] Sahand Zanjani-Pour et al. "Image driven subject-specific finite element models of spinal biomechanics". In: *Journal of Biomechanics* 49.6 (2016), pp. 919–925. DOI: 10.1016/j.jbiomech.2016.02.025.

[301] Andrea Malandrino. "Multi-scale biomechanical study of transport phenomena in the intervertebral disc". In: *PhD Thesis, Universitat Politecnica de Catalunya* (2012).

[302] Daniel M Espino et al. "Stochastic finite element analysis of biological systems: comparison of a simple intervertebral disc model with experimental results." In: *Computer methods in biomechanics and biomedical engineering* 6.4 (2003), pp. 243–8. DOI: 10.1080/10255840310001606071.

[303] Cédric Barrey et al. "Pedicle-Screw-Based Dynamic Systems and Degenerative Lumbar Diseases: Biomechanical and Clinical Experiences of Dynamic Fusion with Isobar TTL." In: *ISRN orthopedics* 2013.Figure 1 (2013), p. 183702. DOI: 10.1155/2013/183702.

[304] Hugh David Thomas. "Finite element analysis of an intervertebral disc posterior dynamic stabilisation device". In: *Master Thesis, University of Birmingham* (2015).

[305] C E Lavecchia et al. "Finite Element Model of the L4-L5 functional unit with a posterior stabilisation device: a preliminary study." In: *ESB congress* (2017), p. 604935.

[306] Thomas J. Joyce et al. "Analysis of Explanted Magnetically Controlled Growing Rods From Seven UK Spinal Centers". In: *SPINE* 43.1 (Jan. 2018), E16–E22. DOI: `10.1097/BRS.0000000000002221`.

[307] Haisheng Yang et al. "Effective modulus of the human intervertebral disc and its effect on vertebral bone stress". In: *Journal of Biomechanics* 49 (2016), pp. 1–7. DOI: `10.1016/j.jbiomech.2016.02.045`.

[308] Donita I. Bylski-Austrow et al. "Flexible growing rods: A biomechanical pilot study of polymer rod constructs in the stability of skeletally immature spines". In: *Scoliosis and Spinal Disorders* 11.1 (2016), pp. 1–9. DOI: `10.1186/s13013-016-0087-6`.

[309] P Guerin et al. "Effect of new dynamic stabilization system on the segmental motion and intradiscal pressure: An in vitro biomechanical study". In: *ORS 2011 Annual Meeting* No. 748 (2011), p. 2011.

[310] B. Lawless. "In vivo degradation of the BDyn spinal posterior dynamic stabilisation device: a retrieval analysis". In: *Under preparation* (2018).

[311] Bernard M. Lawless. "Biostability of an orthopaedic device and its long-term implantable biomaterials". In: *PhD Thesis, University of Birmingham* (2018).

[312] S. C. Barnes et al. "Frequency dependent viscoelastic properties of porcine bladder". In: *Journal of the Mechanical Behavior of Biomedical Materials* 42 (2015), pp. 168–176. DOI: `10.1016/j.jmbbm.2014.11.017`.

[313] Daniel M Espino et al. "Viscoelastic properties of bovine knee joint articular cartilage: dependency on thickness and loading frequency". In: *BMC Musculoskeletal Disorders* 15.1 (2014), p. 205. DOI: `10.1186/1471-2474-15-205`.

[314] Eenas A Omari et al. "Dynamic and Quasi-Static mechanical testing for characterization of the viscoelastic properties of human uterine tissue". In: *J Biomech* 48.10 (2016), pp. 1730–1736. DOI: `10.1016/j.jbiomech.2015.05.013.Dynamic`.

[315] S. Kitazaki et al. "a Modal Analysis of Whole-Body Vertical Vibration, Using a Finite Element Model of the Human Body". In: *Journal of Sound and Vibration* 200 (1997), pp. 83–103. DOI: `10.1006/jsvi.1996.0674`.

[316] R N Stiles et al. "Mechanical factors in human tremor frequency." In: *Journal of applied physiology* 23.3 (Sept. 1967), pp. 324–30.

[317] Lea Artibai et al. "Dynamic Stiffness and Damping Prediction on Rubber Material Parts , FEA and Experimental Correlation Zorion Kareaga Laka PhD - Doctor Europaeus". In: *PhD Thesis, London Metropolitan University* (2016).

[318] Fatima Somovilla Gomez et al. "Improving the process of adjusting the parameters of Finite Element Models of healthy human intervertebral discs by the Multi-response Surface Method". In: *Materials* (2017). DOI: `10.3390/ma10101116`.

[319] Visakh. P. M. *Advances in elastomers II : composites and nanocomposites.* Springer, 2013. ISBN: 3642209289.

[320] Leonard R. Herrmann et al. "Nolinear Behavior of Elastomeric Barings. I: Theory". In: *Journal of Engineering Mechanics* 114.11 (Nov. 1988), pp. 1811–1830. DOI: `10.1061/(ASCE)0733-9399(1988)114:11(1811)`.

[321] G. F. Smith et al. "The strain-energy function for anisotropic elastic materials". In: *Transactions of the American Mathematical Society* 88.1 (1958), pp. 175–175. DOI: `10.1090/S0002-9947-1958-0095618-2`.

[322] Stephen J. Ferguson et al. "Fluid flow and convective transport of solutes within the intervertebral disc". In: *Journal of Biomechanics* 37.2 (Feb. 2004), pp. 213–221. DOI: `10.1016/S0021-9290(03)00250-1`.